



Advanced Technologies for Energy and Environment

*edited by
Henryka D. Stryczewska
Kenji Ebihara*



MONOGRAPHIE

Lublin 2023

Advanced Technologies for Energy and Environment

Monographs – Lublin University of Technology

Scientific Council of the Lublin University of Technology Publishing House

Head of the Council:

Agnieszka RZEPKA

Director of the Centre of Scientific and Technical Information:

Katarzyna WEINPER

Lublin University of Technology Publishing House

Magdalena CHOŁOJCZYK

Jarosław GAJDA

Anna KOŁTUNOWSKA

Katarzyna PEŁKA-SMĘTEK

Representatives of the scientific disciplines:

Marzenna DUDZIŃSKA

Małgorzata FRANUS

Arkadiusz GOLA

Paweł KARCZMAREK

Beata KOWALSKA

Anna KUCZMASZEWSKA

Jarosław LATALSKI

Tomasz LIPECKI

Zbigniew ŁAGODOWSKI

Joanna PAWŁAT

Lucjan PAWŁOWSKI

Natalia PRZESMYCKA

Magdalena RZEMIENIAK

Mariusz ŚNIADKOWSKI

Honorary representatives:

Zhihong CAO, Chiny

Miroslav GEJDOŚ, Słowacja

Karol HENSEL, Słowacja

Hrvoje KOZMAR, Chorwacja

Frantisek KRCMA, Czechy

Sergio Lujan MORA, Hiszpania

Dilbar MUKHAMEDOVA, Uzbekistan

Sirgii PAWŁOW, Ukraina

Natalia SAVINA, Ukraina

Natia SHENGELIA, Gruzja

Daniele ZULLI, Włochy

Advanced Technologies for Energy and Environment

edited by
Henryka D. Stryczewska
Kenji Ebihara



POLITECHNIKA
LUBELSKA
LUBLIN UNIVERSITY
OF TECHNOLOGY

Lublin 2023

Reviewers:

Prof. Seiji Kanazawa, Oita University, Japan

Prof. Karol Hensel, Comenius University, Slovakia

Editors:

Prof. Eng. Henryka Danuta Stryczewska, Lublin University of Technology, Poland

Prof. Kenji Ebihara, Kumamoto University, Japan

Technical editor: Oleksandr Boiko

The monograph has been co-financed from the funds of the Polish National Agency for Academic Exchange NAWA, project No PPI_APM_2019_1_00009: "Polish-Japanese Energo-Eco Studies and Expert Visits".

Publication approved by the Rector of Lublin University of Technology

ISBN: 978-83-7947-556-8

Publisher: Wydawnictwo Politechniki Lubelskiej
www.wpl.pollub.pl
ul. Nadbystrzycka 36C, 20-618 Lublin
tel. (81) 538-46-59

Printed by: Agencja Reklamowa TOP Agnieszka Łuczak
www.agencjatop.pl

The digital version is available at the Digital Library of Lublin University of Technology: www.bc.pollub.pl

The book is available under the Creative Commons Attribution license – under the same conditions 4.0 International (CC BY-SA 4.0)

Circulation: 40 copies

Table of contents

Streszczenie.....	9
Abstract	10
List of abbreviations and symbols	11
Preface.....	15
<i>Henryka Danuta Stryczewska, Kenji Ebihara</i>	
1. Sustainable development of energy and environment	18
<i>Henryka Danuta Stryczewska, Oleksandr Boiko</i>	
2. Plasma properties and generation	22
2.1. Properties and classification of plasma	22
2.2. Gliding and dielectric barrier discharges for plasma generation	23
<i>Fumiaki Mitsugi, Henryka Danuta Stryczewska, Kenji Ebihara, Shin-ichi Aoqui</i>	
3. Non-thermal plasma reactors	27
3.1. Brief characterization of non-thermal plasma reactors	27
3.2. Arc and gliding arc discharges as a source of plasma.....	33
3.3. Mathematical modelling of AD and GAD plasma reactors	39
3.4. Modelling of temperature distribution in the discharge chamber of GA plasma reactor	46
<i>Henryka Danuta Stryczewska</i>	
4. Power systems of non-thermal plasma reactors.....	52
4.1. Introduction	52
4.2. Power and efficiency of supply systems for non-thermal plasma reactors.....	53
4.3. Power supply systems for plasma reactors with DBD.....	54
4.4. Power supply systems for plasma reactors with GAD.....	57
4.5. Summary	62

*Kenji Ebihara, Fumiaki Mitsugi, Henryka Danuta Stryczewska,
Oleksandr Boiko, Jacek Majcher*

5. Cold plasma for agricultural applications.....	64
5.1. Introduction.....	64
5.2. Plasma in agricultural soil treatment.....	66
5.3. Advanced techniques for agriculture management, pest control and plant growth	72
5.4. Pre-sowing seed treatment with cold plasma	85
5.5. Measurement of soil moisture.....	86

Michał Majka

6. Superconducting fault current limiters	90
6.1. Introduction.....	90
6.2. Tests of superconducting tapes parameters for fault current limiters	92
6.3. Soldered connections of superconducting tapes	97
6.4. Cooling of superconducting devices	99
6.5. Inductive type superconducting current limiters with shielded core	102
6.6. Coreless inductive superconducting fault current limiters.....	103
6.7. Superconducting fault current limiter 6.9 kV/600 A	106
6.8. Superconducting fault current limiter 15 kV/140 A	108
6.9. Contact-cooled superconducting fault current limiter rated at 6 kV/140 A.....	110
6.10. Summary	113

Jacek Majcher

7. Electrostatic field in the process of separation of loose materials.....	115
7.1. Introduction.....	115
7.2. Segregation methods for crushed materials	116
7.3. Use of electrostatic field in separators	118

7.4. Application of electrostatic fields in industrial practice	119
7.5. Summary	122

Paweł A. Mazurek

8. Electromagnetic compatibility of devices and installations in electrotechnologies supporting environmental protection.....	123
8.1. Introduction.....	123
8.2. Electromagnetic compatibility testing and analysis.....	124
8.3. Methods of testing radiated emissivity of devices	125
8.4. Methods of testing conducted emissivity of devices	126
8.5. Immunity test methods for electrical equipment.....	127
8.6. Electromagnetic compatibility of plasma reactors.....	128
8.7. Electromagnetic compatibility of electric vehicle chargers.....	132
8.8. Summary	137

Masaaki Yamazato, Akira Higa, Oleksandr Boiko

9. Innovative and energy-saving materials, electronic and power engineering technologies	138
9.1. Environment-friendly materials	138
9.2. Advanced granular nanomaterials for nanoelectronics.....	146

Marcin Buczaj

10. Environmentally friendly electricity management.....	165
--	-----

Yuto Nomaguchi, Kasumi Nagata, Takumi Furusawa, Seiji Kudo, Shuto Fujiko, Yasuo Ogimi, Aleksander Chudy, Sławomir Durak, Michał Lech, Damian Kostyla, Alicja Zielonka, Bartłomiej Stadnik

11. Selected problems of electrotechnology in master and PhD students' research.....	183
11.1. Brief reports on electrotechnology in agriculture.....	183
11.2. Brief reports on amorphous carbon nitride thin films	184

11.3. Measurements and analysis of power quality parameters during electric vehicle charging 186

11.4. Parameters of vacuum interrupters designed for modern switchgear..... 195

11.5. Vacuum switchgear pressure measurement in Smart Grid networks 204

11.6. Bifacial photovoltaic panels in PV installations for increasing the efficiency of electricity generations 210

11.7. Executive elements and application of automation 219

12. Summary 227

References..... 229

ZAAWANSOWANE TECHNOLOGIE W ZAKRESIE ENERGII I ŚRODOWISKA

Streszczenie

Książka stanowi podsumowanie współpracy Wydziału Elektrotechniki i Informatyki Politechniki Lubelskiej w uniwersytetami japońskimi w obszarach zaawansowanych technologii inżynierii elektrycznej i inżynierii środowiska. Obejmują one technologie nietermicznej plazmy, nadprzewodnictwo, kompatybilność elektromagnetyczną urządzeń technologicznych, inteligentne (smart) instalacje elektryczne, nowoczesne i przyjazne środowisku materiały i urządzenia, energetykę odnawialną oraz oszczędną dla środowiska elektroenergetykę.

Taki zakres tematyczny wynika z realizowanego w ramach programu NAWA, Akademickie Partnerstwa Międzynarodowe projektu zatytułowanego Energo-Eco Studies and Expert Visits realizowanego w latach 2019–2022, którego partnerami są 3 uniwersytety japońskie: Kumamoto, Sojo i Ryukyus oraz Laboratorium Środowiska i Energii. Główne cele projektu to wizyty studyjne i wymiana studentów, ich mentorów i ekspertów w dziedzinie elektrotechniki i ekologii na uczelniach partnerskich, promowanie najlepszych praktyk i innowacyjnych rozwiązań w zakresie zaawansowanych, energooszczędnych i przyjaznych dla środowiska technologii do zastosowań w elektrotechnice, elektronice, energetyce, inżynierii środowiska i rolnictwie a także definiowanie nowych dyscyplin badawczych w zakresie B+R. Nie mniej ważne cele projektu to umiędzynarodowienie kształcenia, podniesienie konkurencyjności absolwentów uczelni uczestniczących w projekcie na lokalnych i międzynarodowych rynkach pracy, promowanie kierunku elektrotechnika wśród kandydatów na studia, poprzez wizyty studentów i ich opiekunów w uczelniach partnerskich. Temu celowi służy rozdział 11 monografii, który zawiera przegląd tematyki badawczej realizowanej przez studentów i doktorantów uczelni partnerskich pod kierunkiem ich mentorów.

Książkę adresujemy do studentów i doktorantów uczelni partnerskich, ich mentorów a także absolwentów uczelni partnerskich, którzy wykorzystują zaawansowane i przyjazne środowisku technologie elektrotechniczne w swej pracy zawodowej i chcą je upowszechniać, doskonalić i wdrażać do praktyki inżynierskiej, także we współpracy międzynarodowej.

Słowa kluczowe: energia, środowisko, technologie plazmowe, urządzenia elektromagnetyczne, materiały funkcyjne

ADVANCED TECHNOLOGIES FOR ENERGY AND ENVIRONMENT

Abstract

The book is a summary of the cooperation between the Faculty of Electrical Engineering and Computer Science of Lublin University of Technology and Japanese universities in areas of advanced technologies in electrical and environmental engineering. These fields include non-thermal plasma technologies, superconductivity, electromagnetic compatibility of technological devices, smart electrical installations, modern and environmentally friendly materials and devices, renewable energy and environmentally friendly electricity.

This thematic scope is a result of the project implemented under the Polish National Agency for Academic Exchange (NAWA) Academic International Partnerships programme entitled “Energco-Eco Studies and Expert visits”, carried out between 2019–2022, whose partners are three Japanese universities: Kumamoto, Sojo and Ryukyus, and the Environment and Energy Laboratory. The main goals of the project are study visits and exchange of students and their mentors, who are experts in the field of electrical engineering and ecology at partner universities, promoting best practices and innovative solutions in the field of advanced, energy-saving and environmentally friendly technologies for applications in electrical engineering, electronics, energy, environmental engineering and agriculture as well as defining new research disciplines in the field of R&D.

No less important as goals of the project are the internationalisation of education, increasing the competitiveness of graduates of universities participating in the project on local and international labour markets, and promoting the field of electrical engineering among prospective students, through visits of students and their supervisors to partner universities. This purpose is served by Chapter 11 of the monograph, which contains an overview of research topics carried out by students and doctoral students at partner universities under the supervision of their mentors.

The book is addressed to students and doctoral students at partner universities, their mentors as well as graduates of partner universities who use advanced and environmentally friendly electrotechnical technologies in their professional work and want to disseminate, improve and implement these in engineering practice and in international cooperation.

Keywords: energy, environment, plasma technologies, electromagnetic devices, functional materials

List of abbreviations and symbols

Symbol/ Abbreviation	Description
a	distance from the centre of the cathode
A_s	normalisation factor
AC	alternative current
AD	arc discharge
ARS	abnormal resistance switching
B_1	first harmonic induction
B_{30}	third harmonic induction
B_r	remanence induction
B_s	saturation induction
BMS	building management system
c_p	specific heat
C_p	capacitance measured in parallel equivalent scheme
C_s	capacitance in series circuit
CAD	computer-aided design
CAP	cold atmospheric plasma
d	gap width in Townsend discharge
D	distortion reactive power
d_f	film density
d_w	winding diameter
DBD	dielectric barrier discharge
DC	direct current
DL	deep learning
f	frequency
F_e	electrophoresis force
f_{RP}	resonant frequency in parallel circuit
f_{RS}	resonant frequency in series circuit
E	electric field intensity
E_p	electric field strength from the space charge
E_{Tauc}	optical bandgap energy
E_z	external electric field
EMC	electromagnetic compatibility
EV	electric vehicle
FWHM	full width at half maximum of I_{mn}
g_0	discharge conductance at the point of ignition
$g(t)$	instantaneous conductance of the arc column
GD	glow discharge

Symbol/ Abbreviation	Description
h_w	winding height
HMI	human-machine interface
HTS	high temperature superconductor
$i(t)$	electric current vs. time dependence
I	electric current
I_H	integrated intensity of absorption band
I_{overload}	overload current
i_p	first peak limiting current
i_{peak}	prospective peak current
I_c	critical current
I_{mn}	normalised value of greenness index
I_{max}	peak green index
I_n	nominal current
IPS	integrated power supply system
IR	infrared spectrum
l_0	initial electrode length
$l_i(t)$	discharge length
$l(t)$	time-varying GAD length
L1	first phase working wire
L2	second phase working wire
L3	third phase working wire
L_p	inductance in parallel circuit
L_s	inductance in series circuit
LUT	Lublin University of Technology
m	weight
m3f	magnetic frequency tripler
M_H	mass of the hydrogen atom
M_C	mass of the carbon atom
N	neutral wire
n_e	electron density
n_H	hydrogen concentration
N_H	atomic hydrogen concentration
NAWA	Polish National Agency for Academic Exchange
NC	nanocomposite
p	gas pressure
P	active power
P_0	power given off per unit length of an arc column
p_{ref}	reference pressure

Symbol/ Abbreviation	Description
pH	potential of hydrogen
PEN	protective earthed neutral wire
PLC	programmable logic controller
q	density of heat flux
Q	capacitive reactive power
Q_C	compensating reactive power from capacitors
Q_{ch}	power of the compensation choke
Q_L	chokes limiting power
q_m	maximum flux flowing out of the cooled surface
q_p	electric charge of the particle
r	polar coordinate
r_{nc}	distance between adjacent potential wells
R_p	resistance measured in parallel equivalent scheme
R_s	resistance in series circuit
R&D	Research & Development
RFID	radio frequency identification
S_0	maximum value of the local greenness index S_{mn}
S_{mn}	greenness index intensity
S_t	apparent power of the transformer
SDBD	surface dielectric barrier discharge
SL	local greenness index intensity
t	time
T	temperature
T_c	critical temperature
T_e	electron temperature
T_g	gas temperature
t_k	period of time for superconducting tape current switching off
T_{kmax}	maximum temperature of superconducting tape
T_{max}	maximum temperature at the cathode
T_p	measuring temperature
t_z	time corresponding to the moment of ignition of the discharge
TDD	total demand distortion
$tg\delta$	dielectric loss coefficient
U	electric voltage
U_{db}	breakdown voltage
U_n	nominal voltage
U_{SFCL}	Voltage on the limiter at I_n
U_{st}	arc voltage in steady-state conditions

Symbol/ Abbreviation	Description
UV	ultra-violet
u	axial plasma velocity
$u(t)$	voltage vs. time dependence
v	radial plasma velocity
v_g	gas flow velocity
v_w	wavenumber
x	metallic phase content
x_c	percolation threshold
XPS	X-ray photoelectron spectroscopy
y	oxygen content
Z_N	impedance connected in series in the neutral conductor
α_{db}	experimentally determined constant
α_r	value close to the reciprocal of the location radius
α_w	absorption coefficient
β	electrode flare angle
β_r	numerical factor
ΔE_σ	activation energy of conductivity
ΔP_{at}	power losses in autotransformer
ΔP_t	transformer power losses
ΔT	temperature difference
ϵ_r	relative permittivity
η	transformer's efficiency
φ	phase shift angle
λ	gas thermal conductivity
λ_{pf}	ozone generator's power factor
μ	gas viscosity
ρ	specific gas density
ρ_{nc}	electric resistivity
σ	electric conductivity
σ_0	material constant
τ_c	time constant of arc under Cassie's assumptions
τ_M	time constant of arc under Mayr's assumptions
γ	secondary emission factor
ω	angular frequency
ω_{RP}	resonant angular frequency in parallel circuit
ω_{RS}	resonant angular frequency in series circuit

Preface

The aim of this book is to present the ecological applications of non-thermal plasma, superconductivity and other chosen electrotechnologies. The book contains the results of research conducted at the Department of Electrical Engineering and Electrotechnology of Lublin University of Technology in cooperation with Japanese universities and laboratories – Kumamoto University, Sojo University, and the Environment and Energy Laboratory at Kumamoto and Ryukyus University in Okinawa.

Japan and Poland, which have quite limited energy resources, should attach special importance to ecology, especially the economical use of energy resources and environmental protection.

At the turn of the twenty-first century, Kumamoto University established the Endowed Chair in Advanced Technology for Electric Energy, funded by the Kyushu Energy Corporation, to which scientists from all over the world were invited every year. They conducted scientific research, participated in joint research projects, and gave lectures for Japanese students, sharing their knowledge and experience in Advanced Technologies for Electric Energy and Environment.

The co-founder of this idea and co-editor of this book, Professor Kenji Ebihara, at that time the head of Electric Energy Conversion Laboratory and presently the head of the Environment and Energy Laboratory, had the goal of rapid implementation of many advanced technologies in Japan and developing joint research and international cooperation in the field of energy-saving and environmentally friendly technologies.

It is today, when none of the world powers are self-sufficient in energy production, and the pollution resulting from energy production and processing has no limits and causes global environmental problems, an idea worth following by everyone, no matter where we work and live and what our share of technological development and environmental pollution is.

The co-editor of this book, Professor Henryka Danuta Stryczewska from the Department of Electrical Engineering and Electrotechnology of Lublin University of Technology in 2003–2004, worked as a visiting professor in the Endowed Chair of Advanced Technology for Electric Energy for one year, conducting research on soil treatment with ozone and giving lectures on cold plasma application in power engineering and ecology. Joint research on the use of non-thermal plasma technology in agriculture resulted in numerous publications and the implementation of international projects in cooperation with Kumamoto and Sojo universities.

Lublin University of Technology (LUT) has been cooperating with Japanese universities for over forty years. The initiators of this cooperation were faculty members of the Department of Electrical Engineering, among whom the main role in the initial period was played by Professor Tadeusz Janowski, professor emeritus

of LUT and Professor Andrew Nafalski. The contacts between the Faculty of Electrical Engineering and Computer Science of Lublin University of Technology and Japanese universities date back to 1983, when the first bilateral agreement with Kanazawa University was signed. Since then, many researchers from partner universities and students have participated in annual exchanges, doctoral studies, scientific conferences, visits with lectures, etc. Moreover, above mentioned Faculty also works closely with Kumamoto University, Sojo University, Saga University and since 2019 with the University of the Ryukyus.

This cooperation covers innovative areas of electrical engineering and ecology: research on low-temperature plasma – its generation, diagnostics and applications; plasma methods of reducing the emission of gaseous and solid pollutants in conventional energy and from alternative sources; ozone generation and its use in water and soil treatment as well as in sterilisation and disinfection processes; applications of superconductors in electrical devices, metrology and electronics, etc. This cooperation is very valuable for the units involved due to the similar research directions and complementary laboratories and research apparatus.

In 2020–2022, Lublin University of Technology, in cooperation with Kumamoto, Sojo, Ryukyus universities and the Laboratory of Environment and Energy, have been implementing a project financed by the Polish National Agency for Academic Exchange (NAWA) as part of the International Partnership with the acronym *Pol-Jap Energy-Eco Studies and Experts Visits*. It aims to update the results of joint research in electrical and ecological engineering.

Cooperation with Japan is very important for Poland due to the research on related topics in the field of generation applications of non-thermal plasma, as well as in the field of superconductivity and other technologies that are based on electric and magnetic phenomena. The objectives of the project include, inter alia, the organisation of study visits and the exchange of experts in the field of electrical engineering and ecology in partner universities, laboratories and local enterprises; promoting best practices and innovative solutions in the field of non-thermal plasma generation and application of superconductivity in environmental protection processes; strengthening cooperation with Kumamoto University, Sojo University and the Environment and Energy Laboratory and establishing a new one with University of the Ryukyus in Okinawa to intensify and develop innovative solutions in the field of R&D and internationalisation of education.

The target groups are students at partner universities, academic staff, local and international participants of conferences in Lublin and Kumamoto, as well as representatives of local enterprises in Japan and in Poland. The benefits of the NAWA project include increasing the mobility of the academic community of partner universities; defining new and strengthening the existing research disciplines in the field of R&D and in cooperation with the needs of local enterprises; increasing the competitiveness of university graduates participating in the project on local and international labour markets, and promoting engineering studies in the electrical engineering among students.

The problems of using electrotechnology in the production and processing of energy in an ecological way have always been a subject of interest and research of the Department of Electrical Engineering and Electrotechnology of LUT.

A significant distinction was the fact that in 2002 the team of the Department in the 5th Framework Program of the EU obtained the status of a Centre of Excellence for the Application of Superconducting and Plasma Technologies in Power Engineering ASPPECT – a scientific unit that has been operating successfully to this day. The Department of Electrical Engineering and Electrotechnology actively participates in the implementation of many European research projects, both as a coordinator and a consortium member. The most important projects financed from the 7th Framework Program and Horizon 2020:

- **Plasma Sterilisation** – Sterilisation of a Variety of Materials, Biomedical and Food Production Equipment Using Low Thermal Atmospheric Pressure Plasma Jet Combined with Advanced Oxidation Process;
- **KORANET2** – Environmental and Biomedical Applications of Microplasmas Produced by Gliding Arc Discharges;
- **KONNECT** project entitled “Plasma catalysis for the sustainable production of hydrogen from hydrocarbons, using energy from renewable sources” – CatPlas, and others.

The Department of Electrotechnical Engineering and Electrotechnology has been organizing the ELMECO – Electromagnetic Devices and Processes in Environmental Protection cyclical international conference for over 30 years. The issues addressed at the conference are related to electromagnetism and ecology such as low-temperature plasma generation, diagnostics, applications; plasma methods of reducing the emission of gaseous and solid pollutants in conventional energy and alternative sources; ozone generation and use in water and soil treatment as well as in sterilisation and disinfection processes; superconductors in electrical devices, metrology and electronics, new electrotechnologies for ecology, broadly understood.

The intention of the editors and authors of the book is to present the basics of knowledge about electrotechnologies in contemporary water, air and soil purification processes as well in energy generation, conversion and utilisation, and to show the results of common studies and projects.

The book was published with the financial support of the NAWA project, for which its editors and authors would like to express their sincere thanks.

1. Sustainable development of energy and environment

Henryka Danuta Stryczewska, Kenji Ebihara

Sustainable development is a philosophy of action and a decision-making process according to which the needs of present generations should be met in a way that does not compromise the ability of future generations to meet these needs. Therefore, decisions made currently must be based on existing solutions or the search for solutions, which will take into account the three most important elements determining the quality of our life: health and well-being, resource management and the environment in which we live. If these three elements interpenetrate and complement each other in all our activities, the idea of sustainable development will be made real and future generations will be able to use the Earth's resources and the natural environment to the same extent as the present ones. The idea of sustainable development, which is schematically presented in Figure 1, is therefore a way of managing Earth's resources to meet the needs of present and future generations and to ensure harmony between development and the need to protect the natural environment.

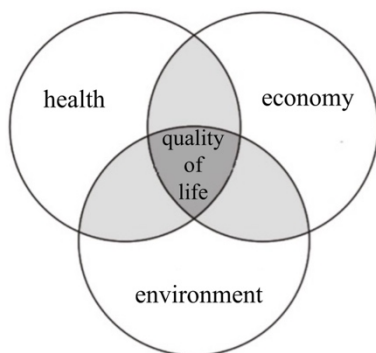


Figure 1. Illustration of the idea of sustainable development. Source: own elaboration based on [1]

In order to implement the principles of sustainable development in practice, it is necessary to [1]:

- use energy resources efficiently,
- participate in making sustainable development decisions,
- ensure equal access to information for all,
- integrate decision-making and planning processes,
- strive to minimise losses and waste,
- develop research and innovation.

The above directions leading to the implementation of the principles of sustainable development apply equally to every human activity, but in the energy sector they acquire a special meaning.

In any energy system, the final product – energy – is the result of many successive energy transformations, using various carriers, such as heat, electricity, fuels or mechanical energy. Usually, as energy sources we understand the primary energy carriers that occur in nature (solid, liquid and gas, the energy of the sun, water, wind, tides). Therefore, energy in the system undergoes many changes, from the extraction of the energy carrier, through its transport, distribution and multiple conversions, to obtaining energy in its final form. This chain of changes causes many problems related to power losses, energy quality degradation and contributes to environmental pollution [2–4].

It can be said with all responsibility that energy systems are not sustainable. Most of them are based on the production of energy from non-renewable sources. A significant part of the power contained in the fuel is irretrievably lost, the quality of the energy deteriorates, and the emission of fossil fuel combustion products into the atmosphere pollutes the natural environment.

Air pollution is the biggest environmental problem because combustion products in the form of volatile carbon compounds, sulphur and nitrogen are often transported with the wind to regions distant from the place of production. There, reacting with the moisture in the atmosphere, they form acids and get into surface waters through rainfall, causing acidification of the environment, damaging vegetation and adversely affecting water resources and soil [1, 5].

Air pollutants can be divided into volatile and solid, and organic and inorganic. We distinguish the following groups of these compounds:

Carbon compounds – carbon monoxide and dioxide (CO , CO_2), organic carbon compounds – hydrocarbons are responsible for the greenhouse effect. The production of carbon dioxide and volatile organic substances is growing rapidly and is discharging enormous amounts of carbon into the environment, mainly due to the burning of solid fuels and to a lesser extent from land consumption and deforestation. Organic carbon compounds, containing chlorine, iodine, bromine and fluorine, did not exist in the atmosphere in pre-industrial times and are the main cause of periodic ozone depletion in the upper atmosphere (ozonosphere), as well as global warming.

Sulphur compounds – sulphur oxides (SO_x), hydrogen sulphide (H_2S), sulphurous and sulfuric acids (H_2SO_3 , H_2SO_4) – are among the main pollutants of the environment. Produced by burning fossil fuels and other sulphur-containing compounds in the presence of water vapor, they form the acid rain.

Nitrogen compounds – nitrogen oxides (NO_x , NO_2 , N_2O), ammonia (NH_3). These are usually produced by high-temperature combustion processes. A significant proportion (60%) is the result of natural nitrogen release from the sea and land, 15% from burning fossil fuels, 10% from biomass combustion and the remaining 15% comes from the use of nitrogen fertilisers [6, 7].

Solid contamination (the so-called insoluble) – dust, soot, coal ash, lubricants, lime, metal oxides, asbestos, silicon compounds (SiO₂), antimony, zinc, radioactive isotopes. Solid contaminants can have various dimensions, from 30 µm to 0.01 µm and smaller. Larger particles settle quickly on the Earth’s surface, but smaller particles remain in the atmosphere for a long time, forming aerosols [5].

The classification of air pollutants and their chemical composition are presented in Table 1.1.

Table 1.1. Classification of air pollutants

Type of contamination	Chemical composition
Organic volatile substances	Hydrocarbons, terpenes, mercaptans, formaldehydes, dioxin, fluorocarbons
Inorganic volatile substances	Sulphur dioxide, hydrogen sulphide, nitrogen oxides, hydrochloric acid, silicon trifluoride, carbon monoxide and dioxide, ammonia, ozone
Organic solids	Dusts, soot, fly ashes
Inorganic solids	Lime, metal oxides, silicon, antimony, zinc, radioactive isotopes and others

Like air quality, water resources and quality are fundamental to life on Earth and to all activities. The main problems with water quality are related to biological and chemical pollution. Biological pollutants are bacteria, viruses and some higher-order organisms that occur naturally in water or are the result of human activity. They can be a source of a wide range of diseases and epidemics. Chemical pollutants generated during industrial processes, agricultural activities or land and waste management are in the form of sediments from toxic substances, fertilisers and sewage and are the cause of soil contamination. We see many examples of the negative impact of technology and human activity on water quality, which covers large areas and huge amounts of water bodies. One such phenomenon is industrial and municipal waste, including toxic waste, the storage, neutralisation and utilisation of which causes air, surface and groundwater and soil pollution. Soil and land are also subject to adverse impacts related to agricultural activity and the use of artificial fertilisers, which significantly contributes to the deterioration of their biological and chemical quality.

Conclusion

Modern energy systems do not develop in a sustainable manner. The progressive increase in demand for electricity brings with it challenges for the power industry in order to develop technologies that allow efficient and environmentally compatible energy generation.

Currently, the greatest potential lies in the use of renewable energy sources, in particular solar energy. Another is the improvement of the efficiency of conventional electricity generation systems through the use of heat and electricity cogeneration. Great hopes are placed on the use of fuel cells and superconducting electrical energy storage systems.

Thanks to the proper use of various electromagnetic technologies, including superconducting and plasma technologies, the emission of harmful compounds has been partially inhibited and power losses related to the production, distribution and use of energy have been reduced, but many problems still await solutions and electrotechnology can contribute to improving this situation.

2. Plasma properties and generation

Henryka Danuta Stryczewska, Oleksandr Boiko

2.1. Properties and classification of plasma

Plasma, called the fourth state of matter, due to its properties different to the solid, liquid and gas phases, is formed at temperatures where the average kinetic energy of particles exceeds the value of the ionisation potential. The moment of change in the physical properties of gas, among which the appearance of electrical conductivity and the loss of insulating capacity are the most important ones, are the boundary separating the gas state and plasma.

In the universe, plasma is the basic state of matter. Stars, nebulae and interstellar material are in the plasma state, and it is estimated that 99.9% of its mass is in this state [8–10]. In terrestrial conditions, plasma is a relatively rare phenomenon. The thick gas layer covering the Earth, called the Earth's atmosphere, absorbs a large part of the ionising radiation, while, like other celestial bodies with a gas atmosphere, our planet has an outer ionised (plasma) shell called the ionosphere. Today, the source of plasma in terrestrial conditions are technological devices as well as processes generating plasma as a side effect (nuclear research, jet and rocket engines, explosives, lightning discharges).

The history of plasma research dates to the mid-eighteenth century, but the concept of plasma was first introduced by the American scientist Irving Langmuir in 1923. It is a state of matter characterised by a very high level of energy band of the particles. Attempts to define the concept of plasma have been made by many researchers. Plasma is a conductive gas so ionised that this determines its macroscopic properties, with positive ions and electrons in such proportions that the resultant charge is equal to zero. Plasma is therefore an ionised gas that is a quasi-neutral mixture of free positive ions and electrons, and disturbances of neutrality appear only in a very small volume of plasma and for short times [11].

The degree of ionisation and the composition of the plasma vary widely. At low temperatures, there is a process of single-electron detachment [12], which is called single ionisation. We are talking then about a partially ionised plasma in which there is a certain number of positive ions, electrons and a large number of non-ionised gas molecules. The increase in temperature causes stronger ionisation of the gas, called enhanced single ionisation and multiple ionisations involving the separation of many electrons from an atom. Complete ionisation takes place at very high temperatures and the plasma becomes a mixture of positive ions and electrons without the participation of neutral particles. In molecular gases, simple ionisation processes are often followed by the phenomenon of dissociation, i.e., the breaking of multi-molecular structures into single atoms.

Plasma exists in a very wide particle energy range, e.g., in the case of electrons, it is from 0.2 eV to 2 MeV. States with even higher energies are theoretically predicted and attempts are being made to study them [11, 13]. The basic classification of plasma in technological applications is the division into low-temperature, non-thermal and nonequilibrium plasma commonly known as “cold”, “warm” plasma in thermo-dynamic equilibrium and high-temperature, and “hot”, produced during thermo-nuclear fusion (called plasma fusion).

Hot plasma occurs in the energy range above a dozen eV, is usually almost completely ionised, and its source in terrestrial conditions are thermonuclear reactions. The technique mainly uses low-temperature plasma, but the mastery of the fusion reaction and the use of hot plasma to generate energy is the subject of advanced research in European, American and Japanese laboratories and gives hope for solving the world’s energy problems.

Cold plasma is assumed to be in the energy range of 0.2 eV to 3 eV, which roughly corresponds to the temperature range of 2000 K to 30000 K (the ratio is $1 \text{ eV} = 11600 \text{ K}$). Low-temperature plasma is usually a slightly ionised gas with a high or very high content of neutral particles. The importance of these particles, for example in the collision process, is decisive for the plasma behaviour.

2.2. Gliding and dielectric barrier discharges for plasma generation

Plasma for technological purposes is usually produced by means of electrical discharges, which can occur in various forms, depending on the geometry of the electrodes and the electrical supply system.

Generation of cold plasma under vacuum or high negative pressure does not present any significant difficulties, but it is expensive and requires special plasma reactor designs. Hence the need to search for reactors in which cold non-equilibrium plasma can be generated under atmospheric pressure conditions.

When analysing the mechanisms of the development of an electric discharge in a gas, we must remember that the electric field in the discharge space affects only previously charged molecules – ions. Thus, the charged gas molecules must be in the discharge space before we apply voltage to the electrodes. In the discharge space there is always a certain number of free electrons emitted by the electrodes due to the ubiquitous cosmic radiation, too few, however, to sustain an electric discharge in the absence of an external potential.

The application of strong electric field to the system of cathode (high negative potential) and anode (high positive potential) electrodes nearby, leads to the electron’s attracting from the cathode’s surface to anode. The electrons are accelerated by the electric field and, as a result of collisions with gas atoms, they excite and ionise it. The generated ions, hitting the cathode, release secondary electrons, causing a new ionisation processes and the formation of avalanches.

The processes of excitation and ionisation in gases can take place in the gas volume and on the electrode surfaces – volume and surface ionisation. The volume ionisation processes include thermo-ionisation, photo-ionisation and collision ionisation, and the processes that take place on the surface of the electrodes are thermo-emission, photo-emission, field emission and secondary electron emission. Collision ionisation processes in the gas volume, called α -processes and secondary electron emission from the electrode surface, γ -processes, have the largest share in the generation of charged particles (electrons and ions) that participate in the electrical discharge. In addition, the number of ionised gas particles in the discharge space, the processes of recombination and electron attachment and detachment have an influence.

There are two main mechanisms of electron avalanche formation: streamers and Townsend. The research shows that the streamer mechanism explains well the development of discharges in gases with a homogeneous or almost homogeneous distribution of the electric field intensity. Streamers (cylindrical current streams) are created when the starting electrons excited by the electric field reach the critical local density, at which the value of the electric field strength from the space charge E_p near the front of a single electron avalanche, reaches the value of the external electric field E_z ($E_p = E_z$). Such significant values of the electric field due to the space charge may arise due to the much greater mobility of electrons than of positive ions. The spread of the streamers is sustained by secondary avalanches composed of electrons generated in the process of inter-electrode gas photoionisation. The increase in the number of streamers causes widening of the plasma channel at the inter-electrode space.

The classic Townsend discharge or the discharge under Paschen's conditions (Paschen's law) is also a form of electro-avalanche, however, unlike to a streamer discharge, they are supported by secondary electron emission from the cathode. Thus, according to the streamer mechanism, the electric discharge in gas consists of single fast micro-discharges, while according to the Townsend discharge, it consists of a large number of consecutive electron avalanches. The mechanism of Townsend discharge, compared to the streamer discharge, is applicable in case of lower values of the product of the gas pressure p and the gap width d , and slower changes in the supply voltage as well as characterized by relatively high secondary emission factors γ . The discharge takes place according to the streamer mechanism in case of higher values of the product pd , low coefficients of secondary emission γ , and higher voltages.

Both mechanisms of the formation of micro-discharges are observed in reactors with DBD (ozone generators). For lower voltages, when the discharge current is much less than the displacement current (caused by the electrodes structure), the discharges can be described by the mechanism of Townsend discharge. Intensive discharges, the average current of which is comparable to the displacement current, are described by a streamer mechanism.

The discharge space breakdown mechanisms at constant supply voltage are well known and described in the extensive literature on electrical discharges [8–13]. Therefore, it is limited to recalling the basic gas ionisation phenomena occurring in its volume and on the surface of electrodes, which are used in plasma processes.

The collisions of ions and electrons in the inter-electrode space and on the electrodes are accompanied by the processes of sputtering the cathode material, its diffusion and deposition on the anode as shown in Figure 2.1.

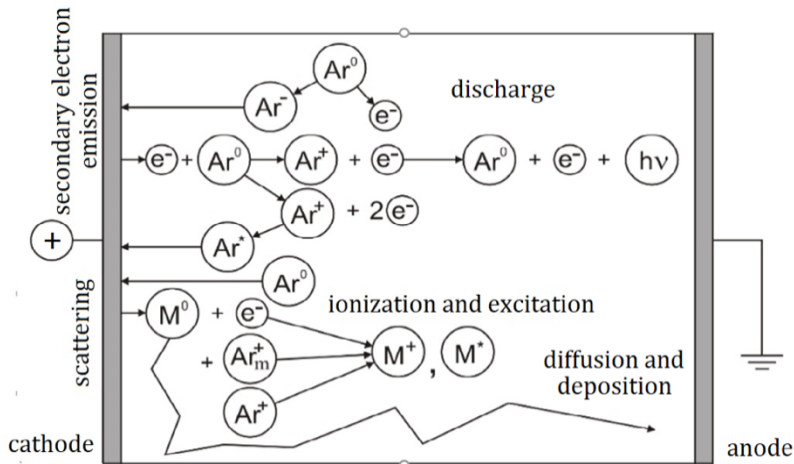


Figure 2.1. The phenomena accompanying the ionisation processes in the discharge space between metal electrodes with argon as a plasma gas. Source: own elaboration based on [8]

The phenomenon of cathode sputtering is used in analytical spectrochemistry (mass spectrometers) and in material technologies for the deposition of thin layers of cathode material on the anode acting as a substrate. The basic phenomena observed in a glow discharge (GD) at constant voltage are elastic and inelastic collisions between gas molecules leading to their excitation and ionisation, formation of electron avalanches, acceleration of ions by an electric field towards the cathode, causing the knocking out of secondary electrons and cathode from it, diffusion of the cathode towards the anode and its deposition.

The potential between the DC discharge electrodes is unevenly distributed and an almost complete decrease of it is observed in the vicinity of the cathode. The largest part of the DC glow space is occupied by the so-called negative glow, the voltage of which, called the plasma potential, is constant and only weakly positive. At greater inter-electrode distances in the DC discharge, two additional regions in the inter-electrode space are observed: the Faraday space and the positive column, which are characterised by an electric field causing the electron movement towards the anode. However, in most GD plasma applications, the inter-electrode gap is small.

A glow discharge with a constant DC excitation may occur over a wide range of gas pressures, from 1 Pa to atmospheric pressure or higher; the operating voltage is typically several hundred volts, but in some applications, it may be several kilovolts and the discharge current is in the milliampere range. DC discharges can occur in noble gases (argon, helium) and in reactive gases (N_2 , O_2 , H_2 , CH_4 , SiH_4 , SiF_4) and their mixtures. A special type of discharge between metal electrodes are corona discharges, which occur in systems with significant electric field heterogeneity, resulting from the geometry of the reactor electrodes. To sustain a glow discharge at a constant DC voltage, both electrodes must be conductive. If one or both electrodes are covered with a non-conductive (high resistivity) material, or become non-conductive during the discharge, then due to the accumulation of charges on the electrodes, the discharge is extinguished at a constant supply voltage. This happens when the glow discharge is used in the analytical spectrochemistry of non-conductive materials as well as in the application of dielectric layers, or in electrostatic precipitators, during the deposition of fine particles of highly resistive dust on the collecting electrode. This can be prevented by using a pulsed voltage supply to the plasma reactor.

A promising source of plasma for industrial scale applications are discharges in the presence of a dielectric barrier DBD and gliding arcs [14–16]. Plasma, produced by electrical barrier discharges (also called silent or partial discharges), is non-thermal and non-equilibrium. Electrons, ions and inert gas particles are not in thermodynamic equilibrium, and electric energy, due to the short duration of micro-discharges and the low mobility of ions, is supplied to the electrons. Thus, the electrons are “hot” while the rest of the gas particles are “cold”. This determines the high efficiency of the process of energy transfer to chemical transformations in non-thermal plasma [17, 18].

Various types of electrical discharges at atmospheric pressure are investigated [19], but special attention is paid to impulse discharges – the energy supplied to electrons in a very short time (in nanoseconds) of the pulse duration does not heat the surrounding medium (gas, liquid, cells) [20, 21]. Chapter 3 reviews basic designs of cold atmospheric pressure plasma reactors.

3. Non-thermal plasma reactors

Fumiaki Mitsugi, Henryka Danuta Stryczewska, Kenji Ebihara, Shin-ichi Aoqui

3.1. Brief characterization of non-thermal plasma reactors

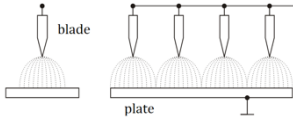
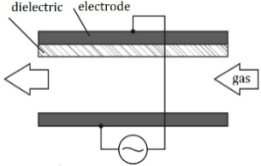
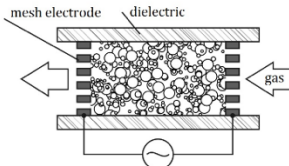
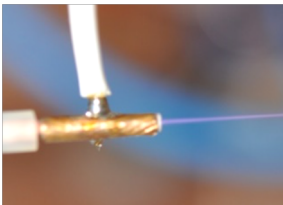
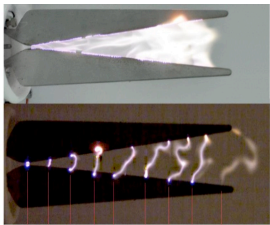
Low-temperature plasma, also known as non-thermal or “cold”, has been used in electrical, environmental and biomedical technologies for over one hundred years. Such plasma is also non-equilibrium, which means that the energies of the electrons are much greater than the energies of its other particles. The interest in the production and applications of non-thermal and non-equilibrium plasma is still growing, and the reason for this is the ability to widely control its parameters, depending on the application, through:

- working gas composition, which determines the type and energy of active plasma particles (electrons, atoms, molecules, ions, radicals);
- pressure – ranging from near vacuum to atmospheric pressure; higher pressure leads to a reduction in the free path of plasma particles and thermodynamic equilibrium;
- structure of the electromagnetic field; an externally excited field is used to accelerate, heat, compress and direct plasma particles;
- discharge geometry – lack or presence of electrodes, presence of a dielectric, volume of the discharge space – low-volume discharges mean a deviation from thermodynamic equilibrium;
- parameters of the supply system (power, voltage, frequency, number of phases, supply voltage, internal impedance of the supply system).

In non-thermal plasma, the majority of the energy is used to produce high-energy electrons, not to heat the gas. Thus, the energy of the plasma is directed to dissociation caused by collisions with electrons and ionisation of the gas to produce radicals that break down toxic gas molecules. Colloquially speaking, in non-thermal plasma, electrons are “hot”, while the remaining plasma particles are “cold” – they may have ambient temperature and lower. In many applications, especially in the removal of very dilute air pollutants, the technique of applying low temperature plasma is the most suitable and is irreplaceable due to the selectivity of energy and the possibility of removing several air pollutants simultaneously. In other applications where mixed types of waste are present, a thermal plasma is used to incinerate all the waste, including the canister, and then a low temperature plasma is used to clean the combustion gases.

To date, many types of low-temperature plasma reactors used in environmental protection have been tested (Table 3.1). The potential capabilities of these devices have been confirmed during the removal of nitrogen oxides NO_x , sulphur dioxide SO_2 , heavy metals and volatile organic substances generated in the processes of painting, varnishing and chemical processes [16].

Table 3.1. Non-thermal plasma discharges

Discharge type	Reactor construction	Power supply
<p>Corona discharges (CDs) Barrier corona discharge with metal mesh (BCD)</p>		<p>PP and DC</p>
<p>Dielectric barrier discharges DBD, atmospheric pressure glow</p>		<p>AC voltage with a frequency range of MHz</p>
<p>DBD with dielectric/ferroelectric packing Surface discharges</p>		<p>DC, pulse power (PP) and AC</p>
<p>Atmospheric pressure plasma jet APPJ, Plasma needles (PN)</p>		<p>High-frequency AC and PP</p>
<p>Gliding arc discharges (GAD)</p>		<p>PP and AC</p>

As an ionised gas, plasma molecules easily react with various chemicals, which allows the decomposition of toxic compounds, modification of polymer structures, the destruction of bacteria and fungi and affecting their biological structures and DNA.

Among the environmental applications, the technology of drinking water treatment is the most technologically advanced and used in practice. These were created in Europe almost at the beginning of the twentieth century (Nice 1907) and in the world (Los Angeles 1987) water treatment stations that were able to replace environmentally unfriendly chlorine with ozone produced in barrier discharge reactors. In the mid-twentieth century, pool water ozonation began to be used.

Other environmental applications of ozone generated in dielectric barrier discharges (DBD) in air or oxygen include [14, 15, 19]:

- *sterilisation of air, water, soil, surface and packaging* – various types of discharges in air, above the water surface and directly in water are tested, especially with impulse power supply; attempts are being made to remove microbiological contamination of paper, plastic packaging, to reduce nitrogen oxides from exhaust gases from natural gas combustion, remove nitrogen oxides (NO_x), sulphur dioxide (SO_2), heavy metals and volatile organic substances generated in the processes of painting, varnishing, incineration of post-hospital waste and other chemical processes; recycling and removal of pollutants – decomposition and incineration of organic, volatile and solid waste, exhaust gases from diesel engines, used batteries, printed circuit boards, with the use of arc and quasi-arc plasma;
- *supporting chemical reactions* – selective removal of acetylene from ethylene, decomposition of ethylene, trichlorethylene, ethyl acetate and toluene, production of hydrogen gas by the decomposition of hydrocarbons.

Most of the studies mentioned are well-advanced and some of them have already been put into practice. The biological and medical applications of low-temperature plasma take advantage of the bactericidal properties of electrical discharges, especially the compounds ozone (O_3), nitric oxide (NO), and hydrogen peroxide (H_2O_2) produced during these discharges.

A desirable feature of plasma in these applications is thermodynamic imbalance – low gas temperature and high electron energies initiate chemical reactions that affect the biological structures and DNA of bacteria, viruses and fungi, but do not destroy other components or cells (healthy and beneficial for the functioning) of the biological environment subjected to plasma treatment.

Currently, biological and medical applications include [19]:

- *sterilisation of living human and animal tissues and support of treatment* – killing microorganisms, especially bacterial spores that are difficult to remove, bio-disinfection by means of discharges in the form of a gliding arc,

DC discharges in the air, mechanisms of the action of non-thermal plasma on bacteria, low-temperature sterilisation in pulsed plasma; coagulation and sterilisation of surface wounds, blood, applications in dentistry, supporting the treatment of skin cancer;

- *sterilisation of medical tools* – especially elements made of plastics not resistant to high temperature; a pulsed microwave plasma is used in both dry and wet environments;
- *coating of implants and lenses with biocompatible layers* – production and biological applications of plasma polymers in treatment and diagnostics, improvement of the properties and biocompatibility of thin amorphous layers on dental prostheses, titanium surface, nano-layers on contact lenses, plasma deposition of composite, bioactive intraosseous implant coatings;
- *tissue engineering* – plasma supports the production of bio-active factors and drugs, immobilises biological molecules, modifies surfaces to regulate cell behaviour, and improves blood adhesion;
- *medical diagnostics* – biosensors manufacturing for medical diagnostic equipment with use of polymer and amorphous thin films.

Plasma methods in biomedicine, and especially ozone therapy, which is already widely used in medical practice, show high efficiency, eliminate most bacteria, viruses, fungi and moulds, activate the action of antioxidant enzymes, and stimulate the production of white blood cells. In interaction with living organisms and tissues, in safe doses, they do not produce side effects, are painless, do not cause allergic reactions, and often eliminate the need for pharmacological treatment.

Research works on the use of non-thermal plasma in technologies related to environmental protection and in biotechnology are aimed at, among others:

- evaluation of the suitability and effectiveness of various types of electric discharges for the production of non-thermal plasma, especially at atmospheric pressure;
- pollutant-removing system's development on the basis of electron-generating processes;
- obtaining an exact gas mixture composition and effective harmful compounds conversion after reactions of catalysis (steam, ammonia);
- significant energy consumption decrease;
- power source and plasma generator matching.

The power supply system, regardless of the type of electric discharges used to generate the plasma, determines the efficiency of the entire plasma process and, consequently, the possibility of its industrial application. Therefore, in this monograph, after the review of electric discharges used for the generation of non-thermal plasma, the basic systems of power supply systems of plasma reactors are described in Chapter 4.

The basic design of a non-thermal plasma reactor used at atmospheric pressure is a needle-plate configuration operated by a DC power supply. The DC power supply should output positive high voltage as negative streamers are hardly formed under negative high voltage. The adjustment of the high voltage amplitude of the DC power supply and the optimisation of the roughness and curvature of the needle electrode realises the continuous generation of pulsed streamer discharges. This is the simplest way to generate streamer discharges which is one form of non-thermal plasma. In spite of the applied DC voltage, pulsed streamer discharges occur from the needle toward to the plate electrodes.

The pulse duration of each streamer is in the order of 100 ns where electron current flow is completed immediately due to the much less mass effect of electron. The next streamer occurs with approximately 100 μ s delay after the previous streamer where residual ions are neutralised in the form of ion current that is determined by their mobility under DC electric field.

As such, a series of pulsed streamer discharges show a specific repetition rate of the order of kHz, which is decided in nature, and we cannot control the natural repetition rate of pulsed streamer formation. This technique is already used in commercial products including air purification instruments as the power supply is inexpensive. When we control the repetition rate of streamer discharges artificially, pulsed power supplies or high-frequency AC high voltage power supplies are employed. A pulsed power supply, which makes it possible to apply very short-pulsed voltage in μ s or ns duration, realises short streamers that have less heat effect despite high electron temperature. The repetition rate of streamers can be controlled by that of power supply that depends on recent power semiconductor technology. In this type of pulsed streamers, however, the techniques to suppress of secondary streamers and breakdown, which are induced after the primary streamer, are necessary to emphasise only the advantage of pulsed primary streamers and to furthermore reduce working temperature. Generally, because a negative streamer is hardly generated, it is difficult or impossible to have both polarity streamers at the same time with high-frequency AC power supply.

Therefore, the high frequency alternating current supply in non-thermal plasma generation is combined with a dielectric barrier configuration and/or with a forced gas flow to avoid breakdown between the two electrodes. These types of reactors are called dielectric barrier discharges.

Barrier dielectric discharges are produced over a relatively wide range of pressures, typically from 10 kPa to 100 kPa, with alternating voltages as high as 100 kV in some applications, and frequencies from a few hertz to hundreds of kilohertz. The length of the discharge gap, depending on the application, may range from 0.1 mm for plasma displays, a few millimetres in ozone generators and up to several centimetres in CO₂ lasers. The dielectric barrier is in most DBD reactors made of glass, quartz, ceramics or polymers.

There are three basic electrode configurations in barrier discharges that lead to (1) volumetric discharges, (2) surface, and (3) coplanar discharges. Reactors are also built in which all of the above-mentioned discharges occur. Figure 3.1, prepared on the basis of [21], shows the value of density volumetric power in kW/m^3 for selected discharges occurring in the presence of a dielectric barrier.

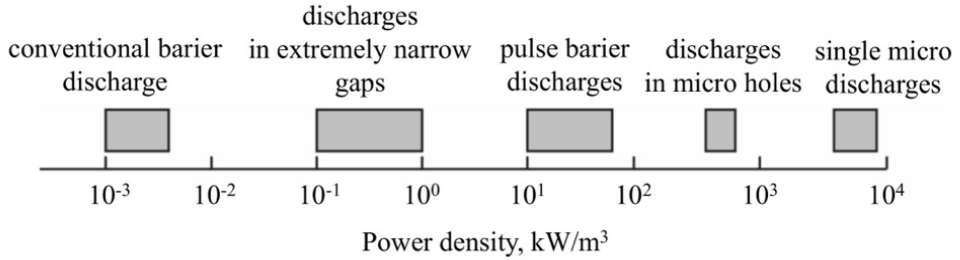


Figure 3.1. Power density of selected discharges at presence of dielectric barrier.
Source: own elaboration based on [21]

This shows that the highest power density of 10^4 kW/m^3 can be achieved in a single micro-discharge, while in a classic barrier discharge the obtained power densities are in the order of 10^{-3} kW/m^3 , so several orders smaller.

Increasing the discharge power density is theoretically possible in the ways of using special electrode and dielectric structures so that the discharges occur in very narrow discharge gaps (10^{-1} kW/m^3) or in micro-holes (10^2 – 10^3 kW/m^3), and through the use of pulse power sources (10^2 – 10^3 kW/m^3).

On the other hand, a high-frequency AC power supply is useful to get arc discharges (AD) and it is applied to the two metal electrodes without any dielectric with a small air gap. When supplying a gas into the arc plasma, it starts gliding along the electrodes, which is called gliding arc discharges [22]. Basically, an arc discharge shows properties of thermal plasma and the beginning of the gliding arc discharge is considered to be thermal plasma while after gliding with fast gas flow seems to be a source of a non-thermal plasma. Because the current flow of the gliding arc discharge is not limited by a dielectric barrier, it is difficult to suppress its power consumption and Joule heating, then applications such as gas treatment are the main targets of the system. However, advanced gliding arc discharges that suppress temperature and power increase have been developed by the improved design of power supply and the utilisation of the UV photo-electric effect. Such a wide range control in power and temperature of the gliding arc discharge can cover many applications in various fields.

Dielectric barrier discharges basically use ceramics and are classified into normal dielectric barrier discharge, surface (creep) discharge, and packed-bed discharge, which are distinguished by location where discharge plasmas are generated at. The typical designs of dielectric barrier discharges are coaxial

cylindrical and plate to plate where one or both of the electrodes are covered by dielectric ceramics and discharges are generated in the space between the electrodes. A high-frequency AC power supply around 10 kHz is necessary to realise the dielectric barrier discharge continuously, because the opposite polarity of applied voltage works to reduce residual charges generated in the previous half period of the applied voltage. This design is often used to generate ozone by considering toughness, durability, stability, and safety.

Surface discharge is a design which is very thin as one of the two electrodes is on the surface of the thin ceramics plate and another electrode is inside or backside of the plate. Due to the unique and compact configuration, it has attracted attention in aeronautics for the application on a plasma actuator that changes air flow around airplane wings. Discharges occur in the air from the exposed electrode on the ceramic plate along its surface and cause strong ionic wind and pressure waves that contribute to air flow changes.

Packed-bed discharge generates plasmas among a ceramic particles bed between coaxial cylindrical configurations. At the strong electric field in the gap between adjacent ceramics, discharges occur and the space occupied with plasmas is suitable for the decomposition of exhaust gas, and so on. Its efficiency in the decomposition rate of polluted gas is improved by attaching a photo catalyst on the surface of the ceramic as it is activated by the UV photoemission from the plasmas.

Plasma jets, which are currently focused on the medical and agricultural fields, are also driven by an AC power supply at operating frequencies from kHz to MHz. Basically, the plasma jet device uses a glass tube and plasmas are formed inside the glass tube in an inert gas flow. There are mainly two configurations of the plasma jet. One is needle type electrode configuration where the needle is set inside a glass tube and breakdown plasma generated from the tip of the needle exits from the glass tube by the gas flow. Another type is classified as capacitive discharge, whose configuration consists of two metal sheet electrodes wrapped at the outer wall of the glass tube, that is, the glass tube works as a barrier layer between the two electrodes. Discharge occurs inside the tube but with less power due to the glass barrier and exits with the gas.

3.2. Arc and gliding arc discharges as a source of plasma

Electric arc plasma reactors have been used in industrial technologies for many years. Their main applications are welding, melting, spraying, surface treatment of materials, especially those difficult to machine, and chemical syntheses. Recently, arc discharges have also been used to synthesise new materials, including nano- and bio-materials with special properties in microelectronics, biotechnology, medicine and environmental protection processes, like waste incineration and vitrification.

The rapid development of plasma generation techniques has significantly expanded the possibilities of using electric arc plasma devices. In many applications, the plasma source is an electric arc stabilised by the walls of the reactor and the gas flowing through it, producing a stream of plasma flowing out of the plasma reactor at high velocity. The regulation of the electrical, thermal and gas dynamic parameters of the plasma stream in such a plasma reactor is relatively easy and can be carried out within wide limits. A characteristic feature of a stabilised arc plasma stream is the possibility of achieving very high energy and power concentrations, reaching 40 kW/cm^3 in a relatively small space, and therefore plasma-arc heating is one of the most promising methods of electric heating.

Electric arc reactors generate thermal plasma, the particles of which are present in a state of thermodynamic equilibrium. When neutralizing industrial gases (e.g., exhaust gases of power plants or combined heat and power plants), the electric arc as a plasma source is of little use, because it is not able to effectively penetrate the space filled with contaminated air in a way that allows the removal of contaminants contained in it. The length of the free arc, its position in space, the volume and the characteristics of the plasma generated by it constantly change randomly. This makes the AD and the plasma generated by the medium poorly controllable from the point of view of maintaining the required characteristics for processes carried out with the participation of non-thermal plasma. Warm plasma in thermo-dynamic equilibrium can be also generated by microwave discharges, plasma torches and plasmatrons. In processes related to environmental protection, quasi-arc reactors are used, generating plasma in the non-equilibrium phase and at atmospheric pressure. These include AC plasma reactors with an expansion arc.

The twelve-electrode plasma reactor shown in Figure 3.2.a is designed for the synthesis of carbon nanotubes [15]. The technological process is carried out in a helium atmosphere with a pressure of 600 mmHg, and the arc discharge occurs at a voltage of 20–45 V and current 70–100 A. Under such conditions, layers of nanotubes with diameters 20–40 nm can be obtained on a steel plate placed inside the discharge chamber. The use of twelve electrodes allows more uniform filling of the discharge chamber with plasma than in the case of a smaller number of reactors.

A photo of the interior of the discharge chamber during the operation of the twelve-electrode reactor is shown in Figure 3.2.b. The electrodes in the reactor are made of a material, 99.9% of the volume of which is pure graphite, in the form of round rods.

Another type of expansion arc discharge is the gliding electric arc, known in the world literature as the “gliding arc”. The discharge moves along the discharge electrodes in a gliding motion, significantly changing its physical properties – from those characteristics for plasma in a state of thermodynamic equilibrium to those typical for non-equilibrium plasma.

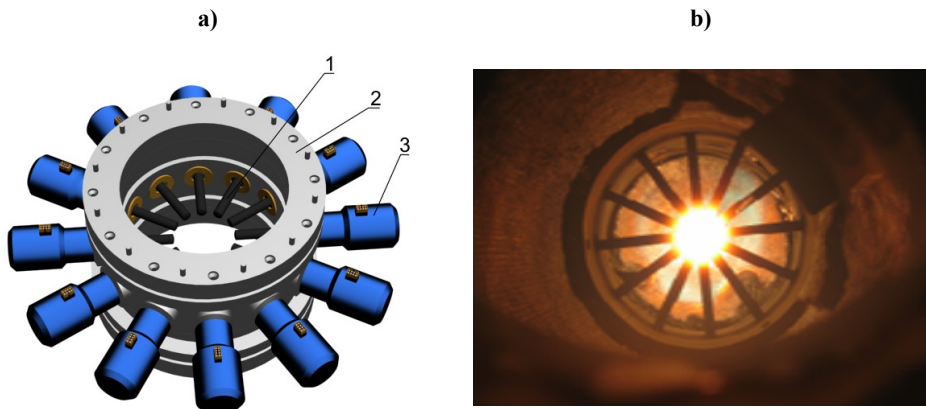


Figure 3.2. Twelve-electrode plasma reactor for arc discharges: a) model with the main elements: 1 – graphite electrodes, 2 – discharge chamber, 3 – automatic electrode length adjustment system; and b) inside view of the discharge chamber. Source: own elaboration based on [15]

Gliding arc discharge as a source of non-thermal plasma generated at atmospheric pressure was proposed by Albin Czernichowski and a team from the Plasma Physics Laboratory of the University of Orleans, France in 1990 [23–26]. Its main feature is the ability to generate non-thermal plasma directly in the polluted gas, at atmospheric pressure and under the conditions in which the exhaust gases are emitted to the atmosphere, without the need for pre-treatment.

GAD plasma, like other arcs, can be generated at direct, alternating, and pulsed voltages. Gliding arc plasmotrons used in industry are constructed as two-, three- and multi-electrode and often have an additional ignition electrode. The plasma reactor shown in Figure 3.3.a generates a three-phase arc discharge with a power of up to 500 kW [27]. The water cooling of the electrodes and the discharge chamber allows the use of materials that are not very resistant to high temperatures in the structure of the reactor.

The rapid movement of the arc attachment points along the electrodes, mainly under the influence of gas dynamic flow and to some extent also electrodynamic forces, does not cause local heating of the electrodes. The element initiating the discharge in the reactor shown in Figure 3.3.a is a low-power plasma reactor generating a plasma stream with the electron concentration $n_e = (10^{13} - 10^{14}) \text{ cm}^{-3}$ directed to the area where the distance between the working electrodes is the shortest. The concentration of electrons in the discharge ignition zone enables reliable ignition of the electric arc on the working electrodes.

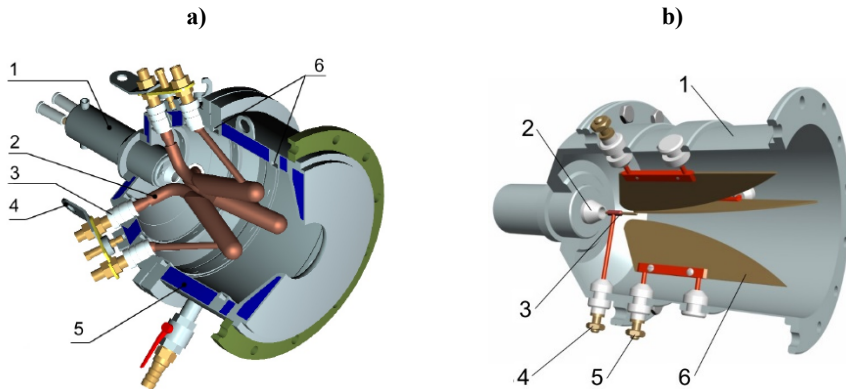


Figure 3.3. Plasma reactors for arc discharges: a) Three-electrode reactor: 1 – single-phase plasma reactor, 2 – working electrode, 3 – insulation, 4 – power terminal, 5 – cooling water, 6 – gas supply channels; and b) GAD reactor with an additional ignition electrode: 1 – discharge chamber, 2 – gas inlet nozzle, 3, 4 ignition electrode, 5, 6 working electrodes. Source: own elaboration based on [26]

The same function is performed by the ignition electrode in the three-electrode reactor shown in Figure 3.3.b [28]. The low-power electric spark produced by it is sufficient to ionise the inter-electrode space, which facilitates the ignition of the proper discharge between the working electrodes in each operation cycle.

In order to ensure non-equilibrium and non-thermal conditions of the generated plasma, the supply voltage is usually in the range from 1 kV to 2 kV, and the current of the electrode pair does not exceed 10 A. Such voltage and current values are not typical for an arc discharge. Moreover, the voltage required to hold the discharge between the working electrodes is of insufficient value to ignite the discharges in each subsequent reactor cycle, and therefore an additional ignition electrode is introduced into the inter-electrode space, in the so-called ignition zone.

The ignition of the discharge on the working electrodes of the GAD reactor is initiated by a flashover of an electric spark between the ignition electrode and one of the three working electrodes. A single electric spark channel is blown with the gas flowing from the nozzle to the reactor discharge chamber. As a result, the spark discharge consists of a tree of branching channels, which facilitates the initial ionisation of the area at the point of ignition of the main discharge, between the working electrodes. After breaking the inter-electrode gap, its resistance becomes very low and the voltage in the discharge area drops below the quenching voltage value, which results in the spark discharge being interrupted. Thereafter, the inter-electrode voltage increases again, and the duty cycle is repeated. In a three-phase plasma reactor with an additional ignition electrode, the distance between the electrodes in the discharge ignition zone is less

than 1 cm, and the spark discharge development at the ignition electrode can be described by the mechanism developed by Townsend [29]. For larger inter-electrode gaps, the spark discharge develops in an uneven electric field and at lower field strengths than would appear from Townsend's calculations.

To sum up, GAD at the point of ignition is in a state of thermodynamic equilibrium. Under the influence mainly of gas-dynamic and to some extent also electro-dynamic forces, the discharge moves along the electrodes and is sustained at a voltage much lower than that required for ignition. This is accompanied by a several-fold increase in the length and volume of the discharge, which has the features of a long arc. At the same time, the temperature of the gaseous medium inside the arc column is reduced and the transition to the non-equilibrium phase occurs. The discharge is extinguished when the electricity supplied from the power source is not able to compensate for the power losses of the elongated arc column. The operating cycle of a GAD reactor can be traced on the example of a two-electrode reactor (Figure 3.4).

As soon as the electric spark channel between the working electrodes is closed, the power delivered to the discharge increases. With the increasing power of the source, the spark channels expand into wide bands and the discharge turns into the so-called condensed spark discharge. With a further increase in the power of the source, the discharge transforms into an electric arc.

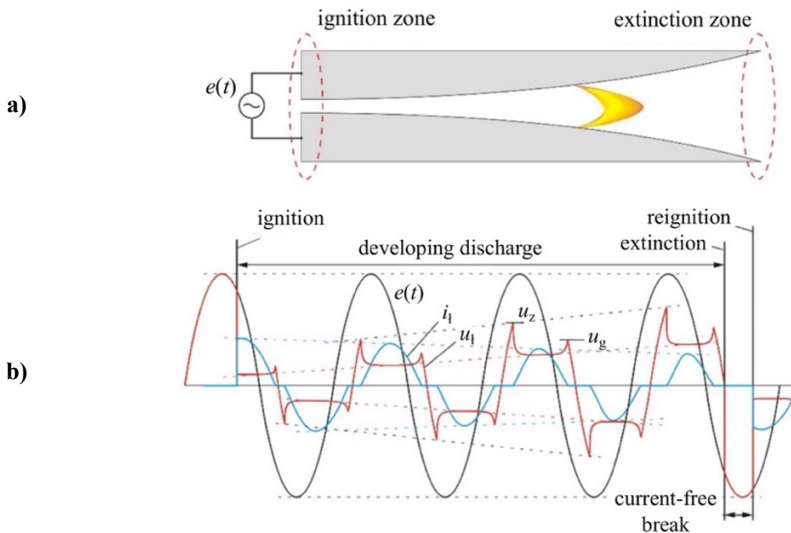


Figure 3.4. Voltage and current waveforms of the two-electrode GAD reactor: a) electrode sketch, b) instantaneous waveforms: $e(t)$ – power source voltage, u_1 – arc voltage, i_1 – arc current, u_2 – discharge ignition voltage, u_g – discharge extinction voltage. Source: own elaboration

In an electric arc, the emission of electrons from the electrodes is thermal, therefore it is characteristic of the arc that the higher the discharge current, the less voltage is needed to keep it burning. Relatively large increase in current causes a slight decrease in voltage resulting the increasing in dissipated power.

The arc column temperature is within the range (4000–7000) K and increases with the gas pressure. In gliding arc plasma reactors, the aim is to achieve a long arc with a relatively wide column. This arc must be cold enough not to melt the material of the electrodes and structural elements of the reactor. At the same time, the arc burning in the reactors must provide the appropriate parameters of the plasma generated by it to properly conduct plasma-chemical reactions. Such an arc can be obtained with relatively high voltage and low current values. The electrical strength of the inter-electrode gap depends on the thermodynamic parameters of the gas in which the arc occurs, and in particular on its composition, pressure, temperature and, to a lesser extent, its velocity in the discharge chamber.

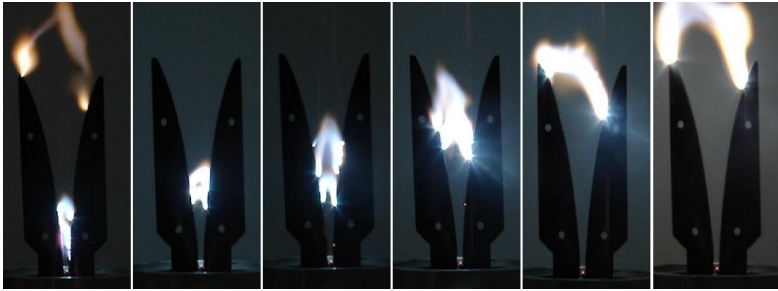


Figure 3.5. Photo of GAD developing during the operating cycle from ignition to the extinction in a two-electrode plasma reactor. Source: reprinted from [30] after obtaining the authors' permission

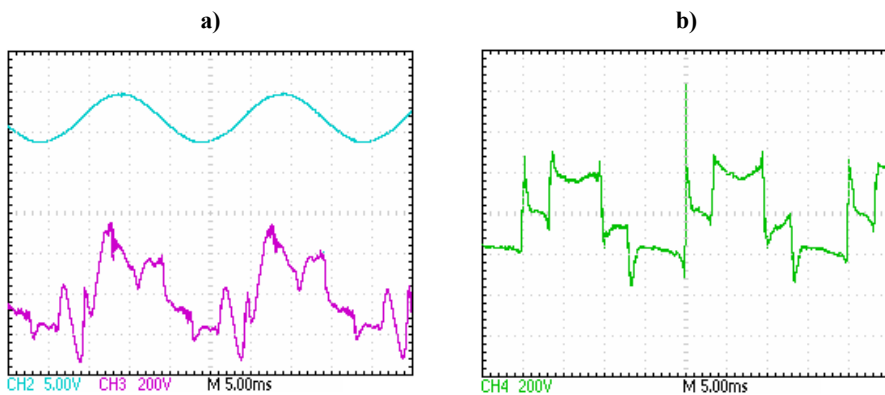


Figure 3.6. Plasma reactor current and voltage waveforms: a) phase current and voltage, b) phase-to-phase voltage. Source: own elaboration

A GA, as a receiver of electric energy, together with the power supply system form a non-stationary and non-linear circuit. The development of the GA in the air (without blowing the working gas) during the operating cycle of the two-electrode plasma reactor from the discharge ignition to the extinction, corresponding to the instantaneous waveforms presented in Figure 3.4, is shown in Figure 3.5.

The characteristics obtained by measurement in a three-electrode plasma reactor powered by a sinusoidal voltage source (Figure 3.6), show that the arc current is practically sinusoidal, while the voltage is strongly distorted. The duration of one reactor operation cycle, from ignition of the discharge to its extinction at the ends of the electrodes, depends on their dimensions and shape, gas flow velocity, its type and temperature, and may vary from few to dozen periods of supply voltage at 50 Hz mains frequency.

3.3. Mathematical modelling of AD and GAD plasma reactors

The history of the theory and practice of mathematical modelling of electrical discharges is almost as long as their industrial use. The entire last century was devoted to modelling various phenomena related to arc discharges and resulted in many models, the usefulness of which was practically verified in research on the theory of short-circuits and switching processes, in the construction of current circuit breaker extinguishing chambers, designing arc furnaces and plasmatrons for applications in metallurgy and surface treatment. The main problem in testing commutated circuits is arc suppression. The arc discharge models for these purposes are defined so as to correctly study the phenomena occurring near the zero current crossing – the site of the natural arc quenching. They allow conclusions to be drawn regarding the selection of geometry and parameters of the circuit breaker chambers and to design them so that the arc is extinguished at the first zero current crossing [31, 32]. The main goal of modelling discharges in plasma reactors is to select their parameters and the characteristics of the supply system in a way to ensure uninterrupted stable non-equilibrium discharge, while ensuring high efficiency and the efficiency of plasma-chemical processes.

The phenomena accompanying AD used in plasma technologies are extremely complex, and their analysis requires determination of the distribution of electromagnetic and temperature fields, their mutual couplings and solution of the energy, charge and mass flow equations. The non-linear nature of the phenomena in the arc, the need to consider and link the physical parameters of the ionised gas, the arc cooling conditions and the electrical parameters of the power supply system, when constructing a mathematical model always force one to adopt significant simplifying assumptions and often require empirically determined discharge characteristics.

The model of a GAD, the parameters of which differ significantly from the classic electric arc, should take into account the several-fold increase in the length of the column and the discharge volume, its ignition and the cyclic operation of the reactor. An important issue is to ensure non-equilibrium conditions for the generated plasma, which is related to the temperature distribution in the reactor's discharge space and the determination of the energy (temperature) of plasma particles, especially electrons, whose energies in the non-equilibrium plasma are much higher than in other plasma particles. These phenomena are difficult to diagnose and require special methods and research devices. Mathematical and numerical modelling of these phenomena is an alternative to costly experimental research. Depending on the purpose of modelling and the type of phenomena that we intend to map in the studied plasma process, the arc discharge models can be divided into deterministic and stochastic, static and dynamic, channel and terminal.

The basis for the formulation of all models are the equations of the hydrodynamics of the heated gas, related to the electric energy generated by the discharge, and the mechanisms of the exchange of this energy with the discharge environment. The increase in temperature and pressure of the gas in which the discharges occur, affect the variability of the dissociation and ionisation processes, and this in turn affects the value of the electrical and hydrodynamic parameters of the arc discharge plasma.

The first models of the electric arc were proposed at the beginning of the twentieth century. One can mention here the terminal empirical model of an electric arc that burns freely between carbon electrodes, given by Herta Ayrton [31] in the form of a dynamic current-voltage characteristic considering the length of the discharge column.

The division of mathematical models into two main groups is often introduced [32] as:

- channel models, also known as mathematical and physical,
- terminal models, called adaptive.

Using channel models, we can calculate the local parameters of the arc plasma and its surroundings (temperature, pressure, gas flow velocity) and select the most desirable shapes of chambers and the geometry of the reactor's electrodes. In terminal models, the physical phenomena occurring in the arc are reduced to a substitute electric two-terminal with a non-linear relationship between current and voltage. On this basis, we count the current, voltage, power and conductance waveforms in the power supply circuits of plasma reactors.

A breakthrough in the field of mathematical modelling of an electric arc were the clamp models of Mayr and Cassie, which, later modified by many authors, allowed description of the conductance of the arc discharge column taking into account the mechanisms of energy exchange with the plasma environment, its conductivity and changes with temperature and thermal time constant [33–35].

Separate studies concern stochastic arc models and the use of chaos theory, especially when we are interested in the dynamic properties and stability of systems with arcing discharges. The conductance of the arc, determined with the use of deterministic models, corresponds to its averaged characteristics and does not consider small changes in conductance around the mean value. They can cause, for example in current circuit breakers, different switching conditions, especially when they occur near the zero crossing of the discharge current. In order to define the stochastic model of the arc and determine its parameters, it is necessary to conduct many experiments, from which one can select the necessary information about changes in the conductance of the discharge.

In GAD reactors, we aim to achieve thermodynamic imbalance conditions typical of low-pressure discharges, such as glow discharges. The characteristics of GAD depend on many parameters (electrode geometry, the physical properties of the working gas, its speed and chemical composition, the value of current and voltage, supply system impedance). The use of analysis methods based on chaos theory should provide a lot of information about the behaviour of the system and its sensitivity to changes in these parameters [36].

A modified Ayrton's model

The dependence on the dynamic current-voltage characteristic of an arc, considering its length, first given by Herta Ayrton, is shown in the next equation:

$$u_1(t) = A + B \cdot l_1(t) + \frac{C + D \cdot l_1(t)}{i(t)} \quad (3.1)$$

where: A , B , C and D are experimentally determined constants, $l_1(t)$ – discharge length, and $i(t)$ – arc current. In relation (3.1), the length of the discharge column is constant and such an assumption for a freely burning arc between electrodes with a constant spacing is justified. The length of the GA increases several times during the work cycle via the distance between the electrodes at the point of ignition, which is too much of a simplification.

The relationship (3.1) was modified by making the length of the discharge at the extinction site dependent on the electrode flare angle β , gas flow velocity v_g and time t , according to [34]:

$$l_1(t) = l_0 + \beta \cdot v_g \cdot t \quad (3.2)$$

where: l_0 – initial electrode distance at the point of discharge ignition. Therefore, it was assumed that the discharge velocity was equal to the gas velocity, and the column had the shape of a part of a circle based on the angle β of the electrodes' dispersion (curve a in Figure 3.7). GAD time functions of conductance for three gas velocities, current and voltage in successive cycles of the reactor operation are shown in Figure 3.8.

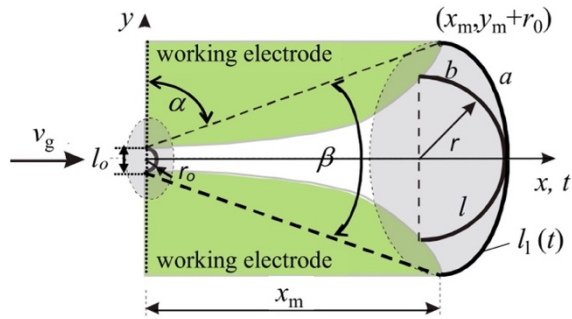


Figure 3.7. The geometry of the electrodes with the assumed shape of the GA: a – arc column assumed as incisal based on angle β , b – arc column assumed as semicircular. Source: own elaboration

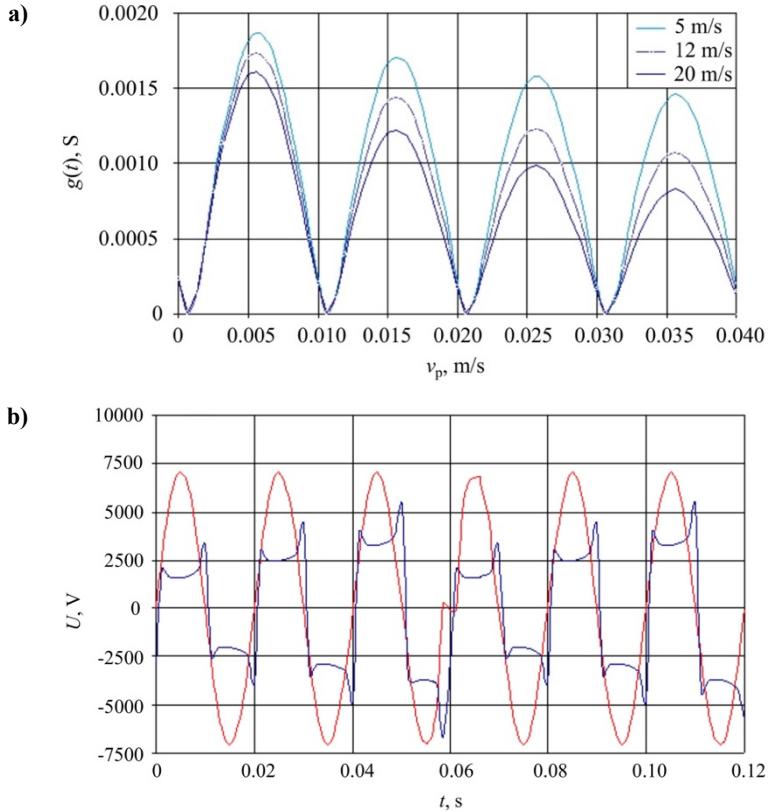


Figure 3.8. GAD time functions of: a) conductance for three gas velocities; b) current and voltage in successive cycles of the reactor operation. Source: own elaboration

Selected results of mathematical modeling of a GAD powered from a real sinusoidal voltage source in MathCAD are shown in Figures 3.10.a and 3.10.b. It has been found that the dependence on the current-voltage characteristics of the arc given by Ayrton can well represent the qualitative waveforms of currents and voltages in a gliding arc reactor.

Mayr and Cassie terminal models of GAD

The attempt to adapt the terminal models to the analysis of the GAD reactor results from a simple mathematical description of the dynamics of the arc discharge, and the multiple verification of these models in the modelling of electric circuits with current circuit breakers.

The dynamic arc conductance characteristics given by Mayr and Cassie are represented by following equations [34, 35]:

$$\frac{dg(t)}{dt} + \frac{1}{\tau_M} g(t) = \frac{1}{\tau_M P_0} i^2(t), \quad (3.3)$$

$$\frac{dg^2(t)}{dt} + \frac{2}{\tau_c} g^2(t) = \frac{2}{\tau_c U_{st}^2} i^2(t), \quad (3.4)$$

in which:

- $g(t)$ – instantaneous conductance of the arc column,
- τ_M – time constant of arc under Mayr's assumptions,
- τ_c – time constant of arc under Cassie's assumptions,
- U_{st} – arc voltage in steady-state conditions,
- P_0 – power given off per unit length of an arc column.

The main difficulties in applying the Mayr and Cassie terminal equations when modelling GAD are the need to consider the discharge ignition, the correct mapping of the current-voltage characteristics in the range of small current values, on the order of a few amperes, and the modelling of the cyclic operation of the reactor [34, 36].

To overcome these difficulties, the mathematical model of a GAD should meet the basic energy relations postulated by Mayr and Cassie, namely:

- have appropriate dynamic properties,
- a good approximation of the real course of the static current-voltage characteristic of a discharge in the range of currents with relatively small values, as is the case in a reactor with a GAD,
- allow modelling of the voltage ignition of the discharge in the cold inter-electrode space,
- consider the cyclicity of the discharge and the time variability of its parameters.

The solution of the Mayr and Cassie equations, given by (3.4) and (3.5), are the functions on the instantaneous non-linear conductance according to:

$$g(t) = g_0 \cdot e^{\frac{1}{\tau_M} \int \left(\frac{u(t)l(t)}{P_0} - 1 \right) dt}, \quad (3.5)$$

$$g(t) = g_0 \cdot e^{\frac{1}{\tau_c} \int \left(\frac{u^2(t)}{U_{st}^2} - 1 \right) dt}, \quad (3.6)$$

where: g_0 – discharge conductance at the point of ignition.

In order to correctly reproduce the static and dynamic characteristics of GAD and to take into account the above-mentioned postulates, the dependence on GAD instantaneous conductance was modified, according to:

$$g(t) = g_0 \cdot e^{w(t) + \int \frac{1}{\tau(g)} \left(\frac{p(t)}{P_0(g,t)} - 1 \right) dt}, \quad (3.7)$$

where: $w(t) = - \int_0^{t_z} \frac{1}{\tau(g)} \left(\frac{p(t)}{P_0(g,t)} - 1 \right) dt,$

wherein: $\tau(g) = h \cdot g^j(t)$, $P_0(g) = a \cdot g(t) + c$, $a(t) = a_0 \cdot l^2(t - t_z)$, $c(t) = c_0 \cdot l(t - t_z)$, in which: $l(t)$ – time-varying GAD length, t_z – time corresponding to the moment of ignition of the discharge, h, j, a, a_0, c, c_0 – constants determined empirically.

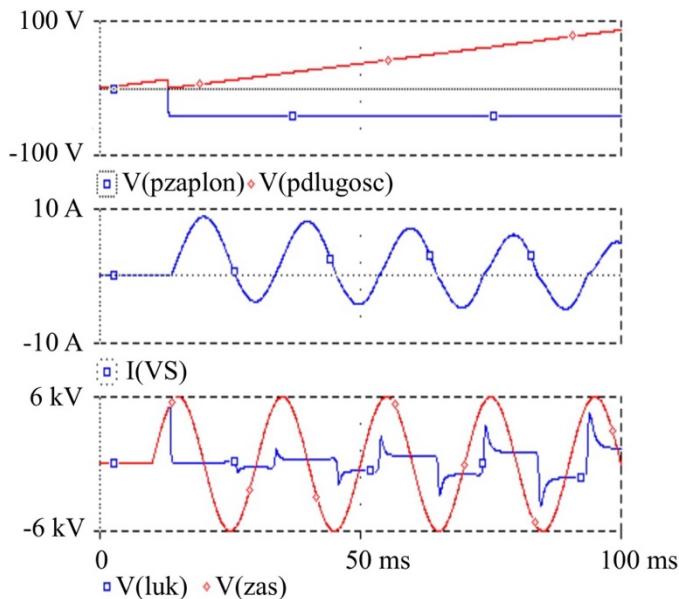


Figure 3.9. GAD modelling results in a single-phase RL circuit during one cycle of operation.

Source: own elaboration

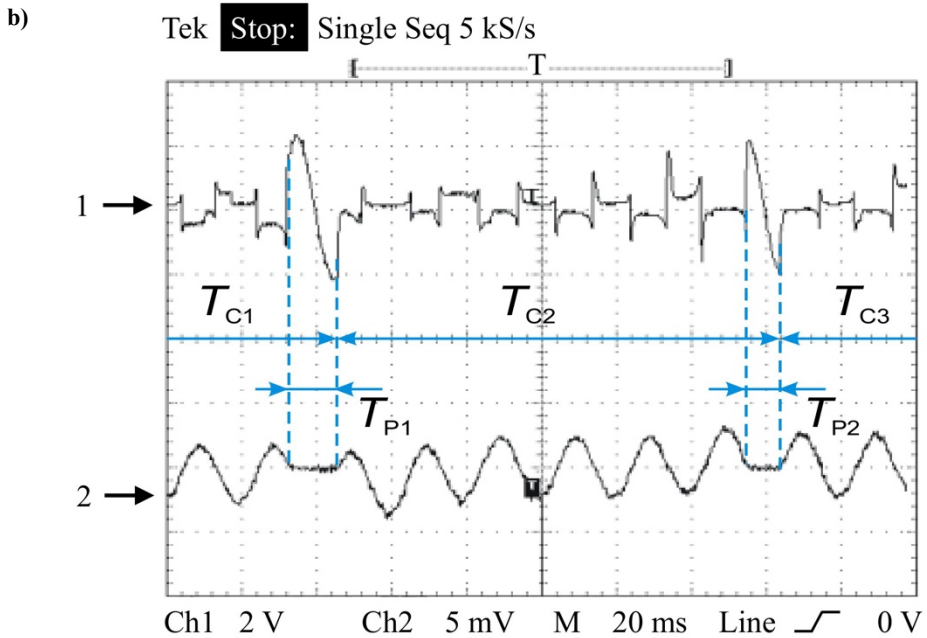
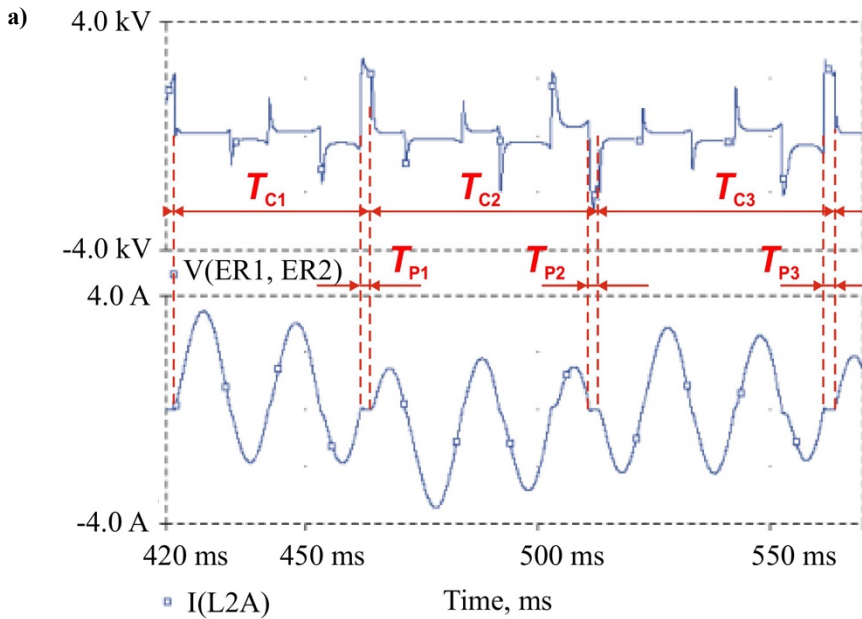


Figure 3.10. Voltage (upper wave) and current (below) of the GAD results: a) obtained numerically, b) obtained experimentally. Source: own elaboration

Nonlinear GAD conductance was modelled in the PSPICE software and solved with the technique of analogue behavioural modelling. The calculations were performed assuming that the discharge column has the shape of a semicircle, as shown in Figure 3.9 (curve *b*), and the discharge is supplied by a true sinusoidal voltage source.

Numerical simulations were carried out using the TRANSIENT type analysis, and their results were presented in the form of instantaneous current and discharge voltage transitions. Experimental verification of the results of the numerical analysis on a GAD plasma reactor model was also carried out.

The voltage and discharge current waveforms as well as the static characteristics obtained during the numerical analysis are shown in Figure 3.9, and the comparison of the calculation results with the waveforms recorded on the oscilloscope in Figures 3.10.a and 3.10.b.

Modifications of the mathematical terminal models of the GAD allow numerical analysis and simulation of the interaction of the plasma reactor-power supply system, in different operating states and with different simplifying assumptions. The inclusion of a variable discharge length in the Ayrton model allows one to obtain qualitative results consistent with the experiments, although it does not allow their generalisation to a wider class of reactors, due to the occurrence in the discharge model of the empirical coefficients which must be determined in a real object.

Modifications of the Mayr and Cassie terminal models allow one to obtain modelling results that demonstrate high quality compliance with the course of phenomena in a GAD reactor.

Comparison the results obtained from the numerical model with those recorded on the oscilloscope in a real object (Figure 3.10) shows that the model accurately reflects the cyclicity of the reactor's operation, current less interruptions as well as current and voltage shapes of a GAD reactor and can be used to simulate such objects.

3.4. Modelling of temperature distribution in the discharge chamber of GA plasma reactor

Research on the parameters of the plasma produced in plasma reactors plays an essential role in the design of industrial systems. In low-temperature plasma there are favourable conditions for the course of various types of chemical reactions due to the presence of high-energy particles in it [37]. The study of the plasma process is based on determining its properties, which include the chemical composition of the plasma, the energetic distribution of its components and the transfer processes such as the thermal and electrical conductivity of the plasma. These problems are very difficult to solve under non-isothermal plasma conditions, where not only are the kinetic temperatures of particles of different kinds different, but also there is a significant deviation

from the Maxwell distribution and the Stefan-Boltzmann law and the law of mass action are not satisfied. Under these conditions, it is not possible to use the appropriate relationships developed on the basis of thermodynamics and the kinetic theory of gases. From the thermodynamic point of view, when the interaction energy between the molecules is small compared to the thermal energy, it can be assumed that the plasma behaves like an ideal gas. Then, with some approximation, the Maxwell velocity distribution and the Boltzmann particle energy distribution are justified. However, it follows from the nature of the plasma that the interactions by collisions of pairs of particles must be supplemented or even replaced by a so-called collective interaction. That is, each particle interacts with many others simultaneously, since the forces acting between the charged plasma particles are electrostatic in nature. It should also be remembered that plasma, unlike an inert gas, conducts an electric current, which results in its specific behaviour in a magnetic field. For a non-isothermal electric discharge plasma, the average kinetic energy (temperature) of the electrons is an important quantity. This energy can be compared to the mean kinetic energy of gas particles which have a Maxwell velocity distribution corresponding to a certain temperature. The value of this temperature is called the plasma electron gas temperature, although there is no thermodynamic equilibrium in a non-isothermal plasma. The temperature of the electron gas is therefore arbitrary, and no conclusions based on the laws of thermodynamics can be drawn. Likewise, thermodynamic calculations cannot be made from the temperature of the inert components of the non-isothermal plasma. The parameters of non-thermal and thermal plasma are presented in Table 3.2.

Table 3.2. Comparison of thermal and non-thermal plasma parameters

Pressure	Non-thermal plasma	Thermal plasma
Type of equilibrium	Kinetic	Thermal
Electron density, n_e, m^{-3}	$10^{20} < n_e < 10^{21}$	$10^{21} < n_e < 10^{23}$
Pressure, p (Pa)	$10^{-1} < p < 10^5$	$10^5 < p < 10^7$
Electrons' temperature, T_e , eV	$0.2 < T_e < 2.0$	$1.0 < T_e < 10$
Gas temperature, T_g , eV	$0.025 < T_g < 0.5$	$T_g = T_e$
Discharge current, I , A	$1 < I < 50$	$50 < I < 10^4$
Radiation	Undefined	Equilibrium
The degree of ionisation	Undefined	Saha

Non-equilibrium non-thermal plasma is difficult to describe theoretically, because it is at best in kinetic equilibrium (quasi-equilibrium plasma), but it cannot be assumed to be in thermal equilibrium, and therefore the plasma composition cannot be analysed using the Saha equation, nor the radiation calculated using the Stefan-Boltzmann equation. Plasma properties are most often calculated assuming a thermal equilibrium that is close to reality. Since calculation of the properties of a non-equilibrium plasma is very complex, and in arc plasmatrons, deviations from the equilibrium state are not very large, the equilibrium relationships are often used to determine plasma properties.

An important parameter is the temperature distribution in the discharge chamber of the reactor. Its analysis can be carried out in various ways, depending on the type of reactor used (electrode geometry) and on the physicochemical processes taking place in the reactor. The mathematical model of a non-equilibrium plasma reactor requires the determination of:

- *geometric parameters of the system* (length, diameter and shape of the electrodes, distance between the electrodes, discharge space volume),
- *parameters of the flowing gas* (type of flow – laminar, turbulent, flow velocity, pressure, degree of ionisation, viscosity),
- *power system parameters* (supplied power, frequency, value and voltage shape, impedance of the power supply).

The energy transformation in a non-thermal plasma can be represented as the diagram shown in Figure 3.11.

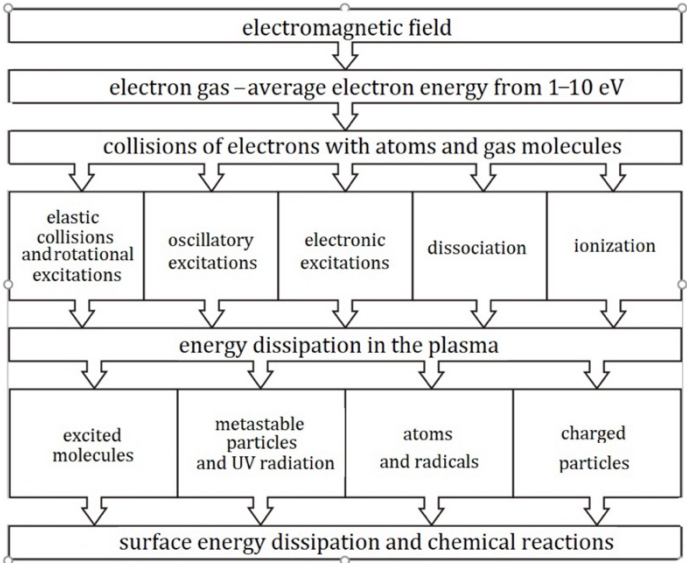


Figure 3.11. Energy transformations and phenomena in non-thermal plasma. Source: own elaboration

The analysis of the physical model and the phenomena related to energy transformations allows one to determine the parameters of non-thermal plasma necessary to construct a mathematical model and divide them into *dependent on temperature* T (gas thermal conductivity λ , specific heat c_p , plasma conductivity σ , specific gas density ρ), and *independent of temperature* (plasma velocity – radial v and axial u , gas viscosity μ , pressure p , discharge current I , electric field intensity E).

The degree of gas ionisation, velocity, particle temperature and pressure are described by the equations of conservation of mass, momentum and energy. Assuming laminar plasma flow in the reactor, the equations relating the basic physical parameters of the plasma resulting from the equilibrium equations in the cylindrical coordinate system are as follows:

$$\frac{\partial}{\partial z}(\rho u) + \frac{1}{r} \frac{\partial}{\partial r}(r \rho v) = 0, \quad (3.8)$$

$$\begin{aligned} \frac{\partial}{\partial z}(\rho u^2) + \frac{1}{r} \frac{\partial}{\partial r}(r \rho uv) &= 2 \frac{\partial}{\partial z} \left(\mu \frac{\partial u}{\partial z} \right) + \frac{1}{r} \frac{\partial}{\partial r} \left(r \mu \frac{\partial u}{\partial r} \right) + \frac{1}{r} \frac{\partial}{\partial r} \left(r \mu \frac{\partial v}{\partial z} \right) - \frac{\partial \rho}{\partial z} \\ \frac{\partial}{\partial z}(\rho uv) + \frac{1}{r} \frac{\partial}{\partial r}(r \rho v^2) &= \frac{\partial}{\partial z} \left(\mu \frac{\partial v}{\partial z} \right) + \frac{2}{r} \frac{\partial}{\partial r} \left(r \mu \frac{\partial v}{\partial r} \right) + \frac{\partial}{\partial z} \left(\mu \frac{\partial u}{\partial r} \right) - \frac{2\mu v}{r^2} - \frac{\partial p}{\partial r} \\ \frac{1}{r} \frac{\partial}{\partial r} \left(r \lambda \frac{\partial T}{\partial r} \right) - \rho u c_p \frac{\partial T}{\partial z} - \rho v c_p \frac{\partial T}{\partial r} + \sigma E^2 &= 0, \quad (3.9) \end{aligned}$$

where $E = \frac{I}{2\pi \int_0^R \sigma \cdot r \cdot dr}$.

The above equations can be solved by any numerical method, and the easiest way is to use the finite difference or finite element method. The basic equation that allows one to determine the temperature distribution in the arc column is the power balance equation described with the relationship (3.9). Due to the small value of the plasma radial velocity v , compared to the axial velocity u ($v = 0.05 \cdot u$), the factor related to it in the power balance equation can be omitted. This simplifies the Eq. (3.9) without significantly affecting the calculation results.

In practice, difficulties arise with solving equation (3.9) due to the complex dependence of the parameters λ , c_p , σ and ρ on the current temperature in the discharge space. Based on the measurements, the mathematical model assumed that the above-mentioned parameters are nonlinearly dependent on the temperature. Other temperature-dependent parameters were introduced in a similar manner into the mathematical model.

Taking into account the cylindrical structure of the reactor, the polar coordinate system (z, r) was adopted (Fig. 3.12), for which the boundary conditions are:

- condition on the axis of symmetry for $r = 0$, then $\frac{\partial T}{\partial r} = 0$,
- condition on the sidewalls for $r = R$, when $T = 300$ K,
- condition at the end of the plasma reactor electrodes $\frac{\partial T}{\partial z} = 0$.

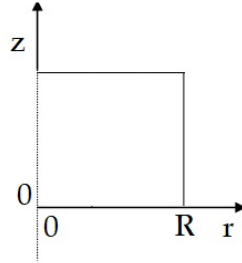


Figure 3.12. Geometry of the plasma region in cylindrical coordinates. Source: own elaboration

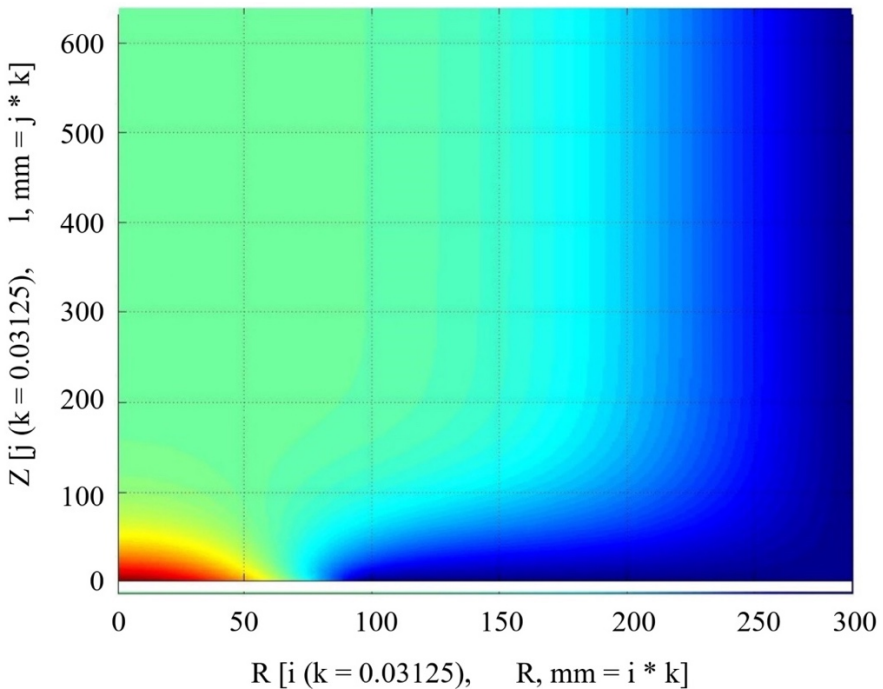


Figure 3.13. The result of the numerical simulation of the temperature distribution in the discharge chamber of the GAD reactor. Source: own elaboration

A different temperature of the source-cathode was assumed, which was described at each point with the following relationship:

$$T = \frac{T_{\max}}{a^2}(a^2 - r^2) + T_0, \quad (3.10)$$

where: r – polar coordinate, T_{\max} – maximum temperature at the cathode, T_0 – temperature outside the cathode region, a – distance from the centre of the cathode.

In summary, the numerical analysis of GAD reactors is a relatively complex issue due to the need to model very complex nonlinear phenomena accompanying electrical discharges. Correct modelling of discharge ignition phenomena, cyclic reactor operation and its dynamic characteristics, with parameters characterised by significant spatio-temporal variability, requires significant modification of the known arc discharge models used in practice. The numerical analysis carried out on the example of the plasma reactor with GAD showed that it is possible to correctly model the above-mentioned phenomena, using the terminal models of the electric arc (Figure 3.13). The compliance of the numerical calculations with the results of the experiment allows a good assessment of the terminal models of the GA that were adopted for the analysis.

The proposed numerical models of GAD do not consider all parameters that may affect the operation of the reactor. Further research should be focused on the analysis of the influence of such factors as the chemical composition of the working gas, its velocity and the electrical parameters of the power supply on the characteristics of the GAD reactor. The stochastic models and the application of chaos theory to modelling phenomena in GADs also seem promising. The presented numerical analysis can be a convenient tool in the design and construction of GA plasma reactors and other plasma reactors with similar current-voltage characteristics.

4. Power systems of non-thermal plasma reactors

Henryka Danuta Stryczewska

4.1. Introduction

Plasma reactors are very unusual receivers of electricity. Their macroscopic characteristics are strongly non-linear in nature, and they are usually operated at high voltage, often with increased or high frequency. The discharge power, which is a measure of the plasma reactor's efficiency, is regulated by the voltage or current value, depending on the type of discharge, and the correct cooperation of the plasma reactor, which in industrial applications is a high-power device, with a power supply network, requires additional devices such as reactive power compensation systems and filters reducing mains current distortions. Correct operation of the plasma reactor depends on the characteristics of the power supply system. On the other hand, the power supply system reacts to such an unusual receiver as a plasma reactor. Therefore, the plasma reactor feed system must be designed and constructed together with the plasma reactor. Various power sources are used in practice to supply plasma reactors, which can be divided into two main groups [39–43]:

- transformer systems, using the properties of magnetic circuits,
- systems with power electronic elements.

This division is arbitrary, because all power supply systems usually contain both magnetic and power electronic elements. Systems with electronic elements, due to the enormous progress in the field of power electronics, are increasingly used to power plasma reactors. The use of the latest, fully controllable semiconductor elements, such as gate turn-off thyristor, metal–oxide–semiconductor field-effect transistors and insulated-gate bipolar transistors, allows the design of power supply systems for high-power plasma reactors and with high switching frequencies. Converter power supplies can provide the current-voltage characteristics required by the plasma reactor and good current, voltage, power and frequency control properties. Moreover, they enable the automation of the plasma reactor operation by controlling the position of the electrodes, the composition and volume of the treated gas flow, and the plasma temperature. In order to choose and design a power supply system for a given plasma process, it is necessary to define the requirements and parameters of the plasma receiver, the most important of which are:

- supply voltage,
- type of supply current, method of discharge ignition,
- plasma reactor power and possible power of the supply system,
- the ability to regulate the current value and maintain its continuity in the entire operating area of the plasma reactor,

- ability of the power source to work in automatic control and regulation systems and to adjust the parameters to various plasma gases and their mixtures,
- correct cooperation with the power supply network; high efficiency,
- simplicity and safety of operation, low construction and operating costs.

In order to meet the above-mentioned requirements of plasma reactors, their power supply systems are very complex. In addition to the power supplier, they include systems of gas preparation, speed control and security.

Recently, pulsed energy has been used more and more frequently to power non-thermal plasma reactors. Thanks to the improvement of semiconductor and integrated circuit technology, as well as the properties of magnetic materials, the use of pulsed energy to power plasma reactors is growing. The following chapter presents the analysis of the power and efficiency of selected power supply systems of DBD and GAD reactors. In both cases, three supply systems for industrial applications were compared.

4.2. Power and efficiency of supply systems for non-thermal plasma reactors

The discharge elements of the non-thermal plasma reactors with DBD and GAD are specific non-linear receivers for the power supply system. Apart from the active power related to the plasma-chemical processes and the losses taking place in them, there is a distorted reactive power D , and in a reactor with barrier discharges there is also a capacitive reactive power Q . Supply systems comparison, and simplified analysis of their power losses and efficiency were carried out for an ozone generator with a power of 160 kW, ozone productivity 10 kg O₃/h and its concentration of 18 g/m³ (Table 4.1) and for a plasma reactor with a GAD with a power of 50 kW (Table 4.2). On the basis of catalogue data of system elements, the power losses occurring in them under rated operation conditions were estimated and the active power consumed from the network and efficiency were determined for each system. The discharge elements of the non-thermal plasma reactors with DBD and GAD are specific non-linear receivers for the power supply system. Apart from the active power related to the plasma-chemical processes and losses taking place in them, there is a distortion reactive power D , and in a reactor with barrier discharges also a capacitive reactive power Q . A simplified analysis of power losses and comparison of power supply systems was carried out for an ozone generator with a power of 160 kW, efficiency 10 kg O₃/h and an ozone concentration of 18 g/m³ (Table 4.1) and for a plasma reactor with a GAG with a power of 50 kW (Table 4.2). On the basis of catalogue data of system elements, the power losses occurring in them under rated operating conditions were estimated and the active power consumed from the network and efficiency were determined for each system.

4.3. Power supply systems for plasma reactors with DBD

The efficiency of the ozone generator depends on the electrical parameters of the supply system, such as voltage value, its frequency and shape [39]. Increasing the supply voltage frequency is one of the ways to increase the efficiency of the DBD reactor, but the need to equip the system with additional frequency conversion systems increases the total power losses in the system and makes the ozone generation process less efficient than at the mains frequency.

In the supply systems of plasma reactors with DBD, single-phase transformers operating in the range of non-linearity of their magnetisation characteristics are used. In the configuration shown in Figure 4.1, three single-phase transformers connected as a star on the primary side and an open delta on the secondary side, thanks to the free return path for higher harmonics of the magnetic flux, result in obtaining a frequency at the output of the power supply 3-times higher than that on the primary side. The structure of the power supply, known as magnetic frequency tripler (m3f) shows a full analogy with a transformer.

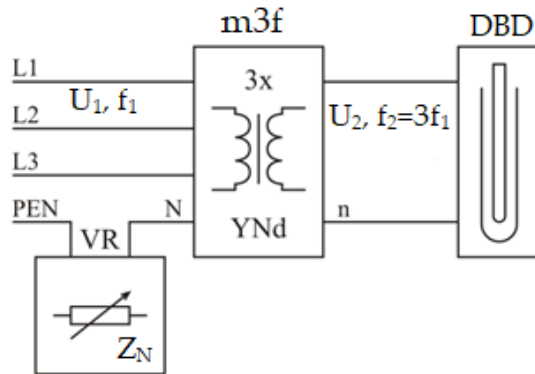


Figure 4.1 Power supply of DBD plasma reactor [40]: m3f – transformers of magnetic frequency tripler, VR – voltage regulation, YNd-3-single-phase transformers with star connection of primary windings and delta connection of secondary windings with neutral wire (N) on the primary side.

Source: own elaboration

Due to the three times increased frequency of the supply voltage, a DBD plasma reactor can be supplied at more than 30% lower voltage than at 50 Hz, having the same active power P [40]. What is more, the voltage to the DBD plasma reactor can be easily adjusted by the impedance Z_N connected in series in the neutral conductor of the primary side of the m3f, between the PEN and N terminals. In this way we get increased frequency of supply voltage and its regulation as well as reactive power compensation required in other transformer systems, due to the capacitive receiver that the DBD plasma generator's is.

The active power P of the ozone generator results from the required amount of produced ozone, which is provided by an appropriate number of discharge elements connected in parallel. The power of a single discharge element depends on the dimensions and properties of the dielectric materials used in its construction, and the voltage and frequency of the power source. The tubular elements most commonly used in ozone generators have an active power of 350 W and an ozone productivity from air of 60 g O₃/kWh at a frequency of 50 Hz and approximately 800 W and 50 g/kWh at 600 Hz. The number of discharge elements in one generator can be from 200 to 1000, thus the active power of one industrial generator can be from 50 kW to 900 kW.

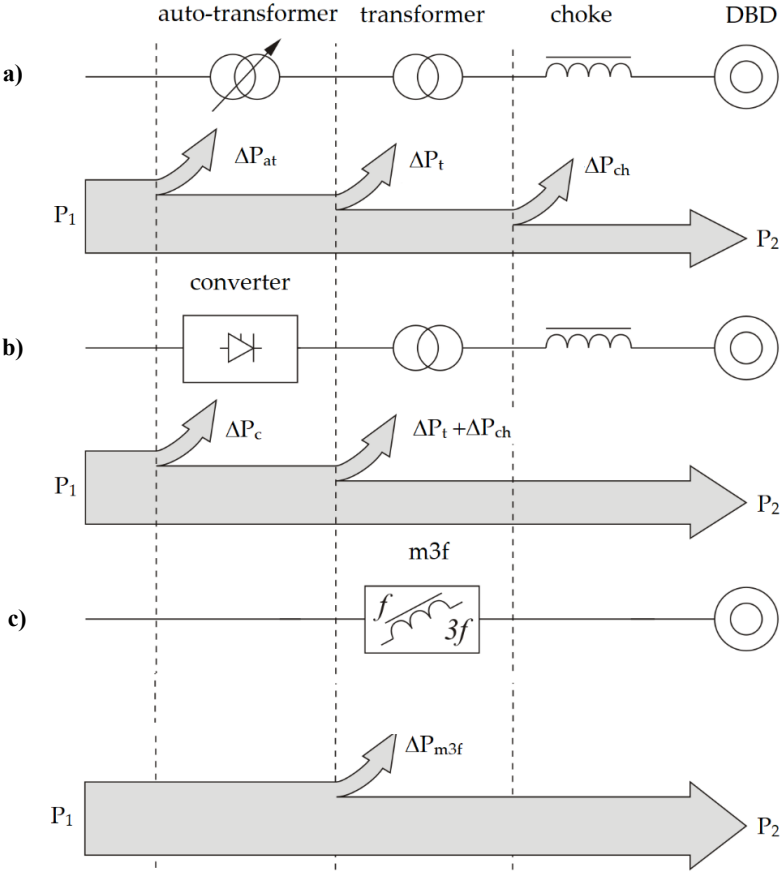


Figure 4.2. Block diagrams of the analysed power supply systems for DBD reactors [40]: a) 50 Hz system with auto-transformer, choke and transformer, b) 600 Hz converter system with transformer and choke, c) magnetic frequency tripler system. Source: own elaboration

The power factor of the discharge element ranges from 0.3–0.8 [39, 40]. The power loss analysis was carried out for three supply systems, the block diagrams of which are shown in Figure 4.2:

- 50 Hz mains frequency system, consisting of a transformer, choke and auto-transformer for voltage regulation,
- a converter system operating at a frequency of 600 Hz,
- magnetic frequency tripler (Figure 4.1).

In order to minimise the power losses and dimensions of the elements of the power supply system, the capacitive power of the ozone generator is compensated for by the choke. After the ozone generator's capacitive current is compensated for, the power factor λ_{pf} is in the range of 0.8–0.9 (the distortion power cannot be easily compensated for), which means that the apparent power S_t of the transformer in the supply system must be greater about (10–20) % than active power P and was assumed to be $S_t = 200$ kVA. The transformer power losses ΔP_t are proportional to S_t and due to distorted currents and voltages was assumed to 5% of $S_t - \Delta P_t = 10$ kW. The power of the compensation choke Q_{ch} is close to the active power $Q_{ch} = (0.7-1.2) P$. The choke is also a source of active power losses, the value of which is of the same order as the losses in the transformer. If there is an auto-transformer in the system, it is also a source of losses ΔP_{at} . The power of the auto-transformer S_{at} depends on the control range and was taken as $0.8 S_t$, and the power loss in the auto-transformer $\Delta P_{at} = 0.8 \Delta P_t$. In the converter system for 600 Hz frequency (Fig. 4.2.b), despite a certain reduction in the dimensions of the power supply system components, power losses were assumed to be 10% higher than those that occur at 50Hz.

Table 4.1. Power losses in supply systems of DBD generator from Figure 4.2

System	mains frequency 50 Hz system			frequency converter 600 Hz			m3f 150Hz		
	S	ΔP	ΔP	S	ΔP	ΔP	S	ΔP	ΔP
System element	kVA	kW	%	kVA	kW	%	kVA	kW	%
Chokes	160.0	4.8	3.0	160.0	5.6	7.0	-	-	-
Transformer	200.0	10.0	6.2	200.0	11.0	6.8	200.0	11.0	6.8
Auto-transformer	200.0	6.0	3.7	-	-	-	-	-	-
Converter	-	-	-	200.0	8.0	5.0	-	-	-
System	200.0	20.8	13.0	200.0	24.6	15.5	200.0	11.0	6.8
Active power P_2	160.0 kW								
Active power P_1	180.8 kW			184.6 kW			171.0 kW		
Efficiency $\eta = P_2/P_1$	88.5%			86.7%			93.6%		

In the m3f system (Fig. 4.2.c), due to the increased magnetic flux density in the cores and the power losses in the control system, the total power losses were assumed to be 20% higher than in a transformer of the same power – $\Delta P_{m3f} = 11 \text{ kW}$.

The results of the analysis of power losses in the system elements from Figure 4.2 are shown in Table 4.1. As can be seen from the table, the highest efficiency η is found in a system with an m3f. The high efficiency of this system results from the limitation of the number of elements of the power supply system, because the functions of the chokes and autotransformer, elements necessary in other systems, are performed in m3f. In addition, the system does not require compensation for capacitive reactive power of the DBD ozone generator, and the threefold increase in the operating frequency allows to lower the operating voltage of the DBD while maintaining the same efficiency and with unchanged electrode cooling conditions.

4.4. Power supply systems for plasma reactors with GAD

GAD plasma reactors have different requirements for the supply system than reactors with DBD discharges of electrical discharges. The discharge ignition is carried out at a voltage of several kilovolts (depending on the spacing of the working electrodes), while the voltage of the burning discharge is several times lower and amounts to several hundred volts. This disproportion of the ignition voltages and stable operation as well as the strong non-linearity of the discharge conductance creates a difficult task for the supply system, which must have the properties of both a high-voltage ignition system and a system that follows the rapid temporal changes of the non-linear current-voltage characteristic of the GAD [44, 45].

Power systems with a transformer as the main component are used in laboratory systems, pilot plants and industrial systems. In the simplest solution, it is a classic power transformer, and then, due to the reactor's characteristics, the voltage drop after ignition must be compensated by additional chokes, which should be connected in series with each pair of electrodes. At the same time, the chokes limit the electrode current. Instead of chokes, it is also possible to use transformers with increased internal reactance (so-called leakage transformers).

The phenomenon of non-linearity of the magnetisation characteristics is an inherent feature of circuits with a magnetic core and in classic power transformers we try to minimise its impact on the transformer characteristics. In the integrated power supply system (IPS), the higher harmonics of the voltages induced in the cores of operational transformers were used to ignite the discharge. In the basic solution of the integrated system, three single-phase working transformers, with magnetic circuits ensuring free return paths for higher harmonics of the magnetic flux, are supplied from a symmetrical three-phase network. Both the primary and secondary windings of the transformers are star-connected with the terminals

of the secondary windings connected to the electrodes of the plasma reactor. The fourth transformer, called the ignition transformer, is connected to the voltage, which is induced between the neutral point of the three-phase supply network and the star point of the primary windings of the working transformers (Figure 4.3.a). The voltage at the output of the ignition transformer is sufficient to ionise the inter-electrode space, allowing the discharge to ignite between the main electrodes of the reactor. After ignition, the discharge is picked up and sustained by operating transformers, which are designed and built for a voltage several times lower than the ignition voltage. The three times higher frequency of the ignition voltage, in relation to the operating voltage, improves the ignition efficiency and shortens the currentless breaks. A photo of the inside of the integrated 5 kW power supply is presented in Figure 4.3.b).

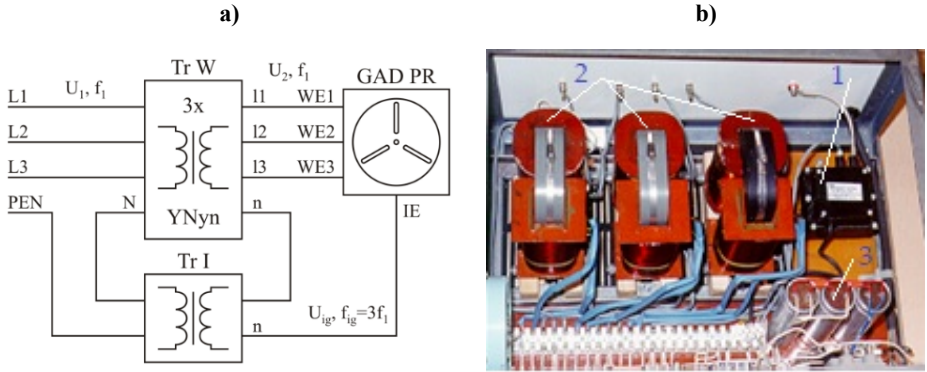


Figure 4.3. IPS system of GAD reactor (PR), where: a) Tr I – ignition transformer, WE1, WE2, WE3 – working electrodes, IE – ignition electrode, b) photo of the supplier inside, where 1 – ignition transformer, 2 – three single-phase transformers, 3 – bank of capacitors. Source: own elaboration

Block diagrams of the analysed power systems are shown in Figure 4.4. The analysis was performed for the following four power systems:

- system with transformer and chokes,
- system with a leakage transformer,
- system with magnetic frequency tripler,
- integrated system (Figure 4.3).

GAD PR does not take reactive power Q from the network, but there is distortion power D in it. The power factor, defined as the ratio of active to apparent power at the electrode terminals, ranges from $\lambda_{pf} = P / S = 0.6-0.8$. In reactors without an ignition system, the apparent power of the transformer S_t is much higher (5–8 S), and Q_L chokes limiting the current and Q_C capacitors compensating the reactive power of these chokes ($Q_L = Q_C \approx 0.8 ST \approx 7 S$).

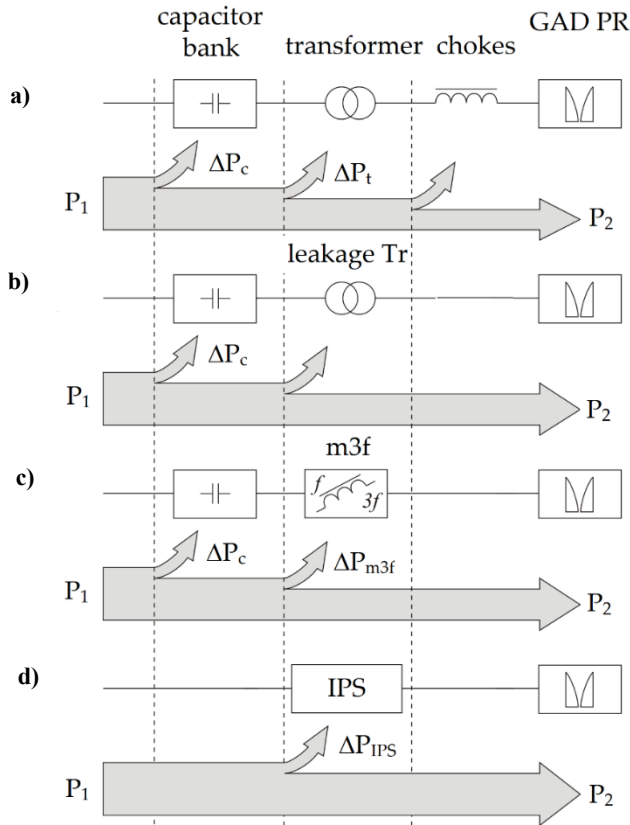


Figure 4.4. Block diagrams of the analysed power supply systems for GAD reactors: a) 50 Hz system with auto-transformer, choke and transformer, b) system with a leakage transformer, c) system with m3f, d) IPS system. Source: own elaboration

In reactors without an ignition system, the apparent power of the transformer S_t is much higher and amounts to (5–8) S , and the power of Q_L chokes limiting the current and Q_C capacitors compensating the reactive power of these chokes is equal to 0.8 of the transformer S_T ($Q_L = Q_C \approx 0.8 S_T \approx 7 S$). In the integrated system, the transformer power S_T is equal to the reactor power S and amounts to $S_t = (1.3–1.6) P$. The results presented in Table 4.2 show that the integrated system has the lowest losses and the highest efficiency.

The reduction of IPS losses and the increase in its efficiency is achieved not only by the elimination of current limiting chokes and compensating capacitors, but above all by a (5–8)-fold reduction in the power of the transformer supplying the GAD working electrodes. Integrating the functions required by the plasma reactor in one power supply system allows to reduce costs and increase its reliability and efficiency.

Table 4.2. Power losses in the power supply systems of GAD PR

System	Transformer with chokes and capacitor bank		Leakage transformer		m3f 150Hz		Integrated system IPS	
	S_n kVA	ΔP kW	S_n kVA	ΔP kW	S_n kVA	ΔP kW	S_n kVA	ΔP kW
System element								
Capacitors	360.0	3.6	240.0	2.4	160.0	1.6	-	-
Transformer	400.0	18.0	320.0	16.0	240.0	14.4	80.0	4.8
Chokes	360.0	11.0	-	-	-	-	-	-
System	400.0	32.6	320.0	18.4	240.0	16.0	80.0	4.8
GAD active power P_2	50.0 kW							
Active power from mains P_1	82.6 kW		68.4 kW		66.0 kW		54.8 kW	
Efficiency P_2/P_1	60.5%		73.0%		76.0%		91.0%	

Designing electromagnetic power supplies for DBD and GAD reactors basically comes down to determining the design parameters of the transformers forming the power supply, either in the form of magnetic frequency multipliers or as an integrated system of four single-phase transformers. The operation of these transformers consists in the use of higher harmonics of the magnetic flux, which induce an operating voltage of increased frequency to supply reactors with DBD, or the discharge ignition voltage, as in the case of GAD reactors.

When designing such power supplies, it is of particular importance to choose the material for the cores and the level of magnetic induction to ensure a sufficiently high value of the higher harmonics of the magnetic flux. The content of higher harmonics in the magnetic flux depends not only on the non-linearity of the magnetisation characteristics of the power supply transformers, but equally on the non-linear characteristics of the receiver. The presence of a high frequency in the ignition circuit and the harmonics induced by this circuit are other reasons affecting the deformation of the magnetic flux curve and the operating voltage waveforms. As results from the analyses and tests of the plasma reactor with a GAD, the material of the transformer core may significantly change the voltage waveforms in the reactor and the ability of the power supply to carry the higher harmonics generated by reactor [45–48].

The material for transformer cores is decisive for a large extent in the frequency conversion, power transmission, losses and efficiency of the power supply, because the phenomena occurring in the cores and their non-linearity are the basis of the operation of electromagnetic power supplies for discharge devices. The core material should meet the requirements of work with significant saturation induction of the magnetic circuit, and the shape of the magnetisation characteristic and the position of the operating point affect the output power and operating parameters of the power supply. The optimal material for transformer cores should be characterised by a high proportion of the third harmonic induction B_{30} to the first one B_1 , low magnetizing current and low power losses. These criteria are well met by the materials with high squareness coefficients, defined as the ratio of B_r remanence induction to the saturation induction B_s . For the electrical sheets commonly used for power transformer cores, the squareness coefficient is within the limits (0.85–0.90), which ensures the share of the third harmonic induction amounting to about 21% of the fundamental harmonic. Amorphous materials (metallic glasses), which are characterised by a magnetisation curve of high rectangularity and low saturation induction, are more and more often used for transformer magnetic cores. This enables the power supply to work with low losses and low magnetizing current. Currently, amorphous materials are available, and their price is slightly higher than that of conventional magnetic materials.

An important issue when designing transformer power supplies for GAD plasma reactors is to ensure the required dissipation (short-circuit) reactance, which, as results from previous research, in integrated power transformers should be (30–40) %. Similar values of the leakage reactance are required in power

supplies based on a five-column transformer [46]. This value is higher than in classic power transformers and lower than in power supplies for arc welding devices. Such a value of the dissipation reactance is difficult to obtain in structures with coaxial windings, where it does not exceed 15%, and in structures with separated windings, where it amounts to over 60%. The leakage reactance of the windings supplying the working electrodes is shaped by the appropriate arrangement of the primary and secondary windings on the transformer columns. The highest value of the leakage reactance is obtained for disc windings. When there is one disc of the primary winding and one disc of the secondary winding, the short-circuit reactance is so high that, in conventional transformers, it causes an unacceptably high voltage loss. By changing the number of discs, the reactance value can be changed within wide limits. In concentric windings it is also possible, to some extent, to influence the value of the leakage reactance by introducing spatial asymmetry of the windings.

4.5. Summary

In the supply systems of arc non-thermal plasma reactors, special transformers and converter systems are used. The transformer systems – integrated, five-column, m3f based, with appropriately shaped external characteristics meet all the requirements of discharge plasma devices. They ensure discharge ignition, support after ignition and limitation of the electrode current, and as power supplies of DBD reactors they compensate the capacitive component of the reactor current, improving the cooperation of the plasma reactor with the supply network. In an integrated system, the discharge ignition is carried out by the third harmonic (150 Hz) of the voltage, induced by the non-linearity of the operating transformers, and the power transmission is carried out by the first harmonic of the main magnetic flux of the operating transformers. Thanks to the integration of the ignition and discharge functions and limiting the electrode current in one device, the work transformers can be designed for several times lower operating voltage (rated powers) than those used so far. Such a solution ensures stable operation of the plasma reactor, short outages, allows reduction of the number of elements used in traditional transformer power supplies.

Converters, commonly used for drive purposes, suitably designed as power supplies for discharge devices, have many advantages and properties unattainable in transformer power supplies. The main advantage of such power supplies is the ability to regulate voltages, currents and power in a wide range, necessary for the correct operation of the plasma reactor. Currently, power systems based on insulated-gate bipolar transistors are built for low and medium powers, in the order of several hundred kilowatts and frequencies up to 20 kHz, while systems based on metal–oxide–semiconductor field-effect transformers have powers of a few kW and switching frequencies up to several hundred kHz.

Selection the operating parameters of a plasma reactor and power and process gas supply systems require to determine which of the parameters must be maintained in strictly defined regimes and which may be out of control. The issue of plasma parameters is as complicated, as we go deeply into its physical and chemical properties. The shaping of plasma parameters is not only limited to supply voltage, current and frequency. Many factors have to be considered, such as gas properties, distribution of flows in the reactor, share of impurities, shape of electrodes and its number, distribution of electromagnetic field and interference.

The AC/DC/AC are also susceptible to interference generated by the plasma reactor, and from this point of view, transformers are better suited as power supplies for plasma reactors. However, the converter power supply has an advantage over them when it is necessary to adjust the parameters of the generated plasma in real time. A disadvantage of the analysed power supply is the lack of the possibility to adjust different settings of current, voltage and frequency values for both reactor stages. It has been noted that within certain limits of electricity supply and gas parameters, the reactor generates a greater number of interferences. However, it is difficult to systematise the influence of particular parameters on AC/DC/AC converter operation.

In AC/DC/AC converters, matching transformers play an important role in the cooperation between the converter and the plasma reactor. By shaping their characteristics in terms of the size of the winding leakage reactance and the material properties of the core, optimum conditions of cooperation between the plasma reactor and the converter can be ensured.

5. Cold plasma for soil treatment applications

Kenji Ebihara, Fumiaki Mitsugi, Henryka Danuta Stryczewska, Oleksandr Boiko, Jacek Majcher

5.1. Introduction

As the global human population is growing continuously, agriculture production systems are facing unprecedented challenges from an increasing demand for food. This must be accompanied with the protection of natural ecosystem by means of sustainable farming.

The quality of the soil has a significant impact on the well-being and prosperity of the region. Agriculture and soil protection includes problems of overuse of chemicals that degrade soil and increase pesticide content in soil, groundwater and food. Chemical farming also affects the quality of cultivated seeds and their ability to germinate. Prevention of microbiological contamination of soil and agricultural products during their processing, transport and storage is important.

Plasma technologies can be implemented for soil contamination and their fumigation, cultivation and storage of agricultural products and food, removal of insects, fungi and molds, sterilization and disinfection of packaging materials that are not resistant to high temperatures, and treatment of living tissues [49–76]. This is due to such features of plasma technologies as reliability, conducting plasma processes at atmospheric pressure, energy selectivity as well as progress in the field of power electronics, which allows high-efficiency and low-price constructions of plasma reactor power supplies [15, 38, 77–84].

The growing emission of greenhouse gases into the atmosphere and the related global warming causes an increase in the number of such ecological phenomena as droughts, floods and violent storms. They lead to environmental degradation, especially crop destruction and deterioration of soil quality. The most difficult challenges in flood relief are: lack of drinking water due to contaminated wells and damage to water treatment plants; deterioration of air quality, especially indoors; the presence of hard-to-decompose sediments carried by flood waters as well as chemical and biological pollutants, leading to contamination of surface waters, bacterial infections and persistent mold, the consequence of which is the smell of rot.

Conventional chemical methods of soil cleaning based on pesticides are effective in preventing and spreading diseases in the soil, however, pesticide residues in groundwater caused by their excessive use have become a serious problem in agriculture. Therefore, alternative methods of soil purification are sought, and the use of ozone generated by electrical discharges is becoming one of the most important techniques to ensure the safety of plant cultivation and the safe processing of soil and food products.

The purpose of agricultural soil treatment is to eliminate the microbial and insect cells found in the soil, but only those that cause a decrease in soil fertility and damage the seeds, roots and leaves of plants. Ozone is a strong oxidant and a much more effective disinfectant than chlorine compounds. The mixture of water mist with ozone produces very reactive intermediate hydroxyl free radicals that have great potential not only in removing pathogenic microorganisms, fungi and insects, but can also contribute to the natural fertilization of the soil [51, 52, 57–59, 85–89].

The topic of plasma application in biomedicine and agriculture is highly interdisciplinary, as it covers such physical and chemical phenomena as etching processes, high-energy UV radiation, heat and alternating electric fields.

Their role and high efficiency in the processes of decontamination, sterilization, treatment and modification of surfaces due to antimicrobial agents produced in plasma, such as charged and excited particles, reactive oxygen species (ROS), atomic oxygen (O), reactive nitrogen species, atomic nitrogen (N), nitric oxide (NO) as well as a large selection of different types of plasma reactors make them suitable for use in agricultural and biomedical processes [73, 90–92].

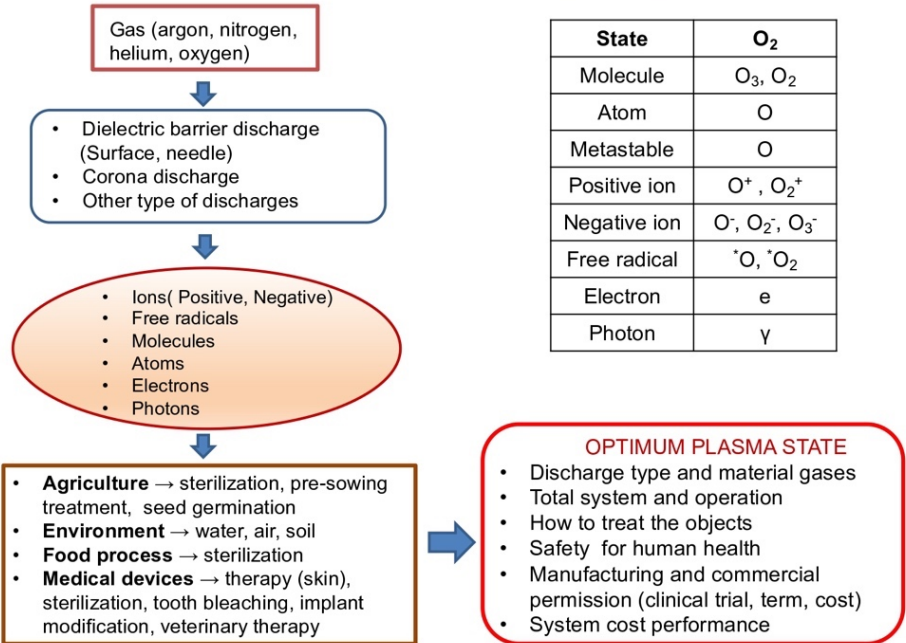


Figure 5.1. The technological complexity of plasma applications in agriculture, biology and medicine. Source: own elaboration

Figure 5.1 shows the technological complexity of cold atmospheric plasma applications in agriculture, biology and medicine. In order to optimize the plasma process for the above-mentioned applications, the following should be taken into account: the type of electrical discharges and process gases, the solutions used for plasma installations and their power supply systems, their economy and, above all, safety for living organisms and personnel.



5.2. Plasma in agricultural soil treatment

Fumiaki Mitsugi, Kenji Ebihara

Recently, agricultural application of plasma has been investigated using non-thermal plasma such as a plasma jet and dielectric barrier discharge for soil remediation to decompose chemical residues, for food preservation to inactivate microorganisms and for seed treatment to enhance germination. Table 5.1 summarises where and when plasma treatment can be applied. Plasma treatment is divided into either direct or indirect ways, which means direct plasma irradiation to targets and ozone gas exposure to targets, respectively. Plasma from a plasma jet or dielectric barrier discharge is applicable directly to seeds before planting or to soil and foods after cultivation. Because the main carrier of plant diseases are worms in soil and pests on leaves, treating soil before seeding and controlling pest during cultivation are necessary and large amounts of chemical pesticide are used for disinfection. Additionally, artificial nitrogen fertilisers in the form of $(\text{NH}_2)_2\text{CO}$, $(\text{NH}_4)_2\text{SO}_4$, NH_4NO_3 are overused to enhance plant growth while they remain in the plant or soil, damaging underwater and human body. When considering the scale of treatment, indirect usage of plasma, that is ozone gas treatment, is the most effective way from the practical point of view and suitable for agricultural application compared to direct usage of plasma regarding speed, volume, and uniformity of treatment, as the agricultural field is too huge compared to the volume of plasma. As for pest control during plant cultivation, an ozone mist sprayer is one of the alternatives to conventional chemical pesticide spray. The ozone mist works for the extermination of aphids, viruses, and so on. Modern agriculture has the problem of plant diseases caused by specific soil worms including nematodes and pathogens living on soil surface as shown in Table 5.2. The root, leaf, and fruit of plant are damaged in various ways and so many chemical pesticides are developed, specialised for each disease. However, the problem is that these pesticides allow the generation of resistant bacteria and remain on products and in the soil as a toxic residue. Because a pesticide basically works on the cell wall, the generation of mutants cannot be suppressed and this induces resistant bacteria. As such, the development of chemical pesticides generates new pathogens which needs to be avoided. Therefore, soil treatment with ozone is a promising technique for soil disinfection because ozone works on targets directly by oxidizing and

damaging the cell wall, protein, and DNA due to its high oxidation potential. As preparation for ozone treatment of soil, the chemical and electrical properties of soil should be understood. Figure 5.1 shows the composition of soil by focusing on how much organic matter is contained in soil. Soil basically consists of inorganic clay, air, water and 5% organic substances.

Table 5.1. Direct application of plasma and ozone in agricultural cultivation

Ozone Plasma	Soil	Seeds Seedling	Plants Foods
Before planting	<ul style="list-style-type: none"> *Soil worm *Growth enhancement (Nitrogen) *Soil virus *Humus 	<ul style="list-style-type: none"> *Bacteria *Germination 	
During cultivating	<ul style="list-style-type: none"> *Soil disease treatment *Ozone-soil solution 		<ul style="list-style-type: none"> *Pest *Virus *Diseases 
After harvest	<ul style="list-style-type: none"> *Residual pesticide 		<ul style="list-style-type: none"> *Residual toxic *Mould *Putrefaction *Bacteria

Microorganisms are part of the organic substances, which are classified as animal, bacteria, and fungi. About 700 kg of microorganisms are living in 1000 m² of soil. That is why most beneficial microorganisms can survive after ozone treatment, as the number of them is much greater than that of the targeted virus. Furthermore, the microorganisms consist of carbon and nitrogen, which are easily oxidised by ozone and decompose immediately into smaller molecules.

Soil acidity is another important factor for soil as plant roots and microorganisms have proper soil acidity to grow up. Soil acidity is complicated because soil is composed of inorganic ions dissolved in soil water and shows a strong buffering function (Figure 5.3). There are two indices of pH (H₂O) and pH (KCl) in the evaluation of soil acidity as shown in Figure 5.2. pH (H₂O) is the conventional index for soil acidity that measures hydrogen ions solved in water. In case of soil, however, detectable hydrogen ions in pH (H₂O) are those dissolved in water and other undetectable hydrogen ions are attracted electrically to soil clay and humus because they charge negative. Therefore, soil acidity in pH

(H₂O) means active acidity where hydrogen ions are free. On the other hand, to evaluate true and total soil acidity including residual acidity, KCl solution is used for measurement, and this is defined as pH (KCl). Moreover, cations like Al₃₊, Ca₂₊ absorbed on the clay surface can easily exchange their locations with hydrogen ions, which is called the buffering function. Due to this buffering function, acidification of soil cannot be determined by the measurement in pH (H₂O), whereas real amount of hydrogen ions increases by acidification.

Table 5.2. Soil worm and pathogens, and necessary chemical disinfectants

Worm, pathogen	Disease	Plant	Pesticide, Disinfectant
<i>Nematode</i>	Nematode disease <i>root knot, Cyst root lesion</i>	Carrot Potato	cadusafos, fosthiazate, oxamyl
<i>Pythium</i>	Damping off	Tomato, Pimento, Eggplant, Potato, Ginger, Spinach	metalaxyl, hydroxyisoxazole, captan
	Root rot		
<i>Xanthomonas campestris</i>	Black rot	Cabbage, Broccoli	kasagumycin, oxolinic acid
<i>Fusarium oxysporum</i>	Chlorosis	Cabbage, Radish, Strawberry	dazomet, chloropicrin
<i>Plasmodiophora brassicae</i>	Root knot	Turnip, Chinese cabbage	amisulbrom, flusulfamide
<i>Ralstonia solanacearum</i>	Wilt	Tomato, Eggplant	dazomet, chloropicrin
<i>Pseudomonas marginalis pv. marginalis</i>	Rot	Lettuce	streptomycin, kasugamycin

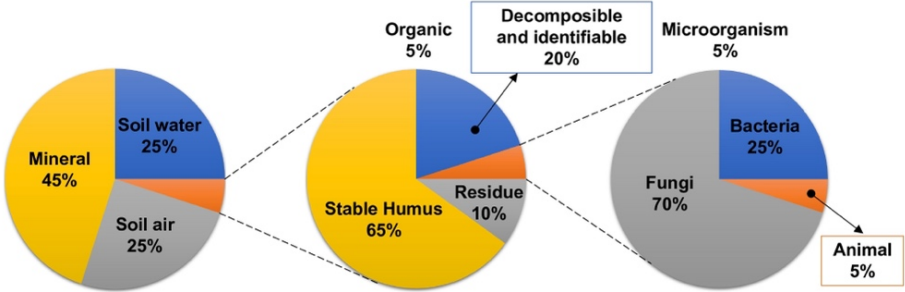


Figure 5.2. Composition of soil and classification of organic substances. Microorganisms (700 kg) are living in soil (1 a = 1000 m²) – Water: 560 kg, Carbon: 70 kg, Nitrogen: 10 kg. Source: own elaboration

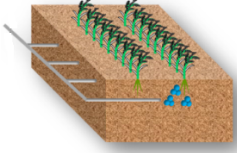
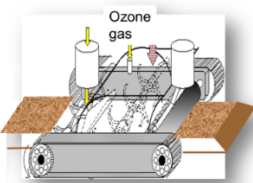
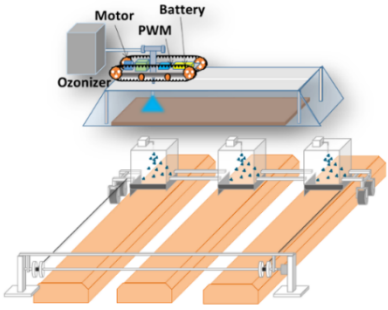
Table 5.3 shows several methods for soil disinfection in contemporary agriculture. Currently, chemical pesticides are mainly used because it is more effective than disinfection using solar heat and hot water. It takes about two weeks for fumigation and another two weeks are necessary for degas. Basically, disinfecting soil by chemical takes time and has some environmental problems. In addition, disinfectors and chemicals are too expensive.

Table 5.3. Comparison among soil disinfection methods

Type	Period	Disadvantage	Machine	Advantage
CHEMICAL	1–2 week (fumigation) 1–2 week (degas)	*Residue, *Resistant worm, *Dangerous/hard (operator)	Disinfector: \$5000	Chemical cost \$300 / 10 a
SOLAR HEAT	3 weeks	*Summer only, *Higher > 60°C *Long anaerobic term	Vinyl sheet	Low cost, Safe
HOT WATER	1 day	*High cost	Boiler: \$50 000	Short term, Safe
OZONE	1 day		Ozone diffusion: \$2000, Ozone injection, Ozone rotary disinfector.	Short term, Gas \$20 / 10 a, Electricity: \$1 / 10 a, No residue. Nitrify. No resistant worm,

Ozone treatment, on the other hand, does not need fumigation and degas, completing treatment in shorter period compared to necessary period in chemical use. Material and electric costs are cheap as the source gas of ozone is oxygen and the dielectric barrier discharge consumes less power and works on many kinds of targets without generating resistant worms and bacteria. Extra ozone that is not used to decompose organic substances for disinfection is returned to oxygen in a short time because the lifetime of ozone is not so long. This is an important characteristic of ozone to complete disinfection safely. Optionally, there is nitrifying function of soil because nitrogen sources contained in soil too much as mentioned before that is oxidised into nitrogen nutrient. Therefore, ozone has both an effect as a pesticide and as a nitrogen fertiliser. Table 5.4 proposes three types of ozone treatment systems for soil disinfection. Ozone injection targets only where treatment is needed but it lacks in uniformity. An ozone rotary tiller overcomes that problem but it is expensive because of material's limitations (oxidation avoiding) for rotational systems.

Table 5.4. Kinds of ozone disinfection method

INJECTION	ROTARY	DIFFUSION
		
Cost		
×	×	O
Up-scale		
O	×	O
Uniformity		
×	O	O

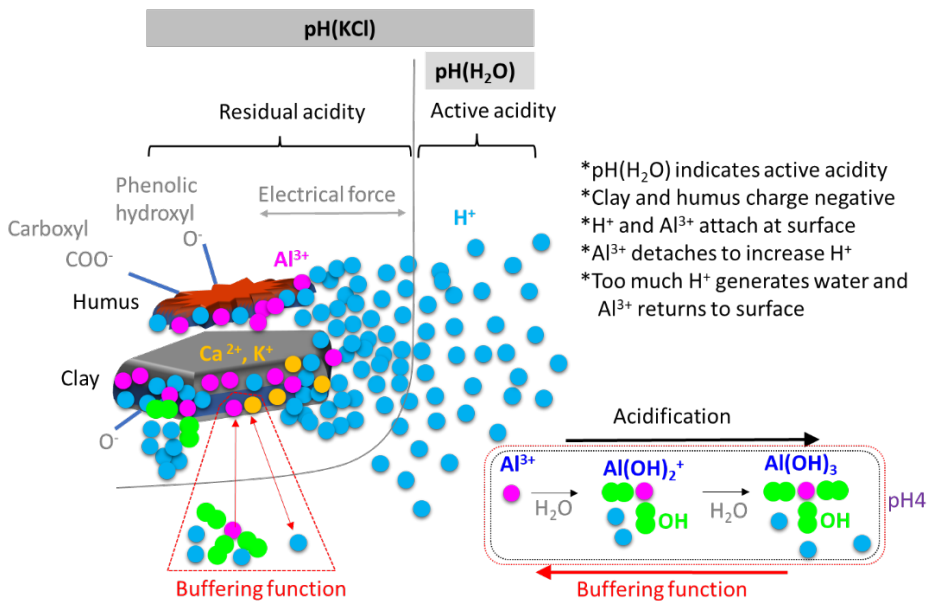


Figure 5.3. Soil acidity and buffering function. Source: own elaboration

Currently, the most effective and reasonable way we employ for ozone treatment of soil is the ozone diffusion method, which realises up-scaled and uniform treatment of soil surface where most soil worms live. In this method, the soil ridge is covered by vinyl or a box and the ozone generated by the dielectric barrier discharge is inside it. The covered system has wheel and is moved over the soil by being pulled with a motor. Ozone diffuses from soil surface and does not reach to the deeper side in soil; however, it works well to kill soil worms like nematode and soil pathogens as they live on the surface of soil.

Figure 5.4 is a diagram of the movement of nitrogen nutrients between compost or fertiliser and plants in the soil and possible mechanisms for plant growth both in nature and ozone treatment. The final form of nitrogen nutrient absorbed by plant roots is ammonium and nitrate ions dissolved in soil water as roots can absorb them in the smallest form of molecules. In nature, living small animals and enzymes decompose the compost of plants and dead animals into smaller molecules of organic nitrogen such as amino acids, formic acid and so on, generating ammonia finally by deamination. Part of the ammonia is dissolved as ammonium ions and the other is oxidised into nitrate ions to be absorbed by plant roots by the activity of nitrification bacteria. Such bacteria use oxygen in soil to complete this chemical reaction, which is a process particular to soil, as the reaction does not occur in normal conditions.

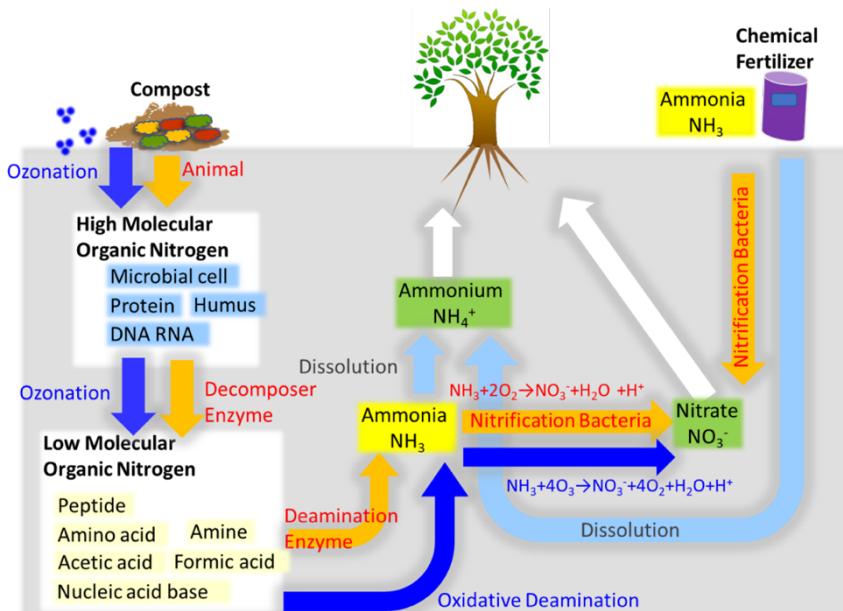


Figure 5.4. Mechanism of ozone soil disinfection to enhance plant growth. Source: own elaboration

The use of chemical fertiliser shortens the time needed for these natural microbial processes to enhance plant growth in a short time. However, the additional nitrogen breaks the natural nitrogen balance, and it is concentrated in ground water and sea water and finally, in the human body. This will be new environmental issue which human beings will face in the near future.

Ozone treatment basically focuses on soil disinfection to exterminate soil worms and pathogens but oxidation of compost progresses simultaneously. The oxidation of compost from high molecular organic nitrogen to low molecular organic nitrogen is done through strong oxidation, called ozonation. Further ozonation induces the final form of nitrogen nutrient of ammonium and nitrate ions by oxidative deamination. This oxidative deamination may be assisted with catalytic metals like iron in soil. Not only the final product, but also those produced in the middle process such as humus and fulvic acid play an important role in enhancing plant growth, as they support beneficial microorganisms living around a plant's root. This is known as a bio-stimulant and it is generated during ozone treatment of soil. The bio-stimulant is also a beneficial material around plant growth and that is why the enhancement of plant growth can be observed after cultivating in ozone treatment of soil. This means that ozone treatment has the function to increase the bio-stimulant and nitrogen nutrients in a short time while maintaining the nitrogen balance.

5.3. Advanced techniques for agriculture management, pest control and plant growth

Kenji Ebihara, Fumiaki Mitsugi

Advanced techniques are greatly needed in agriculture to effectively grow a plant and increase its yield. Insect pests causing between a 20% and 40% percent loss of global crop production is one of the major problems in agriculture.

Recognizing pest insects as well as identifying diseases in plants when they appear are the crucial step for efficient agricultural procedures. Due to the vast number of pest insect species and diseases, their recognition relies heavily on the professional knowledge of agricultural experts and has been done by manual observation which is obviously laborious and time-consuming. Real-time detection and classification of pest insect species in the agricultural field is of great significance to control pests without delay in agricultural procedures. This can contribute toward realising sustainable farming procedures, avoiding the over use of pesticides.

Recently, deep learning techniques have been applied to agricultural management involving the detection and classification of pest insects and plant diseases. Deep learning is a technique of machine learning that uses multi-level neural networks that allow computers to learn and extract deep abstract features

automatically. We have introduced artificial intelligence technologies to identify the pest control characteristics of the non-chemical ozone-mist sterilisation system developed previously [93-100]. Additionally, the technologies are applied to identify the periodic relationship between growth stages and photosynthesis vegetation of some vegetables.

The ozone-mist sterilisation system is composed of an ozone generator, a water-mist supply system, an AC-DC inverter connected to a Li-ion battery, a lightweight oxygen vessel with a pressure regulator, a water tank and a movable spray rod with an ozone-mist nozzle. Figure 5.5 shows the outline of our sterilisation system and a picture of the latest prototype system. High density ozone which is suitable to sterilise insects, worms, bacteria and viruses is generated by surface dielectric barrier discharge (SDBD). The HV electrode of the SDBD is embedded inside the dielectric material and moulded. The DBD is generated on the surface electrode placed on the dielectrics Al_2O_3 . The SDBD is cooled by air.

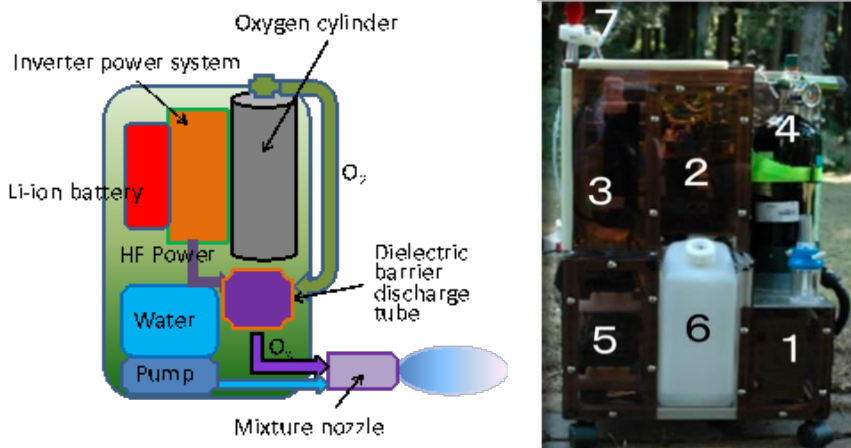


Figure 5.5. Outline of the ozone-mist non-chemical sterilisation system (left) and the picture of latest sterilisation model (right), where (1) DBD ozone generator, (2) HF inverter, (3) Li-ion battery, (4) O_2 vessel, (5) water pump, (6) water tank and (7) ozone-mist spray. Source: own elaboration based on [98]

High density ozone is generated by two types of surface dielectric barrier discharges (flat-plate and cylindrical electrodes). The AC electric power for the high frequency generator was supplied from the AC-DC inverter with Li-ion batteries. High density ozone of 112 g/m^3 and 86 g/m^3 at an oxygen flow rate of 1 litre/min is generated using the cylindrical type and the flat-plate type, respectively. The sterilisation rate of this system is determined mostly by ozone and its derivative concentration, the flow rate, the treatment time and the distance between the target insects and the nozzle.

The sterilisation rate, defined as death number/total number of insects, is a dominant factor in the evaluation of the sterilisation system. Table 5.1 shows typical sterilisation rates of insects treated by an ozone concentration of 68 g/m³ (2 L/min O₂) with mist-water 330 mL/min at treatment time of 10–20 s and by gaseous ozone (86 g/m³ O₃) without water-mist. The sterilisation rate over 80% ~ 100% was attained for aphids (Tobacco *Myzus persicae*, *Solidago Canadensis*, Orange *Toxoptera citricius*) and *Camellia Sinensis*. These results are comparable to the sterilisation rate of chemical synthetics (90% at *t* = 10 s). A longer treatment time was needed to kill the Tobacco green caterpillar of a larger size (about 5 mm).

Table 5.5. Sterilisation rate of pest insects by ozone-mist sterilisation






Insects	Plant	Sterilisation rate
Tobacco <i>Myzus persicae</i>		80% ~ 90% O ₃ : 86 g/m ³ , 1 L/min O ₂ Ozone solubility: 5 ppm Spraying time: 10 sec
Tobacco green caterpillar		50% O ₃ : 86 g/m ³ , 1 L/min O ₂ Ozone solubility: 5 ppm Spraying time: 20 sec
<i>Solidago Canadensis</i>		95% ~ 100% O ₃ : 86 g/m ³ , 1 L/min O ₂ Ozone solubility: 5 ppm Spraying time: 10 sec
Orange <i>Toxoptera citricidus</i>		100% O ₃ : 86 g/m ³ , 1 L/min O ₂ Ozone solubility: 5 ppm Spraying time: 10 sec
<i>Camellia Sinesis</i> (Green tea leaf)		100% by ozone gas O ₃ : 86 g/m ³ , 1 L/min O ₂ Spraying time: 10 sec 90% by ozone-mist

Figure 5.6 presents the pictures of an aphid and its respiratory system. Gaseous ozone and its derivative radicals are taken into the aphid body through spiracles, travel via the trachea through the body and reach the cells. As a result, the aphid may be killed by molecular ozone and its derivative radicals acting on proteins and organelles (e.g., nucleus) of the cell. It is well-known that the tissues of most of aphids shed droplets of water. Considering the adsorption mechanism of ozone and the related radicals for aphids, the ozone-mist sterilisation method developed here is advantageous compared to the conventional ozonated water spray method.

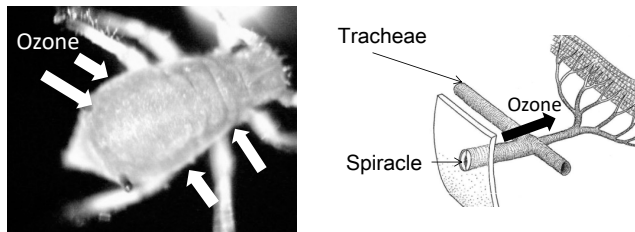


Figure 5.6. Pictures of an aphid treated by ozone-mist and the respiratory system. Source: own elaboration based on [98]

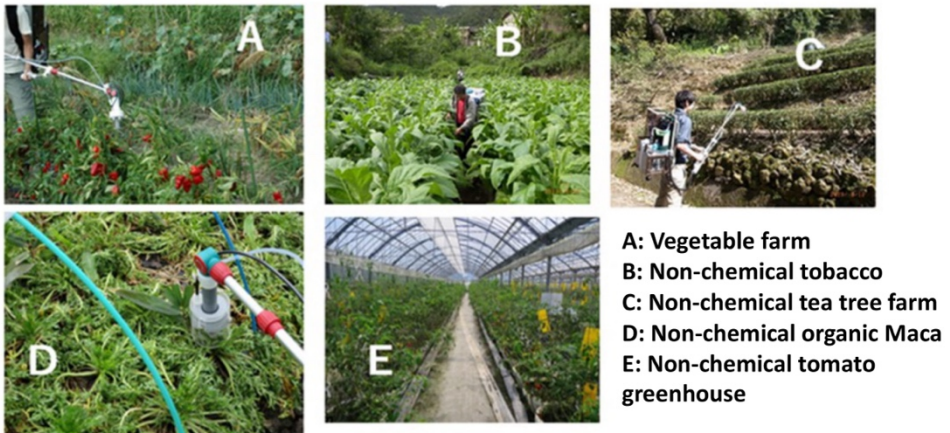


Figure 5.7. Ozone-mist spraying at various agricultural farms. Source: own elaboration

The experiments were carried out in agricultural farms and in the greenhouse as shown in Figure 5.7. The attempts aiming at practical use of this non-chemical system were performed for some kinds of vegetable leaves (Figure 5.7.A), tobacco leaves (Figure 5.7.B), tea leaves (Figure 5.7.C), organic Maca (Figure 5.7.D), and tomato leaves (Figure 5.7.E) in the greenhouse.

Figure 5.8 shows the gaseous ozone concentration of the ozone-mist around the nozzle at the O_2 flow rate of 2 L/min. The commercial ozone generator provides a concentration of 68 g/m^3 at the O_2 flow rate of 2 L/min. Maximum

concentration appeared at $d = 50$ mm, while the lower concentration near the nozzle is due to the air flow from the periphery of the ozone injection tube. The concentration difference between the ozone and the ozone-mist as a function of the distance (d) is caused mostly by the generation of ozone derivative radicals ($*OH$, OH_2). The sterilisation results show that the treatment time on agricultural farms increases enormously compared with the time at the laboratory (Table 5.5). Identification of pest insects as well as weather conditions such as temperature, humidity and wind are also other dominant factors in effectively insects killing.

In order to obtain the treatment conditions for the complicated processes in practical agricultural management, we developed the remote ozone-mist system using deep learning technology. Deep learning is a machine learning technique that teaches a computer to learn from data. This recent and advanced technique constitutes image processing and data analysis with accurate results.

Figure 5.9 shows the ozone-mist system implemented in a greenhouse to sterilise pest insects while monitoring insects and plants. The nozzle of the ozone-mist spray automatically moves to take an optimal position on the leaves infested by insects. The Wi-Fi camera captures the images of the pest and the images are transferred to remote stations where the identification of the pest is carried out. When the pest is detected, the ozone-mist spray will turn on, based on the treatment time determined by the deep learning.

Pest insects such as aphids, whiteflies and moths are killed under appropriate treatment conditions [99]. In order to improve the sterilisation efficiency in pest control, here we have tried to introduce Deep Learning (DL) technology for real-time recognition of pest insects in the greenhouse. The non-chemical sterilisation system is managed by information about insect pest appearance that the DL detects in the testing process for pest insects. The YOLO object detection based on DL is adapted here to make detection and classification of flying insects such as aphids, moths, beetles, flies, white flies, mosquitoes and ants.

Yellow sticky traps were used to collect flying insects because they are always moving, and it is difficult to get clear images of them directly. Other insects which could not be caught with the stick traps were directly captured using a net. Some species have different forms including egg, larva, and pupa. To advance the precision of the pest recognition, we also collect insect images from several large-scale pest insect datasets. The practical application of DL technology to pest insect recognition in the agricultural field is limited. The majority of the insect images used in most research was taken by referring to the existing database set in controlled laboratory environments and a few researchers worked using field-based images in real environments.

Figure 5.10 shows our results of pest detection and identification for remote and real time recognition of non-chemical sterilisation. The total number of images for seven classes of insect pests (aphid, moth, beetle, fly, whitefly, mosquito, ant) collected from sticky traps, the public IP102 dataset, and images on Web sites. Each bounding box includes confidence (precision) and the point

information of the box. The decimal values of each box indicate the identification precision of insect pests. DL technique on Raspberry Pi is applied to detect and identify insects in real time. Raspberry Pi is a tiny and affordable single-board computer. If any insect is detected in the field, the relay turns on so that the pesticide spray starts to operate. We are working to develop an intelligent auto-spraying system able to detect and classify pest insects in agricultural fields.

Numerous techniques have been developed trying to obtain safer agricultural products and lower environmental impacts. In order to meet these requirements, the complex and unpredictable agricultural systems such as plant growth and diseases in plants need to be understood by monitoring, measuring and continuously analysing various physical and biological aspects and phenomena. Practical and effective operation using the above ozone-mist sterilisation system on agricultural farms needs to detect plant state and to monitor the actions of pest insects and infectious diseases.

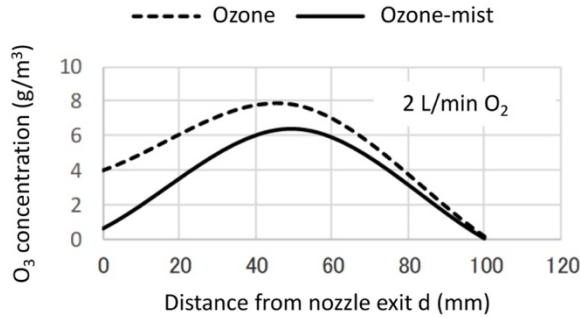


Figure 5.8. Ozone concentration of ozone-mist at nozzle exit. Source: own elaboration based on [99]

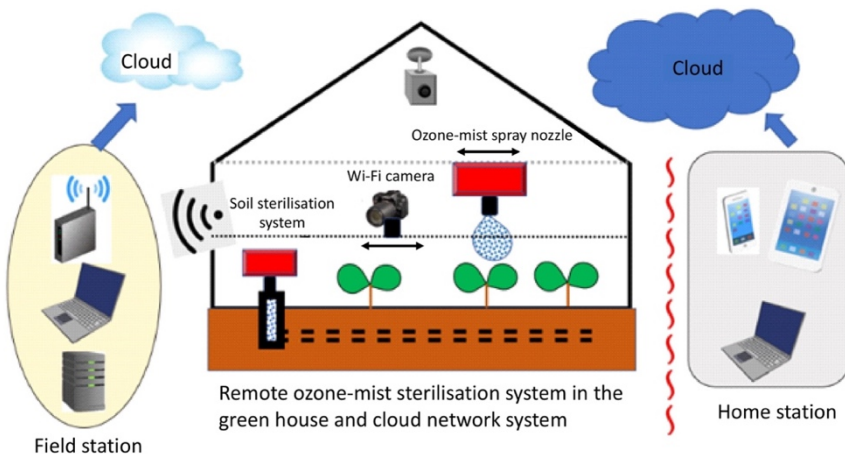


Figure 5.9. Remote ozone-mist sterilisation system in the greenhouse and cloud network system. Source: own elaboration

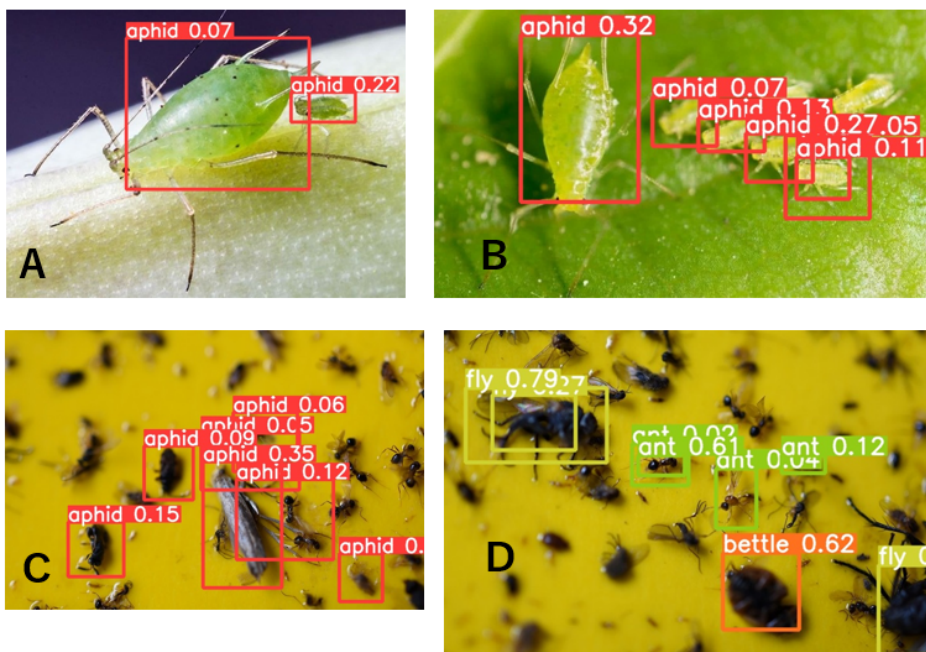


Figure 5.10. Detection of images of aphids on leaves (A, B) and on sticky traps (C, D). The numerical value of the bounding box is the precision. Source: own elaboration

Table 5.6. Characteristic parameters of plants, harmful insects and diseases

plant	species, plant growth (size, colour, biological properties), damages by insects and diseases
harmful insect	species, appearance, outbreak, growth level (egg, larva, adult), size, colour
disease	classification, detection, outbreak, damages on plants, biological effects of ozone-mist on pathogenic bacteria, fungi and viruses
ozone-mist spray	ozone concentration, flow rate, treatment-time, sterilisation rate

We have developed a web-based management system combined with technology for the analysis of the digital camera images of plants. Three colour channels (Red, Green, Blue: R, G, B with) were applied to predict plant growth and to monitor foliar injury. The data analysis and real-time web transmission from the agricultural field to a remote location via the Internet were introduced.

Table 5.6 shows characteristic parameters that are to be analysed using the DL technique. The information of these parameters plays a dominant role in optimal control conditions of the ozone-mist sterilisation system. The current development of the DL-based approach is applied to some kinds of vegetables and harmful insects in agricultural farms.

Vegetation carries out photosynthesis to create energy and this function is performed by chlorophyll. Chlorophyll absorbs light most strongly in the blue portion of the electromagnetic spectrum (465 nm at peak), followed by the red portion (665 nm at peak). The energy absorbed from the blue and red lights is converted to produce carbon dioxide and glucose. Plants use glucose together with nitrogen compounds taken from the soil to form chlorophyll (new leaves). On the other hand, chlorophyll is a poor absorber of green and near-green portions of the spectrum, which is reflected producing the green colour of chlorophyll-containing tissues. The digital images of plants consist of R, G, B channels and each channel has intensity levels from 0 to 255 (integer valued). Richardson et al. [100] showed that the greenness index defined by $(2G-R-B)$ quite clearly responds to the changes caused by emergence of hardwood forest development. The greenness, which increases G value and decreases R and B values, achieved the best accuracy in the vegetation extraction.

We propose this greenness index for the analysis of the digital images of vegetables. Figure 5.11 describes the details of Figure 5.9 and shows a schematic outline of web-based analysis for our image processing. The system consists of a data acquisition part for the agricultural fields, a plant analysis/deep-learning site and a web server for the database system. Several vegetables such as lettuces, cabbages and tomatoes were planted in the greenhouse (W: 3 m, D: 4 m, H: 2 m) and fields. Digital Wi-Fi cameras and smartphones were used to take images of plants under solar irradiation. The complementary metal oxide semiconductor image sensor with an IR-cut filter has a spectral sensitivity of peak intensity around 550 nm.

Photo images were transferred to and stored on the web server at the remote site through the internet. We apply the TensorFlow framework to analyse plant images taken after sowing the seeds. TensorFlow provides a rich set of deep learning application programming interfaces. The database is constructed by storing the analysed results at the remote site on the web server.

Vegetables planted in the greenhouse were observed by taking digital images of their leaves during their growth period from young to ripeness stages. The total number of pixels of the camera image is 12 Megapixels (Mpx) consisting of the row(m) = M (3,000) and the column(n) = N (4,000). The greenness index intensity S_{mn} for the pixel at the row(m) and the column (n) is calculated by the equation $S_{mn} = 2G - R - B$ at a pixel (m, n) and the normalised value I_{mn} is expressed by the equation $I_{mn} = S_{mn} / S_0$, where S_0 is the maximum value of S_{mn} . Figure 5.12 shows a typical greenness index I_{mn} image of a cabbage leaf 67 days after seeding. The grey colour ranges from white ($I_{mn} = 1$) to black ($I_{mn} = 0$).

The total number of pixels in the image, P , and the sum of S_{mn} values, S , and the local intensity, SL , are shown in Figure 5.13 as a function of the green index value I_{mn} . The number of pixels is shown to be 11.2 Mpx for $I_{mn} > 0$; 8.0 Mpx for $I_{mn} > 0.5$ and 1.03 Mpx for $I_{mn} > 0.8$. The sum values S corresponding to these pixels are 6.56×10^6 for $I_{mn} > 0$; 5.49×10^6 for $I_{mn} > 0.5$ and 8.67×10^5 for $I_{mn} > 0.8$.

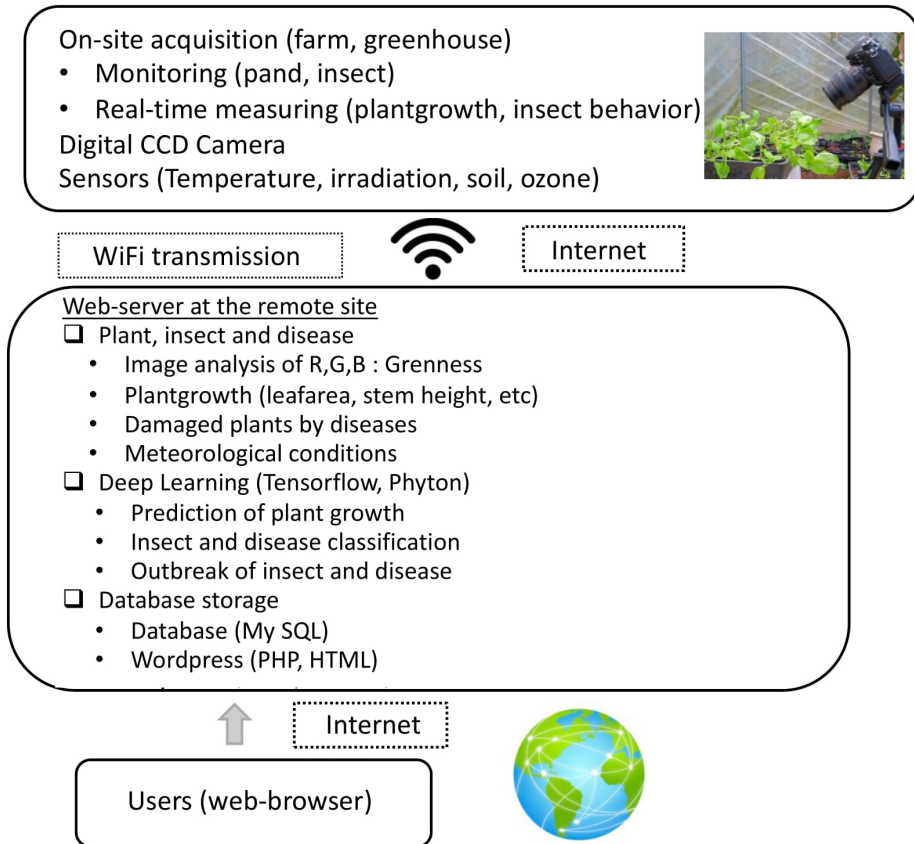


Figure 5.11. A schematic outline of a web-based analysis for images processing. Source: own elaboration based on [99]

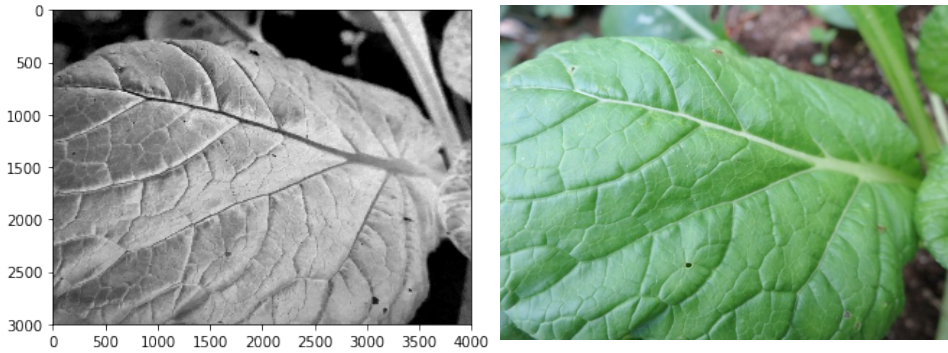


Figure 5.12. Image for green index intensity (left) and the photo (right) of the cabbage leaf 67 days after seeding. Source: own elaboration

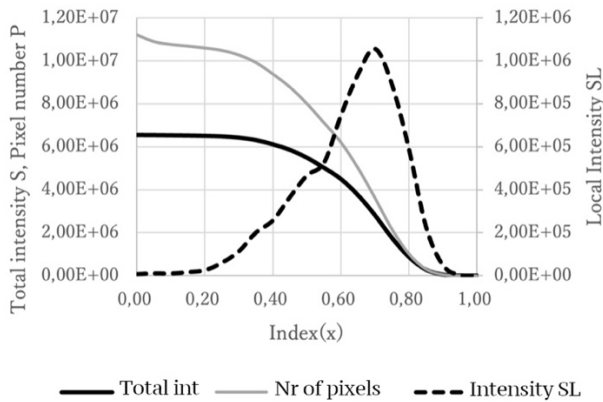


Figure 5.13. Total pixels number, total intensity S and local intensity SL as a function of normalised green index I_{mn} in case of cabbage 67 days after seeding. Source: own elaboration

The local intensity SL is obtained by the sum of S_{mn} ranging from I_{mn} to $I_{mn} + \Delta$, where $\Delta = 0.02$. The SL value expresses the photosynthetic rate due to the change in chlorophyll, area and mass of leaves. The $SL(I_{mn})$ value is also equal to the difference between $S(I_{mn})$ and $S(I_{mn} + \Delta)$ and its profile for the cabbage in Figure 5.12 has a maximum value of 1.16×10^5 at $I_{mn} = 0.73$ and the full width at half maximum (FWHM) of 0.27. The peak index (I_{max}) and the FWHM value are specific and typical parameters which are closely related to the plant growth behaviour.

Figure 5.14 shows the local intensity $SL(I_{mn})$ of the cabbage leaves over the 68 days after seeding. The 36-day profile shows the symmetrically hyperbolic curve having $I_{max} = 0.75$ with $FWHM = 0.27$. On the other hand, the profile for 28 days and 42 days has non-symmetric characteristics with gentle slope at higher I_{mn} and lower I_{mn} side, respectively.

Through photosynthesis, blue light combined with red light can increase plant growth and maturity rates. Green light taken into leaves enhances the production of chlorophyll. The absorbed energy from the light is transformed into the energy to grow the plant. The stored energy in the plant is applied to convert CO_2 with the help of air and water into glucose (sugar molecules) and oxygen. Plants use glucose together with nutrients taken from the soil to make new leaves and other plant parts. The photosynthetic characteristics above can suggest that in Figure 5.14 the chlorophyll is formed actively until 36 days and then the energy contained within glucose is used for plant growth.

Figure 5.15 shows the plant growth of the cabbage after seeding as well as the index I_{\max} and FWHM. The width, the length and the stem height were obtained for the selected samples of cabbages planted in the field.

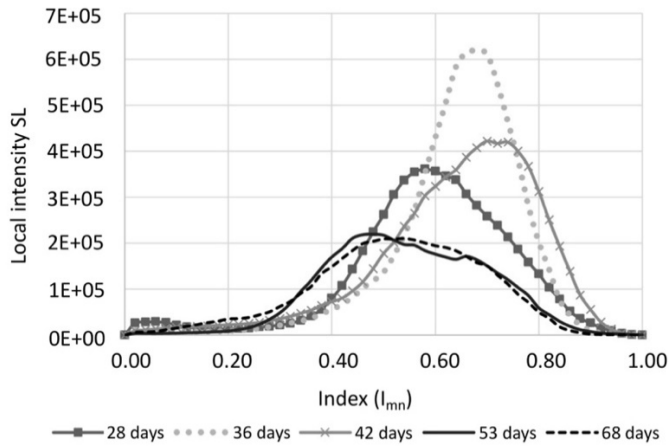


Figure 5.14. Local intensity SL as a function of normalised greenness index I_{mn} . The cabbage sample was observed over 68 days after seeding. Source: own elaboration

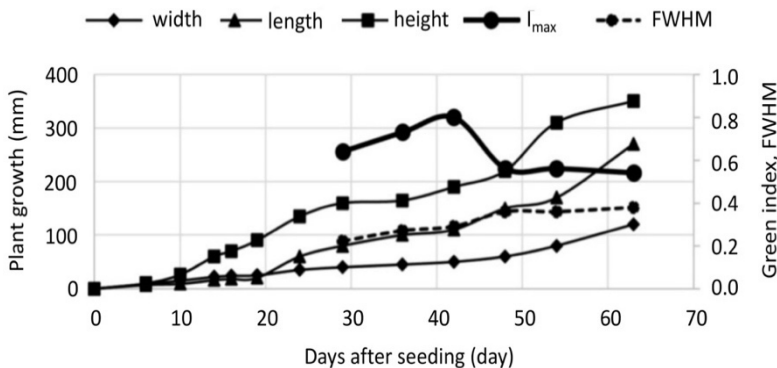


Figure 5.15. Local intensity SL as a function of normalised greenness index I_{mn} . The cabbage sample was observed over 63 days after seeding. Source: own elaboration

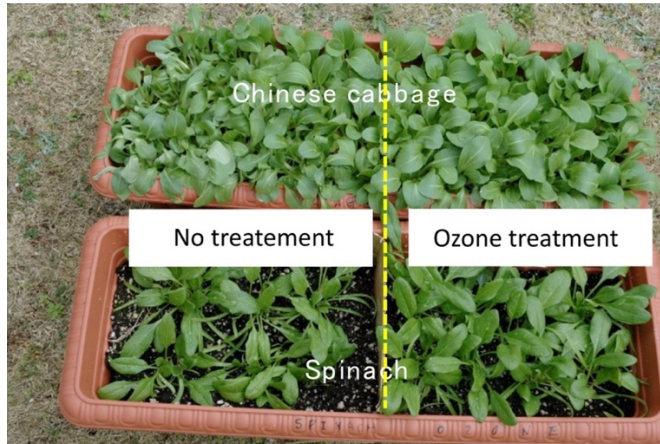


Figure 5.16. Photos of Chinese cabbage and spinach planted in ozone-treated soil (right half part of the container) and in untreated soil (left half). 50 days after seeding. Source: own elaboration

It was found that the width, the length and the height rapidly increase with time. This growth is mostly based on photosynthesis due to blue light with the red light. On the other hand, the I_{max} has a peak value at 42 days and then rapidly decreases following constant values.

Figure 5.16 shows the vegetables planted in ozone-treated soil and untreated soil. Chinese cabbages and spinaches were planted and observed over 50 days. The ozone concentration of 100 g/m^3 at an O_2 flow rate of 2 L/min was supplied to into the soil for 60 min. This treatment condition means that 12 g of ozone was injected into the 3 kg of soil.

The effect of ozone-treatment on the local intensity SL for the cabbage is shown in Figure 5.17. The clear difference of the SL profile appears at 25 days after seeding. I_{max} , defined as the maximum value of the greenness index, is 0.85 for the ozone-treated soil and 0.8 for untreated soil. The I_{max} value at 50 days after seeding is a similar value around 0.75 for both ozone-treated soil and untreated soil.

Figure 5.18 shows the local intensity profiles of the spinach planted in ozone-treated soil and untreated soil. It was noticed that in the case of spinach, the remarkable difference between the I_{max} values (0.75 for ozone treated and 0.60 for non-treated) occurs at 50 days after seeding.

The maximum values of the SL profiles are 2.1×10^4 for the ozone soil treatment and 1.57×10^4 for the non-treatment, respectively. This result indicates that ozone can enhance photosynthetic vegetation by 34% under present ozone-treatment conditions. We measured the average size of spinach leaves grown in the ozone-treated soil and the untreated soil for 50 days after seeding. The result indicates that the leaves of the ozone-treated spinach show 70% increase in the leaf width and 22% in the length in comparison with the untreated samples.

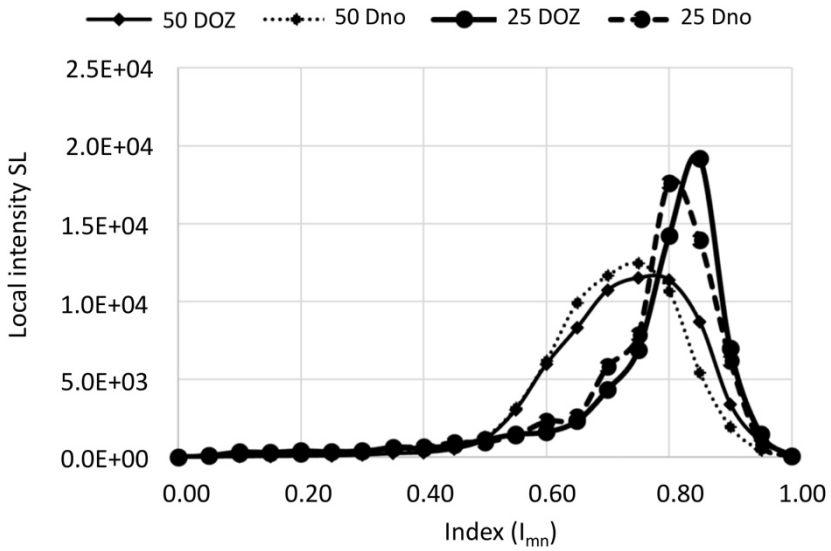


Figure 5.17. Effect of ozone treatment on local intensity SL of the cabbage at 25 days and 50 days after seeding. Source: own elaboration

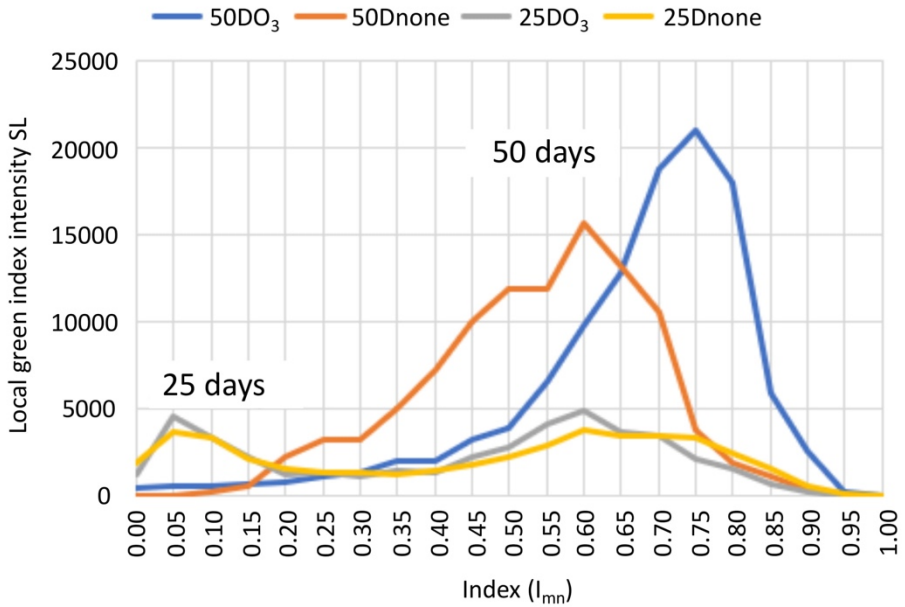


Figure 5.18. Effect of ozone treatment on local intensity SL of the cabbage at 25 days and 50 days after seeding. Source: own elaboration

5.4. Pre-sowing seed treatment with cold plasma

Oleksandr Boiko, Henryka Danuta Stryczewska

It was found that plant treatment with cold atmospheric plasma (CAP) combined with an electromagnetic field is an innovative technology that improves seed germination (up to 20%) and early growth of seedlings as well as significantly removes surface contamination of plants [101–103]. Other valuable advantages of this approach are significant changes in the plant's metabolism that result in biomass production improvement, increasing plant disease resistance and agricultural performance of crops [104–108].

CAP can be effectively used in pre-sowing seed treatment [101, 106, 109, 110]. Papers [101, 109] report CAP exposure of Norway spruce seeds with DBD RF planar reactor and indicate its germination and growth. The CAP treatment (processed by 2, 5, and 7 min) enhances the germination of spruce seeds, while in-vitro treatment causes its decrease. Electromagnetic field generation combined with CAP exposure changes concentration of H₂O₂ in germinating seeds. This technique was used by Ivankov et al. to examine the growth effect and production enlargement of cannabinoids (non-psychoactive) after pre-sowing hemp seeds exposure [110]. They achieved 25% plasma stimulated in vitro rate under the laboratory conditions. It was found that, the treated male plants demonstrated a rapid growth, while female plants seedling inhibits.

Belarussian scientists reported an effect of pre-sowing CAP treatment on the germination, disease resistance, and crop yield of maize, lupine, and winter wheat in laboratory conditions [106]. A DBD capacitively coupled plasma reactor was used for this purpose. The treatment of seeds took place in air with an ambient pressure of 200 Pa and an ambient temperature of 37°C, while the exposure time varied from 2 to 7 minutes. The authors reported a decreasing tendency in case of contamination of maize seeds infected by *Penicillium spp.* after the CAP treatment by 21% as well as positive germination and sprout growth. As for the Lupine seeds, the CAP exposure resulted in the total reduction of *C. gloeosporioides* and *K. caulivora* and a significant reduction of *Cladosporium* and *Alternaria fungi*. Plasma-treated winter wheat seeds affected by *Alternaria* and *Fusarium fungi* demonstrated a significant contamination reduction. The scientists concluded that the CAP exposure stimulated the growth and germination of plant seeds, reduces fungal contamination, and enhances the yield and disease resistance of crop plants.

5.5. Measurement of soil moisture

Jacek Majcher

Soil is one of the life-giving factors. It is thanks to it that plants have the right conditions for growth. According to the definitions found in the literature, soil is a heterogeneous and multiphase material. It consists of a solid phase, air, and water, with a distinction between free water and bound water. There are many parameters describing soil, the most important of which are moisture, conductivity and density. Among the previously mentioned soil parameters, from the biological point of view, moisture is a key parameter. Therefore, many methods and measurement techniques for determining soil moisture have been developed. Soil water content can be related to soil weight or volume, thus obtaining a parameter of moisture (Figure 5.19). These methods can be divided into direct and indirect. The direct method, taken to be the reference one, is the gravimetric method. It involves taking a soil sample, weighing and drying it under controlled conditions. Then the sample is weighed again and the water evaporated from the sample is calculated based on the difference in mass. Another group of methods are indirect methods, in which soil moisture is determined indirectly on the basis of other parameters.

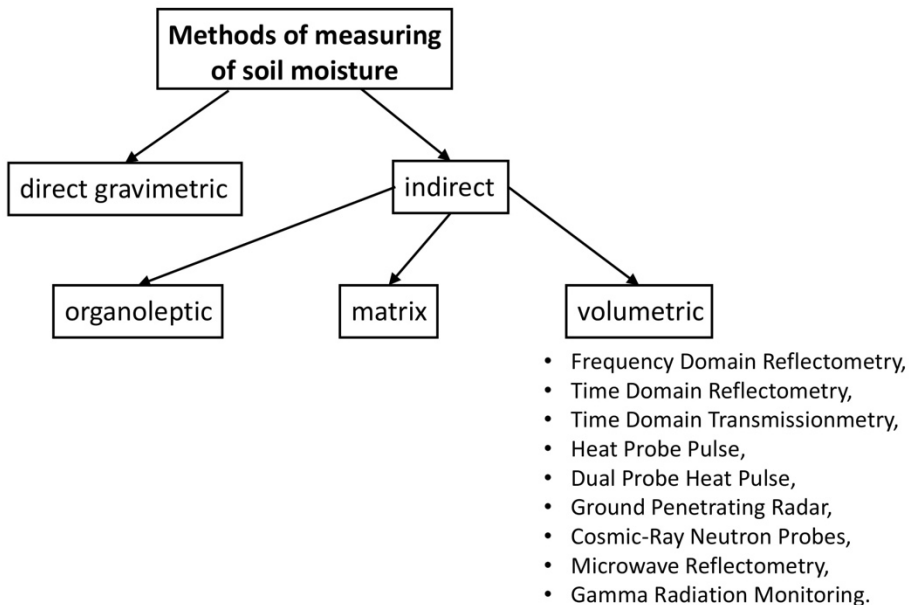


Figure 5.19. Methods of measuring soil moisture. Source: own elaboration based on [111]

Among the above-mentioned measurement techniques, the most rapidly developing are indirect techniques based on the electrical properties of soil. The reason for this is the high precision of the measurement and the almost immediate reading of a given parameter. Such features make these methods applicable in precision agriculture and in automatic irrigation systems [112].

The theoretical basis for indirect soil moisture measurements based on the dielectric properties of the soil is based on the measurement of dielectric permittivity. Since soil is a three-phase system, the read dielectric permittivity will be the resultant of all three phases. It should be noted here that the dominant parameter is the dielectric permittivity of water, which at room temperature is 80, air dielectric permittivity being 1, while soil dielectric permittivity approximating around 4 (depending on the type of soil). Therefore, slight changes in the water content cause significant changes in the dielectric permittivity of the entire medium. Then the obtained dielectric permittivity is converted into soil moisture. Appropriate formulas were proposed by Topp in the 1980s [112].

The use of the indirect method requires calibration – determining the relationship between moisture and dielectric permittivity of the soil. For this type of measurement, measuring probes are used, which are placed in the soil so that it has good contact with it.

One of the most popular techniques for measuring soil moisture is time domain reflectometry. Originally used for cable fault testing, this technique is based on the measurement of impedance discontinuities. It consists in forcing a pin impulse at the input of the tested line, which causes its propagation along this line, and then recording the moment of return of the impulse reflected from the discontinuity of the line impedance at the point of its damage. The nature of the impedance discontinuity can be assessed on the basis of the pulse shape [113]. The transmission line is usually made in the form of two parallel rods driven into the soil (Figure 5.20).



Figure 5.20. Two-rod probe. Source: own elaboration

The reflectogram is then recorded with a vector network analyser. As the probe is driven into the soil, the pulse propagation time depends on the electrical parameters of the medium surrounding the rods. Since the resolution of vector network analysers is high, rods with a length of a few centimetres are sufficient for proper operation. Figure 5.21 shows an exemplary reflectogram obtained for soils with different moisture. It can be noticed that with the increase in soil moisture (and thus its dielectric permittivity) the wave propagation time increases, and at the same time the impulse is damped.

In order for the measurement to be as accurate as possible, it is necessary to select the appropriate probe. There are many different probe designs available on the market. Each of the constructions is dedicated to the appropriate working conditions. The two-rod probe shown in Figure 5.20 is the most widely used. Unfortunately, the sensitivity zone of this probe is very small and is limited only to the space between the rods. Therefore, it is perfect for point measurements. It can be used in laboratory conditions for homogeneous soil. In field conditions, point measurements are not always effective due to the heterogeneity of the soil profile. Therefore, probes with a larger sensitivity zone are more suitable for such applications. An example of such a probe can be the antenna probe with a flange presented in Figure 5.22.a. It can be successfully used in the measurement of heterogeneous soils or soils with plant density [114].

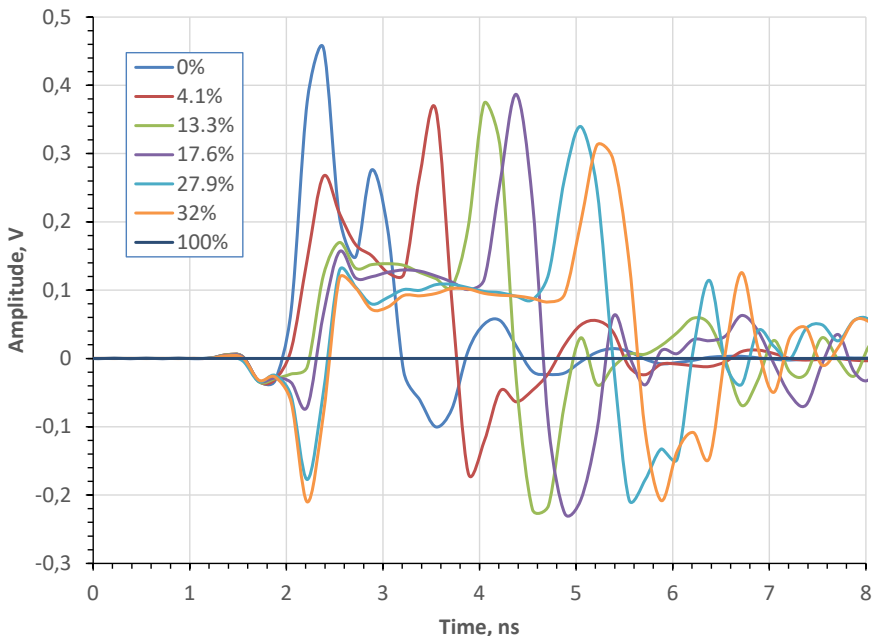


Figure 5.21. Example reflectogram for media with different moisture given in the legend. Source: own elaboration based on [114]

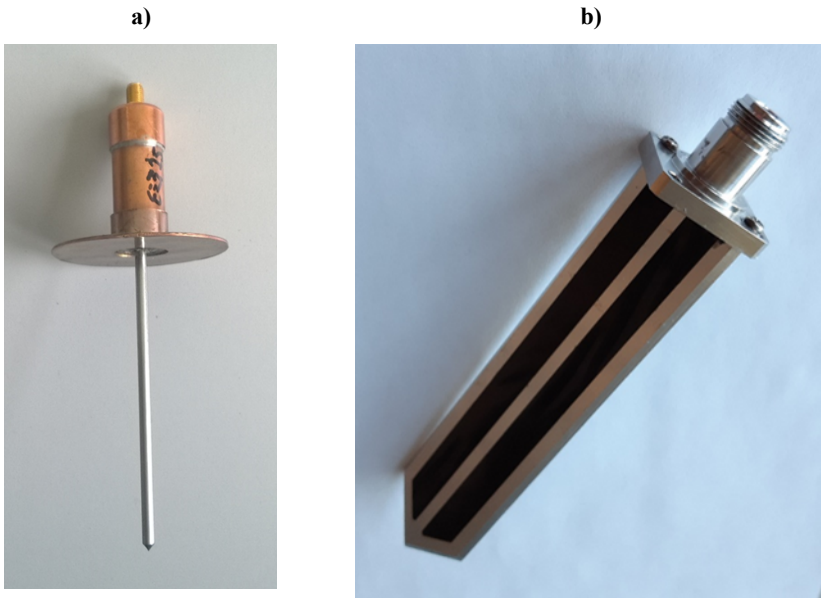


Fig. 5.22. Examples of measuring probes: a) antenna probe, b) dagger probe. Source: own elaboration based on [114, 115]

Another group of probes are probes that are used in automatic measurements. Unfortunately, in this type of measurement, the probe is exposed to mechanical damage. The dagger probe shown in Figure 5.22.b is characterised by high mechanical strength in one plane, which makes it dedicated for mounting on mobile devices for measuring soil moisture [115].

Moisture is one of the most important soil parameters. The proper growth of plants depends on the water content in the soil. Since soil moisture, especially in its upper parts, changes dynamically, constant monitoring of this parameter is necessary. There are many measurement methods and techniques available on the market. Each of these methods is dedicated to the appropriate measurement conditions. Due to the ability to read the soil immediately, indirect methods based on the electrical properties of the soil are gaining popularity. Immediate reading gives the possibility of adjusting agricultural machines and selecting the optimal settings depending on the current soil moisture.

6. Superconducting fault current limiters

Michał Majka

6.1. Introduction

Fault current is one of the basic threats to the elements of power systems. Short-circuits in power systems are usually caused by atmospheric overvoltages, faulty operations in power substations, mechanical damage to cables and poles, moisture or damage to insulation. Fault current in a shorted circuit is usually many times greater than the current occurring during normal operation of the network equipment. Fault current flow can cause harmful thermal and dynamic effects on the operation of power equipment. Large currents, despite the short flow time, cause rapid heating of wires, cables and windings of electric machines, which can lead to damage to their insulation and can cause further short circuits. Electrodynamics forces occurring during the fault current flow can mechanically damage electrical equipment. Any such damage causes costly and time-consuming repairs, so it is very important to secure the network with a reliable protection system [116–126].

An ideal fault current limiter is required to have zero impedance at work currents and substantial impedance in short-circuit conditions. These requirements are met by superconducting fault current limiters which use the phenomenon of transition of a superconducting material from the superconducting state to the resistive state as a result of exceeding the critical current I_c of the superconducting material. A superconducting fault current limiter is an electrical device with low impedance under normal operating conditions that changes into a state of high impedance during a short circuit, limiting the fault current. The operation of the limiters is automatic and almost instantaneous. Superconducting limiters reduce the first, most dangerous peak fault current, thus protecting electrical system equipment from the dynamic effects of the fault current flow. Superconducting current limiters are safe devices and the cooling of devices with liquid nitrogen is environmentally neutral. Superconducting fault current (SFC) limiters may be installed in powering or draining fields. The greatest advantage of a system with a superconducting fault current limiter, which connects two points of a power network of the same voltage, is the decrease of the network impedance and decrease of the fault current in the network. SFC limiters which are installed at the power source or drainage allow limitation of the fault current of the power source.

The idea of a superconducting current limiter operation is illustrated by the current waveforms in a circuit shown in Figure 6.1. When a short-circuit occurs in the power circuit, there is a rapid increase in the current. When the critical current is exceeded, the limiter switches to the resistive state and additional impedance appears in the circuit to limit the fault current. Current

limitation occurs in a time shorter than $\frac{1}{4}$ of the fault current period and depends on the parameters of the superconducting element. The limited fault current, which no longer poses such a high risk to the power circuit, can be switched off after a few periods from the moment when a short circuit occurs by a conventional circuit breaker, which is selected, however, for a much lower value of the short-circuit current.

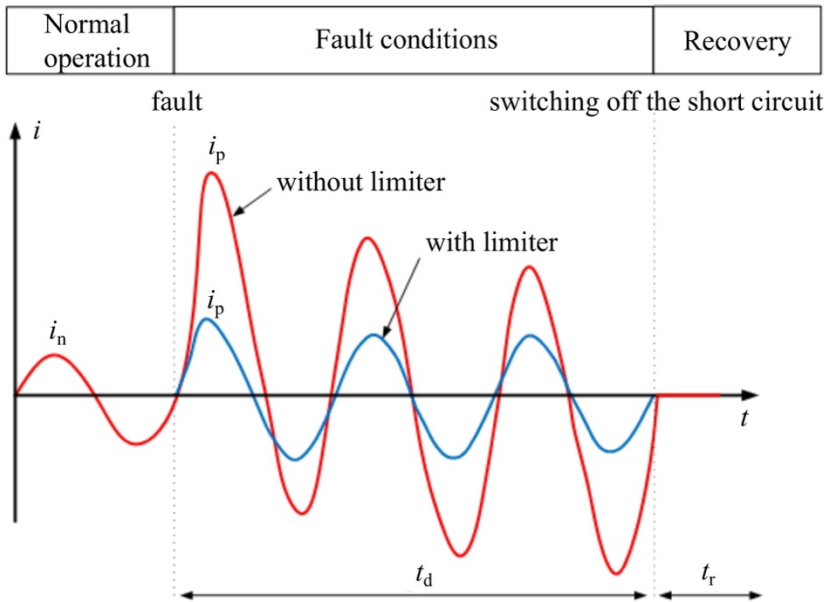


Figure 6.1. The principle of a superconducting fault current limiter operation. Source: own elaboration

Three states of operation of superconducting current limiters can be distinguished (Figure 6.1): the waiting state, the current limiting state and the reactivation state. In nominal conditions, the limiter is in the waiting state, the impedance of the limiter should now be close to zero, and losses for the cooling of superconducting components should be minimised. The operating time in the current limiting state is limited by the maximum temperature of the superconducting elements that can be permitted without damaging them. The duration of the reactivation state depends primarily on the temperature to which the superconductor will be heated in the current limiting state and secondarily on the cooling system used.

The concept of superconducting fault current limiters has been known for many years, but only the advances in High Temperature Superconductor (HTS) technology over the last 10 years have enabled their practical implementation. The chapter describes projects on SFC realized at the Lublin University

of Technology. Until 2008, in the Laboratory of Superconducting Technologies in Lublin tests were carried out on small low-voltage constructions of superconducting current limiters, with open and closed cores, in which the secondary winding of the limiter was a sleeve from the superconductor Bi-2223. Attempts were also made to replace the massive Bi-2223 rings with superconducting windings made of first-generation superconducting tapes (HTS 1G tapes). At present, the use of HTS 1G tape to make windings of current limiters is economically unjustifiable due to the high costs of the tape and, above all, the low resistance value of the tape to effectively limit fault current. Significant progress in the development of superconducting limiters occurred with the development and launch of the production of second-generation superconducting tapes (HTS 2G tapes), in which a thin layer of a superconductor on a non-magnetic and resistive substrate is covered with a thin layer of silver. These tapes enable the construction of effective fault current limiters. Continuous development of HTS 2G tapes and increasing their critical current causes that the cost of making the limiter is constantly decreasing, and the reduction of AC losses through the use of a high resistivity base also lowers the cost of maintaining the temperature of their operation at 66–77 K.

6.2. Tests of superconducting tapes parameters for fault current limiters

Superconductors are in a superconducting state when their operating point, determined by temperature, current density and magnetic field strength, is below the critical surface characteristics for each superconductor. Exceeding of any of the critical parameters causes the transition of the superconductor from the superconducting state into the resistive state. The sudden change in the resistance of superconductors after exceeding critical current is used in superconducting current limiters. This monograph presents a list of critical temperatures for selected superconductors and describes the division of superconductors into first and second type superconductors resulting from different behaviours of superconductors in an external magnetic field [127–133].

Second-generation superconducting tapes are the most frequently used for making superconducting windings of current limiters. HTS 2G tapes have a thin-layer structure. The tapes consist of a number of layers, including the base layer, the buffer layers, the superconducting layer and the stabiliser layer which is most often made of silver (Figure 6.2). The tapes can be covered with copper, stainless steel or brass. The experimentally determined characteristics of resistance of HTS 2G tapes as a function of temperature, which are necessary for designing superconducting current limiters and creating numerical models of limiters.

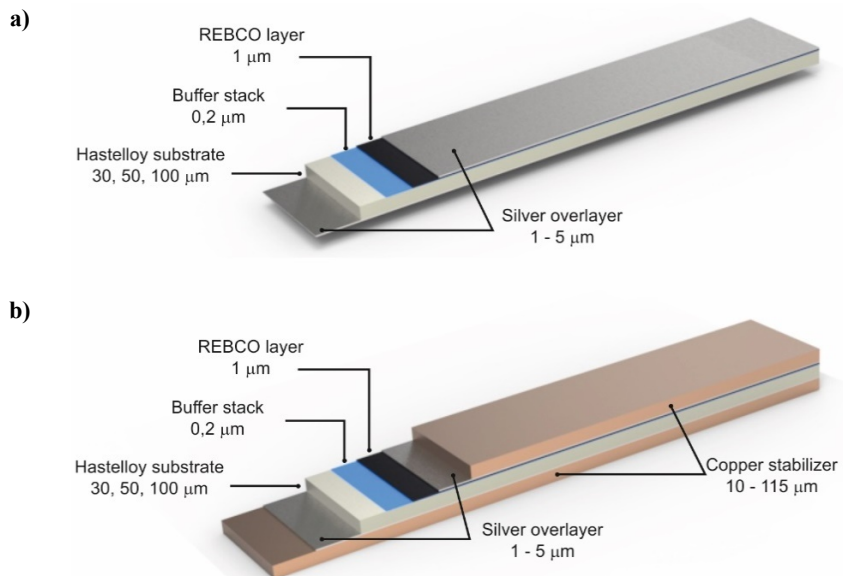


Figure 6.2. Internal structure of 2G superconducting tapes: a) SuperPower SF tape without a copper stabiliser, b) SuperPower SCS tapes with a copper stabiliser. Source: own elaboration

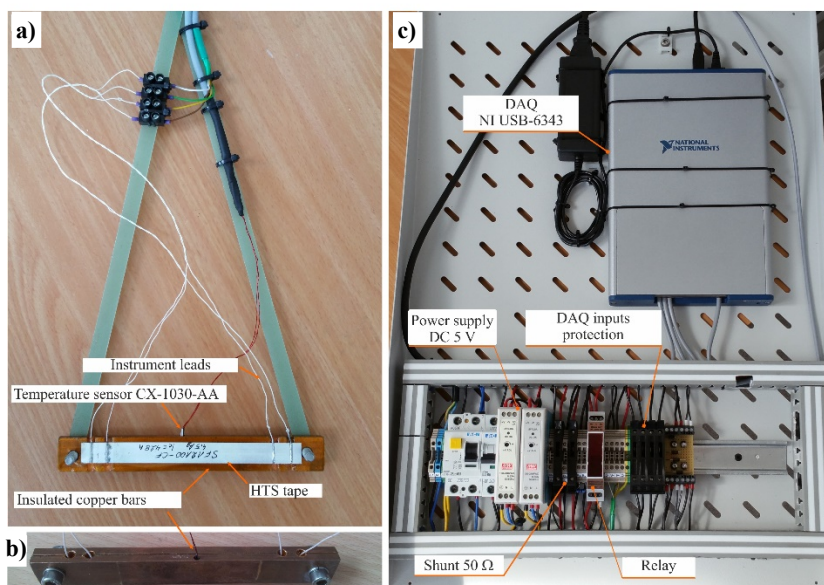


Figure 6.3: Measuring system for automatic characteristics determination $R = f(T)$ of a superconducting tape: a) HTS tape sample holder, b) a tape sample placed between copper blocks, c) the measuring system. Source: own elaboration

To carry out measurements and determine the characteristics of $R = f(T)$ of HTS 2G tapes, a measurement system has been developed as shown in Figure 6.3. The measurement system consists of a measurement computer with the RT IEL program written by the author in the LabView environment. Automatic resistance measurement of the sample was carried out using the four-wire method. The tape sample together with copper flat bars (Figure 6.3.b) is cooled to 77.4 K in a liquid nitrogen cryostat and then slowly heated to room temperature. During sample heating, the sample resistance is measured with simultaneous temperature reading from the LakeShore sensor. Figure 6.4 shows a characteristic transition of a superconducting tape from the superconducting state to the resistive state after heating the sample above the critical temperature $T_c = 90$ K. Numerical models of superconducting current limiters take into account both the characteristics of $R = f(T)$ of the superconducting tape, which affects the limiter's effectiveness in limiting the fault current, and the thermal capacity of the superconducting tape, which affects the heating rate of SC windings during the fault current flow.

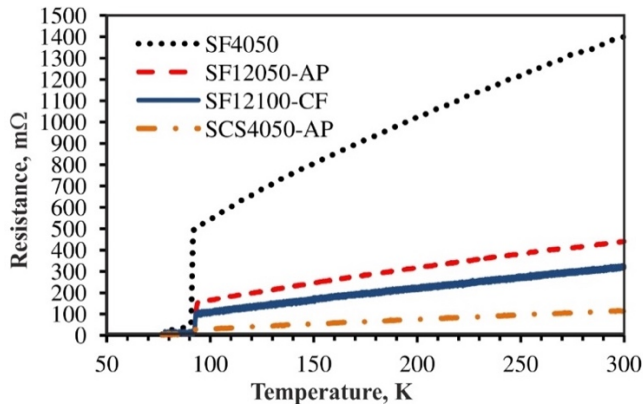


Figure 6.4. Experimentally determined dependence of resistance of HTS 2G tape as a function of temperature (tape length: 100 cm). Source: own elaboration

The relation $R = f(T)$ for superconducting tapes and the calculated thermal capacity of the tapes enables the calculation of the temperature of the windings of the limiter during the fault current limitation. During the fault current flow through the limiter, the superconducting windings heat up very quickly. The temperature of the superconducting windings of the limiter increases within a few tens of milliseconds from 77.4 K to the assumed maximum temperature in the range of 300–450 K, reached when the short circuit is switched off. If the fault current is not switched off by a conventional circuit breaker within a few tens of milliseconds of the short-circuit, the maximum temperature of the limiter will be exceeded and it will be permanently damaged.

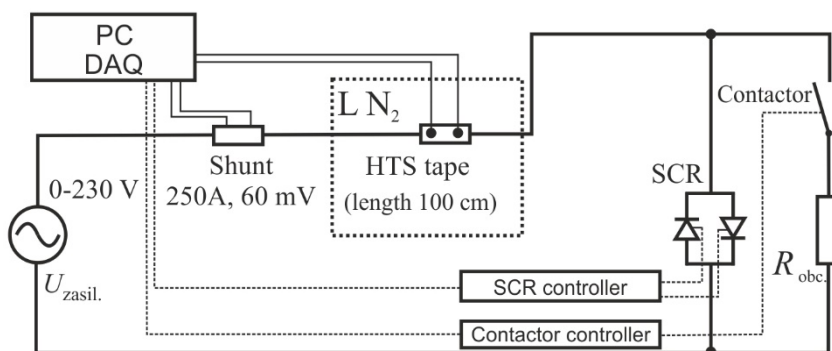


Figure 6.5. Diagram of a laboratory measuring system for testing a superconducting tape in transient states. Source: own elaboration

It is therefore extremely important to match the length of the tape to the expected fault current and to determine the permissible short-circuit duration to prevent the thermal damage to the limiter. The design and construction of superconducting current limiters was preceded by original research on superconducting tapes in transition states. Experimental research was carried out in a laboratory measurement system, a diagram of which is shown in Figure 6.5. The measurement system consisted of a 1 m long superconducting tape, a power supply system and a voltage measurement system. The measuring system enabled the change of the power supply voltage and automatic switching on and off of the fault current after a set time. The power supply system was controlled from a measurement computer equipped with a measurement card and LabView software. The measuring system is equipped with a zero-voltage transition detection system and a short-circuit duration control system. The tests were carried out for different values of supply voltage and fault currents flowing in the tested system.

Typical waveforms of a current, voltage, resistance and temperature changes for a 1 m long SF12050 superconducting tape are shown in Figure 6.6. If the current flowing through the superconducting tape exceeds its critical current I_c , its resistance (Figure 6.6.b) and temperature rise very quickly (Figure 6.6.c). Already after the first 2 ms, the average temperature of the superconductor tape exceeds the critical temperature of the superconductor, causing the entire current to flow through the stabiliser layers and substrates, laid parallel to the superconductor layer, causing their substantial heating. The temperature of the tape increases until the current is switched off after a period of time t_k . During the flow of current, adiabatic heating of the superconducting tape occurs because the heat flow to the cooling liquid is low. When the short-circuit is switched off, the superconducting tape reaches its maximum temperature T_{max} . The maximum temperature increases as the supply voltage rises.

The experimental system from Figure 6.5 was reproduced in a numerical model developed by the author in Cedrat Flux. In the numerical model, we obtained temperature changes of superconducting tapes for different rms values of supply voltage. Calculations were performed for SF4050, SF12050 tapes without a copper stabiliser and for SCS4050 and SCS12050 tapes with a copper stabiliser. An example of heating characteristics for SF12050 tape cooled in a liquid nitrogen bath is shown in Figure 6.7. Heating characteristics allow one to determine the temperature to which a 1 m long superconducting tape will be heated when a short circuit is switched off for a specific voltage per 1 m of tape. An increase in tension per unit length of the superconducting tape causes an increase in current in the superconducting tape and, consequently, an increase in the final temperature of the superconducting wire.

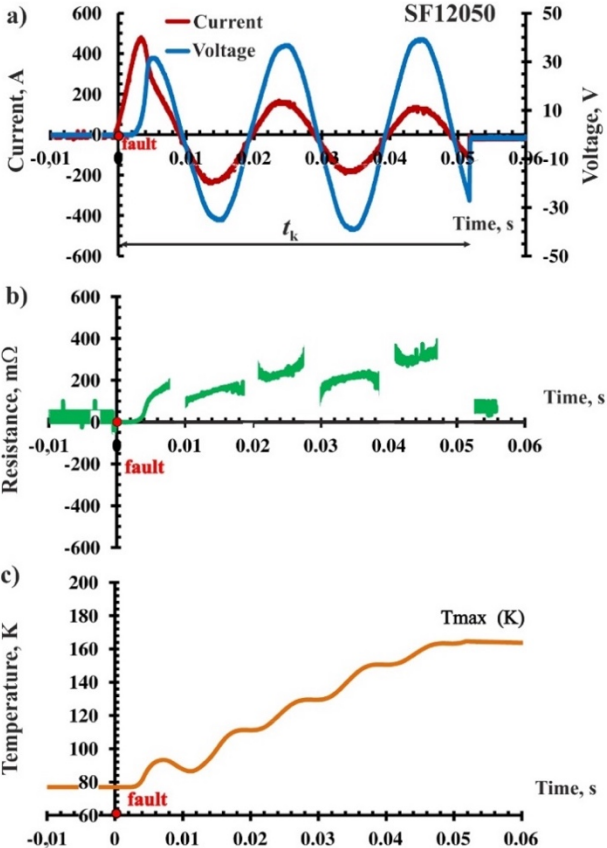


Figure 6.6. Experimentally determined a) current and voltage waveforms, b) resistance and c) temperature changes for type SF12050 when the critical current is exceeded. Source: own elaboration

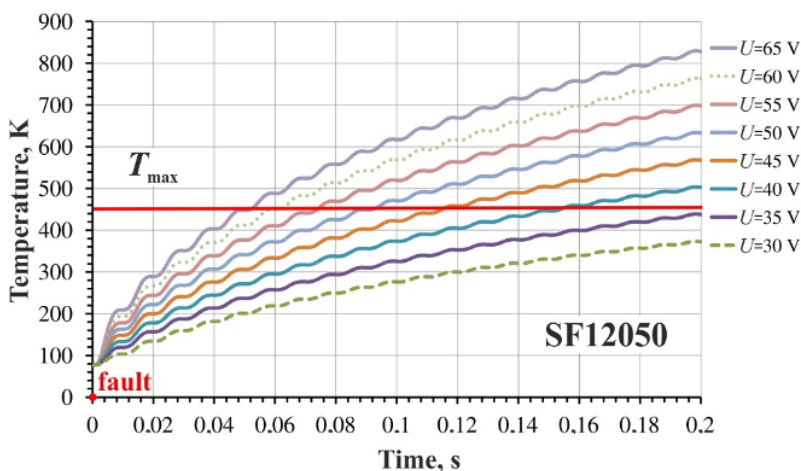


Figure 6.7. Increase in tape temperature SF12050 during fault current flow for supply voltages from 30 V to 65 V. Source: own elaboration

Extending the short-circuit time while maintaining the same tension per unit length of the superconducting tape causes an increase of the final temperature of the superconducting tape. In order not to exceed the maximum temperature of the superconducting cable, the tension per unit of belt length should be reduced by extending the short circuit time.

6.3. Soldered connections of superconducting tapes

Each superconducting winding requires at least two connections of the superconducting tape to the copper current leads – at the beginning and end of the winding. Quite often it is also necessary to connect superconducting tapes with each other. HTS 2G tapes are usually produced in lengths of several hundred metres, so for superconducting windings it is quite often necessary to make connections between several superconducting tapes in order to obtain a section of tape of sufficient length to make a winding.

Development of connection technology with low resistance and appropriate mechanical strength allows the reduction of losses on connection resistance, which has a direct impact on losses in the cooling system and increase of their reliability of operation. Thermal damage to the windings occurs most often at the point of a faulty connection between the HTS tape and current bushings which supply current from a power source operating at room temperature to a superconducting device placed in a cryostat at cryogenic temperature. At the point of a soldered connection of superconducting tapes there are always losses which result from the connection resistance, which may cause local heating of the superconductor and its transition from the superconducting state, which in turn leads to the release of large amount of energy at this point and permanent

damage to the superconducting tape. The probability of thermal failure of a superconducting winding with soldered connections between HTS tape increases many times in devices such as fault current limiters because during current limitation by the winding a fault current is flowing with a value many times higher than the critical value.

This chapter of the monograph contains a description of the method of making soldered connections between HTS 2G tapes and the results of experimental research on measurement of the resistance of soldered joints, both at room temperature and after cooling of samples in a liquid nitrogen bath.

Resistance measurements of HTS 2G tapes were made for five types of connections (Figure 6.8). Connections of tapes were made with two different soldering pastes: series A was soldered with $\text{Sn}_{62}\text{Pb}_{36}\text{Ag}_2$ soldering paste, while series B with $\text{Sn}_{96.5}\text{Ag}_3\text{Cu}_{0.5}$ soldering paste. The laboratory measuring system made it possible to measure the resistance of soldered superconducting tapes by means of an indirect four-wire method with current flow direction change. Measurements were made for three values of measuring current 100, 150 and 200 A.

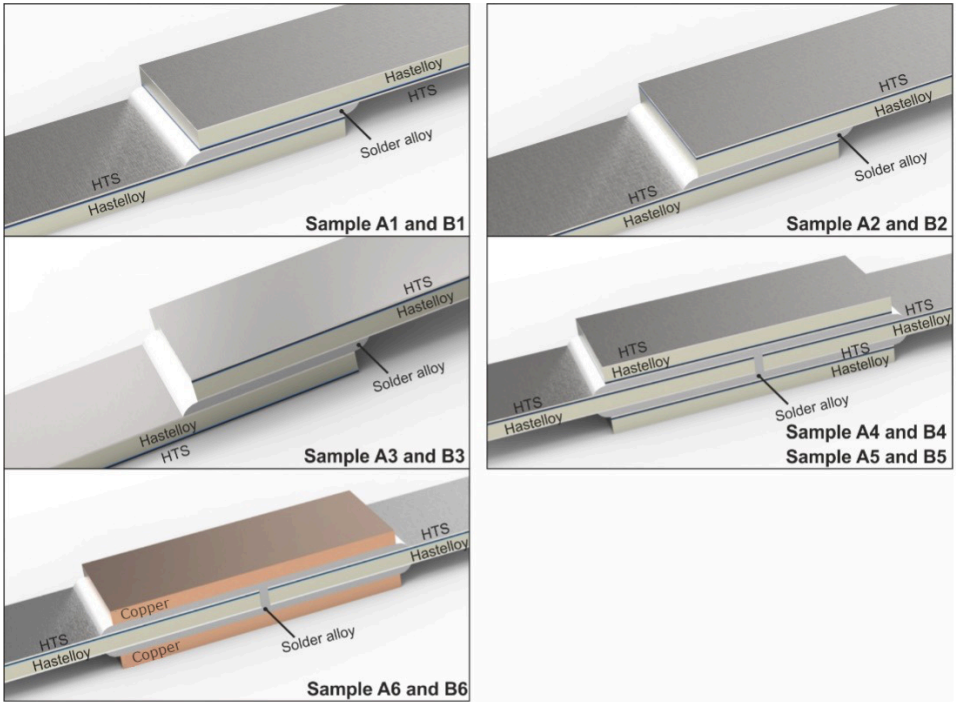


Figure 6.8. Methods of making soldered connections of ReBCO tapes. Source: own elaboration

The analysis of the experimental results showed that in each case the solder joints made with $\text{Sn}_{62}\text{Pb}_{36}\text{Ag}_2$ soldering paste (samples A) have lower resistance than the joints made with $\text{Sn}_{96.5}\text{Ag}_3\text{Cu}_{0.5}$ soldering paste (samples B). An overlapping connection, A1, has the lowest resistance, but it requires reversing the superconducting tape with superconducting layers of the superconducting layers towards each other, which is not always possible when winding the superconducting windings of the limiter. The A4 bridge connection has a similarly low resistance to the A1 overlapping connection and does not require reversing the superconducting tape. This connection requires the preparation of two additional strips of tape soldered on both sides of the connection. $\text{Sn}_{62}\text{Pb}_{36}\text{Ag}_2$ soldering paste should also be used for making connections of HTS tape with copper current leads (connections A6 and B6). The resistance of connections soldered with $\text{Sn}_{62}\text{Pb}_{36}\text{Ag}_2$ paste is twice as low as the resistance of the connection made with $\text{Sn}_{96.5}\text{Ag}_3\text{Cu}_{0.5}$ soldering paste. The highest resistance value was obtained for A3 and B3 type connections (with layers of Hastelloy substrate towards each other).

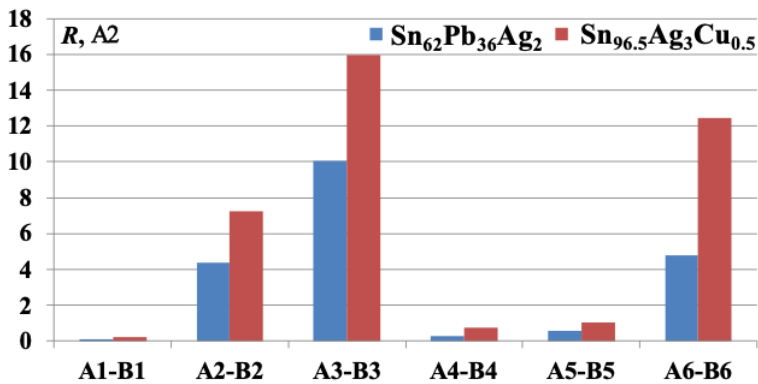


Figure 6.9. Comparison of resistance values of solder connections for two different soldering pastes at 77.4 K. Source: own elaboration

Soldered joints were made with a superconducting tape soldering gun which was designed and constructed in the Laboratory of Superconducting Technologies of the Electrotechnical Institute. The method of soldering copper tips to a superconducting tape has been patented [134].

6.4. Cooling of superconducting devices

This chapter presents non-linear relationships between heat transfer from the surface of the superconducting tape to liquid nitrogen as a function of the surface temperature of the superconducting tape. These characteristics have been implemented in the numerical models of superconducting current limiters.

Superconducting elements of the current limiter require cryogenic cooling in all states of its operation. The superconducting elements of the limiter are to be cooled to below their critical temperature before its first operation. In the waiting state, the rated current flowing through the limiter hardly generates heat because it flows through a superconductor in a superconducting state. The heat generated in the superconducting elements of the limiter and in the current bushings is completely dissipated by the cooling system. During the fault current flow, the limiter switches to the resistive state. A short-circuit current flowing through the superconducting tape in the resistive state generates a huge amount of heat, and the amount of heat absorbed by the cooling system is limited. In the reactivated state of the arresters, after a short circuit is deactivated by the breaker, the superconducting element of the limiter must be quickly cooled below its critical temperature at which it regains its superconducting properties. In the reactivation state of the arrester, two cases can be distinguished: one in which the short-circuit current is switched off after a specified short circuit time and the limiter is cooled back to its operating temperature, and the other in which the current flows through the superconducting element after the short circuit has subsided, resulting in additional heat generation in the superconducting element in the resistive state, which must be discharged through the surface of the limiter to the cryogenic fluid.

One way to cool the limiters is to immerse them in a cryostat containing a cryogenic liquid at atmospheric pressure. Cryogenic liquids whose boiling point is lower than the critical temperature of the superconducting material of which the superconducting elements of the limiters are made may be used to cool the limiters.

The amount of heat transferred from the cooling element to the cryogenic fluid depends on the temperature difference between the surface to be cooled and the temperature of the cryogenic fluid. Figure 6.10 shows the course of heat flux density emitted from the surface of a body submerged in liquid nitrogen as a function of the temperature difference between the cooled surface and nitrogen mass at a gradual increase in body temperature.

If the body heats up slightly, the heat is transferred through conduction: the temperature difference ΔT is then minimal. As heating increases, free convection occurs: the layers of liquid nitrogen heated at the surface of the body float upwards and transfer heat to the surface of the liquid by evaporation. For a greater temperature difference the so-called bubble boiling occurs. In microscopic hollows on the surface of the heated body steam bubbles are formed. The bubbles gradually increase in volume and detach themselves from the surface, but do not reach the surface of the liquid because they condense inside the nitrogen mass. As the surface temperature continues to increase, more and more bubbles form on the surface, they become larger and detached from the cooled surface and already reach the surface of the liquid.

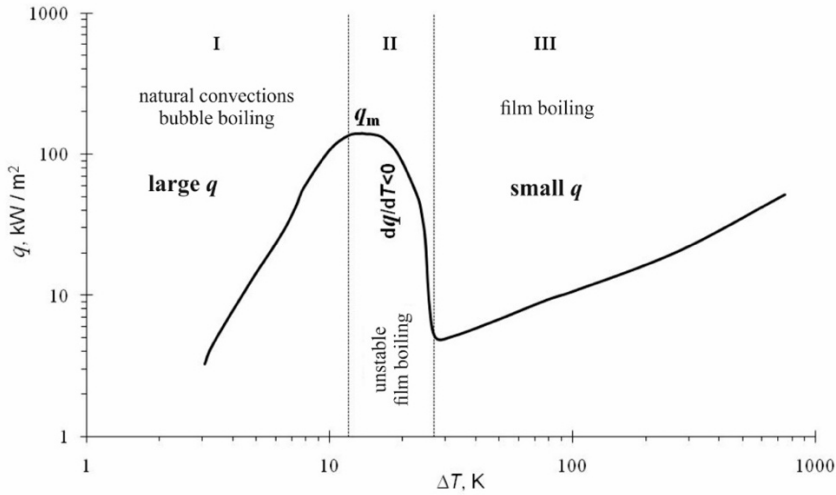


Figure 6.10. Density of heat flux q between metal surface and liquid nitrogen as a function of temperature difference ΔT between surface and liquid nitrogen. Source: own elaboration

Bubble boiling reaches its peak: the highest density heat flux, known as the maximum flux, flows out of the cooled surface q_m . In this phase, the vapour bubbles on the surface are already so numerous and so large that they begin to connect with each other.

Slightly exceeding the body's warmth causes a layer of nitrogen vapour to form on the surface and, as a result, a significant deterioration in heat dissipation. Processes appearing in interval II and III are called film boiling. This boiling is not stable in interval II. The vapour layer on the surface fluctuates continuously; it is formed and disappears as a result of being interrupted by bubbles of vapour escaping from the surface. Most often, after reaching point q_m , there is a jump to the point on the curve in the interval III with a simultaneous rapid increase in the temperature of the cooled surface. In interval III the film boiling is stable.

During a short circuit in a circuit with a current limiter made of a HTS 2G tape, the temperature of the elements of the limiter increases enormously in a short period of time, resulting in a temperature of up to 450 K. A large increase in temperature of the elements of the limiter immersed in a liquid nitrogen bath results in a large temperature difference between the surface of the cooled limiter element and the surrounding liquid nitrogen, which causes an almost instantaneous formation of a thin nitrogen vapour insulation layer on the surface of the cooled element and the occurrence of layered boiling. The transfer of heat to the cooling fluid is then very limited, resulting in a low cooling capacity of the superconducting element, both during and after the fault current flow.

The heat transfer from the surface of the superconducting tape to the nitrogen increases, reaching the maximum value for the tape temperature $T \approx 92$ K. For higher temperatures of the cooled surface, the heat flux reaches significantly lower values. This is very important for HTS 2G tape for which the critical temperature of the superconducting layer is 90 K, so when the critical temperature of the superconducting cable is exceeded, a sudden deterioration in cooling conditions occurs and the heating process is approximately adiabatic.

6.5. Inductive type superconducting current limiters with shielded core

A limiter with a shielded core consists of two windings, a primary copper winding and a compact secondary superconducting winding, placed concentrically on the magnetic core (Figure 6.11). Under normal operating conditions of the limiter, the superconducting winding is in a superconducting state. In the case of a magnetic core limiter, the superconducting winding acts as the screen of the magnetic column of the magnetic core. The time-varying magnetic flux produced by the primary winding induces a current in the secondary superconducting winding, which produces a magnetic flux opposite to the magnetic flux of the primary winding, completely cancelling it, which is manifested by the low impedance of the entire system. The low voltage at the limiter during the nominal current flow is due to the dispersion reactance of the limiter and the resistance of the copper primary winding.

When a short-circuit occurs in a protected circuit, the currents in the primary and secondary superconducting windings increase rapidly. When the critical value of the current in the secondary superconducting winding is exceeded, its resistance increases rapidly and its flow decreases. The magnetic flux induced by the primary winding is not fully compensated for by the opposite secondary winding flux and the limiter for the protected circuit behaves like a high inductance choke. The rapid increase in the inductance of the limiter limits the fault current. The value of the voltage at the limiter depends mainly on its dimensions, the parameters of the superconducting secondary winding and, in the case of magnetic core limiters, also on the properties of the core. After the short-circuit has been switched off, the superconducting secondary winding of the limiter must be cooled down again to the cryogenic temperature. In the first limiters of this type, the secondary windings were made from the Bi-2212 ring, which with the development of superconducting tapes was replaced by windings made from 1st or 2nd-generation superconducting tapes.

Inductive type current limiters with a shielded core have large dimensions and weight. The superconducting windings must be placed in a non-metallic cryostat. The use of a cryostat to cool the superconducting winding creates a large gap between the copper primary and secondary superconducting winding, resulting in a high dispersion flux and voltage at the limiter at rated current.

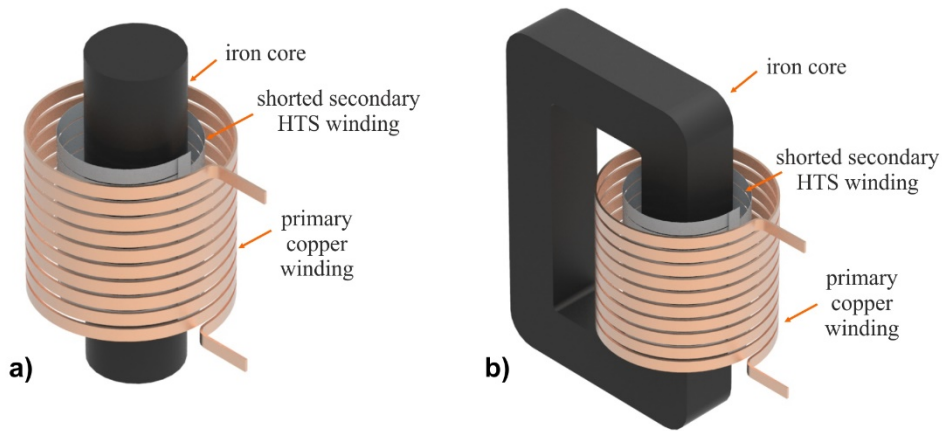


Figure 6.11. Current limiters with a) open and b) closed magnetic core. Source: own elaboration

Physical models of superconducting current limiters of an inductive type with a magnetic core tested in the Laboratory of Superconducting Technologies in Lublin were made for low voltage power networks. Induction limiters may use an open or closed magnetic core, but the use of a magnetic core in a high-power limiter is associated with large dimensions and high weight of the magnetic core. Simulations show that the magnetic core for an inductive type of limiter with nominal parameters of 6.9 kV/1.15 kA should have a magnetic core with a diameter of 1 meter.

6.6. Coreless inductive superconducting fault current limiters

The Laboratory of Superconducting Technologies in Lublin has been conducting research for nearly ten years on the development of an inductive coreless current limiter, which would be characterised by low weight and small dimensions. This research has led to the development of a new three-winding coreless superconducting current limiter of inductive type which effectively limits a fault current despite the lack of a magnetic core. This type of a limiter consists of a primary winding consisting of two copper and superconducting coils connected in parallel and a superconducting shorted secondary winding (Figure 6.12).

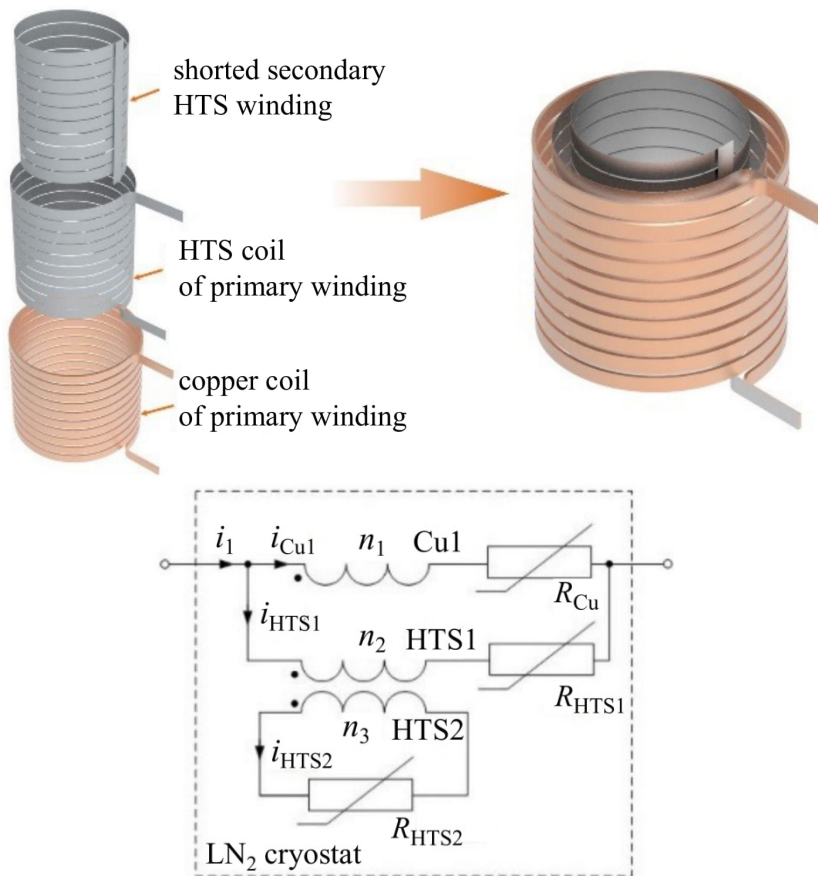


Figure 6.12. Triple-winding coreless superconductive fault current limiters of inductive type.
Source: own elaboration

All the windings are placed in a nitrogen cryostat and cooled to the cryogenic temperature, which allows reduction of the air gap between the primary and secondary windings of the limiter, and to significantly reduce the dispersion flow so that the voltage on the limiter at the rated current flow is minimised. The principle of operation of a triple-core inductive type current limiter is shown in Figure 6.13. Windings of the limiter are located concentrically. In Figure 6.13 the secondary SC winding is moved upwards to increase transparency.

Under normal operating conditions of a three-winding current limiter, the superconducting windings are in the superconducting state. The nominal current flow between the coils of the primary winding of the arrester depends on the impedance of the coils and the degree of magnetic coupling of the coils of the primary winding with the closed superconducting secondary winding of the limiter. If the superconducting coil has a similar inductivity to the copper

coil of the primary winding, the rated current flows through a superconducting coil with zero resistance. The time-varying magnetic flux produced by the primary winding induces a current in the secondary superconducting winding, which produces a magnetic flux opposite to the magnetic flux of the primary winding, completely cancelling it, which is manifested by the low impedance of the entire system. The voltage on the limiter in the waiting state is a result of voltage drop on the resistance of the primary winding (mainly resistance of current bushings and soldered connections) and voltage drop on the dissipation reactance.

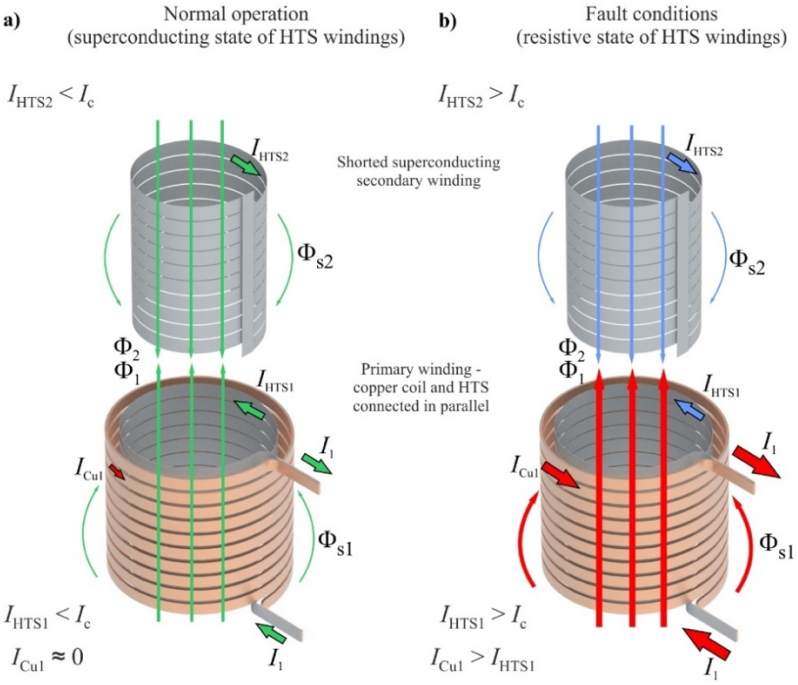


Figure 6.13. The principle of operation of a triple-core inductive type current limiter: a) waiting state, b) fault current limitation. Source: own elaboration

When a short-circuit occurs in a protected circuit, the currents in the primary and secondary superconducting windings increase rapidly. When the critical value of the current in the secondary superconducting winding is exceeded, its resistance increases rapidly and its flow decreases. The magnetic flux produced by the primary winding is not fully compensated for by the opposite secondary winding flux and the limiter for the protected circuit behaves like a choke. The rapid increase in the inductance of the limiter limits the fault current. When the critical current in the superconducting coil of the primary winding is exceeded, it also enters the resistive state.

An increase in the resistance of the superconducting coil of the primary winding causes a change in current flow, forcing the short-circuit current to flow through the copper coil of the primary windings of the limiter.

Due to the fact that the superconducting elements must have operating temperatures lower than the critical temperature, superconducting windings must be placed in a nitrogen cryostat. The copper coil of the primary winding can also be cooled in a nitrogen cryostat. Cooling of the primary copper winding in a liquid nitrogen bath allows a significant reduction of the cross-section of the copper conductor while maintaining the same rated current; it also provides better magnetic coupling between the primary and secondary windings of the limiter. This design of the inductive limiter allows a significant reduction in the weight and size of the copper winding, because the resistivity of copper is about 7.6 times lower at 77.4 K than resistivity at room temperature. Since the primary winding of the limiter consists of two coils – a superconducting one and a copper one – connected in parallel, the protected circuit remains closed in the event of thermal failure of the superconducting coil.

6.7. Superconducting fault current limiter 6.9 kV/600 A

Laboratory tests have confirmed the effectiveness of superconducting inductive-type limiters with a coreless design, and the developed design of superconducting windings allows obtaining a very large feedback coefficient between the windings. Figure 6.14 shows the CAD design of the limiter, and the physical model of the limiter together with the nitrogen cryostat. This limiter works like a transformer with a shorted secondary winding. The primary copper winding is connected in parallel to the HTS primary winding which provides better coupling with the secondary HTS winding. This results in a reduction of the voltage drop on the limiter in nominal conditions when the tape is in the superconducting state. The main parameters of the fault current limiter are presented in Table 6.1.



Figure 6.14. Inductive superconducting fault current limiter rated at 6.9 kV/600 A. Source: own elaboration

Table 6.1. Parameters of 6.9 kV/600 A superconducting fault current limiter

Parameter	Symbol	Value
Nominal voltage	U_N	6 kV
Voltage on the limiter at IN	U_{SFCL}	0.75 V
Nominal current	I_N	0.6 kA
Inrush current	I	0.85 kA
Prospective peak current	i_{peak}	20 kA
First peak limiting	i_p	< 5 kA
Limitation time	t	50 ms
Operating temperature	T	77 K
Weight	m	180 kg

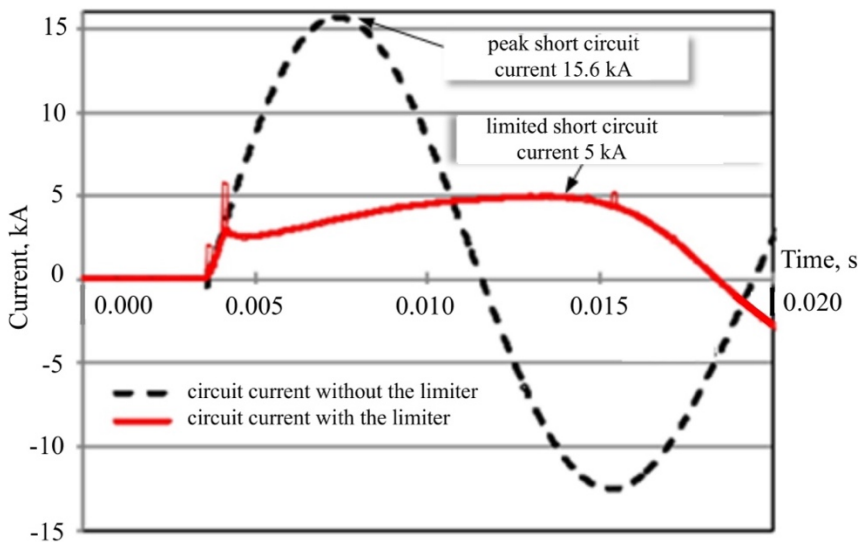


Figure 6.15. Experimentally determined courses of short-circuit current in short-circuit with a 6.9 kV / 600 A limiter and without the limiter. Source: own elaboration

The constructed superconducting current limiter has a lightweight, coreless design. All windings, including the primary copper ones, are cooled with liquid nitrogen, which further reduces the mass of the device. The rated current of the limiter exceeded the critical current of a single HTS 2G tape and required the use of four superconducting tapes connected in parallel. The device consists of four modules connected in parallel. Each module has three windings: a primary copper winding, connected in parallel to which are a primary

superconducting winding and a shorted superconducting secondary winding. The radial forces affecting the windings during a short-circuit were limited by a special construction of the superconducting windings. The primary and secondary superconducting windings were wound simultaneously. Between the turns of the primary winding are the windings of the secondary winding. Such a design provides good magnetic coupling and low leakage reactance. The voltage drop on the limiter during normal operation and at rated current $I = 600 \text{ A}$ is negligibly small $U < 1 \text{ V}$. Partial results of the work carried out are published in articles [122–126].

A short-circuit test of the 6.9 kV/600 A limiter was carried out after the limiter was cooled down with liquid nitrogen. 460 litres of liquid nitrogen were used to cool down the device. The comparison of short-circuit currents in a circuit with and without a limiter shows that the expected peak short-circuit current of 15.6 kA is limited to 5 kA (Figure 6.15).

6.8. Superconducting fault current limiter 15 kV/140 A

The CAD design of the limiter, the assembled physical model of the limiter and the cooled limiter before the short circuit test are shown in Figure 6.16. The 15 kV/140 A limiter consisted of a copper primary winding with 185 coils, of a primary HTS winding with 144 coils and a secondary HTS winding with 144 coils. The winding carcasses and the nitrogen cryostat were made of an epoxy-glass composite. The windings of the current limiter were made on a specially designed and constructed winder on two cartridges of different diameters. Short-circuit tests of the limiter were carried out in the Testing Laboratory of Distribution Apparatus of the Electrotechnical Institute in Warsaw. The limiter was cooled to 77.4 K in a liquid nitrogen bath prior to short-circuit testing.



Figure 6.16. Inductive superconducting short-circuit current limiter rated at 15 kV/140 A.
Source: own elaboration

Table 6.2. Parameters of 15 kV / 140 A superconducting fault current limiter

Parameter	Symbol	Value
Nominal voltage	U_N	15 kV
Nominal current	I_N	140 A
Voltage on the limiter at I_N	USFCL	< 1 V
Prospective peak current	i_{peak}	30 kA
First peak limiting	i_p	3.4 kA
Limiting time	t_{lim}	120 ms
Operating temperature	T	77.4 K
Cryostat height	H	1 m
Cryostat diameter	$O.D.$	0.85 m

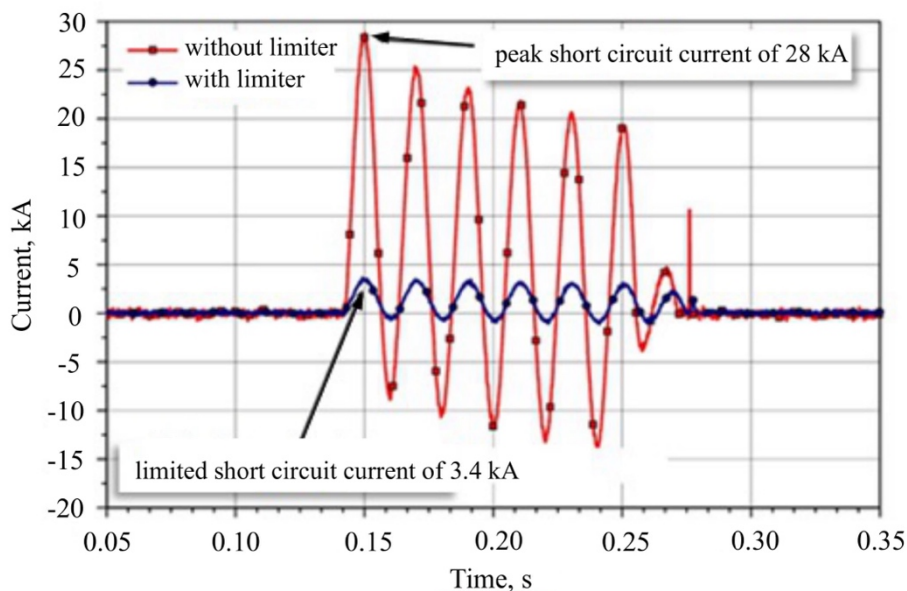


Figure 6.17. Experimentally determined courses of short-circuit current in short-circuit with a 15 kV/140 A limiter and without the limiter. Source: own elaboration

Experimental measurements consisted of a cycle of three short-circuit tests. A comparison of short-circuit currents without and with a limiter is shown in Figure 6.17. During a short circuit, the rms value of the voltage at the limiter was 4.24 kV. The peak short-circuit current was limited from 28 kA to 3.4 kA.

Analysing the obtained results, it can be concluded that an eight-fold limitation of the peak fault current value in less than $\frac{1}{4}$ of the current period allows effective protection of transformers and network equipment against the dynamic effects of the fault current flow. The main parameters of the limiter are presented in Table 6.2. A triple-winding coreless current limiter consists of two superconducting windings and a copper winding which are magnetically coupled with each other. A change in the impedance of the limiter windings results in a change in the current distribution in the windings during the fault current limitation and changes the heating process of the superconductor windings during the short circuit, which has a significant impact on the temperature of individual HTS windings when the short circuit is switched off. An incorrectly selected number of windings of individual windings may cause thermal damage to the primary or secondary superconducting winding. Increasing the number of windings in superconductor windings, and thus increasing their impedance, has little effect on the peak value of the limited current, which is mainly determined by the impedance of the copper winding, which, at the time of fault current limitation, is much lower than the impedance of superconductor windings. To increase the effectiveness of fault current limitation, the number of coils of the copper winding should be increased. The simulations showed that by changing the number of windings it is possible to equalise the heating speed of superconducting windings of the arrester during the fault current flow.

The details of design of the 15 kV/140 A limiter, subsequent stages of its physical prototype, the method of making superconducting windings and copper windings of the limiter, the results of electrical measurements of the limiter and the results of three short circuit tests of the limiter can be found in the articles [117–121].

6.9. Contact-cooled superconducting fault current limiter rated at 6 kV/140 A

In 2015–2017 the Gekon project financed by NCRD and NFOSiGW “A superconducting fault current limiter (NOPZ) as an element increasing the connection capacity of renewable sources of electricity to the power distribution network” was designed in the Laboratory of Superconducting Technology. A consortium consisting of Electrotechnical Institute, Research and Implementation Company Frako-Term sp. z o.o. and the University of Zielona Góra, designed a superconducting resistance fault current limiter for networks with rated voltage of 6 kV and rated current of 140 A with the possibility of overloading to 420 A [135]. The resistance limiter is contact-cooled by means of a single-stage cryocooler (Figure 6.18). It is the world’s first resistance limiter for 6 kV networks which uses contact cooling. Changing the cooling method of the limiter allows increasing the nominal current of the limiter by cooling the windings to lower temperatures and effectively limiting several consecutive

short circuits. Changing the cooling system of the limiter required the development of many new design solutions, which will be the subject of patent applications. The prototype of the limiter was tested in the Research Laboratory of Distribution Apparatus of the Electrotechnical Institute (Figure 6.19) and installed for trials in the GS2 110 kV/6 kV switchgear in the Electrotechnical Institute in Warsaw (Figure 6.20). The short-circuit tests of the limiter showed that the peak fault current was limited from 81 kA to 2 kA in accordance with design assumptions (Figure 6.19). The limiter was installed in the switchgear of GS2 110 kV/6 kV on the premises of the Electrotechnical Institute. The main parameters of the limiter are presented in the Table 6.3.

Table 6.3. Parameters of 6 kV/600 A superconducting fault current limiter

Parameter	Symbol	Value
Nominal voltage	U_N	6 kV
Nominal current	I_N	140 A
Overload current	I_{overload}	420 A
Winding height	h_w	0.44 m
Winding diameters	d_w	0.736 m



Figure 6.18. Contact-cooled superconducting fault current limiter (Electrotechnical Institute, University of Zielona Góra and Frako-Term). Source: own elaboration

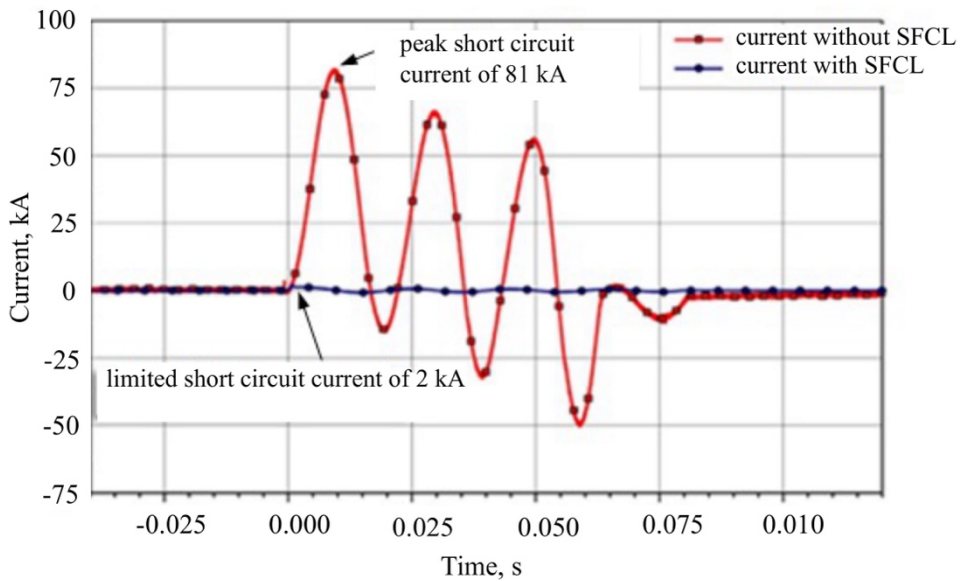


Figure 6.19. Experimentally determined fault current waveforms in a circuit without and with a limiter for a resistance limiter cooled with a cryocooler (Electrotechnical Institute, University of Zielona Góra and Frako-Term). Source: own elaboration



Figure 6.20. A superconducting current limiter installed in GS2 110 kV/6 kV switchgear on the premises of the Electrotechnical Institute. Source: own elaboration

6.10. Summary

Research on the application of superconductors has been carried out at Lublin University of Technology since 1975, when the Cryomagnets Laboratory was established – the Lublin branch of the Basic Research Department of the Electrotechnical Institute headed by Prof. Władysław Lech. Since 1986, for over 30 years, the research work of the Laboratory of Superconducting Technologies of the Electrotechnical Institute was directed by Prof. Tadeusz Janowski [116–133, 136, 137], who was the originator and initiator of several research projects in the field of superconductivity. Thanks to the efforts of Prof. Tadeusz Janowski, a Sumitomo SRDK-408 cryocooler, which is still in operation today, was purchased in 1996 under the TEMPUS Joint European Network Program. The staff of PTN IEL together with the staff of the Institute of Electrical Engineering and Electrotechnology of Lublin University of Technology under the guidance of Prof. Tadeusz Janowski participated in the preparation of the application for funding of the ASPPECT Centre of Excellence in Application of Superconducting and Plasma Technologies in Power Engineering.

At present, the scientific research concerning the application of superconductors is carried out in the Department of Superconducting Technologies headed by Prof. Michał Majka. The Department continues research on superconducting devices, such as short circuit current limiters, magnetic energy storage devices, superconducting electromagnets and transformers. The researchers of the Department of Superconducting Technologies have completed several research projects financed by the Ministry of Science and Higher Education, Polish National Science Centre and National Centre for Research and Development, designed, built and tested the first in Poland second generation superconducting tape magnetic energy storage device, developed short circuit current limiters from small laboratory models to working prototypes for voltages of 6 kV and 15 kV.

This chapter presents a coreless concept of an inductive superconducting current limiter developed in the Laboratory of Superconducting Technologies and the new contact cooled construction of the limiter. The main part of the work is a description of two completed prototypes of coreless limiters, preceded by a description of the preliminary research on the testing of superconducting tapes in transition states and the developed method of soldering second generation superconducting tape connections.

An inductive fault current limiter is a triple-winding construction consisting of two superconducting windings and one copper winding, which are magnetically coupled with each other. Both superconducting windings are wound simultaneously on one carcass, which allows one to obtain a very large magnetic coupling coefficient between the windings, minimise the dispersion reactance of the limiter, which in turn minimises the voltage at the limiter in the waiting state.

The parallel copper primary winding connected in parallel to the primary superconductor winding reduces the power output of the superconductor windings during the fault current flow, as well as protects the short circuit against opening in the event of a failure of the HTS 2G tape of the superconductor winding or the cooling system of the limiter. The limiter is lightweight due to its coreless design and cryogenic cooling of the copper winding.

This chapter concerns an important, current and developing problem of superconducting fault current limiters, which have a good chance to be implemented in power networks. Intensive work on the development of superconducting current limiters is being carried out in many scientific centres around the world. As a result of the research conducted, new designs of limiters whose performance parameters are increasingly close to the requirements of modern power systems are being developed. The work carried out so far has led to the development of a new effective coreless design of an inductive superconducting limiter.

7. Electrostatic field in the process of separation of loose materials

Jacek Majcher

7.1. Introduction

Separation and sorting of bulk materials are one of the basic technological processes in both industry and agricultural processing. To obtain a high-quality final product, it is necessary to ensure that the raw material used for production has certain characteristics. In order to achieve this, the material must be purified (separation of unnecessary or harmful impurities from the useful material). Once the material is cleaned, it is subjected to the next process, which is sorting. This process involves dividing the material into groups with different usefulness. Most of the material's technological properties depend on its degree of purity and homogeneity. Material with a high degree of homogeneity (less impurities) has repeatable quality parameters.

In agrotechnology, e.g., during seed extraction, various seed separation methods have been used for many years. The need for this arises from the fact that the obtained raw material is not always a homogeneous seed mass due to differing content of impurities and immature and unformed seeds, which usually have low biological and technological value. To date, a considerable number of methods and means have been developed to solve the problem of seed cleaning to the satisfaction of breeders. An important problem, still waiting for an effective solution, is the separation of fractions of poorly formed or damaged seeds not useful in further processing, which have identical separation properties used so far, from the remaining collected seeds. This applies specially to fractions with a significant degree of fragmentation (processing), when the mentioned separation properties used in the separation of whole seeds cannot be taken into account [138].

In agricultural processing, especially for food products, quality has become an important and distinguishing characteristic. Attention to quality should be implemented throughout the production system to prevent rather than correct errors. Today, food is mass produced for economic reasons. Therefore, in the case of improper separation of various types of undesirable fractions and impurities, a significant number of consumers may be at risk. One of the important conditions to ensure high quality of the final product of plant origin, is the ability to separate fractions differing in use value.

The extracted plant material may have various types of impurities. The most important ones include mineral, organic, animal, chemical, and biological impurities [139]. During cleaning, it is important to keep in mind that obtaining a perfectly pure raw material is impossible.

In practice, a compromise between purity and loss of basic material is sought. Purity should be understood as a factor, representing the percentage of usable material and impurities in a given batch of material.

7.2. Segregation methods for crushed materials

There are many methods available on the market for separating bulk materials. Each of these methods is directed at a particular separation feature. There are also devices which segregate material with regard to several separating features in one cycle. Among the separating features we can list, among others, geometric dimensions, shape, mass, surface type, coefficient of friction, hardness, elasticity, colour, and electrical parameters. According to the above separation characteristics, we can distinguish the following groups of sorting devices [140, 141]: pneumatic, sieves, trippers, gravitational (seed surface texture), frictional (set of mechanical features), photoelectric, electrostatic.

In the case of a pneumatic separator, the main component of the device is a forced air stream that lifts the lighter contaminants, thereby separating them from the actual material (Figure 7.1).

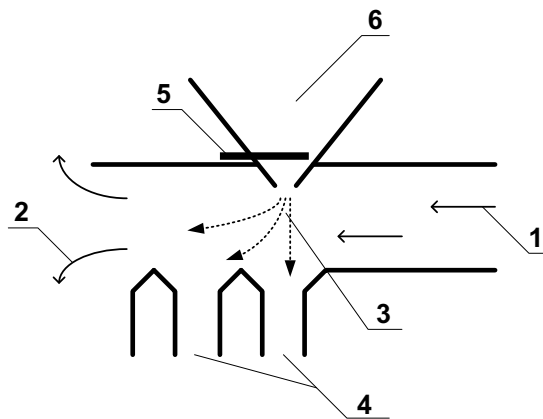


Figure 7.1. Diagram of construction and operation of the pneumatic separator: 1 – air inlet, 2 – air and fine dirt outlet, 3 – grain outlet direction, 4 – grain outlet sorted by weight, 5 – gate valve, 6 – feeder. Source: own elaboration based on [140]

A sieve separator divides material by shape or size, depending on the sieves used. Figure 7.2 shows examples of sieves with different mesh diameters. The principle of this separator is that material which does not have certain dimensions falls through the mesh of the sieves and material which meets the criteria remain in the sieves. In order to sort the material according to differences in texture, separators are used, e.g., canvassing machines with oblique rollers. Material through the feeder is fed to the canvas, which is mounted at an angle.



Figure 7.2. Sieves with mesh diameters: 2.24 mm (left), 1.25 mm (middle), 0.4 mm (right).
Source: own elaboration

Depending on the sorted material, to adjust the coefficient of friction, the canvas is changed as well as the feeder inclination. The canvas rotates in the direction opposite to the direction of the material fall. Material with a low coefficient of friction rolls down, while material with a higher coefficient of friction is moved up the separator. Another separating feature of materials can be colour. On the basis of this feature, we can distinguish a material of equal size and mass that differs from others in its colour. In this case we can e.g., separate immature grains from mature ones. When the material moves past the photocell, the reflected light from the surface of each unit of raw material is measured. This signal is compared with a preset reference signal and if it does not meet the criteria, an air stream is activated which ejects the particles which do not meet the criteria. The disadvantage of this separator is low efficiency because the material has to move over the photocell one at a time [142].

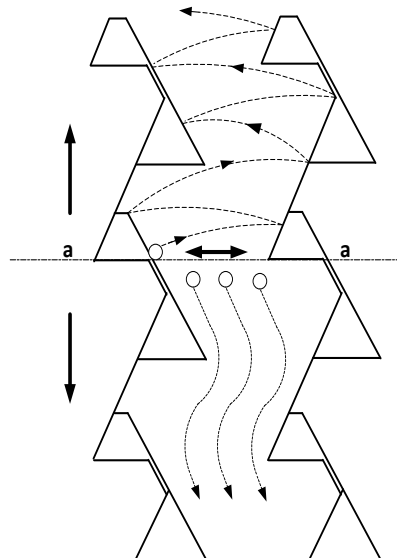


Figure 7.3. Functional principle of the sorting table. Source: reprinted from [143] after obtaining the authors' permission

Currently, especially in the food industry, newer versions of optical separators are used in which the photodetector is replaced by a camera. Through analysis of the image with the database, the material can be distinguished in terms of several separation features simultaneously.

Figure 7.3 shows a separator that sorts material in terms of mechanical features. This takes advantage of the differences in elasticity of the material being segregated. The separator is vibrated up and down with a frequency of approx. 3.6 Hz. The side walls are set at an appropriate angle depending on the material to be sorted. The elastic material bounces off the walls with a force greater than the force of gravity and moves up under the influence of vibrations. On the other hand, less elastic material settles at the bottom of the separator. Thanks to this, it is arranged in layers starting from the least elastic. Such separators are mainly used in the separation of germinated seeds.

These separators distinguish material in terms of physical, external characteristics. However, there are certain groups of materials, e.g., plant seeds, which do not differ in terms of such qualities. Therefore, it should be concluded that they must differ in internal characteristics. One possibility is to cut the seed and find out what the differences are. This approach is not practical because it destroys the usable material. Therefore, other methods of separation are sought, which will separate the material in terms of their internal characteristics.

7.3. Use of electrostatic field in separators

The use of electrostatic fields to separate different types of materials has a long history. As early as the 6th century BCE, the Greeks noticed that when amber is rubbed against fur it attracts small particles such as hair. This phenomenon was first used for separation purposes by Thomas B. Osborn, who patented the first electroseparator in 1880 [144]. This separator was used to remove various types of impurities from flour [145].

In this separation, the electrical properties of the material are used as the separating feature. These properties are understood as the particle's ability to accumulate surface charge, electrical conductivity, as well as dielectric permeability. Separation is possible due to the fact that individual particles behave differently under the influence of an electrostatic field and forces with which the field interacts with particles. Electrostatic forces are created by the interaction of electrified bodies or by placing bodies in an electric field. These forces can be divided into:

- *electrophoresis* – interaction of an electric field with a particle carrying an electric charge,

$$F_e = q_p \cdot E, \quad (7.1)$$

where: F_e – electrophoresis force, q_p – particle charge, E – electric field.

- *diaphoresis* – charge-induced shifts resulting from polarisation [146].

In order for electrophoresis forces to form, the particles should be electrified. There are different methods of electrifying particles:

- triboelectrification,
- induction,
- contact with a charged surface,
- corona discharge,
- bombardment with electrons and ions,
- pyroelectric phenomena,
- field emission (autoelectron emission) [147].

Electrification is a phenomenon that occurs at the surface of a particle, resulting in an electric charge and thus an electrostatic force that is proportional to the surface area of the particle.

7.4. Application of electrostatic fields in industrial practice

One of the basic electroseparators found in the literature is the so-called planar electroseparator. It is constructed from two parallel electrodes (Figure 7.4.a). Between the separator covers, a homogeneous electrostatic field is created, which is shown in Figure 7.4.b. Since the distance between the covers is several millimetres and the voltage applied to the electrodes is of the order of several kilovolts, the intensity of the electrostatic field between the covers is of the order of MV/m. At such a strong intensity, the phenomenon of particle electrification occurs.

Figure 7.5 shows an example of a planar electroseparator. In this separator, the particles fall from the feeder under the influence of gravity and are located between the separator covers. As they are in a strong electrostatic field, they become electrified. At the moment when the particles have a charge, their fall path is appropriately bent by the electrostatic field, thanks to which they are directed to the appropriate chambers of the container. Another example of an electroseparator is an electroseparator based on bifilar winding. A bifilar voltage or current winding is used. In a voltage winding, two wires that are not connected to each other are led side by side. These wires are then energised with high voltage. For separators with current bifilar windings, two wires are wound next to each other and short-circuited at the ends. This winding is supplied from a current source. For practical reasons, a voltage bifilar winding is usually used in electroseparators (Fig. 7.6.a). As can be seen from Figure 7.6.b, a non-uniform electrostatic field is generated between the windings, with the highest value occurring at the junction of the two conductors. The occurring electrostatic field causes electrification of particles that are located on the bifilar winding. This phenomenon was used in the electroseparator's construction shown in Figure 7.7. In this separator, the winding is wound on a rotating drum and is supplied with high voltage.

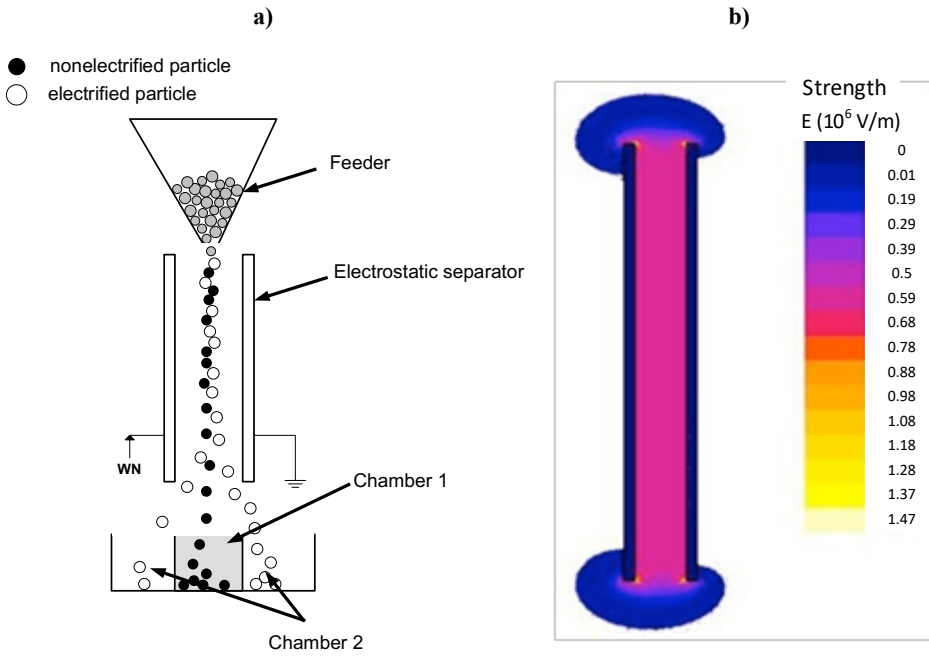


Figure 7.4. a) The principle of separation of loose materials in the electric field, b) electrostatic field distribution. Source: reprinted from [143] after obtaining the authors' permission



Figure 7.5. Flat electroseparator. Source: own elaboration

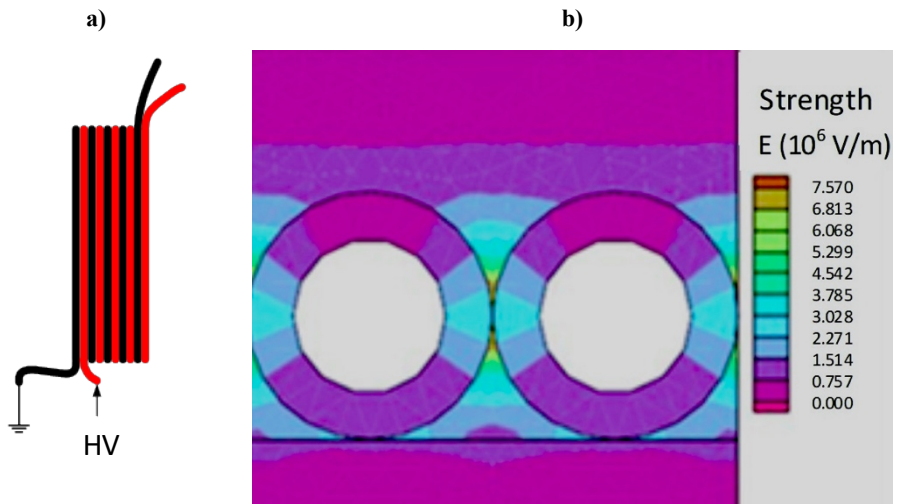


Figure 7.6. Voltage bifilar winding a) winding view, b) distribution of the electromagnetic field around the winding. Source: own elaboration based on [149]

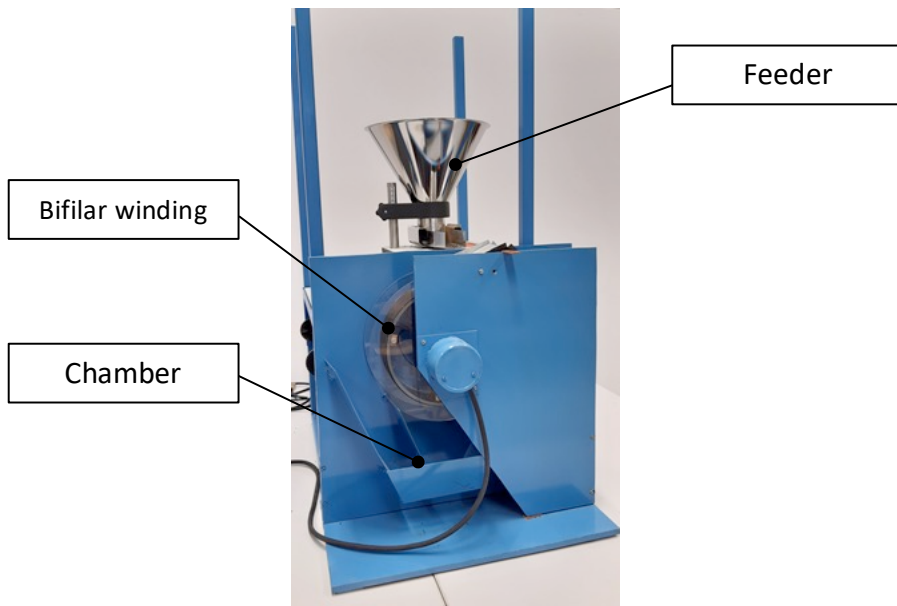


Figure 7.7. Electroseparator with bifilar winding. Source: own elaboration

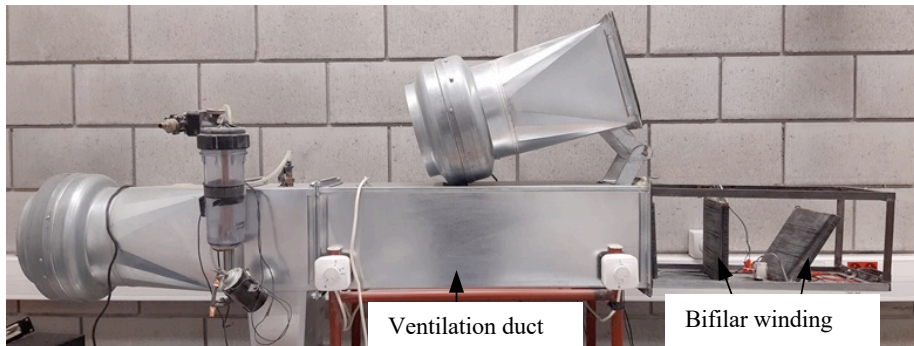


Figure 7.8. The use of bifilar winding in separating industrial dust. Source: own elaboration

The particles from the feeder are brought to the rotating drum with a bifilar winding. As soon as the particles are on the winding, it electrifies under the influence of a strong electrostatic field, so that the particles are attracted to the winding. As the drum rotates, centrifugal force is created which attempts to pull the particles away from the winding. Therefore, depending on the amount of charge accumulated on the particle surface, the particles are directed to the appropriate chambers.

This phenomenon was used for the construction of the dust collection filters described in [146]. Several cascaded electrostatic precipitators are installed in ventilation ducts. These filters are used to capture relevant particles from the air stream. An electrostatic precipitator for dust collection is shown in Figure 7.8. A disadvantage of the presented solution is that this filter should not be used in the case of dust extraction of explosive dusts. Additionally, the electrostatic precipitator should be cleaned from time to time as dust “sticks” to the filter.

7.5. Summary

Electrostatic separators complement a wide range of traditional separators. Due to the complexity of their design, they are usually applied in the end parts of sorting lines. The problem with operating this type of separators are the voltage sources of several or more kilovolts. This voltage causes that these types of separators should be operated only by qualified personnel. In the case of electrostatic separators, the highest efficiency is achieved when separating materials of extremely different electrical properties, e.g., conductors and dielectrics. That is why, apart from the examples of application of electrostatic separators in the agro-food industry mentioned in this paper, they are used, among others applications, in recycling crushed PCB material or, more broadly, in recycling electronic and electrical equipment or WEEE (waste electrical and electronic equipment).

8. Electromagnetic compatibility of devices and installations in electrotechnologies supporting environmental protection

Paweł A. Mazurek

8.1. Introduction

The effect of dynamic technical development in all branches of power engineering, IT, communications and radio-communications is the increase in the number of devices and systems processing and transmitting electrical energy. Ensuring the possibility of undisturbed simultaneous operation of so many different devices and systems determines the further development of technological society. Electrical and electronic devices during operation emit electromagnetic disturbances, which can be divided into low-frequency and high-frequency disturbances. Another division is the classification into disturbances propagated by conduction or radiation. Most often these phenomena are undesirable, although there are machines and devices in which electromagnetic fields are used intentionally (e.g., mobile telephony).

The impact of electromagnetic disturbances may be various and may lead to serious risks. Disturbances cannot be completely eliminated, but techniques and means should be used to reduce their magnitude to an acceptable level.

Electromagnetic compatibility (EMC) is the ability of a given electrical or electronic device, or installation, to function properly in an electromagnetic environment. This means that it meets the criteria of not interfering with its own operation and that of other devices, while at the same time being immune to the electromagnetic emissions of other devices [151–155].

To prevent hazardous situations, any equipment or system containing electrical or electronic components should be designed to cause the least amount of interference. In addition, each device or machine should be designed to be as immune as possible to disturbances emitted by other devices. Electromagnetic compatibility is achieved through proper design, selection of components, connections, filtering and shielding. With the complexity of today's systems, theoretical knowledge is often not enough; it must be supported by special tests. Measurements of the electromagnetic compatibility of technical devices are one of the basic elements of this process and constitute an indisputable source of information about the actual properties of the tested device. When carrying out such measurements, one must bear in mind the specific requirements of the measurement methods used, the instruments used and the physical properties of signals and electromagnetic fields, taking into account their "broadband" nature and the large dynamic range of the measured values. Quantitative, time-consuming control measurements can be replaced by

qualitative tests in the case of preliminary tests at individual stages of construction. The latter are simpler in implementation and much cheaper due to smaller equipment requirements, poorer measurement facilities and are less time-consuming [151–155].

To design an electrical device or installation well, all aspects of electromagnetic compatibility must be considered. This applies not only to such common products as consumer electronics/appliances, computers, telephones, etc., but is also especially important for such complex products as vehicles, aircraft, ships, or large industrial, electrotechnological installations. These are very sensitive to EMC interference, and no one allows possibility of serious interference in, for example, a large chemical factory or steel mill. It is necessary to accurately establish EMC requirements from the very beginning of the product design cycle, apply good EMC engineering practices, prepare auxiliary equipment with the desired electromagnetic compatibility by solving EMC, safety, quality and usability issues early in product development and design. This reduces costs and delays of final product changes and rework.

Electromagnetic compatibility is a field that touches every branch of technology today. Issues have always been strategic for military devices as well as medical devices, because in both cases compatibility is critical. Another sector is the automotive industry, which should gain even more importance in the future with the development of electric transport. In recent years, we have seen the growing importance of the issue in the industrial, telecommunications and even consumer goods industries as overall quality becomes more important. EMC issues will become even more important, because in addition to meeting legal requirements for emission and immunity, ensuring high quality products, security, data protection and protection against intentional attacks on the information and communications technology infrastructure will also become more prominent [151–155].

8.2. Electromagnetic compatibility testing and analysis

Because of the ubiquity and ever-increasing role of electrical and electronic equipment and because of legal requirements, there is a need to test electromagnetic immunity and emissivity and, consequently, to determine specific levels of compatibility of the equipment under test.

There are criteria to define the immunity, emissivity and compatibility levels of equipment. First, it is necessary to define the immunity and emissivity of the analysed object. By electromagnetic immunity to disturbances, we define such a property of the device or system, which is characterised by the ability for it to operate properly without a decrease in quality in the presence of an electromagnetic disturbance, whereas by electromagnetic emission we mean electromagnetic energy entering the surrounding environment due to electromagnetic radiation in free space, conduction through power or signal

wires, capacitive coupling and inductive coupling [151–155]. The compatibility level is the greatest level of interference of a given type that is expected to act on a device operating correctly under given conditions. For a system or installation, the compatibility level is agreed to be the level of disturbance for which the probability of an assembly’s sensitivity to disturbance, and the probability of a disturbance emission of that level, do not exceed an acceptable value of the probability of disturbance. In some cases, standards specify compatibility levels. Graphical relationships of the compatibility, immunity and emissivity occurring in the EMC analysis are shown in Figure 8.1.

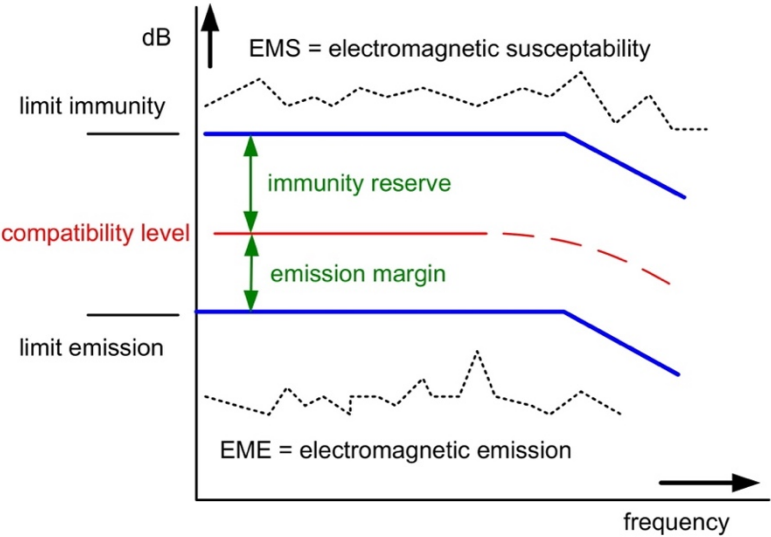


Figure 8.1. The levels of compatibility, emission and immunity of an electrical device. Source: own elaboration

The determination of all levels is made possible by the results of simulations and test runs. Full assessment of the quality of a device from the point of view of EMC recommendations requires a number of control tests to be performed in a specialised laboratory.

8.3. Methods of testing radiated emissivity of devices

Measurements of radiated emissivity are one of the more difficult and expensive tests because they require a suitably large test bench with sufficiently low level of extraneous radiated disturbances coming from other sources. An exemplary arrangement of elements of a test stand for radiated emissivity is shown in Figure 8.2. Interference emission measurements are used to determine the ability of an electrical device to emit interference under standardised conditions in order to compare the measured results with acceptable limit levels.

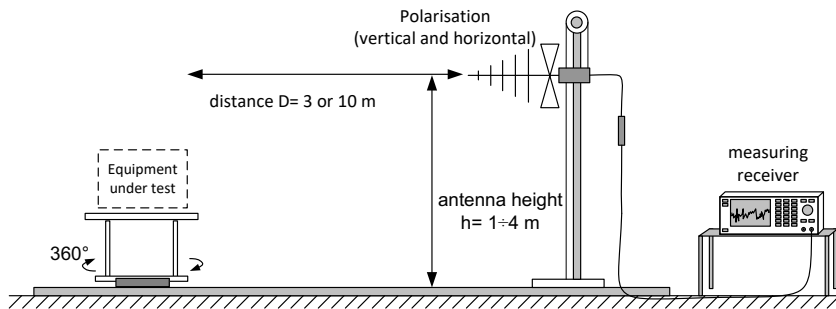


Figure 8.2. The idea of measuring station for electromagnetic emission tests. Source: reprinted from [152] after obtaining the authors' permission

Electromagnetic interference (disturbance) in the frequency range from a few tens of kHz to a few GHz is referred to as radio frequency interference. They are generated in electric circuits containing inductances and capacitances (even when they occur in the form of parasitic parameters), in which sudden changes of flowing current, changes of electric voltage, or feedback take place. The generation and distribution of interference energy in the frequency spectrum and time characteristics depend on the structure and electrical parameters of the device in the high-frequency range, its time characteristics and the impedance loading the source. Considering the temporal characteristics of desired and undesired emissions and conducted interference to the environment, the interference generated by any source can be divided into continuous and short-lived, while with respect to the frequency characteristics, the interference can be divided into narrowband and broadband [151–155].

Classical radiation measurements are made in the frequency range from 30 MHz to 1 GHz, using an interference meter with a quasi-peak or average value detector. Depending on the distance relationship, measurements are performed in the near field or far field. Measurements of the radiated electromagnetic field strength should be made with the antenna placed at a strictly defined distance, measured in the horizontal plane from the boundary with an imaginary straight line drawn along a simple geometrical contour encompassing the device under test.

8.4. Methods of testing conducted emissivity of devices

In the classical approach, conducted interference levels must be tested in the frequency range 0.15–30 MHz. For simplicity, the measured interference voltages are expressed in the decibel (dB) scale. When measuring the interference voltage generated by an electrical object, it is difficult to determine the resistance (impedance) of the interference source in the high frequency range. Therefore, a voltage measurement can only be defined if it is measured at a specific load resistance (impedance) so-called equivalent.

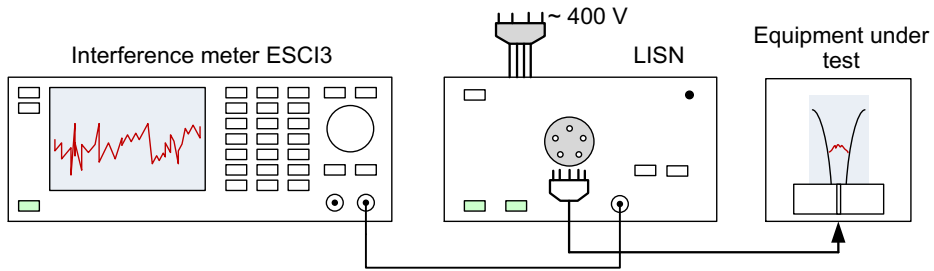


Figure 8.3. The concept of measuring system to conducted interference test. Source: own elaboration

The measured object is connected to a so-called artificial network, which represents itself for the interfering quantity the defined load impedance. The concept of the measuring system is presented in Figure 8.3. The artificial network is connected to the power supply circuit, which has a measuring point for the meter. The artificial network – Line Impedance Stabilisation Network stabilises conditions of disturbance voltage measurements in power supply circuit of tested object. Measurements of conducted disturbances are aimed, first of all, at determining the level of disturbances introduced by systems into the power supply network.

8.5. Immunity test methods for electrical equipment

Immunity of devices to electromagnetic disturbances is tested by conducting immunity tests for standardised emission of disturbances and observing operation of a device or machine. These tests in extreme cases (if the device is poorly designed and constructed) can be destructive or dangerous tests.

The immunity of a device to disturbances does not depend only on its construction. It also depends heavily on the quality of the mass production techniques used. The idea of immunity measurements consists in exposing the tested object to a signal or signals of strictly defined parameters under defined conditions. In the measurements of immunity of devices to electromagnetic fields, it is necessary to create a field in the measurement area, the intensity of which has a specific value and non-uniformity not exceeding the level required by

the standards. Susceptibility tests also include testing the resistance of devices to signals that propagate by conduction. These vary widely and include symmetrical and asymmetrical conducted disturbances, overvoltages, fast pulsed disturbances, and electrostatic discharges. The implementation of these tests requires the generation of signals and their introduction by coupling into the conductors or, in the case of ESD electrostatic discharge, into the enclosure of the test object [151–155].

The immunity test procedure for electrical equipment depends on its classification for environmental operation or other guidelines. An example set of tests might include exposure tests to:

- radio frequency electromagnetic fields from 0.03 to 3 GHz,
- conducted disturbances induced by RF fields from 100 kHz to 200 MHz,
- series of fast electrical transients of burst type,
- surge (imitating lightning)
- electrostatic discharges,
- 50 and 60Hz mains frequency magnetic fields,
- pulsed magnetic fields,
- power failures, short interruptions and voltage fluctuations (PQT).

All the immunity tests (Surge, Burst, ESD, PQT, etc) must be related to the operation of the object under test. The results of electromagnetic exposures are evaluated according to the following criterion:

- a) normal operation within technical requirements
- b) momentary reduction or loss of function or performance that is self-restoring
- c) momentary limitation or loss of function or performance that requires operator intervention or restoration of the initial system state
- d) limitation or loss of function that cannot be restored due to hardware or software failure or loss of data

Successful completion of the tests ensures that the equipment tested complies with the requirements of the technical standards and the EMC Directive. It is then presumed that any product manufactured in accordance with the harmonised standards complies with the relevant directives requirements.

The impact of electromagnetic disturbances can be various and can lead to serious risks. The widespread reliance on electronics in society-critical applications gives special importance to the issue of the immunity of systems to electromagnetic interference [151–155].

An essential part of device quality analysis involves determining the levels of emission, immunity, compatibility and relating them to acceptable values. Determination of the levels of these parameters in the design and construction phases allows one to determine all errors in the functioning of the device. Thanks to such analysis, protections against low immunity or high emissivity of devices can be selected more effectively.

8.6. Electromagnetic compatibility of plasma reactors

As regards the quality and safety requirements for plasmatrons, the key issue turns out to be electromagnetic compatibility testing. Plasma reactor installations built at the Department of Electrical Engineering and Electrotechnology require the design and construction of special power supply systems dedicated to them.

The quality of reactor operation depends on many factors, the most important of which are related to its power supply system, dimensions and shape of the electrodes, speed of the gaseous medium flow through the discharge chamber or the temperature inside the discharge chamber. From the point of view of the user operating a plasma reactor, continuous operation and stability of plasma parameters are desirable. Electromagnetic disturbances in the power system can affect the inhomogeneity of plasma generation, which can affect the efficiency of the destruction of hazardous substances. Therefore, the identification of disturbance levels under different reactor operating conditions is the basis for design of the power supply and anti-interference system [156–162].

The source of the plasma and the means of supplying energy to it is the forced flow of electric current in the gas. Plasma is an ionised gas that conducts electricity, and this property is used in arc plasma generation [49, 162–166]. The nature of the operating reactor is periodic. Due to the electrical discharge, it is also a highly nonlinear consumer (there are large load changes and significant asymmetry in the power path, depending on the length of the burning arc).

Care must be taken when assessing whether a stationary installation is EMC-compliant and each installation must be classified individually. Unfortunately, there are no rigidly defined rules with which to explicitly specify procedures for the EMC compliance of plasma reactor plants. Despite many years of research on non-thermal plasma generation and application technologies, the phenomena that accompany plasma reactor operation are still not fully understood.



Figure 8.4. View during EMC measurements of the GlidArc three-phase plasma reactor installation in the Department of Electrical Engineering and Electrical Engineering. Source: own elaboration

The basic power supply of the 3-phase plasma reactor (used in the tests) is a system consisting of three single-phase transformers presented in Figure 8.4. Transformers are connected to a star-star three-phase system with a neutral conductor. These transformers provide a 1.6 kV sinusoidal power supply. This voltage provides the correct plasma parameters but does not guarantee arc ignition. Therefore, the reactor has ignition electrodes powered by a high voltage

circuit (about 12 kV from ignition transformer FART Resinblock 2000), necessary to initiate the ignition of the electric arc [160, 161]. The power supply is regulated by the Metrel HGT 400/8 three-phase autotransformer. Air is introduced into the chamber from an oil-free Magnum JWA-30 compressor.

The ignition of the discharge on the working electrodes of a plasma reactor, analysed in this text, is initiated by the jump of an electric spark between the ignition electrode and one of the three working electrodes. The spark discharges occur in the air at a voltage of 11–14 kV. In a three-phase plasma reactor with an additional ignition electrode, the distance between the electrodes in the ignition zone was set at approx. 4 mm [159–161].

Measurement of emissivity is reduced to the determination of the electromagnetic field strength in the direction of maximum radiation. The measurement method and sampling ranges were set according to the CISPR 16 standard.

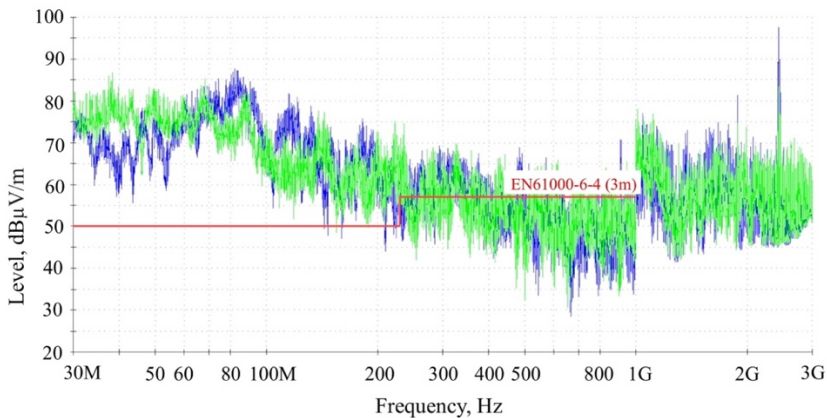


Figure 8.5. Level of radiated emission of GlidArc reactor system in the range of 30–3000 MHz, measured with peak detector. Blue line describes vertical emission, green line – horizontal, and red line – EN61000-6-4 (3m). Source: own elaboration

The green plot shows the electromagnetic spectrum values when the antenna is horizontally polarised, and the blue plot shows the values when the antenna is vertically polarised. The measured values clearly confirm the nonlinear and broadband character of the emitted disturbances, exceeding the acceptable levels for EMC standards. Simultaneously with measurements of radiated emission, measurements of conducted disturbances in the power supply line are conducted. These tests are aimed at obtaining information on the possible impact of the tested object on the power installation. The reactor installation does not have control or data systems, so the tests of conductive electromagnetic interference are limited to the analysis of the power supply circuit.

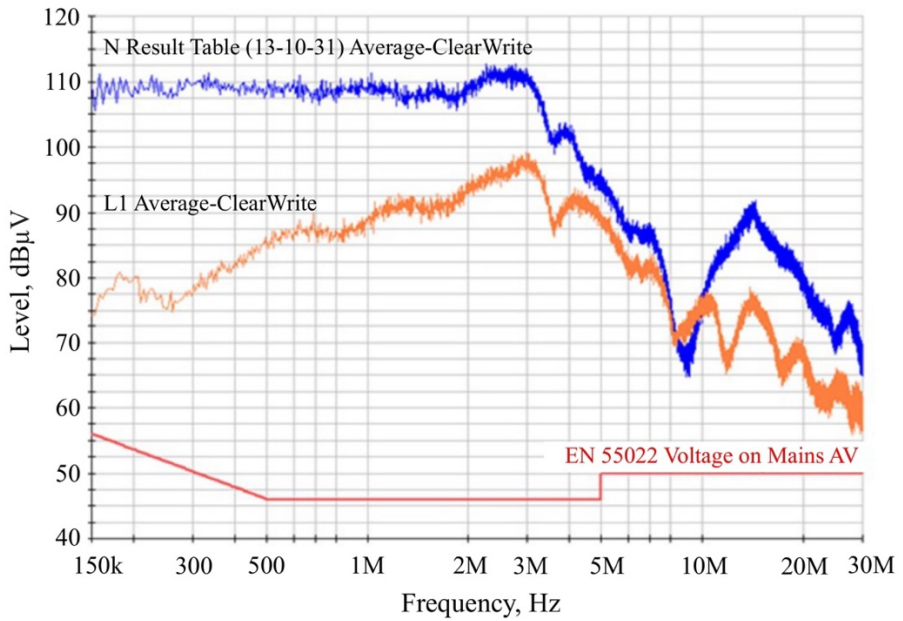


Figure 8.6. Electromagnetic interference values measured in N, L1 lines in a reactor system. Source: reprinted from [160] after obtaining the authors' permission

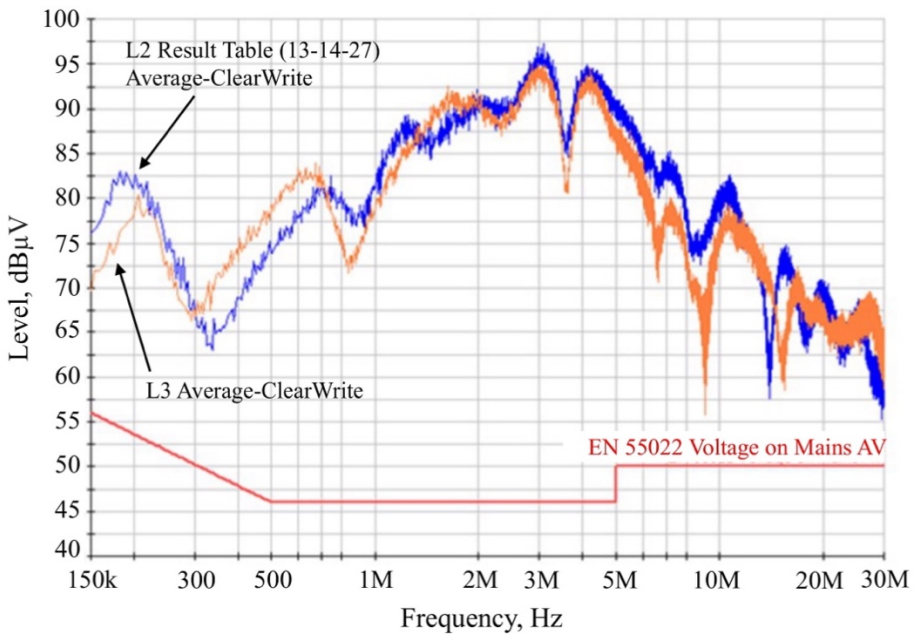


Figure 8.7. Electromagnetic interference values measured in L2, L3 lines in a reactor system. Source: reprinted from [160] after obtaining the authors' permission

For the purpose of identification of electromagnetic disturbances conducted in the working lines (L1, L2, L3, N) of the reactor, a measurement receiver ESCI3 Rohde Schwarz and a three-phase artificial network SMZ-6/50 were used. Examples of test disturbance values in relation to the permissible limit set by the harmonised series standards EN 61000-6-3 and EN55022 are shown in Figures 8.6 and 8.7. The results of this research are presented in two charts. It is related to the ignition system which works on L1-N electrodes. Between these power supply lines, a superposition of interference occurs as well as from the power system and from the ignition system.

Reactor discharge operation generates strong, dynamic and broadband interferences that are difficult to analyse. Analysing individual electrode systems, one can see small differences in the level of disturbances measured. The broadband character of the disturbances is noticeable in the whole measuring range. Small discrepancies are visible both in the low frequency band (hundreds of kilohertz) and in the range of several dozen megahertz.

The electrical discharges and plasma generated by the plasma reactor are a source of strong interference. Interferences are propagated by both radiation and conduction. The results obtained are unambiguous. Regarding the nature of the measured disturbance, it clearly has broadband characteristics. The nonlinear and asymmetric loading that characterises the plasma reactor translates exponentially into a random character of the emission distribution.

The reactor study presented is an example of an incompatible device. High levels of interference do not allow safe operation of this device. At the same time, the test results are a starting point for designing appropriate filtering and shielding systems [156–161, 167, 168].

8.7. Electromagnetic compatibility of electric vehicle chargers

The electric vehicles (EV) could potentially have a significant impact on the power grid and distribution networks due to the fact they are non-linear loads and their charging might result in tremendous power demand. When connected to the utility grid, a large number of EV charging stations from different manufacturers might create significant harmonic current emissions, impact the voltage profile, and eventually affect the power quality [161, 169–181]. Nevertheless, practical examples of disturbances from charging stations have not been made public. This paper aims to clarify the characteristics of conductive disturbances and levels of current harmonics generated by charging stations and their severity on quality of electric energy. The analysis was based on tests of a prototype of an EV charging station integrated with a LED streetlight.

Electric vehicle chargers are a modern and atypical load that must be treated as a new customer by power distribution systems. The increasing number of EV and EV chargers that connect to the power grid entails many new challenges and complications [169–173, 178–180]. The individual behaviour of EV owners

varies greatly. This randomness of EV charging makes it difficult to keep the power grid under control and may have a negative impact on the overall operation of the power grid. Thus, important issues for the power quality in the power system are conductive electromagnetic disturbances and current harmonics. Electromagnetic compatibility analyses ensure that the designed object complies with the standards will not interfere with the operation of other electrical equipment and the power system [151, 170–173, 177, 180].

The electromagnetic emission of the chargers in the area of electromagnetic compatibility is defined by a series of IEC 61851 standards. The analysis must include current harmonics in the range of 50 Hz–2/2.5 kHz, conducted disturbances in the band of 150 kHz–30 MHz. Radiated disturbances are analysed in the range from 30 MHz up to 6 GHz (the limit results from the frequency of signals used in the charger modules) [161, 172, 173, 175–177].

The object analysed is a charging station. The three-phase station for bidirectional fast energy transfer between the power grid and an electric vehicle contains two modules, AC and DC, and is integrated with a LED streetlight (Figure 8.8.) [177].



Figure 8.8. The PLUGinEV charging station, photo in the screen chamber. Source: own elaboration

The electromagnetic emissions analysis of the charging station is regulated by the procedures of the EMC Directive 2014/30/EU. In the field of conductive disturbance emission, the permissible limits are specified in the IEC 61851-21-2 standard [151, 177]. Conductive disturbances in the 150 kHz – 30 MHz band must be analysed.

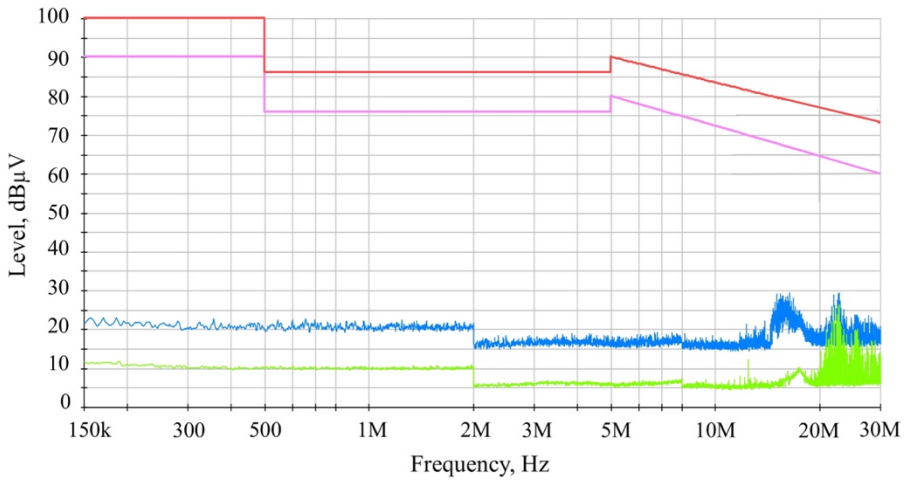


Figure 8.9. Conductive disturbances of the charging station during AC module operation (80% of power) from the peak detector (blue line) [177], from the average detector (green line), and IEC 61851-21-2 limits for average (purple line) and quasipeak detector (red line). Source: own elaboration

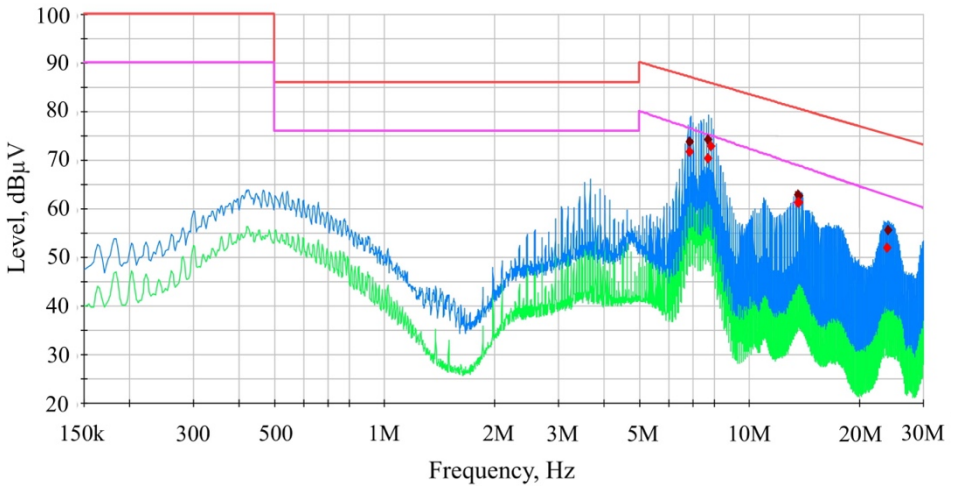


Figure 8.10. Conductive disturbance of the charging station during DC module operation (80% of power), from the peak detector (blue line) [177], from the average detector (green line), and IEC 61851-21-2 limits for average (purple line) and quasipeak detector (red line), final result detector quasipeak (brown dot) and final result from average detector (red dot). Source: own elaboration

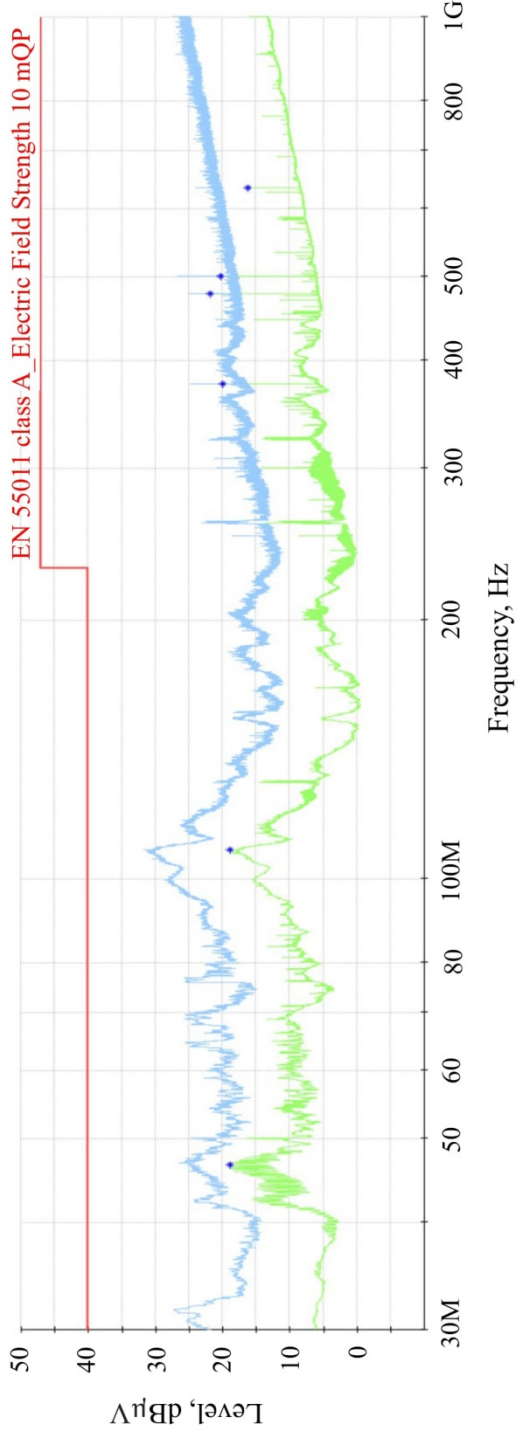


Figure 8.11. Radiated disturbance of the charging station, DC module operation (20% power), IEC 61851-21-2 limits for quasispeak detectors, blue line – disturbance level measured by the peak detector, green line – average detector. Source: reprinted from [177] after obtaining the authors' permission

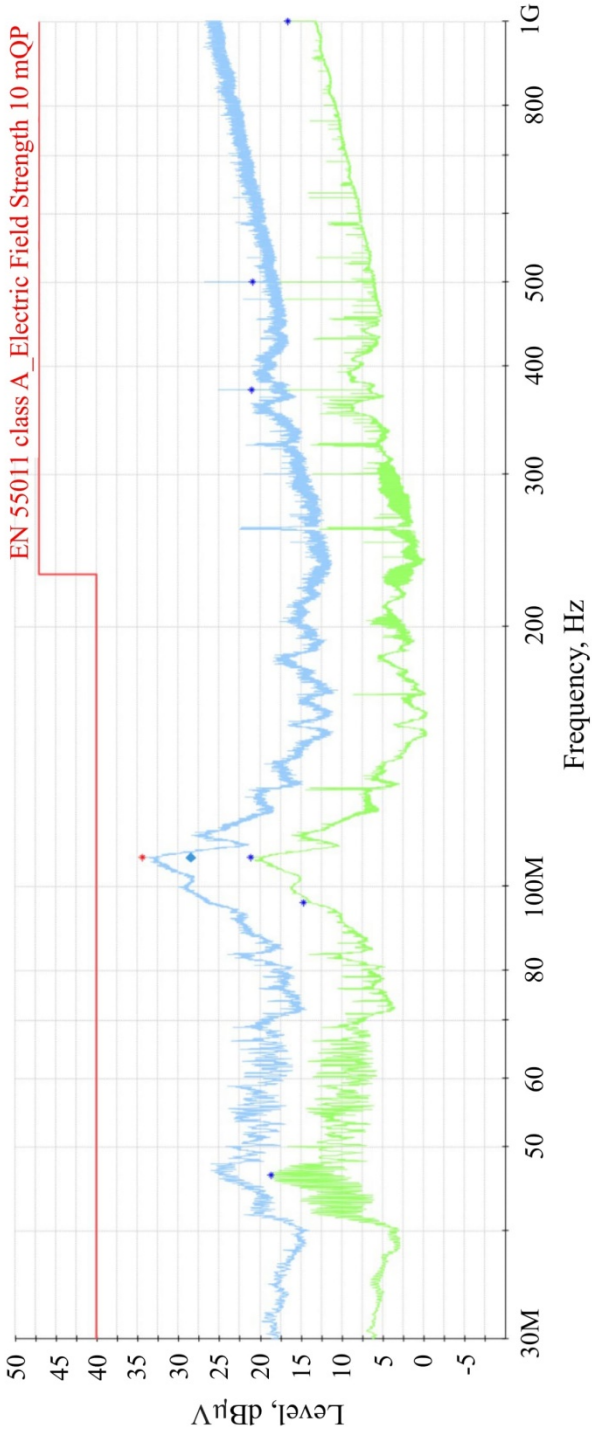


Figure 8.12. Radiated disturbance of the charging station, AC module operation (80% power), IEC 61851-21-2 limits for quasi-peak detectors, blue line – disturbance level measured by the peak detector, green line – average detector. Source: reprinted from [177] after obtaining the authors' permission

The tests were carried out in a system consisting of a measuring receiver, an artificial network in the power supply line and a charging station loaded with a resistance, symmetrical simulator (a 120 kW water-cooled resistive). The second part of the research involved determining the level of radiated emissions. Professional testing is performed in a shielded, reflection-free chamber. Logarithmic-periodic antennas and an interference meter are used for identification. The measurements of conductive and radiated disturbances were carried out in two modes of charger operation for 20% and 80% power transferred by the station. The operating modes result from various legal recommendations that define the safety of charging electric vehicles [177]. The characteristics in Figures 8.9–8.12 show the results of measurements of the charging station loaded with a resistance simulator. In the background of each measurement the permissible limits are visible. No excess emission levels were found while analysing all states of operation. This means that corrective actions ensured that the EMC requirements were met.

The charger tests presented are an example of a compatible device and it is properly designed and manufactured. It uses good anti-interference systems which confirmed the measured interference levels are within limits.

8.8. Summary

Currently, there is a rapid development of electronics, automation, telecommunications and electrotechnological devices and installations. All devices should, already at the design stage, be properly adapted to work in a specific electromagnetic environment. The devices are required to comply with the Electromagnetic Compatibility Directive as well as other applicable standards. The sample analyses for the reactor and charger shown in this chapter demonstrate this. The devices introduce electromagnetic disturbances into the network via the power input and then radiate these disturbances through the enclosure. The value of disturbances should not exceed the levels permitted by applicable standards. The level of emission has a direct relationship to the purity of the electromagnetic environment and the operating conditions of other electronic devices.

Topics related to electromagnetic compatibility are still developing. The development of the latest technologies makes EMC a field of science which requires further research and conclusions for the future. On the one hand, the manufacturers are responsible for an adequate level of EMC protection; nevertheless, adequate supervision of the equipment put into operation must be ensured. Here an important role is played by testing laboratories, which, however, without appropriate guidelines and current standards are not able to properly verify and define the compatibility of the tested device. Therefore, electromagnetic compatibility tests are very important to obtain safety and good quality of the devices introduced to the market.

9. Innovative and energy-saving materials, electronic and power engineering technologies

9.1. Environment-friendly materials

Masaaki Yamazato, Akira Higa

Introduction

Amorphous carbon films have unique properties such as high hardness, low friction coefficient, optical transparency, high resistivity, gas barrier, biocompatibility, and chemical inertness. Because of these properties, a-C:H films are successfully utilised in several areas such as scratch-resistant and wear-protective coatings on mechanical tools, transparent coatings on optical components, gas barrier coatings on PET bottles, and biocompatible and antithrombotic coatings on medical stents [182–186]. In these applications, amorphous carbon films have contributed significantly to CO₂ reduction, and BOD and COD reduction. For example, if amorphous carbon is coated on about 5,000 tons of cutting tools produced in Japan in a year, it is estimated to reduce CO₂ emissions by about 100,000 tons in the process from manufacturing to disposal. Amorphous carbon is an environmental-friendly material [187]. In order to apply amorphous carbon film with such excellent properties to electronic devices, it is required to control conductivity, conduction type, and carrier density. Therefore, doping of several elements into amorphous carbon has been attempted. Some groups have reported the effects of boron, phosphor, and iodine doping to amorphous carbon films [188–195]. On the other hand, we have reported that the structure and the properties of hydrogenated amorphous carbon (a-C:H) films vary depending on the concentration of bonded hydrogen [196–198]. In this section, we report the summaries of our previous results for the relationship between the structure and the properties of a-C:H films and the concentration of bonded hydrogen, and the effects of iodine doping in a-C:H films with different bonded hydrogen concentrations.

Experimental

The a-C:H films were deposited in H₂/He plasma by the RF magnetron sputtering system. The graphite disk (99.99% purity) was used as a target, which was bonded to the water-cooled cathode electrode. Fused silica and Si were used as substrates which were placed on the anode electrode. After film deposition, iodine was chemically doped to the a-C:H films. The doping was carried out in the vessel with Ar flow, and the film was placed beside the iodine solid. The doping time was 30 min, and the temperature was kept at 100°C. The iodine was transformed to gas, the a-C:H film was exposed to iodine vapor, then it was

doped into the film. The bonded hydrogen concentration and the chemical states were evaluated using an FT-IR (Jasco FT-IR/300). The optical gap was estimated by the transmittance spectrum, which was measured with a UV-visible spectrometer (Jasco V-550). The current–voltage (I - V) characteristics of the deposited films were measured by using an electrometer (Keithley 6517A). The film density was evaluated by the buoyancy method using a mixed solution of ethanol, trichloroethane and tetrabromoethane.

Structure of deposited a-C:H film

Figure 9.1 shows the typical IR absorption spectra in the CH_n ($n = 1, 2, 3$) stretching vibration area of the deposited a-C:H film. This absorption band is composed of $\text{sp}^2\text{C-H}$ (3000 and 3050 cm^{-1}), $\text{sp}^3\text{C-H}$ (2890 cm^{-1}), $\text{sp}^3\text{C-H}_2$ (2850 and 2920 cm^{-1}), and $\text{sp}^3\text{C-H}_3$ (2870 and 2960 cm^{-1}). The assignments of these bands were summarised in Table 9.1. The integrated intensity I_H of this absorption band, defined by the following equation, is used to evaluate the concentration of bonded hydrogen in the film by IR absorption spectroscopy:

$$I_H = \int_{2700\text{ cm}^{-1}}^{3200\text{ cm}^{-1}} \frac{\alpha_w(\nu_w)}{\nu_w} d\nu_w \quad (9.1)$$

where ν_w is the wavenumber and $\alpha_w(\nu_w)$ is the absorption coefficient [198]. The bound hydrogen concentration n_H is given by the following equation using the integrated intensity I_H :

$$n_H = A_s \times I_H \quad (9.2)$$

where A_s is a normalisation factor proportional to the inverse of the absorption strength, and Fujimoto et al., reported this A_s is $1.0 \times 10^{21}\text{ cm}^{-2}$ [199]. Also, the atomic hydrogen concentration N_H can be approximately estimated by the following equation:

$$N_H = \frac{n_H}{n_H + \left(\frac{d_f - M_H \times n_H}{M_C} \right)} \quad (9.3)$$

where d_f is the film density, and M_H and M_C are the mass of the hydrogen atom and carbon atom, respectively [198]. Figure 9.2.a shows the relation of film density d_f and integrated intensity I_H . The film density decreased from 1.7 g/cm^3 to 1.4 g/cm^3 with increasing I_H , while the bonded hydrogen concentration n_H increased from $5.0 \times 10^{21}\text{ cm}^{-3}$ to $8.7 \times 10^{22}\text{ cm}^{-3}$ with increasing I_H . Figure 9.2.b shows the hydrogen atomic concentration N_H calculated by Eq. (9.3).

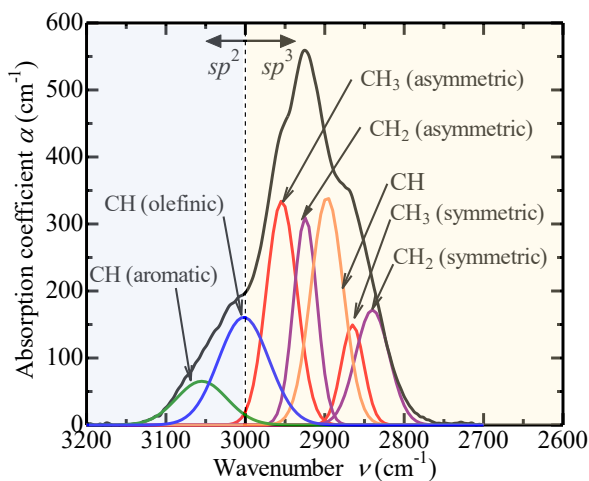


Figure 9.1. Typical IR absorption spectrum of the deposited a-C:H film. Source: own elaboration based on [198]

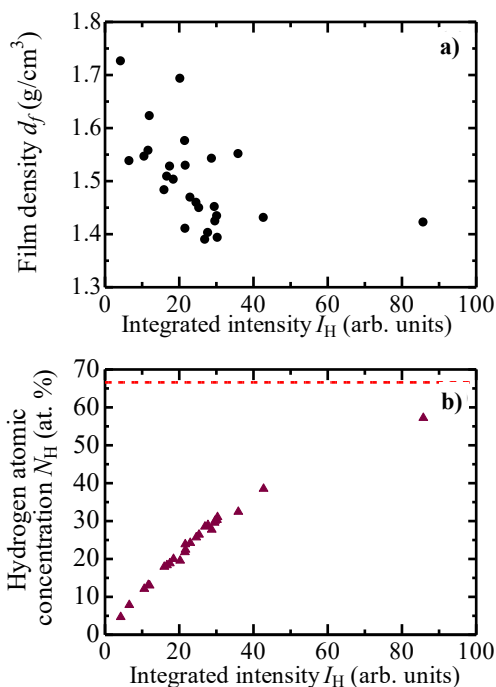


Figure 9.2. a) Relationship between film density and integrated intensity; b) Relationship between hydrogen atomic concentration calculated by Eq. (3). The red dashed line indicates the maximum value of $N_H = 66.6$ at.% at which the hydrogenated carbon could form a film. Source: own elaboration

Table 9.1 Assignments of IR absorption spectrum

Bonding configuration		Wavenumber (cm ⁻¹)
sp ³	CH ₃ asymmetric	2962 ± 10
	CH ₃ symmetric	2872 ± 10
	CH ₂ asymmetric	2926 ± 10
	CH ₂ symmetric	2853 ± 10
	CH	2890 ± 10
sp ²	CH olefinic	3040-3010
	CH aromatic	3030

The N_H increased from 5 at.% to 57 at.% with increasing I_H [197, 198]. For investigation of the fraction of CH_n bonds, the IR spectra of a-C:H films were deconvoluted with seven Gaussian curves corresponding to each of the bonding configurations in Table 9.1. As a result, the sp³-CH₃ bonding configuration increased with increasing I_H , while sp²-CH slight decreased [198]. Also, the spin density of a-C:H film was decreased with increasing I_H . From the IR deconvolution results, it is thought that this decrease in spin density is due to the termination of dangling bonds by hydrogen atoms. Therefore, it is considered that the decrease in the film density with the increase in integrated intensity is due to the increase in the termination of dangling bonds in the film by hydrogen. We could obtain the a-C:H films with a wide range of properties from dense films with low hydrogen content to polymer-like with high hydrogen content.

Optical Properties

Figure 9.3 shows the optical Tauc gap E_{Tauc} of films with different I_H [197]. As shown in Figure 9.3, E_{Tauc} changed from 0.7 to 2.7 eV with increasing I_H . The schematic diagram of density of state for a-C:H film is shown in Figure 9.4 [200]. Figure 9.4.a shows DOS at low hydrogen concentration and 9.4.b at high hydrogen concentration. The π and π^* states of sp² sites lie within the band between the σ and σ^* states. The optical and electrical properties depend on the arrangement of π states because of the π - π^* gap is lower than σ - σ^* gap. The defect state due to unpaired electron locates around the Fermi level. Also, this defect level affects the optical and the electrical properties. As mentioned in Figure 9.2, the sp³ configuration increases with I_H , while the sp² configuration decreases. The dangling bonds concentration in the film decreases with increasing I_H due to the compensation of them by hydrogen atoms.

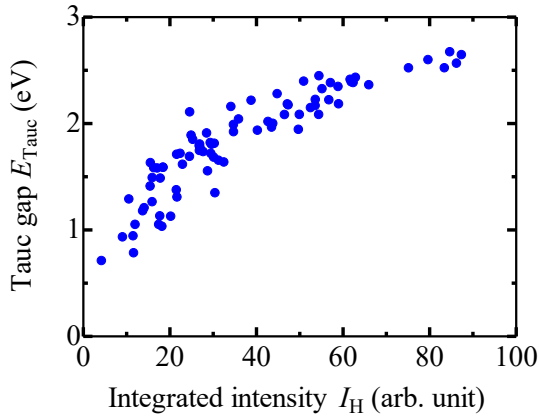


Figure 9.3. Relationship between optical gap E_{Tauc} between integrated intensity I_H for a-C:H films. Source: own elaboration based on [197]

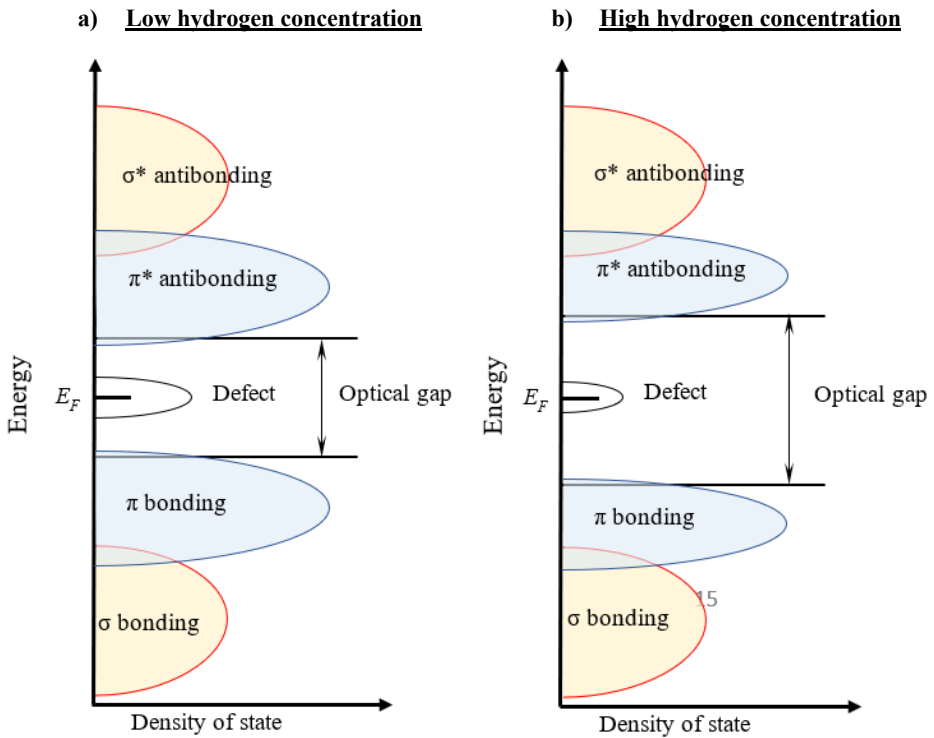


Figure 9.4. Schematic diagram of density of state (DOS) for the gap region a-C:H film. The optical gap depends on the size of each sp^2 cluster and the density of defect level. Source: own elaboration based on [200]

Therefore, it is considered that the size of sp^2 cluster with low hydrogen concentration is smaller than that with high hydrogen concentration, and the defect level decreases with increasing hydrogen concentration due to the decreases in the dangling bonds. For these reasons, the optical gap would be larger in the higher hydrogen concentration film (Fig. 9.3). Also, the hardness of a-C:H films decreased rapidly from 13.0 GPa to 0.7 GPa with increasing I_H . The a-C:H films change continuously from a hard to a soft film with increasing the concentration of hydrogen n_H . These results suggest that the carbon network configuration in the a-C:H film is controlled continuously with n_H [197].

Electrical Properties

Figure 9.5 shows the permittivity ϵ_r with different integrated intensity I_H . The permittivity decreased from 5.6 to 2.3 with increasing I_H . From the result of film density as shown in Figure 9.2.b, this decrease in permittivity corresponds to a decreasing tendency in film density.

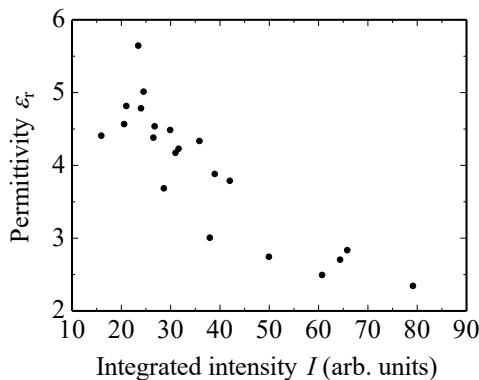


Figure 9.5. Relation of the permittivity ϵ_r and the integrated intensity I_H . Source: own elaboration based on [200]

The increase in the concentration of bonded hydrogen in the film causes the free volume to increase due to the termination of dangling bonds, which is thought to form a porous-like structure in the film. As a result, it is considered that the free volume increases with decreasing film density, and the permittivity is decreased. The electrical resistivities decreased from $10^{13} \Omega\cdot\text{cm}$ to $10^{15} \Omega\cdot\text{cm}$ with increasing I_H . The resistivity is more than $10^{13} \Omega\cdot\text{cm}$ even in the lowest case, which is sufficiently high. The a-C:H film also has chemical inertness; these results indicated that a-C:H thin films have potential as low- k materials.

Effects of Iodine Doping

Figure 9.6 shows the schematic diagram of the iodine doping system. During the doping process, the film and iodine were heated at 100°C. The solid iodine sublimates, and the sample was exposed to iodine vapor, and then iodine was doped into the a-C:H film.

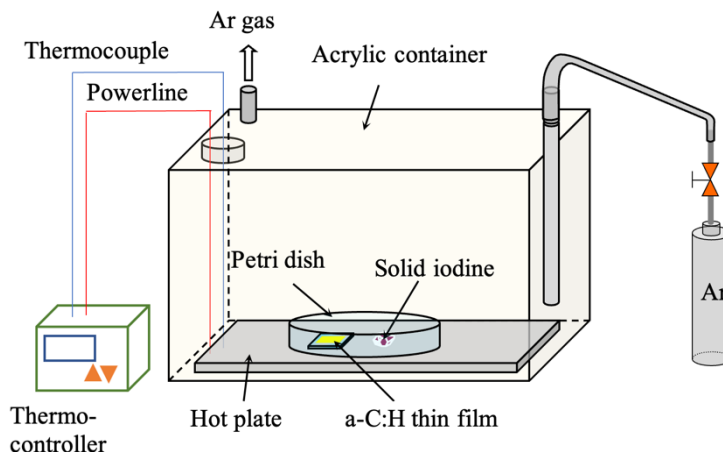


Figure 9.6. Schematic diagram of iodine doping system. Source: own elaboration

a) Before iodine doping



b) After iodine doping

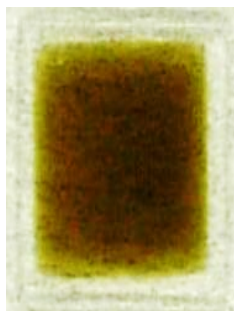


Figure 9.7. Photograph of the a-C:H film on fused silica substrate. Before doping, the film is transparent due to the high optical gap. Source: own elaboration

Figure 9.7 shows photographs of a-C:H films with $I_H = 84$ before and after iodine doping. Before doping, the film was transparent and almost invisible due to the film having a high optical gap $E_{Tauc} > 2.5$ eV. After doping, the film was coloured brown-violet.

Figure 9.8.a shows the XPS spectra of the sample before and after iodine doping. After doping, Iodine related peaks, $I_{3p1/2}$ (873 eV), $I_{3p3/2}$ (744 eV), $I_{3d3/2}$ (629 eV), $I_{3d5/2}$ (617 eV), I_{4d} (48 eV) were observed. Figure 9.8.b shows the XPS

depth profile of the sample, the vertical line shows the iodine atomic composition ratio to carbon atom and the lateral line shows the sputtering time by Ar which corresponds to the depth from the sample surface. As shown in this figure, iodine atoms penetrated the film interior. From these results, Iodine atoms were doped successfully to a-C:H films.

Figure 9.9 shows the UV-Vis spectra of a-C:H film with $I_H = 80$ before and after iodine doping. After iodine doping, the absorption of the sample was increased in all wavelength ranges, and the strong peak appeared at around 290 nm, 380 nm. These two peaks correspond to I_3^- ions. Similar phenomenon was observed the iodine doped polymers [192].

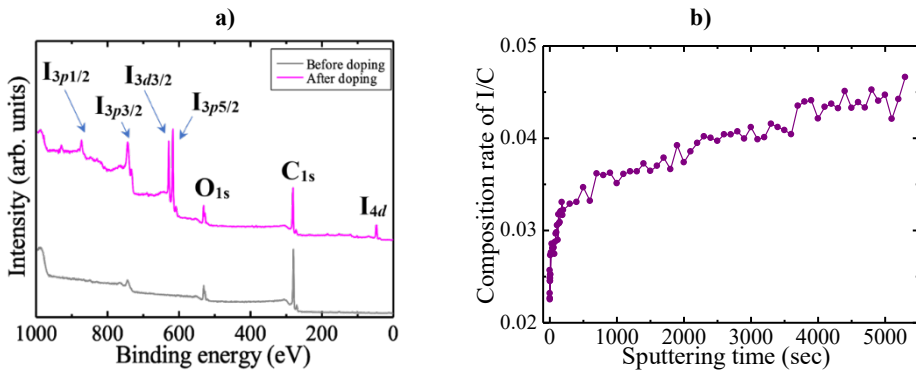


Figure 9.8. a) XPS spectra of a-C:H films before and after iodine doping, b) XPS depth profile for iodine doped a-C:H film. Source: own elaboration

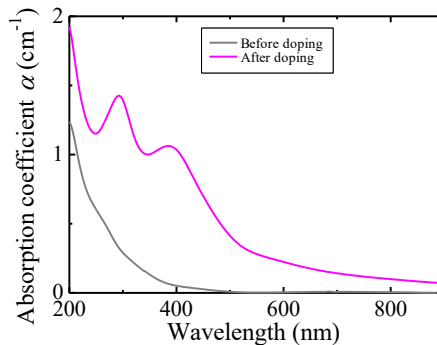


Figure 9.9. UV-Vis spectra of a-C:H film before and after iodine doping. Source: own elaboration

Figure 9.10 shows the relationship between the changing optical gap and the integrated intensity of a-C:H films. The largest change in the optical gap was a decrease from 2.6 eV to 0.9 eV in iodine doped a-C:H film with $I_H = 88$. These decreases in iodine doped a-C:H films may be due to the formation of charge-transfer band between $\pi-\pi^*$ states in density of state shown in Figure 9.4.

As shown in Figure 9.10, the decrease in the optical gap increases with the I_H . As mentioned in the film density and the IR spectrum, the free volume increase due to the termination configuration increases with the I_H . It is thought that the low-density film with a large free volume is more easily doped by the relatively large molecule, such as I_2 or I_3^- . These results suggest that iodine doping into carbon films is more effective in films with high hydrogen concentration than in those with low hydrogen concentration.

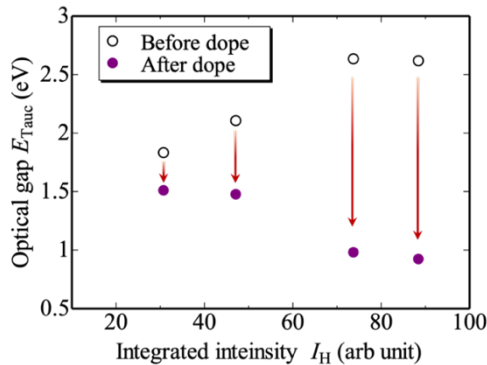


Figure 9.10. The changings of optical gap in a-C:H films before and after iodine doping. The arrows indicate that the change in the optical gap before and after iodine doping. Source: own elaboration

The resistivity of the iodine doped a-C:H film with $I_H = 88$ decreased from $5.5 \times 10^{11} \Omega \cdot \text{cm}$ to $8.9 \times 10^7 \Omega \cdot \text{cm}$ [192]. From these results, the charge transfer bands between the carbon-hydrogen network might be formed in a-C:H film and iodine molecules. It is considered that the donor-acceptor complexes are formed in the a-C:H film. These results showed that iodine is one of the promising candidates for doping elements to amorphous carbon films.

9.2. Advanced granular nanomaterials for nanoelectronics

Oleksandr Boiko

Introduction

The rapid development of nanoscience and nanotechnology in recent decades has completely changed the way we perceive our world. Modern technologies allow the creation of materials with completely new properties and the production of incredibly small, effective and ecological objects. The nanoscale of objects also shows properties that belong to the field of quantum mechanics. Some laws of our everyday reality, based on the principles of classical physics, do not work in the “nano-world”. Quantum mechanics and electrodynamics are the basis for the developing of new nanomaterials and devices.

Among the wide scale of nanostructures produced, binary nanostructured materials in the form of matrices, containing randomly distributed nanoparticles of the filler phase, stand out. After introducing these particles into the matrix, the material obtains completely different properties than the individual components. The properties of nanocomposites have prompted scientists and engineers to use these materials in many fields of science and technology.

One of the important directions of research related to nanocomposites is the study of the physico-chemical properties of various granular disordered systems, which include metal-dielectric nanocomposites [201–203]. These materials are most often presented as systems of grains or their clusters (clusters) or conductive layers of metallic origin with nanometre dimensions separated by a dielectric material. In this case, the size and shape of the particles as well as their mutual arrangement are usually random. Figure 9.11 shows an image of a granular nanocomposite layer with the composition $(\text{FeCoZr})_{42}(\text{Al}_2\text{O}_3)_{58}$ obtained by sputtering using high resolution transmission electron microscopy. The sputtering took place in an atmosphere of argon and oxygen. The figure shows that nanoparticles of the FeCoZr metallic alloy form clusters, marked in the figure with a dashed line, the so-called agglomerations. A characteristic feature of this structure is the relatively homogeneous distribution of metallic nanograins (darker areas). The size of metallic nanoparticles is approx. 6 nm.

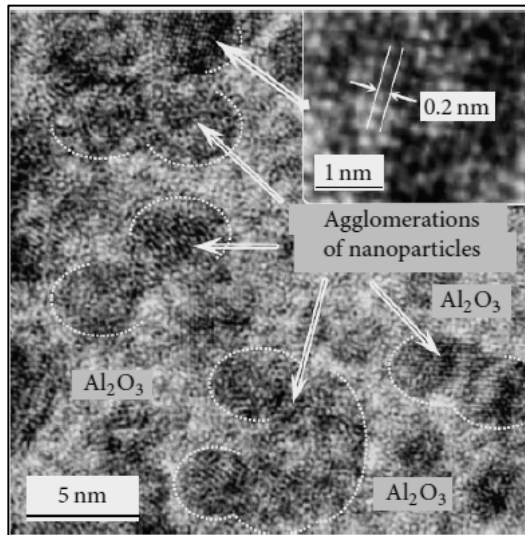


Figure 9.11. Image obtained using the high-resolution transmission electron microscopy method for a granular layer of a nanocomposite with a chemical composition $(\text{Fe}_{0.45}\text{Co}_{0.45}\text{Zr}_{0.10})_{42}(\text{Al}_2\text{O}_3)_{58}$. Source: reprinted from [205], which is under Attribution 4.0 Unported (CC BY 4.0) license

The paper [206] presents the formation of nanostructures in the shape of silver nanoparticles in nanomaterials with the structure $\text{Ag}_x\text{Zr}_{0.9}\text{Ni}_{0.1}\text{O}_y$, produced using the technique of simultaneous precipitation of a soluble compound (ZrNi) from a solution with a sparingly soluble deposit of Ag nanoparticles. The addition of silver nanoparticles ($x = 15.0$ at.%) to the composition results in the formation of uniform elongated spheroidal structures (wires) with a length of approx. $11 \mu\text{m}$ and a diameter of $5\text{--}15$ nm. As the silver content increases, the random distribution of nanowires and the heterogeneity of the surface of the $\text{Ag}_x\text{Zr}_{0.9}\text{Ni}_{0.1}\text{O}_y$ nanocomposite sample increases. Increasing the silver content in the nanocomposite increases the value of the real electric permeability component of the material. After the value of $x = 12.0$ at.% is exceeded, the material shows the electrical conductivity of the metallic type.

Percolation properties of M-D nanocomposites

In addition to the chemical composition and size of the metallic phase nanoparticles, the dielectric material and the surface morphology, the factors determining the physicochemical properties of metal-dielectric nanocomposites include the content of the metallic x phase and the dielectric phase ($100 - x$). Taking into account the content of the metallic phase x , nanocomposites with a granular structure can be arranged in three characteristic compartments: before the percolation threshold ($x < x_c$, Figure 9.12.a) – the dominant phase is the dielectric material (light blue colour); near the percolation threshold ($x \approx x_c$, Figure 9.12.b) and behind the percolation threshold ($x > x_c$, Figure 9.12.c) – the dominant phase is the material of metallic origin (dark grey colour). The x_c percolation threshold is the concentration of metallic nanoparticles at which in the dielectric matrix, a continuous conductive channel (percolation channel) connecting the measuring electrodes is formed from the contacting grains of the metallic phase.

Currently, a number of methods and mathematical algorithms used to calculate the x_c of nanomaterials are known. The most frequently used methods are those based on percolation theory describing the appearance of bonded structures (clusters) in random environments, consisting of separate elements [207] and on mean field theory consisting in replacing direct “particle-particle” interactions with averaged, effective system potential for each particle [208, 209]. The necessity to determine the critical factor x_c results from the fact that when passing through the percolation threshold, there is a radical change in the physicochemical properties of the nanocomposite. In the case of metal-dielectric nanocomposites, this is the transition from dielectric conductivity ($d\sigma / dT > 0$) to metallic type conductivity ($d\sigma / dT < 0$).

The methods of researching percolation phenomena in nanocomposites include the method of impedance spectroscopy, based on the determination of the dependence of the conductivity of nanomaterials σ on the content (concentration) of the metallic phase x [210]. Figure 9.13 shows schematically the dependence of the conductivity σ of metal-dielectric nanocomposites as a function of the filler content x . For small concentration values $x < x_c$, where the conductive nanoparticles are separated by a dielectric matrix, the conductivity is low, close to the conductivity of the dielectric matrix. In the range of concentration $x \approx x_c$, the conductivity increases rapidly reaching, compared to the small concentrations of x , much higher values. Such a sharp increase in conductivity means the formation of conductive percolation channels consisting of a metallic phase in the nano-composite structure, which allows an electric current to flow through the nanomaterial. For concentrations of $x > x_c$, a further mild increase in the conductivity value or its stabilisation is observed.

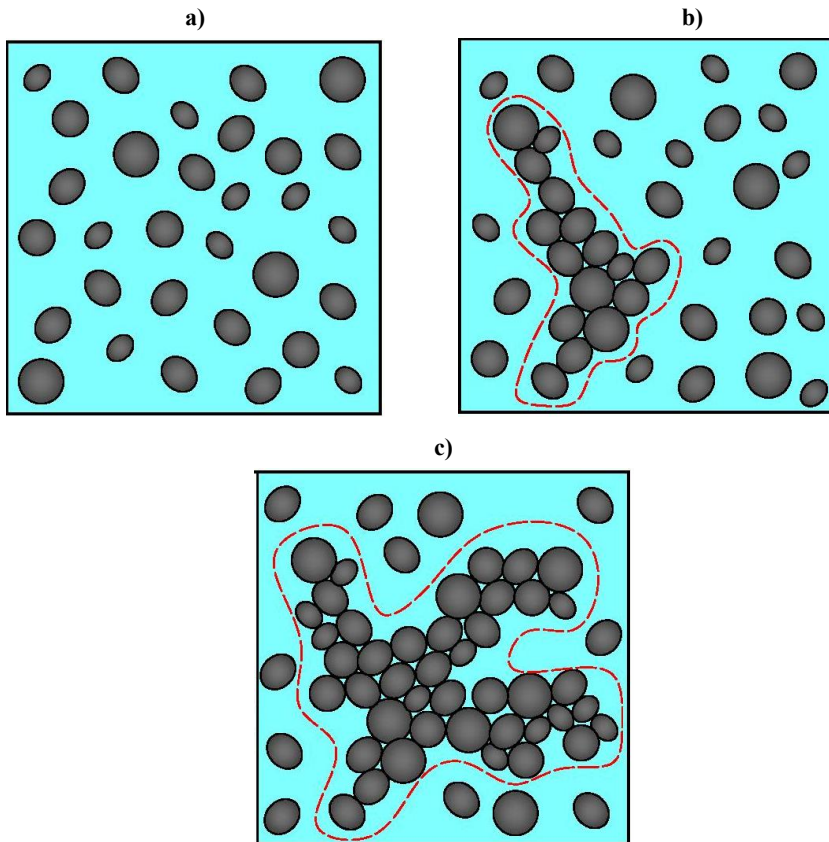


Figure 9.12. Phase-structure model of metal-dielectric nanocomposite: a) before x_c , b) near x_c , and c) above x_c . Source: own elaboration

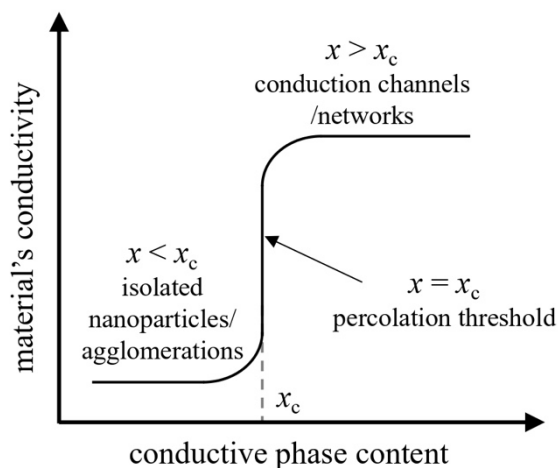


Figure 9.13. Schematic percolation curve for the conductivity of nanomaterials depending on the concentration of the filler phase. Source: own elaboration based on [211]

In summary, the x_c of nanomaterials is a very important critical factor determining the physico-chemical properties of nanostructures. It mainly depends on the method of producing nanocomposites, the type of matrix and conductive nanofiller (nanoparticles, nanotubes, nanofibers), its distribution in the dielectric matrix (creating clusters and conducting paths), the shape and size of nanoelements.

Measurements of electrical parameters

The subject of research in this chapter are granular ferromagnetic-dielectric alloy nanocomposites with the chemical structure $(\text{FeCoZr})_x(\text{PZT})_{(100-x)}$, where the abbreviation PZT stands for ferroelectric ceramics with a chemical composition $(\text{Pb}_{81}\text{Sr}_4(\text{Na}_{50}\text{Bi}_{50})_{15}(\text{Zr}_{57.5}\text{Ti}_{42.5})\text{O}_3)$, while x means the content of the elements of the metallic phase. Nanocomposites are produced by sputtering using a mixture of argon and oxygen ions with different partial pressures. These materials contain FeCoZr alloy nanoparticles randomly distributed in a PZT ferroelectric ceramic matrix. The manufacturing process along with the parameters of the synthesis, the station and the targets used are described in detail in [212, 213]. For the measurement of electrical properties, samples of nanocomposites with x ranging from 39.9 at.% to 74.6 at.% were used. The thickness of the tested layers has been defined in the range of approx. 0.5 to approx. 1.6 μm . The nanomaterial layers were deposited on rectangular dielectric glass-ceramic substrates with a thickness of 0.6 mm and cut into samples 2 mm wide and 10 mm long. An example view of the sample is shown in Figure 9.14 and the test station – in Figure 9.15 respectively.

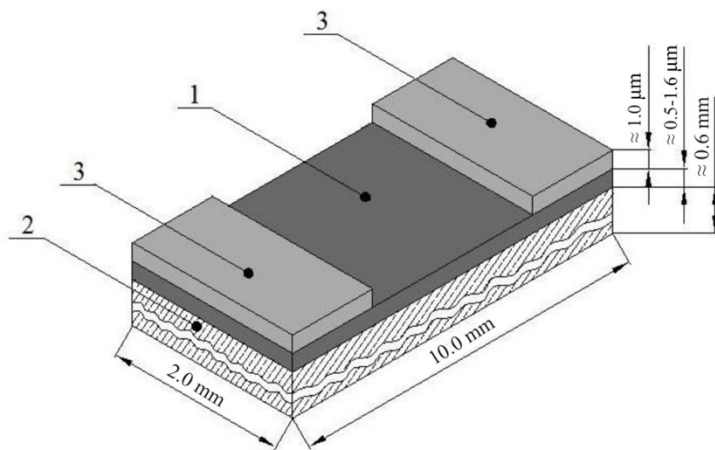


Figure 9.14. View and dimensions of $(\text{FeCoZr})_x(\text{PZT})_{(100-x)}$ nanocomposite sample: 1 – nanocomposite layer, 2 – glass-ceramic substrate, 3 – silver contacts. Source: own elaboration

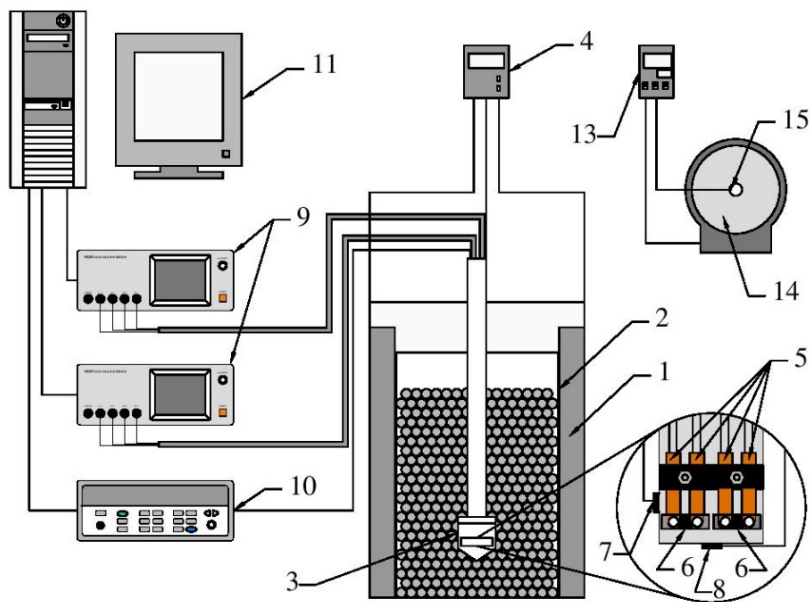


Figure 9.15. Measurement station: 1 – cryocooler, 2 – heating element, 3 – sample holder, 4 – temperature regulator, 5 – measurement probes, 6 – samples, 7 – temperature sensor, 8 –PT-100 temperature sensor connected to the regulator (4), 9 – impedance meter, 10 – temperature measuring device, 11 – laboratory computer, 13 – furnace temperature regulator, 14 – furnace for sample annealing, 15 – thermocouple. Source: own elaboration

The parameters measured during the tests were: dielectric loss coefficient $\text{tg}\delta$, phase shift angle φ , capacitance C_p and resistance R_p , measured in a parallel equivalent scheme. These parameters were measured by digital impedance meters (9) in the measuring temperature range 77–373 K in 5 K steps for selected frequencies in the range of 50–5 MHz. The temperature of the samples was recorded with an accuracy of ~ 0.05 K by a PT-100 sensor (7) connected to a temperature meter (10). The nanocomposite samples were attached in a metal container (3) as shown in the enlargement of Figure 9.15. Temperature control in the range of 77–373 K was done with the use of a regulator (4) connected to a flexible heating element (2), which was placed on the inner walls of the cryostat. After the measurement cycle was completed, the test samples were annealed in a tube furnace (14) for 15 minutes. The annealing temperature range was chosen from 398 K to 873 K with a 25 K step between each annealing.

After the annealing, a full measurement cycle was performed from the very beginning in order to determine the temperature and frequency characteristics of the electrical parameters of the nanocomposites. Based on the resistance measurements and the dimensions of the layers, the resistivity ρ_{nc} and the conductivity σ were calculated. For the measured and calculated parameters, the frequency-temperature spectra were determined. After numerical analysis, the nanocomposite samples were subjected to thermal treatment using an isochronous annealing system (Figure 9.15, elements 13–15).

Conductivity measurements

Using the measurement station presented in Figure 9.15, the conductivity tests of $(\text{FeCoZr})_x(\text{PZT})_{(100-x)}$ samples produced with a beam of low oxygen ions pressure (2.0×10^{-3} Pa) were carried out. Exemplary measurement results are presented in Figures 9.16–9.22. The measurements were performed for measurement temperatures in the range of 133–368 K, and in the frequency range of 50– 10^5 Hz.

In Figure 9.16.a, we can observe the temperature dependence of the NC conductivity $(\text{FeCoZr})_{39.9}(\text{PZT})_{60.1}$. The conductivity increases with increasing measuring temperature by almost an order of magnitude. Such conductivity responses to temperature influences are typical for dielectrics.

We can also observe a weak dependence of the conductivity to the frequency $\sigma(f)$. For the temperatures T_p below 323 K, the frequency dependence of the conductivity is almost constant, while for rest of T_p range a slight increase in the value of about 0.5 order is observed. A similar situation can be seen in Figure 9.16.b. This fact indicates a dielectric nature of the tested samples. On the other hand, in Figure 9.17, a slightly different behaviour of the $\sigma(f)$ characteristic is noticed. The conductivity increases non-linearly in the whole measuring frequency range.

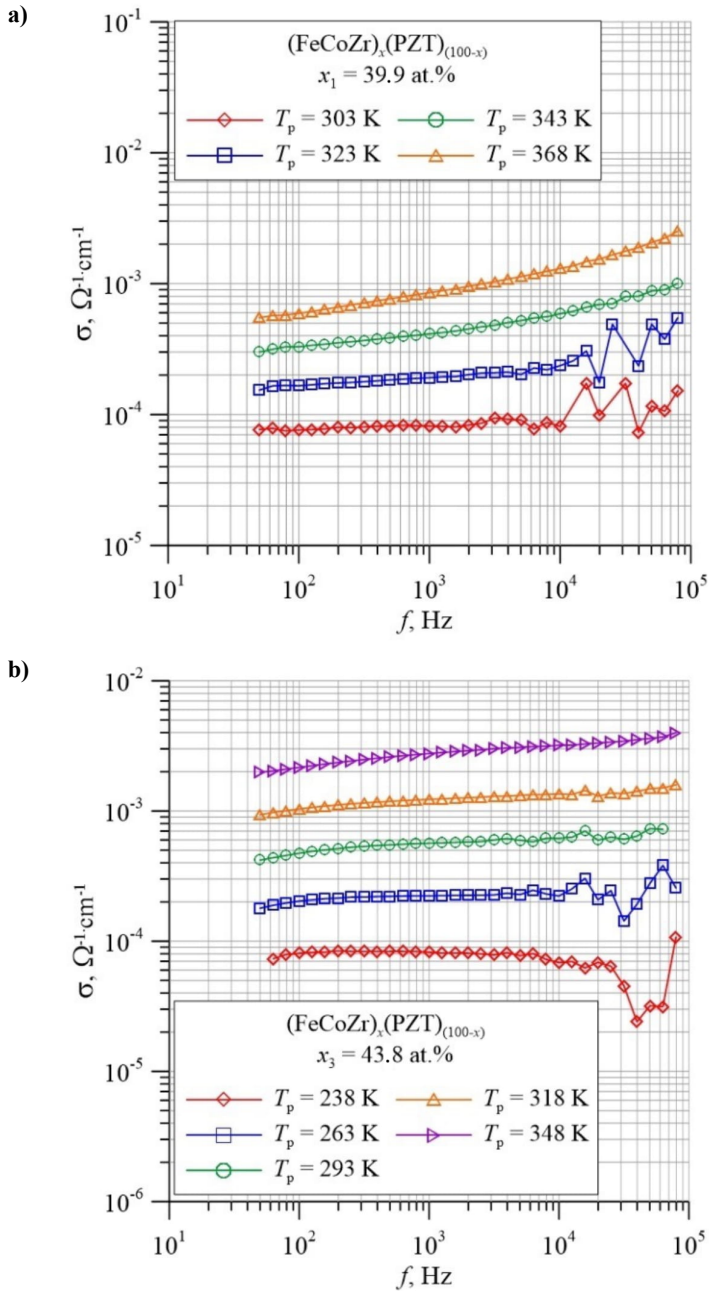


Figure 9.16. Conductivity vs. frequency for $(\text{FeCoZr})_x(\text{PZT})_{(100-x)}$ sample with: a) $x_1 = 39.9$ at.%, and b) $x_1 = 43.8$ at.% measured directly after preparing for the selected temperatures T_p . Source: own elaboration

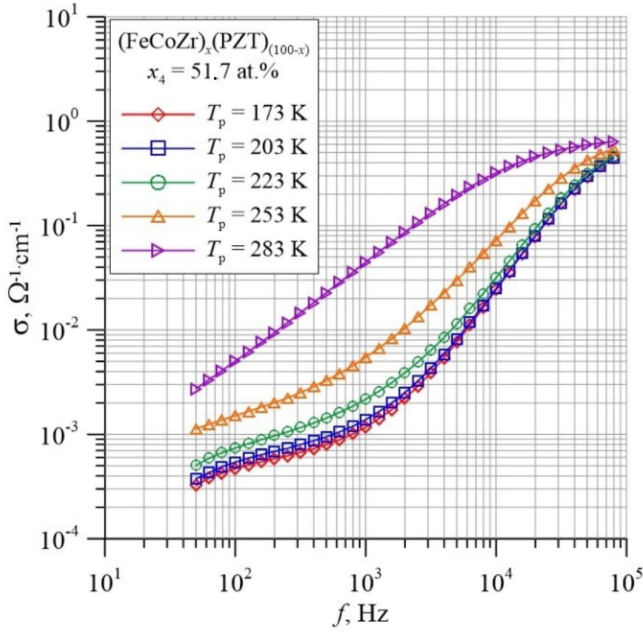


Figure 9.17. Conductivity vs. frequency for $(\text{FeCoZr})_x(\text{PZT})_{(100-x)}$ sample with: a) $x_1 = 51.7$ at.%, measured directly after preparing for the selected temperatures T_p . Source: own elaboration

The influence of the temperature T_p on the electrical conductivity in nanocomposites for specific temperature ranges can be described by the relationship [214]:

$$\sigma = \sigma_0 \cdot \exp\left(-2 \cdot \beta_r \cdot \alpha_r \cdot r_{nc} - \frac{\Delta E_\sigma}{kT_p}\right), \quad (9.4)$$

where: σ_0 – material's constant, ΔE_σ – activation energy of conductivity, r_{nc} – distance between adjacent potential wells, α_r – value close to the reciprocal of the location radius of the hopping electron (the so-called Bohr radius), β_r – numerical factor. A completely different situation was noticed in the case of samples with $x \geq 57.6$ at.%. Figure 9.18.a shows the frequency dependencies of the conductivity $\sigma(f)$ of a nanocomposite with $x_6 = 57.6$ at.%. The conductivity does not show dependence on the frequency at the range of $50 \leq f \leq 10^4$ Hz, while after exceeding 10^4 Hz a weaker (for temperatures $T_p \leq 198$ K) and stronger (in the case of $T_p > 198$ K) frequency dependence is observed. From the Figure, we can also observe the decrease in conductivity while temperature T_p increases. This fact indicates the metallic type of electric conduction in the nanocomposite. Figure 9.18.b shows the frequency dependency of the conductivity of the sample with $x_9 = 74.6$ at.%.

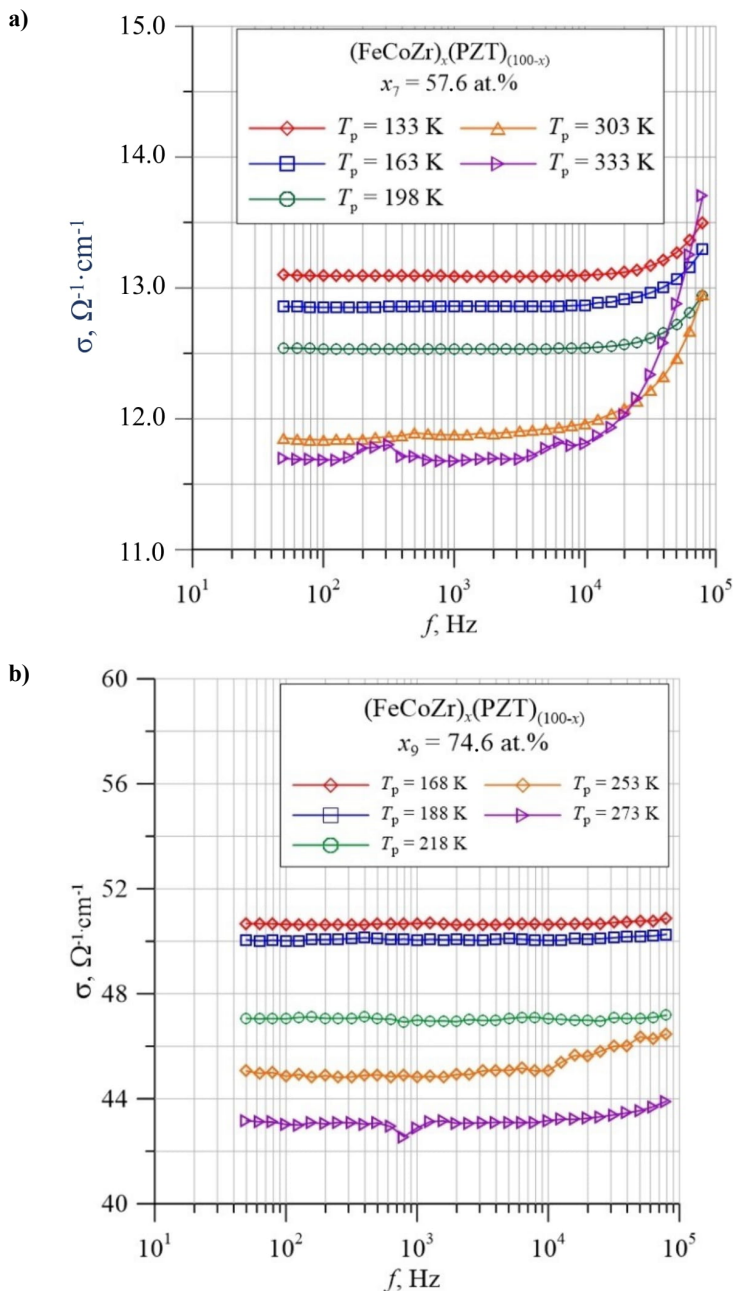


Figure 9.18. Conductivity vs. frequency for $(\text{FeCoZr})_x(\text{PZT})_{(100-x)}$ sample with: a) $x_1 = 57.6$ at.%, and b) $x_1 = 74.6$ at.% measured directly after preparing for the selected temperatures T_p . Source: own elaboration

It is also possible to observe the metallic type of conduction in nanocomposites for the entire range of measurement temperatures in the Figure. Conductivity dependence from Figure 9.18 is typical for metal-dielectric nanocomposites metallic phase contents above the percolation threshold. Taking into account the analysis of Figures 9.16 and 9.17, it can be concluded that the value of x_c lies in the range of $51.7 < x < 57.6$ at.%. In order to determine the exact value of x_c , ten nanocomposite samples of $(\text{FeCoZr})_x(\text{PZT})_{(100-x)}$ for x ranging from 39.9 to 88.4 at.% have been tested. On the basis of the measurements, the dependence of the conductivity on the content of the metallic phase was determined (Figure 9.19).

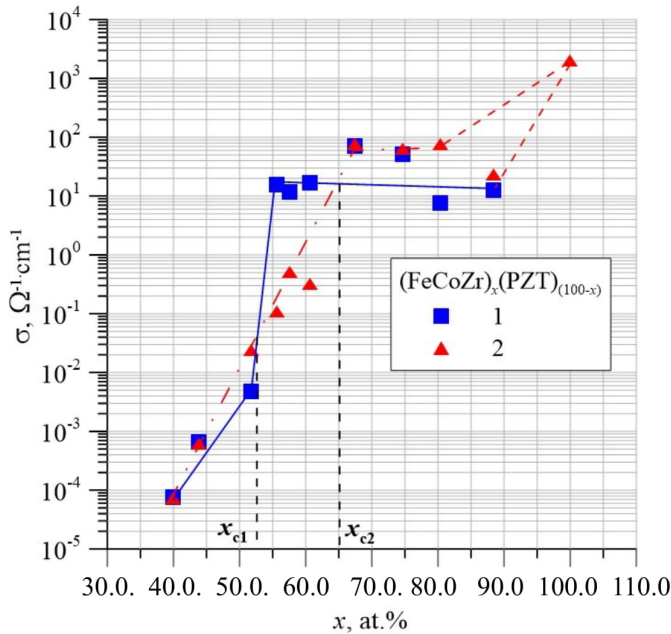


Figure 9.19. Conductivity σ vs metallic phase content x : 1) measured directly after preparing, and 2) measured after the annealing in 448 K. Source: reprinted from [219] after obtaining the authors' permission

For nonannealed nanocomposites in the first section ($x \leq 51.7$ at.%), an increase in conductivity by approx. two orders of magnitude was noticed. In the second section ($51.7 < x \leq 55.5$ at.%) the rapid increase in conductivity by almost four orders of magnitude can be seen. This is due to the passage through the percolation threshold, which is, as shown in Figure 9.19 $x_{c1} \approx (53.5 \pm 2)$ at.%. Such a hop in conductivity indicates the formation in the material structure $(\text{FeCoZr})_x(\text{PZT})_{(100-x)}$ a conductive percolation channels consisting of contacting FeCoZr nanoparticles, followed by the flow of electric current between the electrodes. In Figure 9.19, the solid blue line shows the approximation

of the $\sigma(x)$ relationship for nanocomposites immediately after their production. After annealing at 448 K, the course of $\sigma(x)$ changes radically. In the area of x concentration from approx. 55.0 at.% to approx. 65.0 at.%, the conductivity decreases by almost two orders of magnitude, remaining almost unchanged in the areas of lower and higher contents of the metallic phase. This shifts the percolation threshold to $x_{c2} \approx (65.0 \pm 2)$ at.%. It is related to the oxidation of the surface of the FeCoZr metallic nanograins as a result of thermal treatment of samples in the air, which reduces the conductivity of the annealed nanocomposite in the area of average x content.

Capacitive properties of metal-dielectric nanocomposites

The nanocomposite $(\text{FeCoZr})_{51.7}(\text{PZT})_{48.3}$ was chosen as an example to describe the capacitive type properties that exist in granular metal-dielectric nanocomposites below the percolation threshold. Figures 9.20 and 9.21 show the frequency characteristics of the phase shift angle $\varphi(f)$ and capacity C_p . Based on this data, it can be stated that the material shows capacitive character in the entire frequency range which is evidenced by the negative values of the phase shift angle φ . Moreover, in the case of the curves obtained for temperatures 81–128 K in the flow frequency range (50–1000 Hz), almost ideal capacitive nature when $\varphi \approx -90^\circ$ can be observed.

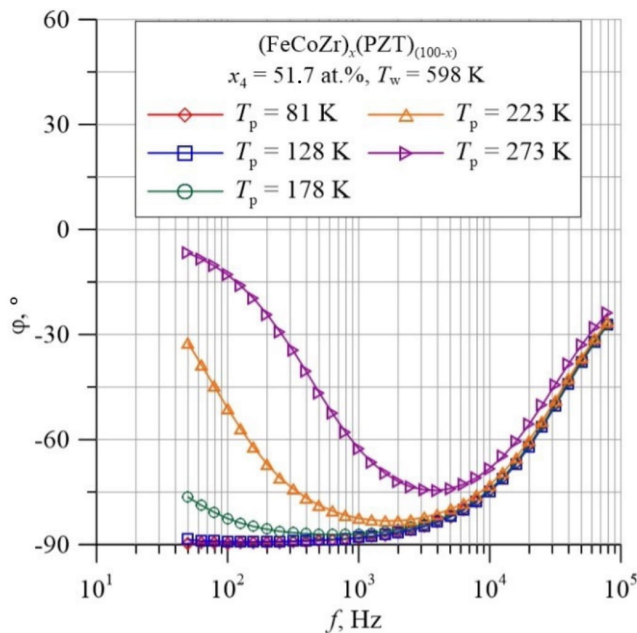


Figure 9.20. Phase shift angle vs frequency characteristics for the sample $x_4 = 51.7$ at.% annealed in 598 K for the selected T_p . Source: own elaboration

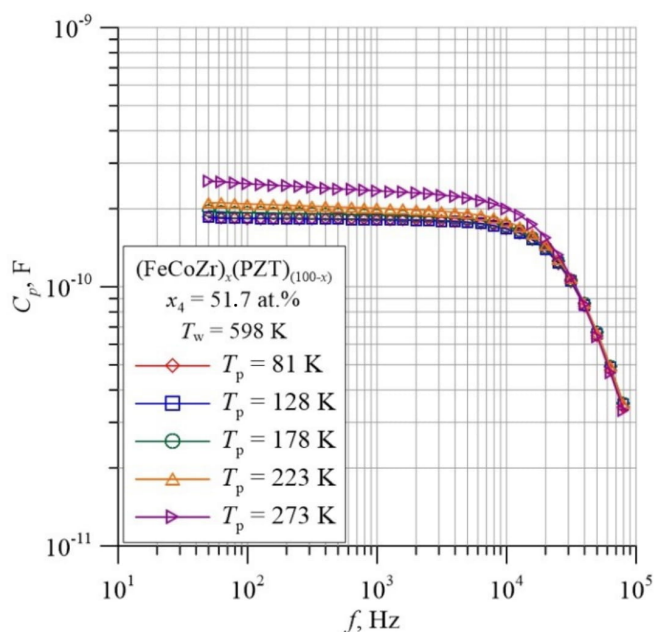


Figure 9.21. Capacity C_p vs. frequency f characteristics for the sample $x_4 = 51.7$ at.% annealed in 598 K for the selected T_p . Source: own elaboration

The above-presented results of the research on the effect of annealing on the nanomaterial capacity $(\text{FeCoZr})_{51.7}(\text{PZT})_{48.3}$ allowed preparation of a patent application [215] presenting a method of manufacturing capacitors for integrated circuits. The essence of the method is the application of a nanomaterial layer with the composition $(\text{FeCoZr})_{51.7}(\text{PZT})_{48.3}$ by means of ion spraying on a substrate plate made of silicon, previously subjected to all the technological operations required to produce an integrated circuit. The layer is applied with a beam of argon and oxygen ions with specific partial pressures. Then, stabilizing annealing is carried out at the temperature of 325°C for 15 minutes. In this way, a capacitor with an increased capacity per unit area is obtained compared to the hitherto known methods. The advantageous effect of the invention is that it allows the production of high-capacity integrated circuits without additional increasing of the surface area of the entire circuit.

Inductive type of properties

The properties of the inductive type are accompanied with the positive values of the phase shift angles of the heat-treated nanocomposites in certain temperature ranges. Figure 9.22 shows the $\varphi(f)$ characteristics obtained for temperatures in the 103–263 K range. The vertical dashed line separates the two regions with opposite signs of the φ .

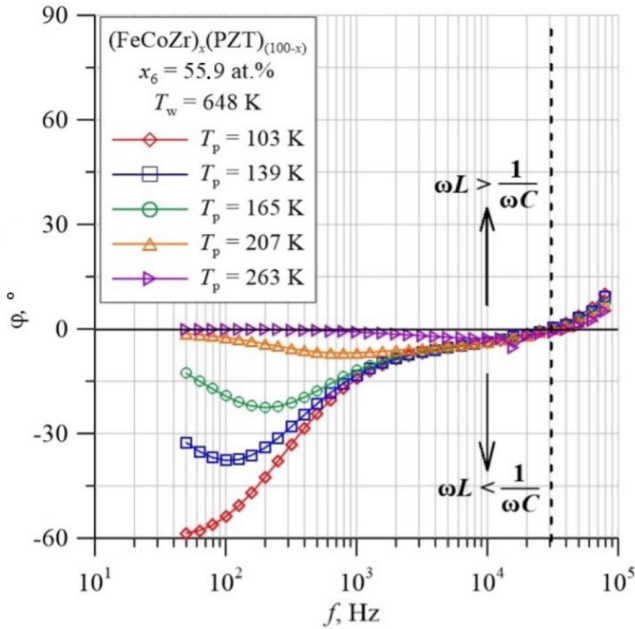


Figure 9.22. Phase shift angle φ as a function of frequency f $(\text{FeCoZr})_x(\text{PZT})_{(100-x)}$ with $x_6 = 55.9$ at.% annealed in 648 K. Source: own elaboration

This means that in the tested material, as in the series connection of passive elements R, L, C (Figure 9.23), the phenomenon of voltage resonance occurs at the frequency $f_{RS} = 4 \times 10^4$ Hz. For the area of negative φ , the inequality is satisfied:

$$\omega \cdot L_s < \frac{1}{\omega \cdot C_s} \quad (9.5)$$

This indicates the capacitive nature of the nanocomposite substitute circuit. For the frequency $f < 10^3$ Hz, the temperature dependence of the curves of the phase shift angle was observed.

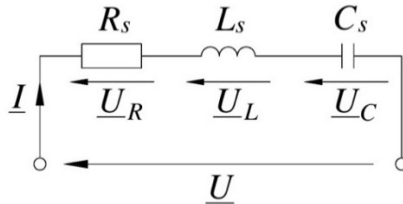


Figure 9.23. Equivalent replacement circuit for the nanocomposite during the voltage resonance (elements in series): R_s – resistance, L_s – inductance, C_s – capacitance, I – flow current, U – AC voltage on the electric contacts. Source: own elaboration

When the characteristic $\varphi(f)$ passes through the value of $\varphi = 0^\circ$ for the equivalent nanocomposite circuit, compensation of the voltages on the capacitive components \underline{U}_C and inductive \underline{U}_L impedance takes place, i.e., $\underline{U}_C + \underline{U}_L = 0$. It follows that the voltage on the resistive component \underline{U}_R is equal to the voltage applied to the periphery \underline{U} , which means that the phase shift angle is zero. This occurs, as shown in Figure 9.24, with $f_{RS} = 4 \times 10^4$ Hz. During the resonance of voltages, the nature of the circuit R, L, C is defined as resistive, because for the inductance L_s and the capacitance C_s the equality occurs [216]:

$$\omega_{RS} \cdot L_s = \frac{1}{\omega_{RS} \cdot C_s} \quad (9.6)$$

then the resonant frequency can be written as:

$$f_{RS} = \frac{1}{2 \cdot \pi \cdot \sqrt{L_s \cdot C_s}} \quad (9.7)$$

In Figure 9.24, for the f_{RS} frequency, we can observe the local minima of the $C_p(f)$ waveforms, which are evidence of the above-described phenomenon. For the frequency $f < f_{RS}$, a rapid decrease in capacitance by almost four orders is visible, in the case of frequencies higher than f_{RS} , an increase in capacitance can be observed.

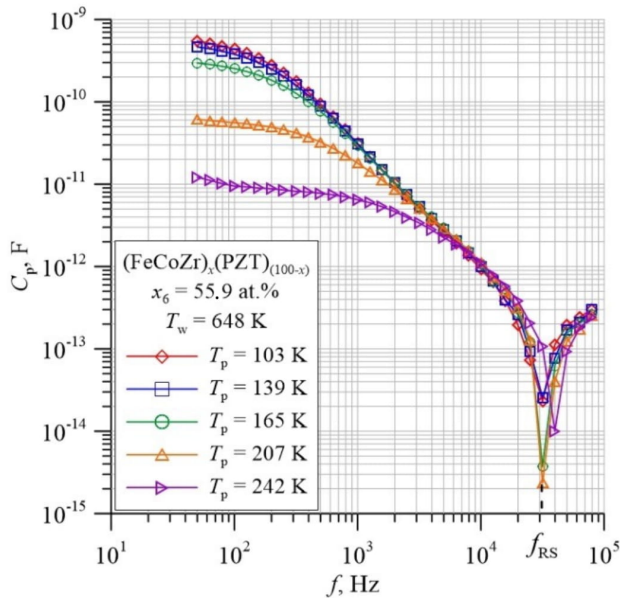


Figure 9.24. Capacity C_p as a function of frequency f for the $(\text{FeCoZr})_x(\text{PZT})_{(100-x)}$ sample with $x_6 = 55.9$ at.% annealed in 648 K. Source: own elaboration

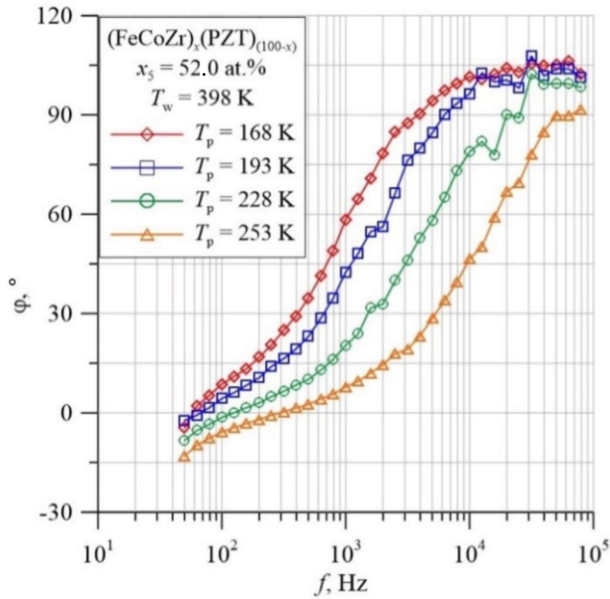


Figure 9.25. Phase shift angle φ as a function of frequency f of tested sample with $x_5 = 52.0$ at.% annealed in 398 K. Source: own elaboration

It is known that the element responsible for the inductive component of electrical conductivity is a coil, which consists of a core made of magnetic, diamagnetic or ferromagnetic material and a number of turns wound on the surface of the core [217]. In the case of nanocomposites $(\text{FeCoZr})_x(\text{PZT})_{(100-x)}$, we can talk about the phenomenon of the so-called non-coil inductance, because the FeCoZr ferromagnetic core does not contain a winding. The electrical properties of nanocomposites indicate the possibility of their potential application as winding inductances in electronic circuits with a gigantic equivalent inductance $L \approx 20 \mu\text{H}$ [213, 218]. This situation is also observed in the case of layers with a similar structure, containing nanoparticles of FeCoZr or copper in matrices made of different dielectrics [201, 216]. The appearance of positive values of φ in the $(\text{FeCoZr})_x(\text{PZT})_{(100-x)}$ layers can be explained by the complexity of the equivalent scheme describing the conductivity caused by the jump mechanism of electric transport. As was found earlier in [219], the mechanism of charge exchange in the tested materials was defined as hopping conductivity. It means that each electron's jump from the neutral potential well (metallic nanoparticle) to the neighbouring one stays there for a time of 10^{-13} s. while the order of electrons hops ranging from 10^{-3} to 10^{-7} s. Thus, for the frequency $f > f_R$ the backward hopping delay of $2\pi f\tau$ (where τ is a relaxation time) may exceed $3/2\pi$, which will lead to a positive phase shift and an experimentally observed inductive properties.

In Figure 9.25 positive phase shift angle values are noticed in almost the entire area of the measurement frequencies. In the area of low frequencies ($f < 500$ Hz), there are visible transitions of the $\varphi(f)$ curves through 0° with a further increase in the value of the phase shift angle until reaching the maximum, even exceeding $\varphi = 90^\circ$. The increase in the measurement temperature T_p causes the transition of the relation $\varphi(f)$ through the characteristic points of 0° and 90° to the area of higher frequencies. On the frequency dependence of the resistance R_p , shown in Figure 9.25, we can observe the local maxima of the experimental curves occurring at frequencies where the phase shift angle φ assumes the value of 90° . This corresponds to the phenomenon of current resonance in R, L, C circuits connected in parallel (Figure 9.27).

The condition for resonance is that the reactive components X_L and X_C of the impedance are equal:

$$\omega_{RP} \cdot L_p = \frac{1}{\omega_{RP} \cdot C_p} \quad (9.8)$$

hence the resonant frequency:

$$f_{RP} = \frac{1}{2 \cdot \pi \cdot \sqrt{L_p \cdot C_p}} \quad (9.9)$$

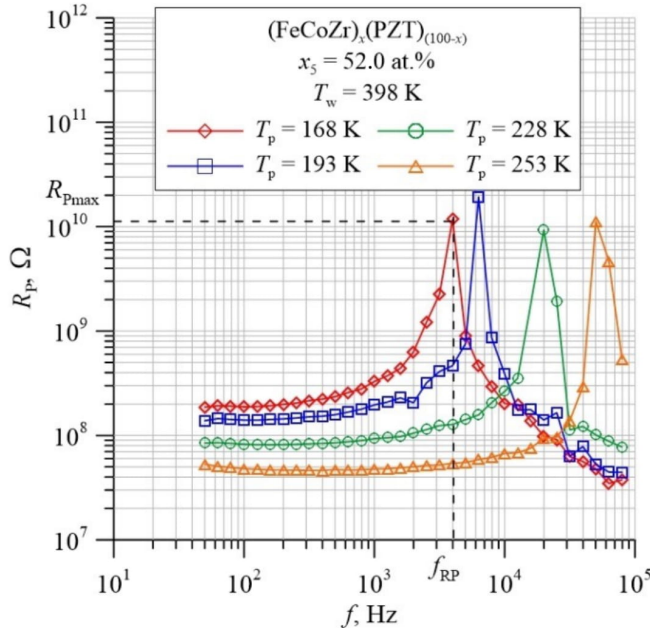


Figure 9.26. Resistance R_p as a function of frequency f of tested sample with $x_5 = 52.0$ at.% annealed in 398 K. Source: own elaboration

The geometric sum of the currents in the inductance branch \underline{I}_L and the capacitance \underline{I}_C is equal to zero ($\underline{I}_L + \underline{I}_C = 0$), and these currents are equal to the modulus ($\underline{I}_L = \underline{I}_C$). The circuit impedance is resistive (R_p) and tends to its maximum R_{pmax} (see maxima of the experimental waveforms in Figure 9.26), with the current \underline{I} in the circuit reaching its minimum value. The analysis of literature data related to the occurrence of resonance phenomena in granular metal-dielectric nanocomposites and information contained in the electrical engineering literature [216, 220, 221] showed that a special case of current resonance occurs in nanocomposites.

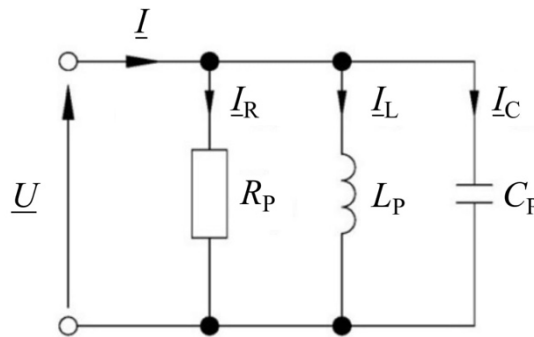


Figure 9.27. Parallel equivalent connection of R , L , C elements. Source: own elaboration

According to the literature, the value of the shift angle between the current \underline{I} and the voltage \underline{U} of the resonant circuit composed of conventional (lumped) elements R , L , C , is $\varphi = 0^\circ$. In the case of the nanocomposite $x_5 = 52.0$ at.%, the current resonance occurs at $\varphi = 90^\circ$. This may be related to the method of measuring electrical parameters using an impedance meter. In the circuit shown in Figure 9.27, both the capacitive and inductive components are in opposite phases at the same time. Simultaneous measurement of these quantities is impossible; therefore, it is performed for the resultant reactive component.

Conclusions

Two types of AC properties of $(\text{FeCoZr})_x(\text{PZT})_{(100-x)}$ nanocomposites have been found – capacitive and inductive. The capacitive properties include changes in the capacitance of nanocomposites in a wide range of measurement frequencies and the capacitive nature of the conduction in materials consisting in the occurrence of negative values of the phase shift angle in the range of $-90 < \varphi \leq 0^\circ$. The properties of the inductive type were characterised by the presence of positive values of the phase shift angle φ , which proves the inductive nature of the conduction in the materials.

Nanocomposites show the phenomena of current and voltage resonances. The phenomenon of voltage resonance consists in the occurrence of local minima on the characteristics $C_p(f)$ for the resonance frequencies f_{RS} , in which the phase shift angle takes the zero value. The phenomenon of current resonance is observed in the case of f_{RP} frequencies where $\varphi = 90^\circ$.

The observed properties indicate numerous applications of the tested NCs in electronic devices from macro- to nanoscale, i.e., microcapacitors for decoupling, filtering, and energy storage applications, magnetic storage and gas sensor elements, and microwave antenna electronics.

10. Environmentally friendly electricity management

Marcin Buczaj

Introduction

A modern electrical engineer is not a person who can only select and connect an electrical device or design and distribute electrical wiring in a building. Currently, an electrical engineer is required to have specialist knowledge in the fields of automation, mechatronics and computer science, as well as knowledge of the principles of economy, ecology, safety and rational use of electricity. Managing tasks related to the supply and settlement of electricity is a complicated process of selecting devices, their appropriate programming and use. An important tool in the engineer's work are also computer programs that enable diagnostics of the condition of devices, monitoring of processes and consumption of energy utilities. Additionally, the management of buildings uses analytical applications that enable computer simulations and tests.

Recent years have brought great socio-economic changes. The observed trend of switching to environmentally friendly energy sources and increasing energy prices translate into a change in the understanding of management systems in buildings. Environmentally friendly and economical management of the distribution and use of electricity in buildings is no longer a fashion, but rather a necessity, even. In many cases, the role of building administrators is assumed by people with knowledge in the field of energy management.

People whose strategy of operation is to understand the needs of users and to select an appropriate policy of servicing energy media, and as a result, to reduce the related costs. For the final cost of the building, use is also of great importance for the proper selection and knowledge of the rules for billing for the electricity supplied. All the above-mentioned aspects are connected with the general and basic concepts of the ideas of intelligent buildings and smart cities.

Supporting the process of managing the distribution and use of electricity is often carried out with the use of appropriate computer programs and analytical tools. Based on the information obtained, you can choose the most favourable electricity tariff, install your own source of electricity (photovoltaic panels, energy storage), check the current condition of the technical infrastructure, change the operating schedules of devices or replace a certain group of receivers with more energy-efficient ones (e.g., when light bulbs or fluorescent lamps are replaced with LED light sources).

Ideas of intelligent buildings and smart cities in the management of technical infrastructure in buildings

The ideas of Intelligent Buildings and more broadly, Smart Cities are inextricably linked with the rational use of the available environmental, technical and human resources. The completion of the set tasks is possible thanks to an efficient information management system supervised by competent people. One of the main goals of implementing the ideas of Smart Cities and Intelligent Buildings is the conscious and reasonable use of natural resources for the purpose of their economic, ecological and effective use [222].

The implementation of the assumed activities by the elements of the technical infrastructure of the building must be based on an effective system of identifying needs, determining the possibilities, analysing measurement and diagnostic data and an efficient process of transferring information between units and cells of the control system. These activities can be carried out by properly prepared, equipped and configured control and surveillance systems as well as specialised and professionally operating management personnel. The decision-making process is only a supplement to this system and is responsible for the reliable and rational use of the available technical, energy and economic means.

The management of general macro-scale processes in buildings is largely carried out by properly equipped and programmed automatic control systems and surveillance systems as well as information transmission systems. These systems make it possible to support human work or replace it in the decision-making process and to implement their own action algorithms based on the interpretation and analysis of the registered environmental and technical parameters. On a smaller scale, similar processes are carried out in each building. In such cases, it is possible to individually define the needs of a given group of recipients and fit a larger whole into the basic specific goals of the users, as well as to the currently implemented socio-political policy (e.g. a preference for selected technical or infrastructural solutions). Ensuring appropriate conditions for the functioning of modern buildings is associated with the constant supply of energy utilities to them. Electricity is the main source of energy supplied to buildings. Electricity enables the realisation and satisfaction of living needs, provides comfort and safety, and gives the opportunity to work and enjoy entertainment.

An important element of the process of using electricity is the supply of and settlements for electricity. Transmission of electricity between the source of electricity and the receiver is a process that requires the fulfilment of a number of technical, organisational and legal requirements. In the case of building structures, organisational and legal requirements are related to the selection of the electricity supplier, determination of the type of power supply system, selection of the method and place of connection of the recipient to the supplier's transmission network, determination of the degree of reliability

of power supply to the building and determination of the method of electricity billing between the supplier and the recipient. On the other hand, meeting the technical requirements is related to the construction of appropriate technical infrastructure enabling the flow of electricity between the point supplying a given facility and the receivers of this energy. Meeting the technical, organisational and legal requirements enables the proper, safe and reliable use of receivers and the proper operation of the electrical installation [223–225].

Effective management of electricity receivers in electrical installations can be manual, automatic or programmable. Manual control is the simplest control system for the operation of electrical devices. A manual control system only performs the on and off functions in devices. This is done using installation fasteners or by directly plugging the receiver plug into an electrical outlet. A higher technical level of control systems are automatic systems that implement control procedures, e.g. declared time schedules or triggered by an event. The functions are controlled by means of electronic circuits. More developed control systems, enabling the implementation of adaptive work algorithms, are programmable control systems. In these control systems, the device management system is equipped with a special HMI communication interface. Due to the availability of specialised measurement systems, sensors and detectors on the market, such systems allow the user to implement a more complex control and regulation process. The further development of control systems is related to the introduction of remote management systems to the control systems, cooperating with computer equipment and mobile devices, e.g., a smartphone. This combination of personal equipment with control systems extended the possibilities of management systems with previously unavailable functions and initiated the process of integration of control and supervision systems installed in buildings [222, 226, 227].

Programmable control systems, often called adaptive or intelligent, are systems equipped with decision-making elements (drivers) that enable the implementation of the assumed scenario. The program includes the assumed control algorithm and, on the basis of information coming to the control system and commands issued by the user, it can adjust the settings of the actuators to the current needs and requirements. Programmable control systems are systems that smoothly adjust the settings of actuators and the operating status of receivers to the current and often individual user requirements. The control process is often influenced by the situation in the facility and its surroundings.

The system work algorithm is often based on the analysis of archived data and an individual control program is selected on the basis of this information. Programmable control consists in adjusting the operating states of devices in given operating conditions to strictly defined requirements written by control rules. Often, the role of humans in such systems is limited to the programming process (creating control procedures) and the management process (introducing appropriate settings into the system).

In such systems, where the control process uses information in many systems and environmental parameters, and where the human role is limited to supervision, we can speak of integrated building automation systems implementing the assumptions of the idea of intelligent buildings.

Managing the functioning of control and surveillance systems

Control and surveillance systems is a term for automation systems with varying degrees of automation, enabling the implementation of tasks related to the use of the facility, maintaining the assumed climatic and technical parameters, ensuring safety and comfort of use and controlling the condition of system elements [226]. Control systems in buildings most often play an energy role. They are responsible for meeting the living needs of users and technological needs in the facility. These systems very often work in cooperation with people or are directly managed by them. Their main task is to ensure appropriate climatic, living and lighting conditions. Control systems also include systems for the distribution and optimisation of electricity consumption as well as production systems, especially related to renewable energy sources (e.g., photovoltaic panel systems) [227–231]. On the other hand, surveillance systems are systems that carry out tasks related to the monitoring of technical and environmental parameters and control of the condition of the entire facility. They perform functions related to management informing about the condition of technical infrastructure, safety and environmental conditions. Supervision systems are characterised by much higher requirements for system self-control and operational reliability. Supervision systems enable local or remote control over the managed area by system users. Supervision systems provide the user with the function of monitoring the current state of the facility (information functions) and the possibility of interfering with the current operating modes of individual system components, as well as insight into the tasks currently performed by the system (control functions). Often, to perform these functions, appropriately equipped computer equipment or other teletechnical devices are used. In modern automation systems, the function of managing the operation of control and supervision systems is not only about controlling the operation of a given device or group of devices. In contemporary automation systems, control and measurement processes also look at possible interactions between devices and systems working together and constituting the equipment and technical infrastructure of a building or field facility. Currently, by monitoring the operation of all systems, automation systems enable the analysis of the operating states of individual systems, detection of irregularities and optimisation of the control algorithm. Thanks to this, the control process is more efficient and faster, and in the case of buildings, it is possible to increase the comfort of use, increase work safety, often while reducing the operating costs of such installations. Meeting these guidelines is a recipe for building an

intelligent control system and implementing the principles of an intelligent building. An intelligent building is defined as a facility equipped with technologically advanced automatic control systems, often supported by computer equipment, which perform their tasks in the formula of an integrated system. What follows, the electrical installation constituting the structural equipment of such a building is an intelligent electrical installation. Intelligent electrical installation is a more extensive building automation system equipped with control algorithms that enable the fulfilment of the user's expectations in terms of use, safety, comfort and costs of building service. The computer hardware supporting the operation of an intelligent control system ensures supervision and management of the operation of such a system. The creation of an intelligent building is associated with the development of automation systems, the progressive process of integration of control systems, their availability and universality, and support for the control process of computer equipment. Such a technical connection of independent systems allows the control process to be carried out more efficiently [225, 226, 227, 232–234].

The concept of an intelligent building and its structural equipment is related to its classification. The classification determines the degree of its capabilities and functions as well as the scope of tasks performed. Due to the functional possibilities and the method of managing the control system, the following classes are distinguished [233]:

- no control systems;
- class 1 – no integrated management systems;
- class 2 – partial monitoring;
- class 3 – full monitoring;
- class 4 – full monitoring and partial central management;
- class 5 – full central management.

Based on the equipment of intelligent installations and the scope of tasks performed, the following categories of intelligent control systems are distinguished [233]:

- category A – full equipment – tasks related to the operation of property security systems and all building automation systems;
- category B – incomplete equipment – tasks of property security systems as well as heating, ventilation and air conditioning and lighting control systems;
- category C – limited equipment – carrying out tasks related to security and safety systems.

If, apart from the systems that perform the functions of automatic control, the technical infrastructure of the building structure also enables the management of the processes being carried out, then such a system may also be referred to as a building management system.

Characteristics of Building Management Systems

The Building Management System (BMS) is a system for managing technical and climatic functions as well as enabling the monitoring of technical and environmental parameters in a building. Most often, the BMS system covers heating, ventilation and air conditioning systems [235], lighting control systems as well as control and measurement systems related to the distribution of electricity, water and heat in the building. The processes of control and supervision of the BMS system include issues related to the distribution and production of electricity and heat in the building as well as the management of essential safety and supervision parameters. For the needs of the task, the system uses its own detection elements and external information (internet, crisis management centres). The idea of the BMS system resulted from the demand of building users and administrators for a computerised system that would enable management, processing and access to information about the condition of the building in one place [222, 225, 232–234]. The structure of the BMS system is presented in Figure 10.1. The functionality of the BMS system results from the implementation of tasks related to [222, 227, 228]:

- operation of the database with information about the facility and parts of the BMS system;
- current analysis of the climatic and technical parameters in the facility;
- registration and handling of alarms and incorrect states;
- self-diagnosis of BMS system elements;
- registration of time histories of technical parameters;
- registration of time courses of climatic parameters;
- the ability to generate reports;
- editing programs and time schedules;
- cooperation with alarm and security systems.

The following levels can be distinguished of the organisation of the BMS system [233, 234]:

- *management level* – grouping operator stations, giving the operator the ability to configure and monitor the entire system. In addition, at this level, data on the operation of a given installation are collected and archived;
- *level of automation* – system and hardware integration, mainly in a situation where several systems operating in different standards interact in an automated building. It consists of drivers, network devices and regulators processing information and implementing the algorithm;
- *detection and executive levels* – sensors, actuators and input/output elements, as well as regulators. Their task is to collect and process data and, consequently, to control the actuators directly influencing the implementation of the assumed tasks in an automated building.

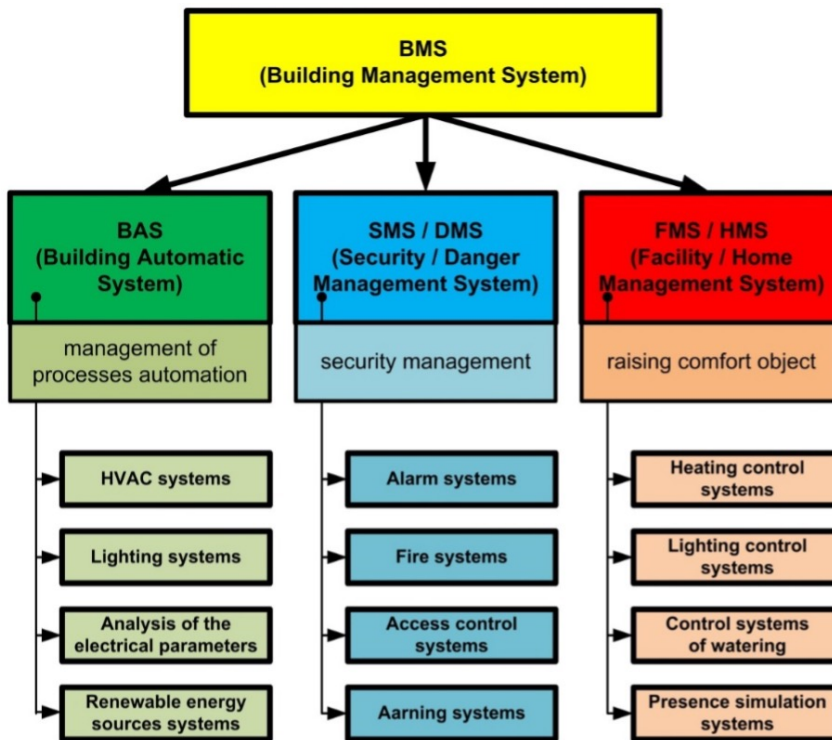


Figure 10.1. The structure of the BMS system. Source: reprinted from [222] after obtaining the authors' permission

With the appropriate technical infrastructure of the building and depending on the equipment of the system, the BMS system enables [222]:

- maintaining the set climatic parameters in the building;
- adequate exchange and circulation of air through ventilation systems installed in the building;
- management of the heat collection process in the ventilation process (heat recuperation);
- cooperation with RES systems that are part of the building's equipment;
- algorithmic, adaptive or individualised control of lighting systems (automatic, time, manual, light scenes);
- building safety supervision;
- reporting on operating conditions of devices in the facility;
- alerting about abnormal states and anomalies;
- ongoing communication with the user;
- remote control of devices and groups of devices in the building.

To control and manage the operation of devices and to ensure safety, control and surveillance systems adapted to the assumed user needs and the characteristics of the facility are used. Such systems are selected on the basis of information about the purpose of the facility, user preferences and technical capabilities of the system components. Their task is to create proper working conditions for the installed devices, enable the implementation of the assumed technological processes and ensure the required level of safety in the facility related to its use and area of operation.

The basic structures of the BMS system are supplemented with analytical programs enabling the determination of optimal settings for devices, the implementation of the diagnosis and forecasting functions, and the performance of calculations most favourable for economic reasons, the configuration of the equipment and the selection of methods and criteria for settlements.

Supporting the work of control and supervision systems users

Effective, and thus also ecological and economic use of the technical infrastructure of a building is associated with its rational use. The rational operation of the technical infrastructure systems largely lies in the setting of appropriate operating parameters of devices and the development of appropriate time work schedules adapted to the way the building is used. Such activities can be implemented in BMS system management programs.

An additional element conducive to pro-ecological activities in building management is ongoing analysis of the consumption of energy utilities supplied to the facilities. More and more often, energy media monitoring systems cooperate with BMS system programs. Energy media monitoring systems enable constant and ongoing supervision over the technical and operational parameters of the main electricity, heat, water and gas supply systems. These systems enable the detection of irregularities and failures and enable the transmission of messages about the occurrence of abnormal states to the system user.

The building management system is supplemented by analytical applications that enable the acquisition, registration, presentation, and in particular the processing of measurement data. Thanks to analysis of the recorded data, it is possible to adopt an appropriate building operation strategy, select the appropriate billing methods (e.g., electricity tariff), find weak points in the technical infrastructure of the building, determine the actual technical parameters of the operating systems or eliminate unfavourable phenomena (e.g., reduce the demand for networks, capacitive or inductive reactive power).

Currently, Lublin University of Technology uses such programs on several buildings. These programs usually operate in a non-integrated manner and are intended for the implementation of control and measurement processes in the building or analytical activities in scientific and research processes.

In these systems, the monitoring of technical parameters is carried out only to a certain extent for selected systems (types of media).

The following computer systems and programs are the programs used at Lublin University of Technology to manage and support the work of building users and administrators:

- the Siemens Desigo system to manage the functioning of the BMS system [236];
- F&F Meternet PRO software for monitoring the consumption of energy utilities [237];
- Numeron's Energia4 software for analysing measurement data and generating reports and defining strategies for cost-effective media settlement [238].

The management of the functioning of the technical infrastructure systems of the building is carried out with the use of the BMS system program. This system works on several levels of access. In the case of the lowest access level, the user level, it is possible to monitor the operation of individual systems on an ongoing basis and to perform the settings control function and to read the current operating parameters (Figure 10.2). At the medium access level, the level of the system manager, it is possible to determine the operating parameters (time schedules) and the presentation of time characteristics. Thanks to this, it is possible to check the policy pursued with regard to the use of individual systems (Figure 10.3). The top access level, the system administrator level, allows you to enter records and control procedures and access system configuration data.

An important element of the system is the alert generator, which enables system users to familiarise themselves with the currently registered irregularities in the operation of individual systems (Figure 10.4).

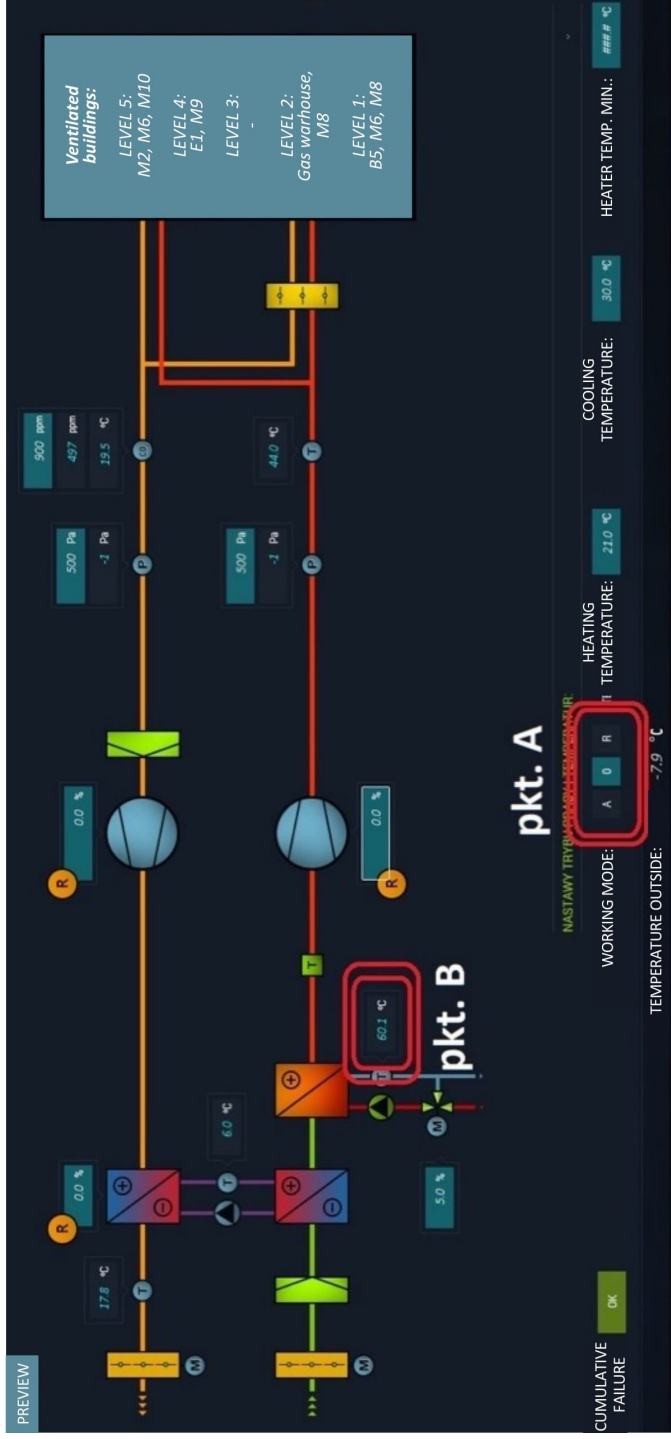


Figure 10.2. Management of the functioning of the BMS system, pkt. A – control function; pkt. B – supervision function. Source: own elaboration

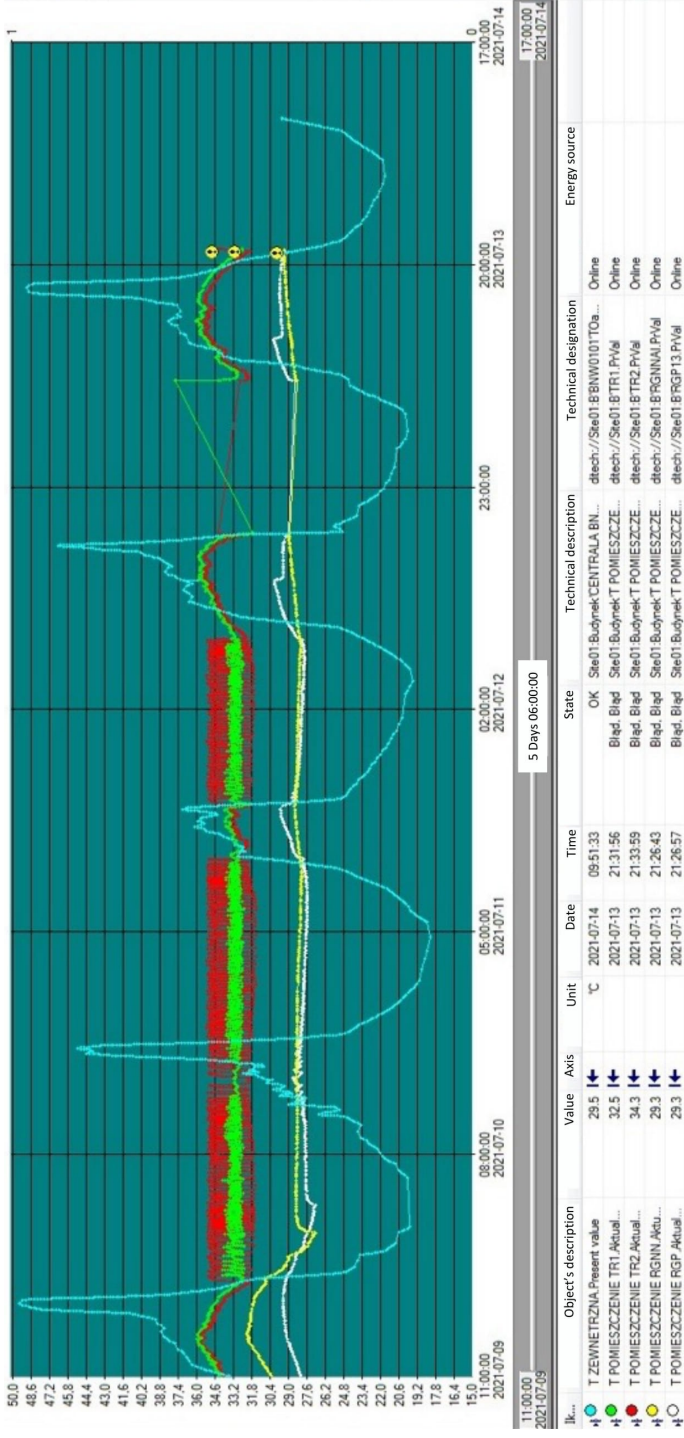


Figure 10.3. Control of environmental parameters in the BMS system. *Błąd* (in Polish) – error. Source: own elaboration

State	Priority	Category	Technical description	Alarm message	State of alarm	Alarm's value	Last change	Visa
▲ Normalny niepotwierdzony	High		Site01: Budynek SZAFa SZSW6'START TN_04		Blad	Off	2017-12-07 08:58:42	▽ 1 Visa
▲ Normalny niepotwierdzony	High		Site01: Budynek SZAFa SZSW6'START TN_04		Blad	Off	2017-12-07 08:58:42	
▲ Normalny niepotwierdzony	High		Site01: Budynek SZAFa SZSW6'START TN_05		Blad	Off	2017-12-07 08:58:42	
▲ Normalny niepotwierdzony	High		Site01: Budynek SZAFa SZSW6'START TN_02_01		Blad	On	2017-12-07 04:23:15	
▲ Normalny niepotwierdzony	High		Site01: Budynek SZAFa SZSW6'START TN_02_02		Blad	Off	2017-12-07 04:23:15	
▲ Normalny niepotwierdzony	High		Site01: Budynek SZAFa SZSW6'START TN_02_03		Blad	Off	2017-12-07 04:23:15	
▲ Normalny niepotwierdzony	High		Site01: Budynek SZAFa SZSW6'START TN_03		Blad	Off	2017-12-07 04:23:15	
▲ Normalny niepotwierdzony	High		Site01: Budynek SZAFa SZSW6'START TN_02_01		Blad	On	2017-12-07 04:23:15	
▲ Normalny niepotwierdzony	High		Site01: Budynek SZAFa SZSW6'START TN_02_02		Blad	Off	2017-12-07 04:23:15	
▲ Normalny niepotwierdzony	High		Site01: Budynek SZAFa SZSW6'START TN_02_03		Blad	Off	2017-12-07 04:23:15	
▲ Alarm niepotwierdzony	Urgent		Site01: Budynek E14 CENTRALA'Plant control	Blad procesu wyprzed	Wyk normal	On	2017-12-06 11:35:42	
▲ Normalny niepotwierdzony	High		Site01: Budynek E14 CENTRALA'Supply air fan'START NAWIEW E14		Wyk normal	On	2017-12-06 11:20:49	

Urgent OR = High

13 positions from 21 filtered

Figure 10.4. Identification of incorrect states in the BMS system. *Normalny niepotwierdzony* (in Polish) – normal unconfirmed, *Alarm niepotwierdzony* (in Polish) – alarm unconfirmed, *Blad procesu wyprzed* (in Polish) – process error, *Blad* (in Polish) – error, *Wyk normal* (in Polish) – normal shutdown. Source: own elaboration

Presentation of alarms and warnings at selected points in the system

The use of a management program (BMS system) enables presentation of alarms and warnings in one place and in a convenient way, adapted to the user's needs, of many important information on the functioning of individual devices in the system. The information on the malfunctioning of individual systems, displayed every time, allowed for a quick reaction of the staff and avoided any failure in the facility

The second type of programs enabling control of the implementation of economic and functional assumptions related to the process of distribution and use of electricity are applications for monitoring of power and energy media consumption.

The F&F Meternet PRO system is currently being tested at Lublin University of Technology. This system enables connection with the data archiver module from the level of a web browser. Thanks to this solution, the user has access to current and archived data readings (Figure 10.5). It is possible to create your own widgets and create your own front panels with measurement data displays (Figure 10.6).

Electricity consumption analysis

The use of such programs allows you to quickly check the current demand for electricity in a given system. Thanks to the data logger, it is possible to identify anomalies related to non-standard electricity consumption, and thus allow the building administrator to react quickly.

The third IT tools related to the operation and rational use of the elements of technical infrastructure installed in the building are analytical applications. At Lublin University of Technology, the Energia4 program by Numeron is used for this purpose. This program, thanks to its cooperation with measuring modules and counters, enables the current reading of technical parameters and analysis of the archived material (Figure 10.7). Owing to the built-in calculation tools, the program enables the user to perform interesting simulations related to the best settlement method and to analyse the possibility of reducing costs related to additional fees. Such analyses and simulations are carried out in order to limit the level of power ordered (Figure 10.8) or to select elements of the reactive power compensation system (Figure 10.9). The program allows you to generate reports with data analysis (Figure 10.10).

Summary data of total demand for electricity in selected periods and the use of analytical tools and programs for the ongoing control of technical parameters and the performance of simulations allow you to check the costs of electricity supply in various tariff variants. The introduction of own parameters and evaluation criteria adapted to a given type of facility facilitates electricity management.

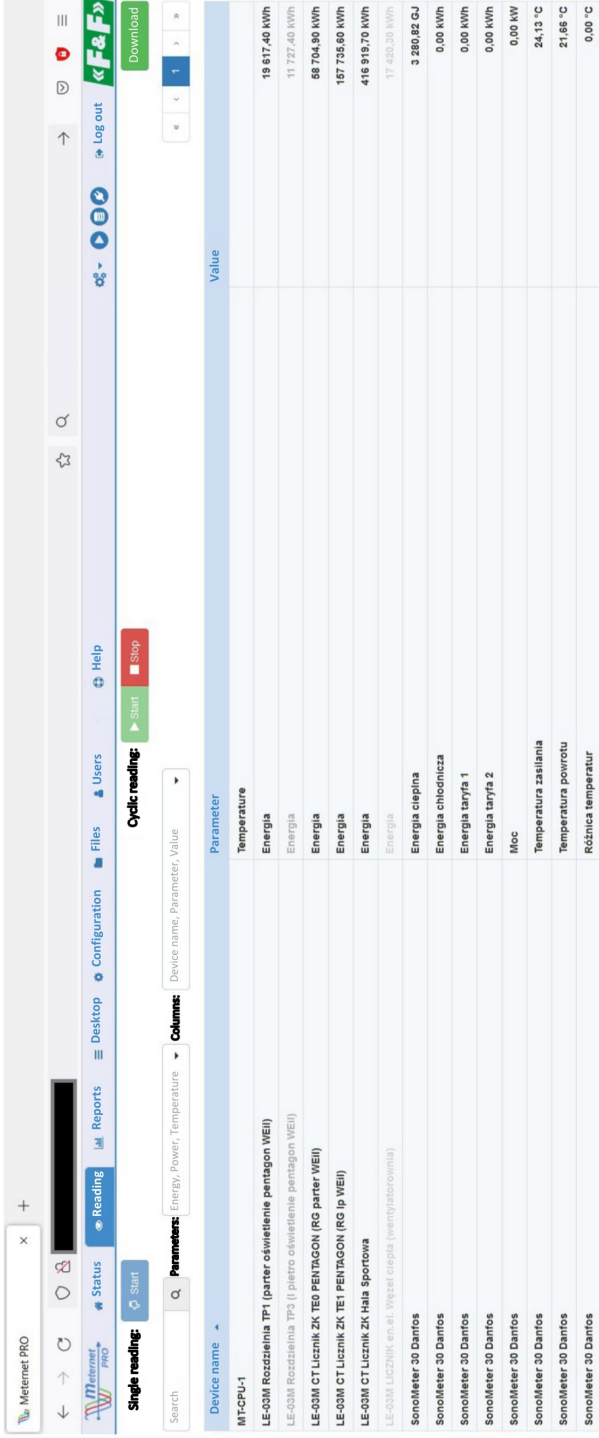


Figure 10.5: Energy media monitoring system. *Energia* (in Polish) – energy, *Energia cieplina* (in Polish) – Thermal energy, *Energia chlodnicza* (in Polish) – Cooling energy, *Energia taryfa I* (in Polish) – Energy tariff I, *Energia taryfa II* (in Polish) – Energy tariff II, *Moc* (in Polish) – Power, *Temperatura zasilania* (in Polish) – Inlet temperature, *Temperatura powrotu* (in Polish) – Outlet temperature, *Różnica temperatur* (in Polish) – temperature difference. Source: own elaboration

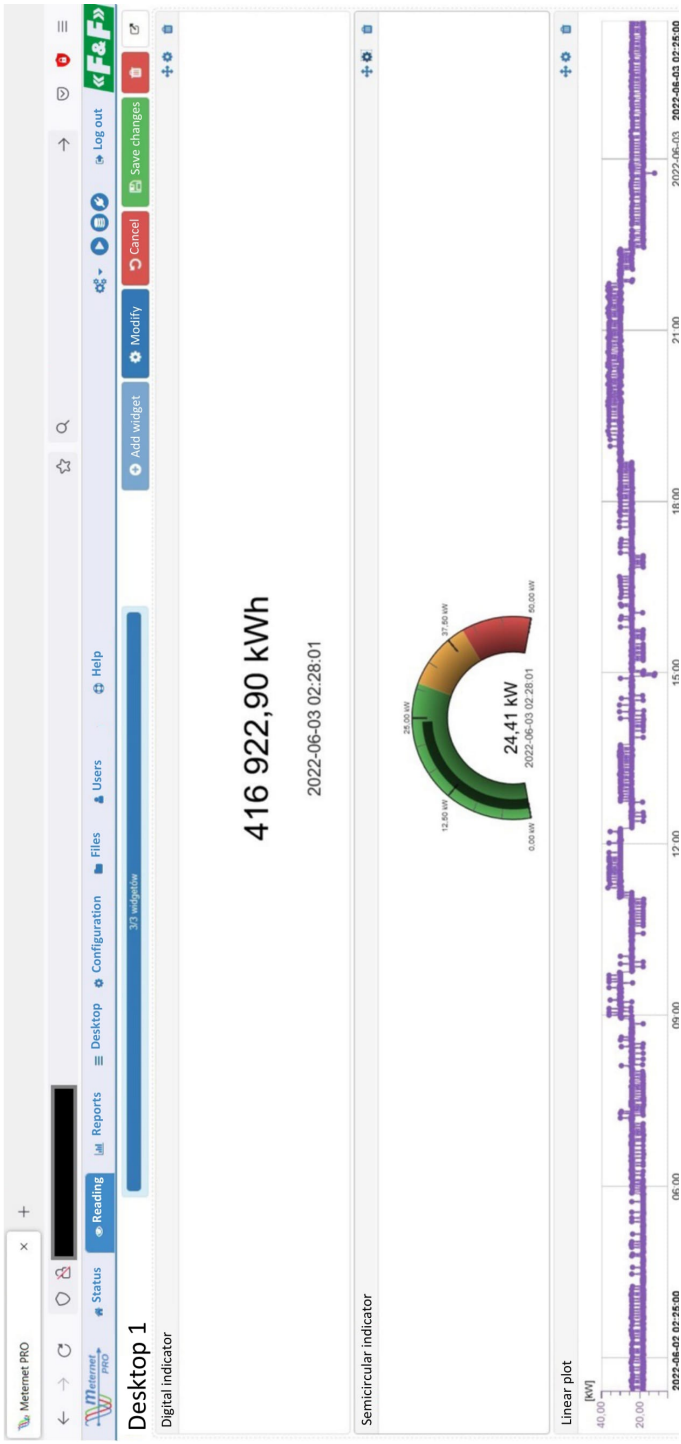


Figure 10.6. Energy media monitoring system. Source: own elaboration

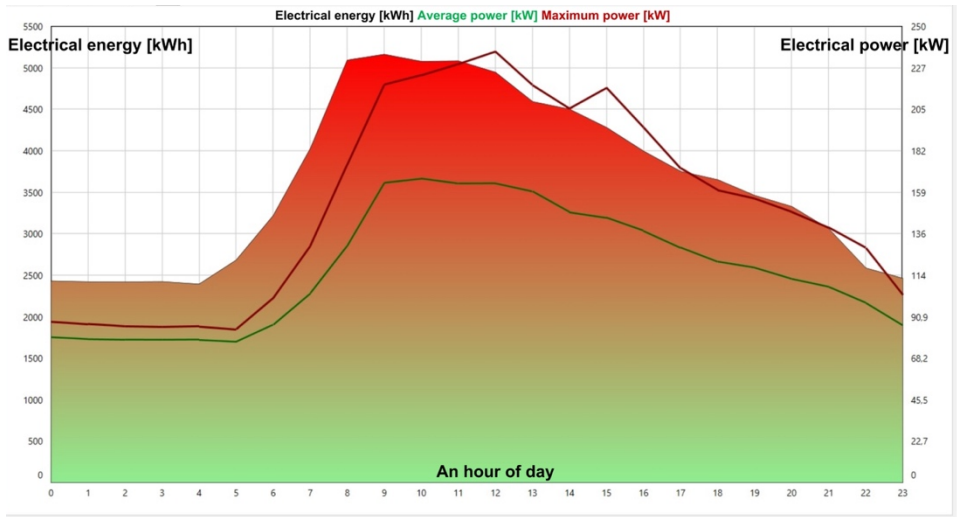


Figure 10.7. Energia4 analytical software. Source: own elaboration

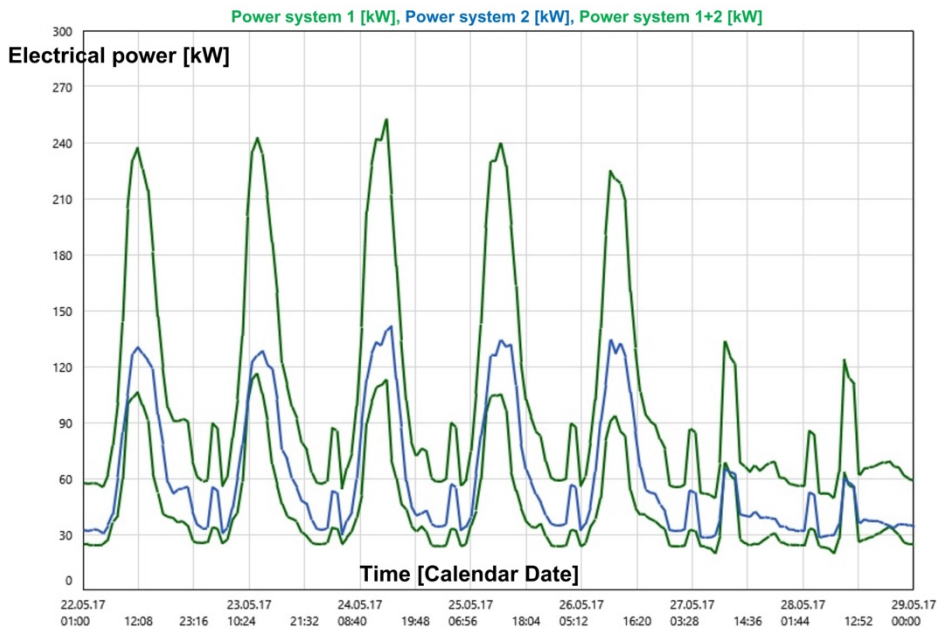


Figure 10.8. Analysis of measurement data in the Energia4 analytical software. Source: own elaboration

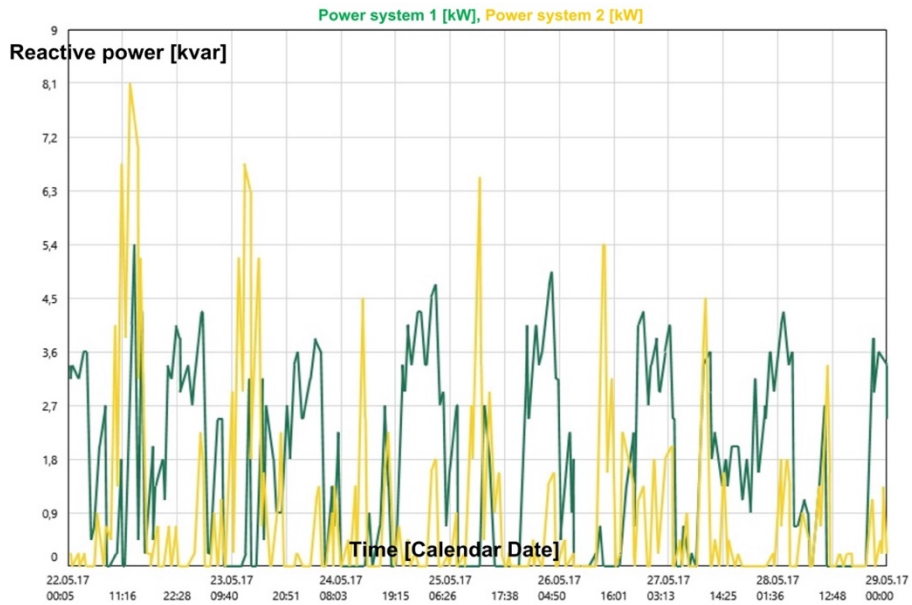


Figure 10.9. Analysis of measurement data in the Energia4 analytical software. Source: own elaboration

Electrical energies in zones of day and globally - data from the load profile

User	Administrator
Date	03.06.2022 02:01:02
Period	01.05.2017 00:00:00 – 01.06.2017 00:00:00
Object	Group of selected objects in LUT
Units	kWh, kvarh

Lp.	Calendar name	Zone code	Zone name	Zone OBIS
1	Unzoned			

Measurement point name	Full name of the measuring point	Channel name	Energy type	Ufn.[%]	Energy meter	Unzoned	
							Global
1P61	CLW\1P61	P-	EP-	100,00	50609581	0,00	0,00
		P+	EP+	100,00	50609581	32 049,56	32 049,56
		QC-	EQ-	100,00	50609581	618,36	618,36
		QL+	EQ+	100,00	50609581	4 179,83	4 179,83
2P61	CLW\2P61	P-	EP-	100,00	50609580	0,00	0,00
		P+	EP+	100,00	50609580	42 551,55	42 551,55
		QC-	EQ-	100,00	50609580	491,29	491,29
		QL+	EQ+	100,00	50609580	1 617,02	1 617,02
TOTAL	TOTAL	TOTAL	EP+			74 601,11	74 601,11
			EP-			0,00	0,00
			EQ+			5 796,84	5 796,84
			EQ-			1 109,64	1 109,64
			tg ø Pob.			0,08	0,08

Figure 10.10. Analysis of measurement data in the Energia4 analytical software. Source: own elaboration

Summary

The use of computer tools and applications in the process of achieving electricity economy enables efficient management of the technical infrastructure potential and elements of building equipment. The presented software tools do not eliminate the human factor from the supervision process, but they do facilitate the work and expand its capabilities. Thanks to the tools enabling the management of the electricity distribution process, the information transfer process and the decision-making process can be improved and shortening the time of identifying a potential threat by the BMS system also reduces the negative economic effects (cost reduction) and ecological failures (limiting the emission of hazardous compounds).

Thanks to the use of software enabling the acquisition and analysis of measurement data, it is possible to change the strategy of using individual systems and, as a result, reduce the demand for electricity in buildings. The use of analytical programs in one of the facilities of Lublin University of Technology made it possible to reduce the demand for electricity by approx. 20% compared to the reference period in which the building was operated with the manufacturer's standard settings. This results in a reduction of electricity consumption by over 250,000 kWh per year.

The use of software for the acquisition and analysis of measurement data allows simulations related to the selection of electricity tariffs and their adaptation to the nature of the building load. Additionally, it is possible to analyse other technical parameters, such as reactive power consumption. Thanks to the analysis of reactive power data and the use of reactive power compensation systems, its share in electricity bills has been limited to trace amounts.

The analysis of time histories and the knowledge of the functioning of the technical infrastructure in the building enables the reduction of daily and monthly power peaks while the demand for electricity remains unchanged. Based on the measurement data, the determination of correspondingly lower expected peak loads reduces the costs of electricity supply. An additional rational distribution of the load variability course also reduces the charges related to the capacity fee.

11. Selected problems of electrotechnology in master and PhD students' research

11.1. Brief reports on electrotechnology in agriculture

Mentor: *Fumiaki Mitsugi*

Japanese spinach planting experiment in ozone-treated soil

Yuto Nomaguchi

The issue in the application electrotechnology in agriculture is how to apply it to reduce the overuse of chemical pesticide and nitrogen fertiliser for agricultural soil. As electrical power tends to be concentrated and is difficult to distribute uniformly over a large area, the direct use of electrotechnology is not suitable for agricultural applications including soil disinfection. The idea to overcome this problem is how to make a beneficial material for soil disinfection using electrotechnology and that is ozone gas disinfection generated by dielectric barrier discharge plasma. This is one of the indirect usages of electrical energy to produce disinfection gas from oxygen by electrical discharge and it works well for soil disinfection without making residuals and hazard chemicals because ozone is one of the natural gasses occurring on the Earth and is not an artificial chemical.

The degradation of recalcitrant substances and the increase of nutrient by ozone

Kasumi Nagata

One of the environmental problems on our Earth is refractory organic substances that exist in lakes, rivers, sea, and soil. They are basically generated artificially from our daily life and flows with wastewater from factories and houses. Apparatus using electrotechnology is expected to decompose such hardly decomposable organic substances, because the bonding energy among atoms in the refractory organic substances is too high to decompose during combustion or during a chemical reaction. Here, the decomposition power of ozone is used to decompose the refractory organic substances by changing electrical energy into chemical power with a dielectric barrier discharge.

Evaluation of plant growth using nutrients obtained from ozone treated soil

Takumi Furusawa

In agriculture, not only nitrogen nutrients but also bio-stimulants are important materials for enhancing plant growth. Nitrogen fertiliser is artificially provided for plant growth as it is absorbed by plant roots. Other beneficial materials including humus and fulvic acids, which is a so-called bio-stimulant, support plant growth by activating microorganisms in soil around plant roots. The bio-stimulant works in nature; however, it takes long time to be produced in soil as the activity of enzymes and bacteria progresses very slowly. Therefore, artificial chemicals are used as bio-stimulant solutions. The best way to produce bio-stimulants is shortening the natural process and ozone treatment of soil is very useful. Here, the development of filtrate solution as a bio-stimulant was done after ozone treatment of soil. Another issue from an electrotechnology point of view is to reveal the mechanism of why ozone-treated soil contains such active stimulants. Then, the development of UV spectroscopy to measure the absorbance of the filtrate solution was done. The system was composed of a halogen lamp, optical fibre, and a spectrometer. As the result, mainly 260–280 nm and 400–600 nm absorbance showed higher values in filtrate solution made after ozone treatment of soil. These are absorptions from DNA, protein, and fulvic acid. Thus, it was found that these bio-stimulants work to enhance plant growth and ozone treatment of soil using dielectric barrier discharge is the best way to produce bio-stimulants in a short time.

11.2. Brief reports on amorphous carbon nitride thin films

Mentor: *Maasami Yamazato*

Electrical and structural changes in amorphous carbon nitride thin films induced by exposure to iodine vapor

Seiji Kudo

Hydrogenated amorphous carbon nitride (a-CN_x:H) films have unique properties such as high hardness, transparency, and chemical inertness. Therefore, carbon nitride has been expected to have a wide range of applications such as mechanical cutting tools, protective coatings, optical materials, and insulating layers in ULSI technology. It has been reported that the resistivity of iodine-doped carbon films decreases for applications in optoelectronic devices such as solar cells. On the other hand, the structure and the properties of a-CN_x:H film strongly depend on the composition ratio of nitrogen and carbon N/C. In this research, we investigated that the effects of iodine vapor exposure on

the electrical resistivity, the optical property of hydrogenated amorphous carbon nitride (a-CN_x:H) thin films which have different N/C ratio. The resistivity decreased remarkably, and especially when the N/C ratio was 0.2, it decreased by 6 orders of magnitude. Also, this resistivity changing appeared immediately when a sample was exposed into iodine vapor. These results showed the a-CN_x:H film could be a candidate for optoelectronic devices and iodine (halogen) detection sensors.

Iodine dedoping characteristics for an a-C:H/iodine doped a-CN_x:H stacked structure

Shuto Fujiko

The phenomenon of dedoping was observed for iodine doped a-CN_x:H thin films. In this research, we attempted to suppress dedoping from iodine-doped a-CN_x:H film by adding an a-C:H film as cap layer to it to create a stacked structure. The bonding hydrogen concentration is estimated from the IR absorption spectrum in the region from 3200 to 2700 cm⁻¹ for an a-C:H film is caused by the stretching mode of CH_n (n = 1, 2, 3) configurations. The integrated intensity of IR spectrum ICH in this region is known to be approximately in proportion to the bonding hydrogen concentration in an a-C:H film. In iodine-doped a-CN_x:H film with a-C:H as the stacked cap layer, the iodine concentration decreases 9% after 1300 hours, while the film without cap layer showed 52% decrease of iodine. This result showed the a-C:H film is effective in preventing the dedoping of iodine. The results also indicate that a-C:H films with lower ICH are considered more effective as cap layers.

Abnormal-Resistive-Switching behaviour of ReRAM utilizing hydrogenated amorphous carbon thin films

Yasuo Ogimi

ReRAM is a non-volatile memory that utilises changes in the resistance state. It is expected to be highly integrated and have large capacities due to its relatively simple structure consisting of an insulator sandwiched between metal electrodes and they do not require electrical charges. Generally, metal oxides are used for insulators, but in this study, we fabricated Cu/a-C:H/Pt structure devices utilizing hydrogenated amorphous carbon (a-C:H) thin film, which has high electrical insulating properties and is mainly composed of carbon which is relatively inexpensive and has abundant reserves. We investigated the effect of a-C:H film thickness and film quality on the device and the mechanism of the switching behaviour. In this study, typical bipolar characteristics were obtained. At low resistance, ohmic characteristics were observed, it indicated a metal filament type of mechanism. On the other hand, non-volatile abnormal

resistance switching (ARS) characteristics were also obtained, and these ARS characteristics were repeatedly confirmed over one month of elapsed time. When the top electrodes change from Cu to Al or Pt, (Pt or Al)/a-C:H/Pt devices, ARS characteristics were not observed. The results of this ARS phenomenon considered to exist of an oxide layer at the interface between the a-C:H film and the top electrode, and the existence of metal nanoparticles invading the insulating film. It is thought that both the interfacial oxide layer type and metal filament type of mechanisms affect the resistance switch.

11.3. Measurements and analysis of power quality parameters during electric vehicle charging

Mentors: *Paweł Mazurek, Janusz Partyka*

PhD students: *Aleksander Chudy, Sławomir Durak*

Introduction

Electric vehicles are increasingly being discussed as part of the worldwide decarbonisation agenda. Currently, a large portion of greenhouse gases are emitted by the internal combustion engines of fossil fuel-based vehicles and account for about 16% of total human-caused CO₂ emissions. These emissions worsen air quality, which is dangerous to human health. The trend of replacing conventional fossil fuel vehicles with EVs is expected to continue to increase in the near future. At the same time, non-linear loads based on power electronics are becoming more common in domestic environments, which affects power quality parameters [239–243]. Electric vehicle fleets are growing rapidly in some of the world's largest vehicle markets, for example, China, the United States, Germany and Norway [243]. According to the Electromobility Counter [244], at the end of the March 2022, there were 45,242 EVs (21,576 battery EVs and 21,789 hybrid EVs) and 2113 public charging stations (1502 slow charging stations and 611 fast charging stations) in Poland.

Monitoring of power quality (PQ) parameters and measurements with portable and stationary meters are necessary to solve problems in industrial and residential systems. These measurements have become an integral part of overall power system performance evaluation procedures. The benefits of power quality monitoring include [245]:

- prioritisation of improvements,
- faster identification of problems in the power system,
- a better understanding of aspects of PQ.

The growing number of EVs is projected to put a strain on existing distribution networks in the future. Electromobility may provide a growing difficulty for distribution network operators, owing to the rather unpredictable behaviour

of EVs owners and difficult-to-predict load profiles [246–248]. Large-scale EV charging, in conjunction with the increasing number of renewable energy sources in the energy mix and the intermittent nature of their work, may lead to local and/or temporary grid overloads and worsening of PQ parameters thus it is important to monitor and analyse PQ parameters during the charging process [249–252]. The subsection presents the results and an analysis of selected PQ parameters measurements during an EV charging with a wallbox charger.

Test setup and analysis of selected PQ parameters

Class A PQ analyser SONEL PQM-711 with F-2 current clamps were used for measurements of PQ parameters (Figure 11.1). The recordings included the minimum, maximum and average values of PQ parameters. The nominal power frequency was 50 Hz and the nominal phase voltage was 230 V. An averaging period of 200 ms was selected which equals to 10 mains cycles. The single period contained 204.8 samples.

The data was stored by the PQ analyser in a .pqm711 file type that was opened with Sonel Analysis 4 software and exported as a .csv file. The EV that was charged was a Nissan Leaf with a 6.6 kW onboard charger. The wallbox charger used for the EV charging was single-phase ABL eMH1 Wallbox 7.2 kW (maximum charging current of 32 A and maximum power that can be delivered of 7.2 kW). The charger had an attached 6 m charging cable and a Type 2 connector (in accordance with the IEC 62196-2 standard).

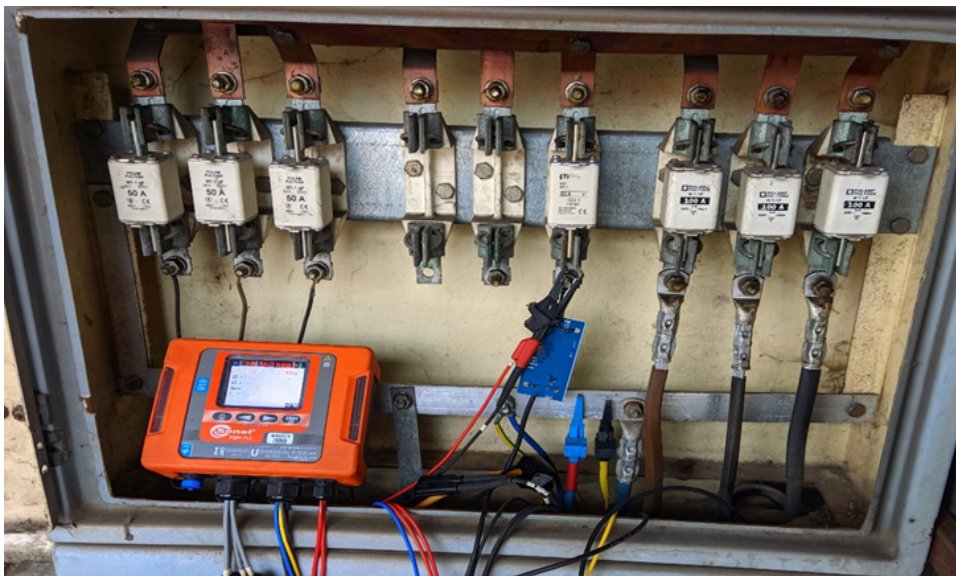


Figure 11.1. Setup during measurements of PQ parameters. Source: own elaboration

This wallbox is intended for charging an EV in accordance with IEC 61851-1 Mode 3. The charging process lasted 3 hours and 37 minutes and the state of charge of the battery after the charging was 100% (16.48 kWh of consumed energy). The measured PQ parameters were mains frequency, phase voltage, current, harmonics, inter-harmonics, values of active and reactive power. The results are presented in Figures 11.2–11.7. Generation and load in a power grid must be equal in real time; otherwise, the power frequency deviates from the nominal value. If the grid is subjected to a high charging demand from EVs, additional power generation will be necessary to keep the power frequency within the permitted range. The mean value of power frequency during EV charging was 49.99 Hz which is within the limits given in the Regulation of the Minister of Economy on the detailed conditions for the functioning of the power system [246]. The limits presented in this document are based on the PN-EN 50160 standard [252]. The value of the power frequency should be 50 Hz \pm 1% (49.5 Hz to 50.5 Hz) for 99.5% of the year and 50 Hz + 4% / -6% (47 Hz to 52 Hz) at all times. Minimum and maximum value of the power frequency was 49.94 Hz and 50.07 Hz respectively. Figure 11.2 shows power frequency variations during the EV charging process. Voltage fluctuations and/or a voltage drop might also be caused by high EV charging demand, but the main problems in low voltage distribution networks are typically drops in the peak load and the voltage rise due to the PV power injection [255, 256].

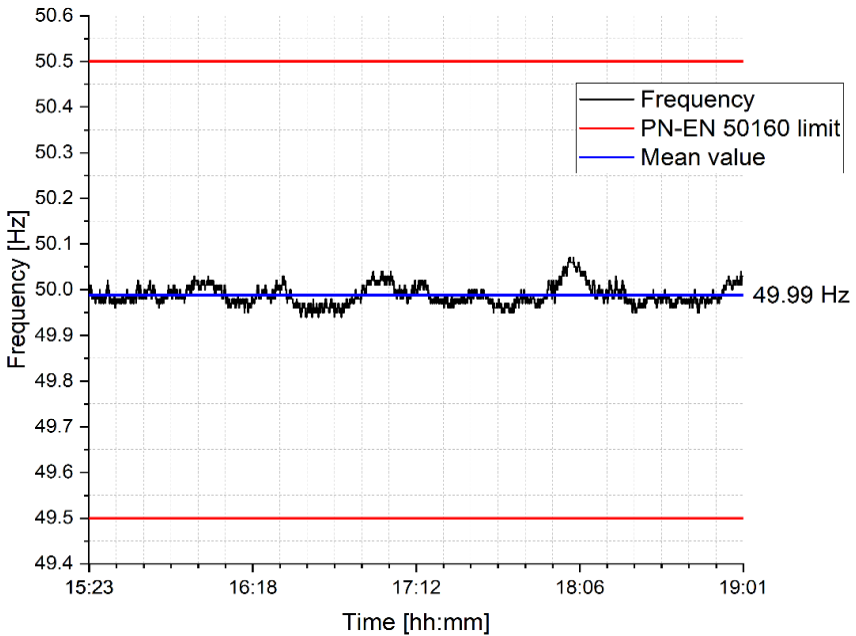


Figure 11.2. Power frequency variation during EV charging (average 10 s values). Source: own elaboration

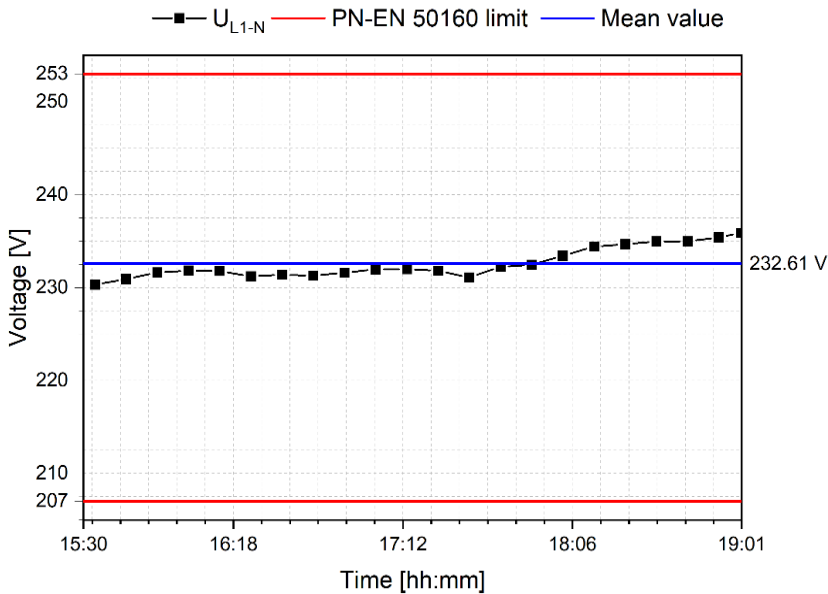


Figure 11.3. Phase voltage during EV charging – average 10-minute RMS values. Source: own elaboration

The measured phase voltage meets the requirements of the Regulation. Mean, minimum and maximum values of the phase voltage were 232.56 V, 227.71 V and 236.84 V respectively. Figure 11.3 shows phase voltage fluctuations during EV charging (average 10 minutes RMS values). What is more, the mean value of the tangent φ was 0.29, and therefore in compliance with the requirements of the Regulation [253] that stipulate that the tangent should not be higher than 0.4. The mean value of charging current was 19.43 A. The maximum value of the current was 29.45 A. The maximum registered power was 6.778 kW (4.55 kW on average). There were two registered 5-minute periods of when the charging current and active and reactive power decreased to 0. The rise of phase voltage (of approximately 5 V) is also visible at the time when the reactive power decreases. Figure 11.4 shows variations of active power and reactive during the EV charging.

Electric vehicle chargers contain non-linear power electronic elements that are able to distort the sinusoidal waveforms of voltage and current. The PQ analyser measured the harmonic components up to the 50th order. The total harmonic distortion of voltage referred to the fundamental component did not exceed the 8% limit given in the Regulation [253] during the EV charging process (mean value was 2.65%). Its value decreased by approximately 0.3% at the time the phase voltage increased by 5 V (the period of aforementioned decrease in active and reactive power). Limits for the magnitude of individual voltage harmonic components were also not exceeded.

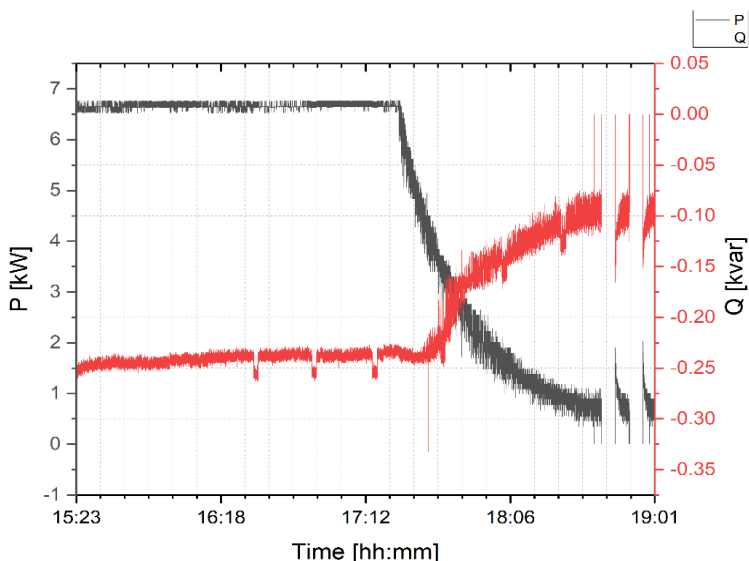


Figure 11.4. Active and reactive power during EV charging. Source: own elaboration

The mean value of the total harmonic distortion of current was 10.39%, although it is better to use the total demand distortion (TDD) indicator because if the current reaches the maximum value, TDD value is close to total harmonic distortion of current; however, if the value of current decreases, the TDD also decreases. The TDD is calculated as:

$$TDD = \frac{\sqrt{\sum_{h=2}^n I_h^2}}{I_L} \quad (11.1)$$

where: I_h – RMS value of the h -th order harmonic, I_L – demand current; maximum mean value of the fundamental component, recorded during the EV charging process, was equal to 29.46 A.

The mean value of TDD was 3.7% while its maximum value – 5.6%. Fig. 11.5 shows average 10-minute values of TDD during EV charging. The value of the fifth voltage harmonic was the highest (2.19%). In the spectrum of current harmonics, the value of the third harmonic was the highest (8.91%). The sixteenth voltage inter-harmonic subgroup was the highest (0.044%). The current inter-harmonic value was the highest in the group below the fundamental frequency. Figure 11.7. presents spectrum of voltage and current harmonics and inter-harmonics. No values are given for voltage harmonics of an order higher than 25, as they are negligibly small. Variations in the luminous flux created by electric light sources are the flicker phenomenon.

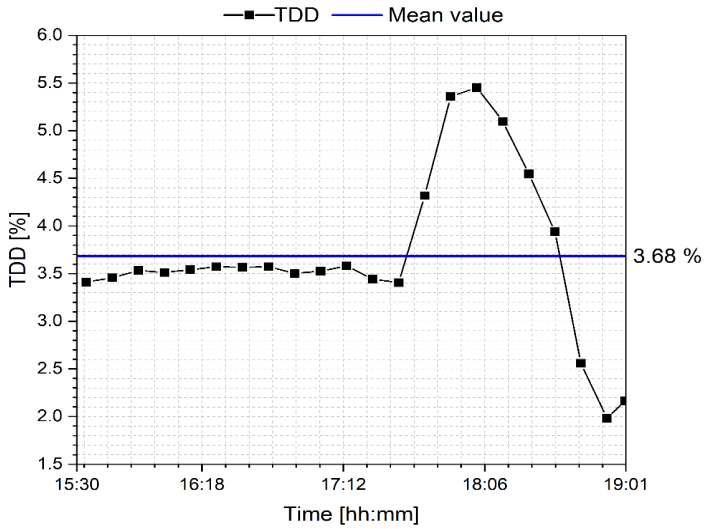


Figure 11.5. TDD during EV charging (10-minute averaged values). Source: own elaboration

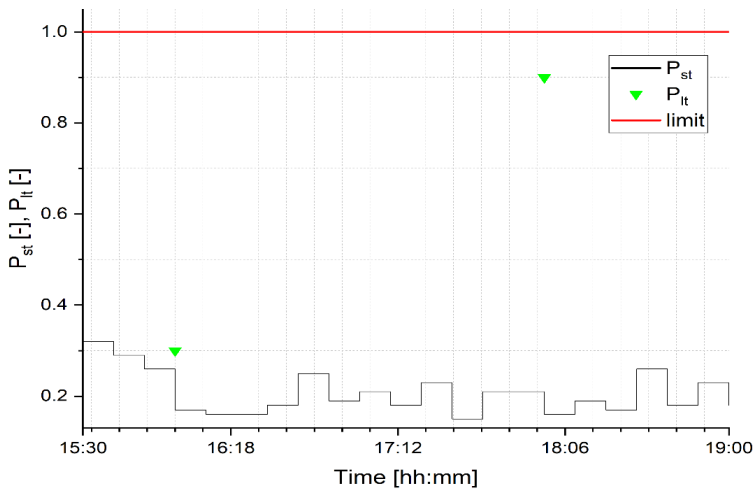


Figure 11.6. Short- and long-term flicker perceptibility variation during EV charging. Source: own elaboration

They occur when voltage changes have the character of regular fluctuations and are present over an extended period of time. Flickers have an adverse impact on the human health (e.g., impaired vision, headaches or even seizures) [257]. The measured values were all below 1 (within allowable limits given in the Regulation [253]). Figure 11.6. presents the short (P_{st}) and long term (P_{lt}) flicker perceptibility.

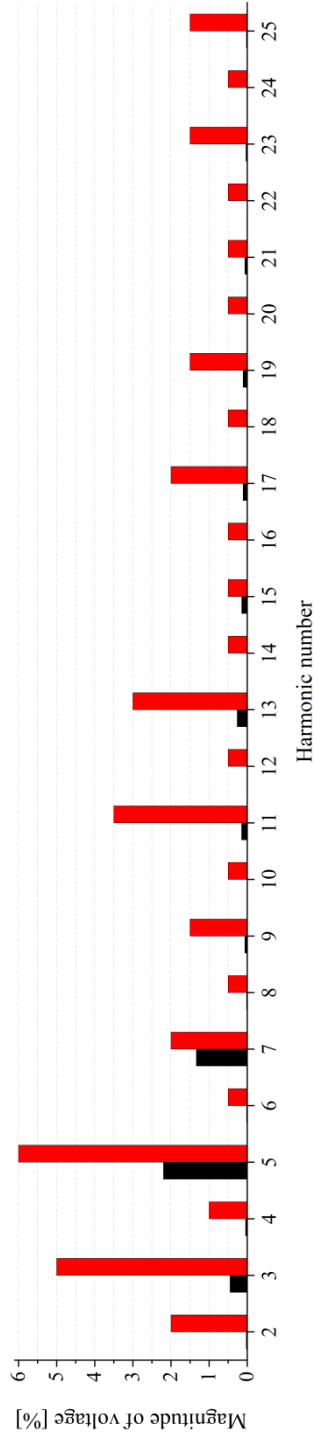


Figure 11.7a. Spectrum of voltage harmonics; black – magnitude of measured individual voltage/current harmonic; red – individual voltage harmonic limit in accordance with the Regulation [253]. Source: own elaboration

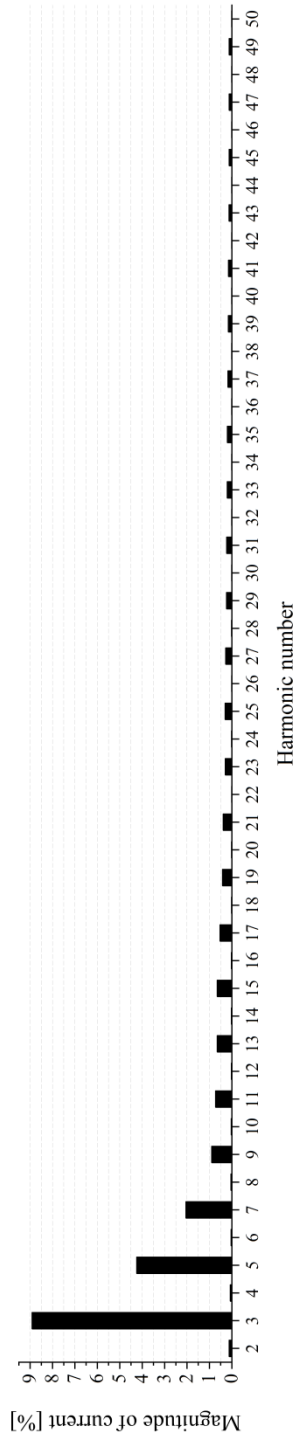


Figure 11.7b. Spectrum of current harmonics; black – magnitude of measured individual voltage/current harmonic; red – individual voltage harmonic limit in accordance with the Regulation [253]. Source: own elaboration

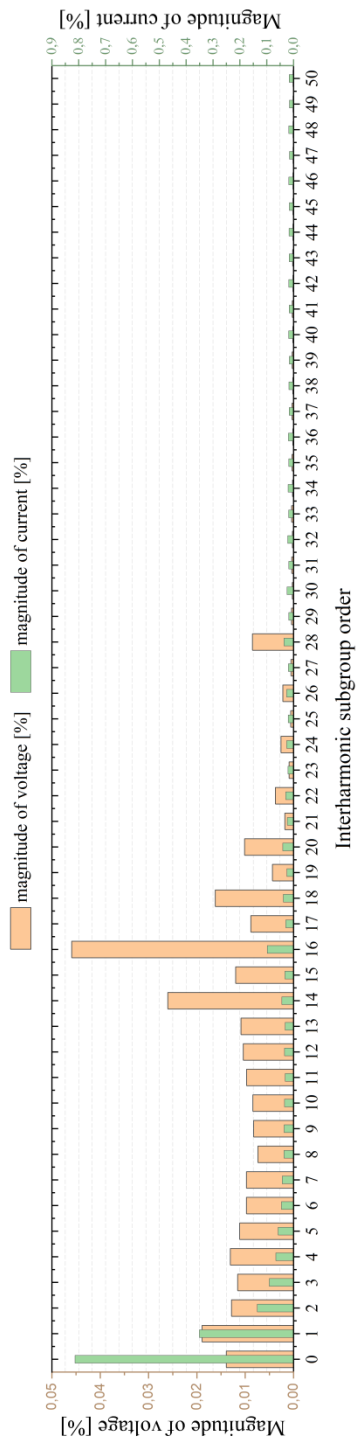


Figure 11.7c. Spectrum of voltage and current interharmonics; black – magnitude of measured individual voltage/current harmonic; red – individual voltage harmonic limit in accordance with the Regulation [253]. Source: own elaboration

Conclusions

Results of PQ parameters (frequency, phase voltage, current, active and reactive power, harmonics and inter-harmonics, short- and long-term flicker) measured during Nissan Leaf mode 3 charging with the use of wallbox charger have been presented.

It can be concluded that the measured PQ parameters meet the requirements of the Regulation and PN-EN 50160 standard. It is noteworthy that the measurements considered a single-phase slow charger only, but when these become more common it might result in more serious exceedances and disturbances of PQ parameters. Due to this fact it is important to measure and analyse PQ parameters further when more chargers are in use which will be done in future work.

11.4. Parameters of vacuum interrupters designed for modern switchgear

Mentor: *Paweł Węgierek*

PhD student: *Michał Lech*

Introduction

Currently produced modern power switching equipment operating at a medium voltage level mainly uses sulphur hexafluoride (SF6) and vacuum as an insulating medium [258]. The interest in vacuum technology in recent years is connected with it not being harmful to the environment. It is a completely environmentally neutral medium, which is not the case for SF6 gas.

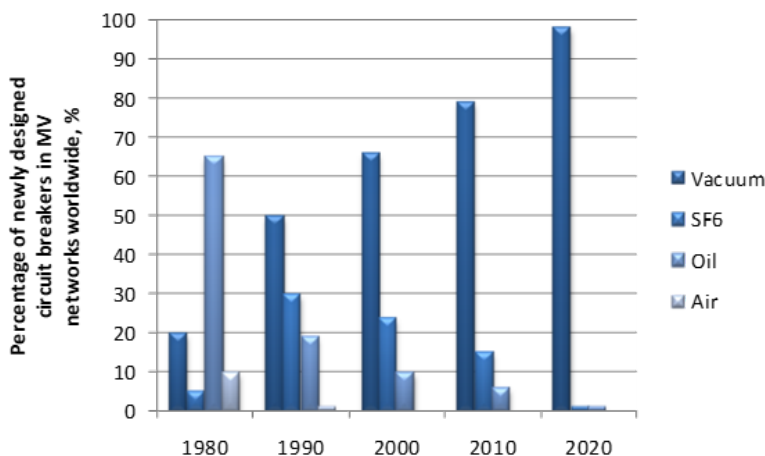


Figure 11.8. Circuit-breakers in MV networks divided into the applied insulating medium. Source: own elaboration based on [258]

Figure 11.8 shows the development of vacuum switchgear over 40 years [258]. When considering SF₆ gas in comparison to other substances utilized in the electric power industry, special attention must be given to its environmental implications. SF₆ is categorized as an F-gas, specifically a fluorinated greenhouse gas, which contributes to the elevation of atmospheric temperature when present. The International Panel on Climate Change and the U.S. Environmental Protection Agency have acknowledged SF₆ as a compound that significantly contributes to the greenhouse effect [259–261].

The Global Warming Potential (GWP) serves as a measure to assess the impact of a substance on the greenhouse effect, and for SF₆, it exceeds 22,000. This indicator compares the heat retained by a certain mass of carbon dioxide, which has a GWP of 1. Table 11.1 presents the GWP values for various substances of interest.

Table 11.1. List of selected substances with corresponding GWP₁₀₀ [259–261]

Substance	GWP₁₀₀
Carbon dioxide CO ₂	1
Methane CH ₄	23
Nitrous oxide N ₂ O	296
Carbon tetrafluoride CF ₄	5 700
Freon R-12 (CFC-12)	10 600
Sulphur hexafluoride SF₆	22 200

In addition to the visible development of vacuum switchgear, the need to improve the technical parameters of vacuum interrupters mounted in these devices is key. Due to the increasing demand for electricity, as well as the fact that medium voltage power grids are outdated, as almost 80% of these grids were built more than 25 years ago [262], it is necessary to develop new devices and components with better parameters, such as continuous, withstand, and switching currents, mechanical durability, dielectric strength, or lower arc-fault current [263–269]. Next chapter presents the results of electrical strength testing of a medium voltage vacuum interrupter.

Test stand

The test stand consists of a specialised mobile structure in which it is possible to mount the vacuum interrupter under test, and to connect the power supply and the load to the stand using electric cables terminated with angular connector heads. The possibility to set the specified contact gap precisely was ensured by mounting the extraction screw with a thread of 1 mm pitch. In order to equalise the distribution of the electromagnetic field inside the stand, shields made of copper pipes and stainless-steel balls were mounted. The workstation was equipped with a dedicated platform for stable location of the vacuum pump set.

The test object in the above-described test stand are vacuum disconnector interrupters designed for connecting current circuits of medium voltage over-head power networks. They are characterised by small dimensions, high reliability of operation, insulation of the arc from the environment, quiet operation, any position of operation and resistance to vibrations and shocks. They consist of a moving contact and a stationary contact made of copper-filtered tungsten (W-Cu) with a ratio of 70% tungsten to 30% copper. Movement of the movable contact is enabled by an elastic bellows. The interrupter also contains a metal condensation screen to protect the interrupter casing from conductive particles that, if deposited on the interrupter, could degrade its performance. The special design of the tested interrupters consists in the possibility of repeated filling with gas due to their unsealing and adaptation for connection to a set of vacuum pumps.

The main element of the test set supplying power to the above test stands (Figure 11.9) is a high voltage transformer cooperating with a modern, programmable control panel, greatly facilitating the testing. An additional capacitive divider, based on selected low-loss polypropylene capacitors, ensures precise voltage measurement. The control panel is equipped with a brush voltage regulator with a drive. The control part is a PLC SIMATIC S7 1200 and dedicated measuring module. The user interface consists of touch screen HMI and a number of buttons and indicator lamps.

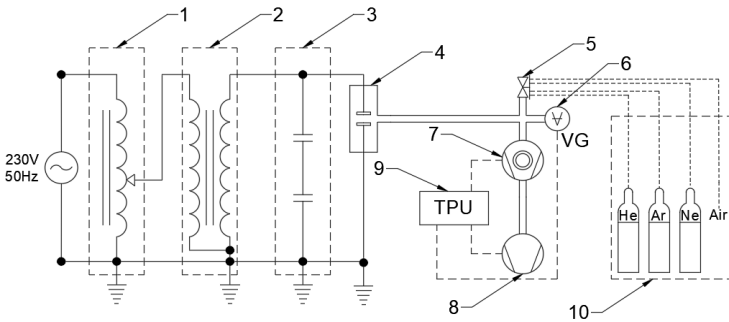


Figure 11.9. Schematic of the system designed for dielectric strength testing. Source: own elaboration

Results of experimental studies

Initially, the breakdown voltages of the disconnecting vacuum interrupter were assessed by introducing air into the interrupter, considering contact gaps ranging from 1.0 mm to 5.0 mm and pressures spanning from 8.0×10^{-4} to 3.0×10^1 Pa. Figure 11.10 portrays the relationship between the measured breakdown voltages and the contact gaps $U_{db} = f(d_{db})$ at different pressure levels. It is evident that when the pressure inside the tested vacuum interrupter surpasses 7.05 Pa, the electrical strength of the interrupter is no longer influenced by the contact gap. Under such circumstances, the dielectric strength of the system solely depends on the internal pressure. However, for pressure values lower than $p = 7.05$ Pa, the electrical strength of the vacuum interrupter is influenced by both the contact gap and the pressure. The breakdown voltage increases with larger contact gaps, as per the established correlation:

$$U_{db} = C \cdot d_{db}^{\alpha_{db}}, \tag{11.2}$$

where: U_{db} – breakdown voltage, d_{db} – contact gap, C , α_{db} – experimentally determined constants. Figure 11.10 shows the dependence of the measured breakdown voltages both as a function of the pressure inside the tested interrupter $U_{db} = f(p)$ for all contact gap settings.

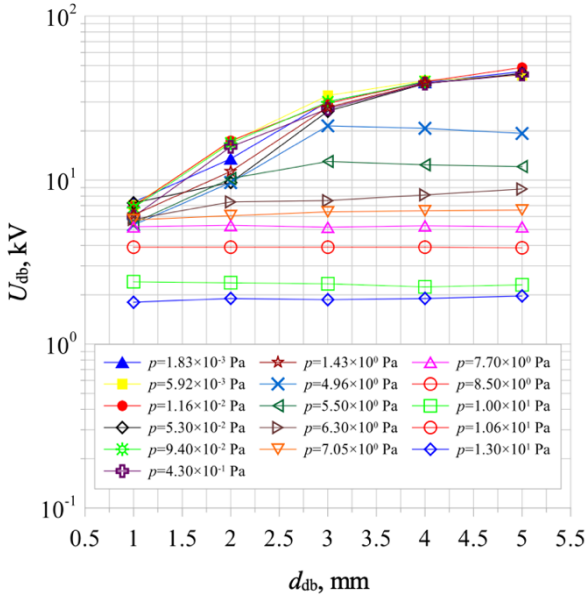


Figure 11.10. Dependence of breakdown voltages U_{db} as a function of contact gap d_{db} for selected pressure values, for residual gases. Source: reprinted from [270] after obtaining the authors' permission

Table 11.2. Measured values of U_{db} breakdown voltages in the compartment with constant dielectric strength for a vacuum interrupter

Electrode spacing	Breakdown voltage	Pressure range
d_{db} , mm	U_{db} , kV	p , Pa
1.0	7.00	$8.00 \times 10^{-4} - 7.70 \times 10^0$
2.0	17.00	$8.00 \times 10^{-4} - 5.50 \times 10^0$
3.0	31.00	$8.00 \times 10^{-4} - 4.20 \times 10^0$
4.0	40.00	$8.00 \times 10^{-4} - 4.00 \times 10^0$
5.0	47.00	$8.00 \times 10^{-4} - 3.00 \times 10^0$

Each contact gap exhibits two distinct pressure ranges with specific characteristics. In the first range, the dielectric strength of the vacuum interrupter remains relatively constant, and these values are consolidated in Table 11.2. It is important to note that as the contact gap diminishes, the corresponding pressure at which the interrupter retains constant dielectric strength increases. Notably, considerable variations in breakdown voltages were observed within the provided pressure ranges for contact gaps of 1.0 mm and 2.0 mm. Above the pressure values indicated in Table 11.2, a sharp decline in the dielectric strength of the tested cell occurred, signifying a loss of its insulating properties. The breakdown voltages within these sections of the characteristics are solely influenced by the pressure and not the contact gap, as depicted by the horizontal segments in Figure 11.10.

Similar measurements were conducted on the same vacuum interrupter by augmenting the pressure inside with the introduction of helium (Figure 11.11). Figure 11.12 illustrates the relationship $U_{db} = f(d_{db})$ for specific pressure values, while Figure 11.13 demonstrates the relationship $U_{db} = f(p)$ for contact gaps ranging from 1.0 mm to 5.0 mm. It is evident from Figure 11.12 that, for pressures exceeding $p = 4.0 \times 10^1$ Pa, the contact gap has minimal impact on the breakdown voltages. Conversely, at pressures below this threshold, an increase in the contact gap corresponds to an increase in the breakdown voltage. In Figure 11.13, distinct characteristic intervals of $U_{db} = f(p)$ can be discerned for each contact gap d . Within the intervals where the system's dielectric strength remains constant, the measured U_{db} voltages exhibited less variability compared to the vacuum interrupter subjected to air dosing. These values, alongside their respective pressure ranges, are summarized in Table 11.3.

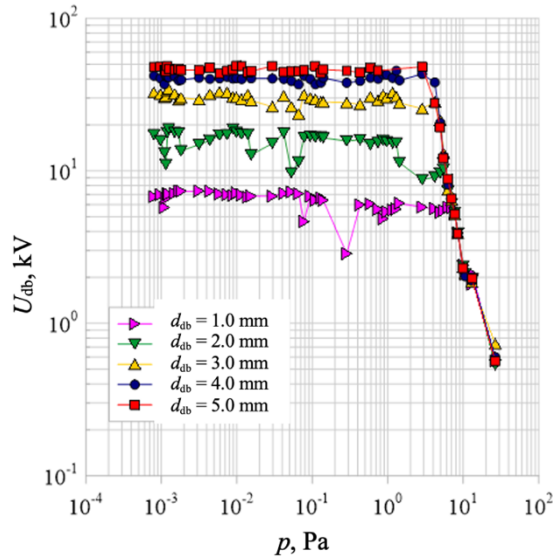


Figure 11.11. Dependence of breakdown voltages U_{db} as a function of pressure p inside the tested interrupter, for residual gases being pure air. Source: reprinted from [270] after obtaining the authors' permission

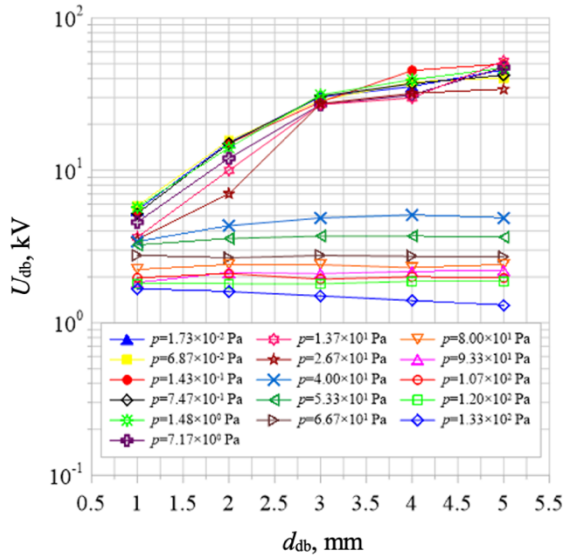


Figure 11.12. Dependence of breakdown voltages U_{db} as a function of contact gaps d_{db} for selected pressure values for residual gases being helium. Source: reprinted from [270] after obtaining the authors' permission

Table 11.3. Measured values of breakdown voltages U_{db} in a compartment with constant dielectric strength for a vacuum interrupter with helium

Electrode Spacing	Breakdown Voltage	Pressure Range
d_{db} , mm	U_{db} , kV	p , Pa
1.0	5.00	$8.00 \times 10^{-4} - 5.33 \times 10^1$
2.0	13.00	$8.00 \times 10^{-4} - 2.67 \times 10^1$
3.0	29.00	$8.00 \times 10^{-4} - 2.67 \times 10^1$
4.0	36.00	$8.00 \times 10^{-4} - 2.67 \times 10^1$
5.0	46.00	$8.00 \times 10^{-4} - 1.37 \times 10^1$

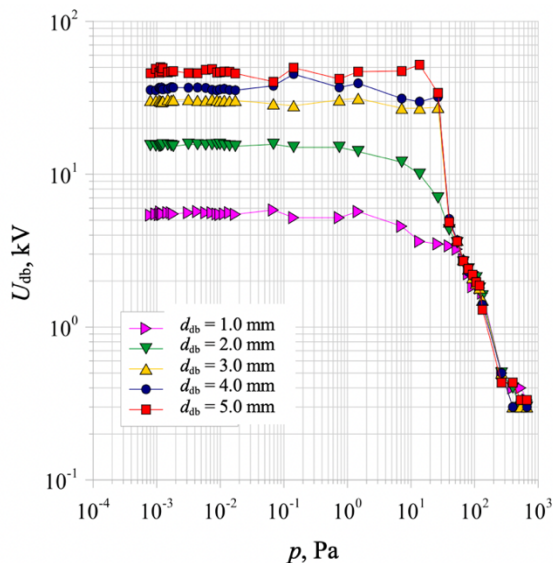


Figure 11.13. Dependence of breakthrough voltages U_{db} as a function of pressure p inside the tested interrupter, for residual gases being helium. Source: reprinted from [270] after obtaining the authors' permission

Likewise, as in the case where the interrupter was filled with air, a significant decline in the system's dielectric strength was observed when surpassing the pressure values indicated in the table below. It is of utmost importance, concerning the electrical strength of the vacuum interrupter, to compare the measured breakdown voltage values U_{db} for different residual gases, specifically air and helium. To assess this, the breakdown voltages U_{db} were studied in relation to pressure (air and helium), denoted as p , for two selected contact gaps: 3.0 mm (Figure 11.14) and 5.0 mm (Figure 11.15).

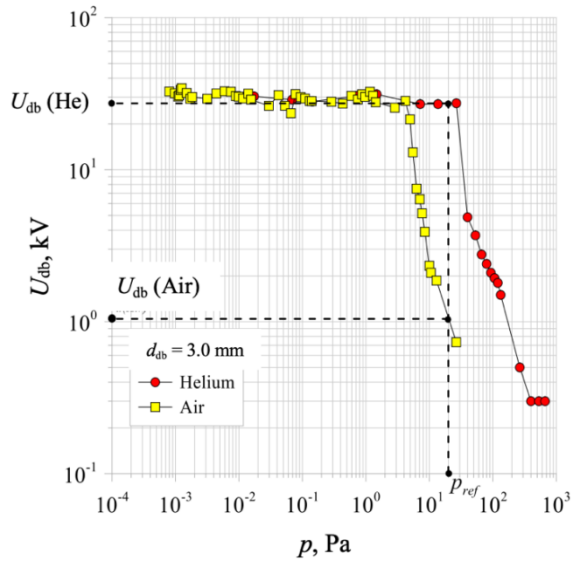


Figure 11.14. Comparison of the dielectric strength of a vacuum interrupter filled with air and helium for contact gap $d_{db} = 3.0$ mm. Source: reprinted from [270] after obtaining the authors' permission

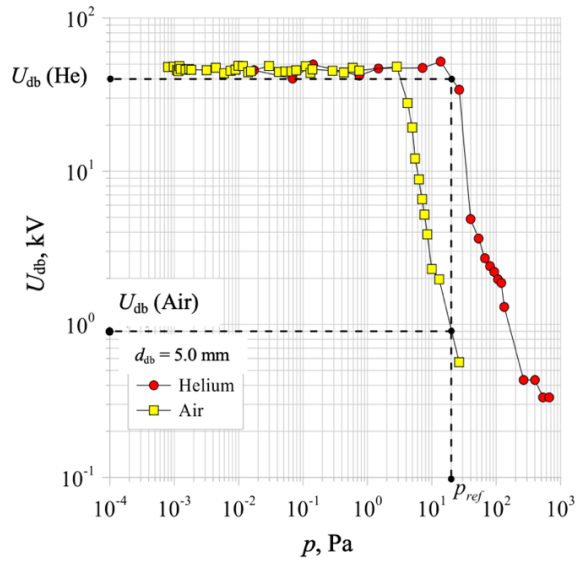


Figure 11.15. Comparison of the dielectric strength of a vacuum interrupter filled with air and helium for contact gap $d_{db} = 5.0$ mm. Source: reprinted from [270] after obtaining the authors' permission

In the case of a 3.0 mm contact gap, the maximum breakdown voltages U_{db} for both air and helium converge at approximately 30.0 kV. However, what holds significance in this scenario is the point at which the interrupter loses its insulating properties. When air is introduced, there is a sharp decline in dielectric strength once the pressure exceeds $p = 4.20 \times 10^0$ Pa, whereas for helium, the decline occurs beyond $p = 2.67 \times 10^1$.

A similar situation arises for a 5.0 mm contact gap. When air is dosed into the vacuum interrupter, the constant electric strength is sustained until a pressure of approximately $p = 3.0 \times 10^0$ Pa, reaching approximately 46.0 kV. In the case of helium-filled interrupters, a similar constant electric strength is maintained, but up to a pressure of approximately $p = 1.37 \times 10^1$ Pa.

Table 11.4. Comparison of the breakdown voltages U_{db} of vacuum interrupters filled with air and helium, contact gaps 1.0 to 5.0 mm and pressure $p_{ref} = 2.00 \times 10^1$ Pa

Electrode Spacing d_{db} , mm	Breakdown Voltage U_{db} , kV	
	Residual Gas Type	
	Air	Helium
	$p_{ref} = 2.0 \times 10^1$ Pa	
1.0	$U_{db(Air)} = 1.20$	$U_{db(He)} = 3.50$
2.0	$U_{db(Air)} = 0.90$	$U_{db(He)} = 8.00$
3.0	$U_{db(Air)} = 1.10$	$U_{db(He)} = 27.00$
4.0	$U_{db(Air)} = 1.00$	$U_{db(He)} = 31.00$
5.0	$U_{db(Air)} = 1.00$	$U_{db(He)} = 40.00$

To demonstrate the superior insulation capabilities of the helium-filled vacuum interrupter at higher internal pressures in comparison to the air-filled interrupter, a comparison was conducted across various contact gaps ranging from 1.0 mm to 5.0 mm. A specific reference pressure value, $p_{ref} = 2.0 \times 10^1$ Pa, was selected, and the breakdown voltages U_{db} for both residual gases were compared. At the reference pressure, the insulating properties of the air-filled vacuum interrupter were compromised for all tested contact gaps. Conversely, the helium-filled interrupter maintained its insulation properties at a satisfactory level. The measured values for this analysis are consolidated in Table 11.4.

Summary

Based on the conducted tests on vacuum interrupters filled with air and helium, it was observed that the interrupter filled with helium retains its full switching capability over a wider range of pressures. These findings hold promise as they indicate the potential to increase the operating pressure of vacuum interrupters. Currently manufactured vacuum interrupters have a rated operating pressure of approximately 1.0×10^{-3} Pa. However, the proposed insulating medium discussed in this article enables a significant increase in the pressure inside the interrupter. This advancement offers several advantages, including easier maintenance of the vacuum interrupters' tightness in switching devices and a reduction in switching overvoltages experienced in power systems. Furthermore, the complete elimination of harmful greenhouse gases like SF₆ aligns with the European Union's current climate policy.

11.5. Vacuum switchgear pressure measurement in Smart Grid networks

Mentor: *Paweł Węgierek*

PhD student: *Damian Kostyła*

Introduction

The constantly increasing demand for electricity, resulting from rising standards of living, urbanisation or technological progress, makes it necessary, in order to efficiently manage the network and eliminate potential interruptions in supply, to use devices supporting the supervision of the extensive, often difficult to access electrical power infrastructure. The vast majority of electricity consumption takes place in cities, as up to 80% of the energy produced is used in urban agglomerations, which has an impact on the environment. The high consumption of electricity from conventional grids releases significant amounts of greenhouse gases [271, 272].

Popular power grids limit their function to the generation, transport and verification of electricity consumption [273], which makes them susceptible to failures and, consequently, to interruptions in electricity supply causing an increase in reliability indices. In the current electricity grids, an insufficient amount of apparatus monitoring and controlling network parameters in real time is apparent, which significantly hinders the creation of a smart transmission network that bases its operation precisely on parameters read in real time. Efficient use of electricity and increasing the significance of “green energy” in the power system will make it possible to reduce carbon dioxide emissions into the atmosphere. The Smart Grid concept aims at monitoring as many network parameters as possible, enabling control of network resources in order to achieve

higher efficiency and increase energy security with an emphasis on economic and technical aspects of the network [274]. In order to make such a network possible, appropriate switching devices are necessary. EKTOS, an innovative overhead vacuum medium voltage switch disconnector in a closed construction, dedicated to Smart Grid, meets these requirements.

Despite the great interest in smart grids, there are still many aspects that can be improved and there are also many parameters that are not monitored in real time, which constitutes a research space for improving the operation of existing, as well as creating new, better, more efficient Smart Grids. This article presents the application of the EKTOS as a device ideally suited to Smart Grids through the use of innovative switching and measurement techniques.

The concept of Smart Grids

The Smart Grid concept has no specific date of origin, but has evolved with the development and evolution of electricity grids in response to the technical and operational challenges of monitoring and controlling the processes that take place during the transport of electricity from the power station to the consumer (Figure 11.16). Typically, the conversion of a conventional network to a Smart Grid necessitates the installation of a sufficient number of sensors to read the necessary network parameters. Initially, these sensors were used to provide information about the consumer back to the grid [274]. To understand the concept of smart grids, it is necessary to know what distinguishes a smart grid from a classic grid. The basic differences are shown in Table 11.5 [275].

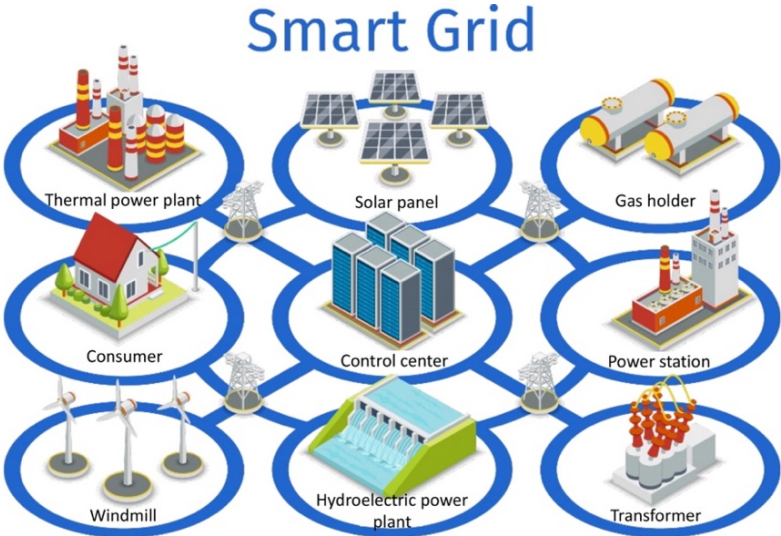


Figure 11.16. Smart Grid structure. Source: reprinted from [276], which is under Attribution 3.0 Unported (CC BY 3.0) license

Table 11.5. Installed photovoltaic capacity at the end of 2020 [275]

Smart Grid	Traditional electricity grid
Online bidirectional communication between cameras	One-way communication
Decentralised electricity generation system	Centralised form of electricity generation
Large number of extensive sensors installed in the network	Use of a small number of necessary sensors
Digital/electronic operation	Mechanical operation
Automatic monitoring and control	Manual monitoring and control
Wide range for adjustment	Limited adjustment possibilities
Cyber-security risks	No cyber security issues

Unfortunately, there is no single model for a smart grid, as its design is variable depending on the needs and data acquired. The National Institute of Standards and Technology in the United States has created an illustrative model of a smart grid including the relevant apparatus, communication between the elements of the apparatus, and technological requirements [276]. At the beginning of 2005, the European Union launched the European Technology Platform to promote smart grids on the old continent.

European countries have made a number of investments in response to this promotion. One of the first countries to respond to this promotion was Portugal, which implemented a management and control system into its grids as part of a pilot grid development programme [277, 278]. Much research on the optimisation of regulation and applied apparatus is carried out on the Apennine Peninsula [279, 280]. The University of Genoa is conducting extensive work to determine the optimal operation of multi-generation microgrids based on a mathematical model [281, 282]. On the other hand, the analysis of the benefits of converting conventional grids to Smart Grids in the context of the financial expenses incurred is the subject of research in the Czech Republic [283].

Smart Grid development

The prevailing trend in the utility power industry is to reduce the amount of equipment based on SF₆ as the insulating medium and to upgrade traditional networks to a smart grid, where the dispatcher's interference in reconfiguration processes is reduced to a minimum [284].

EKTOS – an innovative overhead vacuum medium voltage disconnecter in a closed housing dedicated to Smart Grids – meets technological and environmental requirements (Figure 11.17). EKTOS is an innovative device featuring environmental neutrality thanks to the elimination of sulphur hexafluoride from its design, as well as much better parameters than commercially available switching devices with a closed design. The use of innovative switchgear and distribution equipment also requires innovative measurement techniques allowing control of the state of the equipment. Taking into account the fact that the vast majority of the equipment used in modern Smart Grid networks is based on ecological extinguishing media, i.e., vacuum (similarly to EKTOS), the problem of control arises [285].

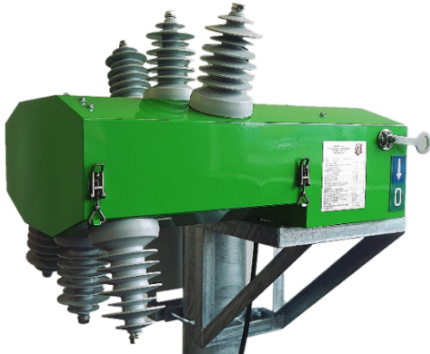


Figure 11.17. Illustration of the EKTOS disconnecter. Source: reprinted from [284], which is under Attribution 3.0 Unported (CC BY 3.0) license

Table 11.6. Comparison of conventional and EKTOS switch disconnectors [284]

EKTOS	Conventional apparatus
Electric arc extinguishing in vacuum	Electric arc extinction in SF6
Innovative motorised hopper drive	No known solution of this type
Innovative design to eliminate switching overvoltages	Creation of switching overvoltages during opening and closing operations
Nominal continuous current of 800A	Rated continuous current of max. 630 A
Rated short term withstand current 20 kA	Rated short term residual current max. 16 kA
Wide range adjustment	Limited adjustment possibilities
Cyber-security risks	No cyber security issues

Control of the pressure state in vacuum apparatus remains extremely important due to dielectric properties. Vacuum shows excellent insulating properties for pressures not exceeding 1 Pa, after pressure increases above this value the dielectric strength of the vacuum system decreases dramatically [285, 286]. The measurement of pressure in vacuum apparatus is the subject of research, which is confirmed by the number of publications on this subject [287]. Many traditional methods of pressure measurement in vacuum chambers are known; however, they are of low accuracy or impossible to use in operation.

The ideal solution to this problem is to develop a pressure monitoring system dedicated to vacuum equipment that allows online measurement.

Research work

Research work to be initiated in the near future will focus on the use of elastic bellows as an element to transmit deformation under an applied pressure load, allowing this deformation to be measured.

Bellows made of stainless steel, copper and nickel, and bronze and metal were selected for laboratory work. An important aspect of the laboratory work is the selection of bellows whose range of shape changes will be as large as possible in relation to the range of pressure changes in the system under study. The problem of using elastic bellows for pressure measurement is the assembly of the device in the measuring system and the non-linearity of deformation in the context of pressure changes. The bellows presented in Figure 11.18 has a maximum deflection over 4.5 mm and an elasticity of 8.3 N/mm.

A fibre optic Bragg grating, whose changes in the optical spectrum are read out using the optical spectrum analyser shown in Figure 11.19, is responsible for detecting the deformation of the bellows. The analyser has a wide spectral range up to 1620 nm with a dynamic range of more than 55 dB and an attenuation factor of 70 dB. Despite its many advantages, this instrument is not the best option for field measurements, mainly due to its high price and large size.



Figure 11.18. The elastic bellows used in the study. Source: own elaboration



Figure 11.19. Optical spectrum analyser. Source: own elaboration

As an alternative to measurements with an optical spectrum analyser, the construction of a measuring system is planned, which will enable direct reading of the deformation and thus the detection of any leak in the vacuum apparatus.

The vacuum pressure monitoring system must not interfere with the operation of the apparatus regardless of the operating state of the apparatus. Measurement must be possible in both normal and fault conditions.

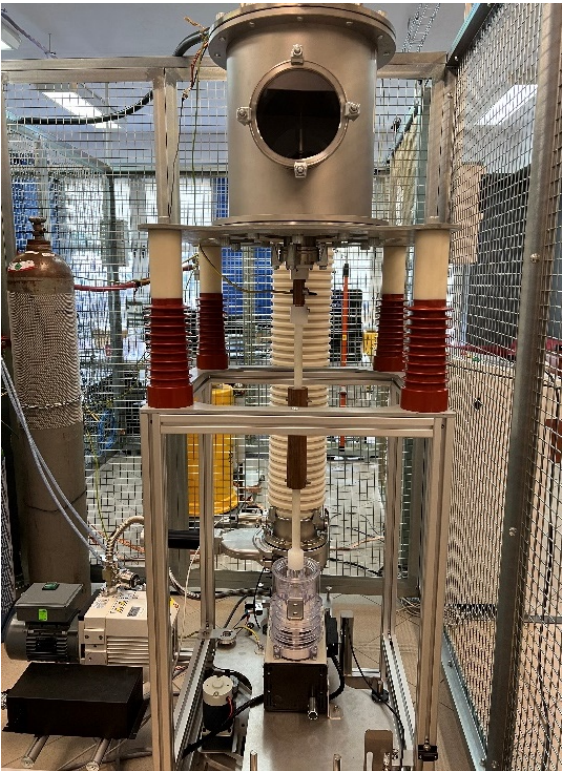


Figure 11.20. Demountable vacuum chamber. Source: own elaboration

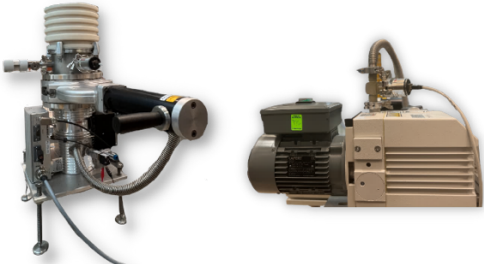


Figure 11.21. Vacuum pump set used in the research. Source: own elaboration

For testing the sensor in both cases, the demountable vacuum chamber is the ideal solution, thanks to which it is possible to implement the measuring system in the physical device in order to carry out measurements under conditions similar to those in nature. The demountable vacuum chamber, illustrated in Figure 11.20, allows observation of phenomena occurring inside the chamber thanks to two glass sights. The most important equipment during the work is the set of vacuum pumps shown in Figure 11.21. This is what makes it possible to achieve the nominal pressure in which modern vacuum chambers operate, i.e., 10^{-3} Pa. This pressure is achieved by running a rotary pump that reaches a pressure of 6×10^2 Pa and then attaching a turbomolecular pump that allows the pressure of 10^{-4} Pa to be reached. The pressure offered by the set of vacuum pumps mounted on the test bench is completely sufficient for research work, as the key element of the experimental work is the detection of the unsealing of the chamber, i.e., the increase in pressure above 1 Pa.

Conclusions

The development of an innovative fibre optic sensor for online vacuum pressure measurement fits perfectly into the Smart Grid concept. The system is a response to the needs of the electricity market and manufacturers of vacuum equipment.

The use of this pressure control system will reduce the reliability coefficients, planned, caused by maintenance work, and unplanned, caused by equipment failures that could not be foreseen and eliminated.

11.6. Bifacial photovoltaic panels in PV installations for increasing the efficiency of electricity generations

Mentor: *Pawel Węgierek*

Master's degree student: *Alicja Zielonka*

Introduction

Solar energy is one of the largest and most efficient types of renewable energy in the world. The natural power of the sun is exploited to produce electricity. Fossil fuel reserves are running out and the demand for energy is constantly increasing, which means that other ways of obtaining energy are being sought. This results in an increasing number of PV plants being installed.

When investing in photovoltaics, you should pay attention to the performance of the panels you install. Every PV installation works and produces energy all year round – they are efficient, during this time they convert from 15 to 20% of the sun's energy into usable energy; the amount depends on many factors. The use of bifacial photovoltaic panels can significantly increase the efficiency of the installed system.

Current state of photovoltaics in Poland

According to the Energy Market Agency, at the end of February 2022, the installed photovoltaic capacity in Poland was 8768 MW (more than twice as much as in February 2021, when the capacity was 4244 MW). In addition, more than 45,000 new PV installations were built, with a total capacity of 392.96 MW. In the renewables sector in 2022, PV ranks first with a 48% share, thus overtaking wind power for the first time [288]. The growth rate in Poland in the last four years was 114%, where the average in European countries is 10.3%. The installed photovoltaic capacity is increasing day by day, moreover for the last two years the rate is high [289] (Figure 11.22).

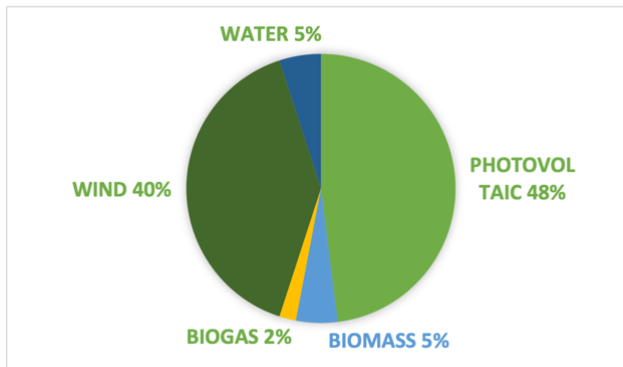


Figure 11.22. Installed photovoltaic capacity against RES in February 2022. Source: own elaboration based on [289]

Photovoltaics in Poland, compared to other countries in Europe, is prosumer-driven; a big reason for this is primarily the interest in generating energy on one's own and, thanks to subsidy programmes, in purchasing PV systems for households (e.g., 'Mój Prąd', 'Czyste powietrze') and businesses (e.g., the 'Energia Plus' programme). Previously, photovoltaics was not common in Poland; moreover, due to the high costs, not everyone could afford to purchase and install a PV system.

Photovoltaic installations

Photovoltaic installations can be divided on the basis of many different criteria, the most common division being the coupling of PV installations to the grid. The difference lies mainly in the configuration of the installation and the monetary input for energy production. The most general division of PV installations is as follows:

- on-grid installations,
- off-grid installations (not connected to the power grid).

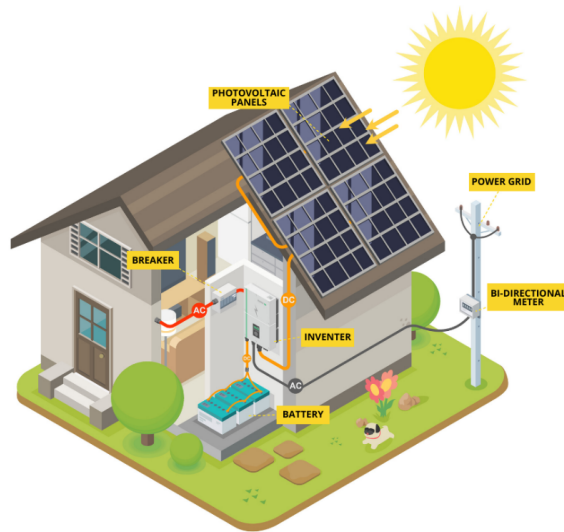


Figure 11.23. Components of a PV installation in a home. Source: own elaboration based on [290]

Each installation contains the same components, which are illustrated in Figure 11.23. These are the PV module, the energy receiver, appropriately selected auxiliary devices (e.g., inverter and charge controller), control or measurement tools, which are adjusted depending on the settings and application of the PV power plant [291, 292].

Photovoltaic installations in Poland

Photovoltaic installations account for the largest percentage of all renewable energy installations in Poland. Based on data from the Energy Regulatory Office, the number of photovoltaic micro-installations in Poland was about 460 thousand at the end of 2020. The installed capacity has been increasing regularly for more than six years, but in recent years growth dynamics and impact on the RES structure can be seen. According to forecasts, by 2030 the installed capacity will increase by about 6 GW, and in 2040 it will grow by almost 16 GW. The capacity of all RES sources in the power system is almost 10 GW [293]. In individual installations this is as is presented in Table 11.7.

Table 11.7. Installed photovoltaic capacity at the end of 2020 [289]

Type of installation	Installed capacity, MW
Micro installations	3.022
Small installations	0.065
Large installations	0.075

According to forecasts, by 2030 the installed capacity will increase by about 6 GW, and in 2040 it will grow by almost 16 GW. The capacity of all RES sources in the power system is almost 10 GW [293]. In individual installations this is as is presented in Table 11.7.

Micro-installations have the largest market share in Poland, with a total of 466,167 PV micro-installations in operation, representing 77% of all photovoltaic installations in the country. A large percentage are household installations [294]. The electrical output of small PV systems ranges from 50 kW to 500 kW. They represent about 36% of all PV installations installed in the previous year.

Large PV installations are those with a rated capacity of more than 4500 kW, and are mostly owned by corporate or industrial prosumers. Many plants have their own PV installation and produce electricity for their own needs, thus minimising the cost of purchasing electricity [293].

According to a report by the Institute for Renewable Energy, Poland ranks first place in the Europe in terms of the growth dynamics of photovoltaic capacity. This was determined on the basis of the integrated growth rate – CARG.

Photovoltaic panels

Photovoltaic panels are made up of individual solar cells that have two layers of semiconductor. The first layer is thin and semi-transparent with a negative electrode and an anti-reflective coating above it and a positive electrode underneath.

The second sheath is thicker than the first, both are separated by a suitably matched potential barrier which is based on p-n junctions. The basis of solar cell design is presented in Figure 11.24 [295]. When sunlight shines on a cell, it can be reflected, absorbed or pass through the cell, which consists of a semiconductor material. When the semiconductor is exposed to light, it absorbs energy and translates it into negatively charged electrons.



Figure 11.24. Construction of a photovoltaic cell. Source: own elaboration based on [295]

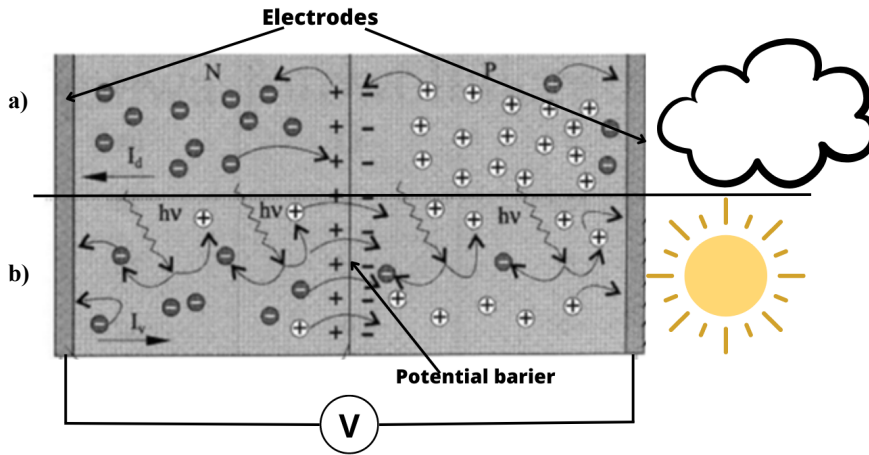


Figure 11.25. Photovoltaic mechanism: a) without lighting, b) with lighting. Source: own elaboration based on [296]

The excess energy allows the electrons to flow through the material in the form of an electric current. The metal contacts (lines on solar cells) draw current, which can later be used to power the house and the electrical grid [296]. The amount of electricity generated depends on the characteristics of the available light and a number of cell performance specifications [297]. A photovoltaic mechanism without and with light is depicted in Figure 11.25.

Comparison of photovoltaic modules

Bifacial panels generate solar energy from both sides of the module. Where classical panels do not have a transparent back and are single-sided, in bifacial panels both the front and back side of the solar cells are visible. According to technical data, when installed on a highly reflective surface (such as a white TPO roof or a floor of light-coloured stones), production can increase by up to 30% due to the generation of more electricity. Figure 11.26 a) and b) shows a single plane module and Figure 11.26 c) and d) a solar cell [298, 299].

Bifacial modules consist of a glass or transparent polymer sheet on the back side. Using both sides of the module, the panel has to be fixed on an aluminium frame, but the rigidity of the glass module is sufficient, so in some cases the frame is no longer needed, but only seals the edges. The mounting method depends on whether the module has a frame [298, 300].

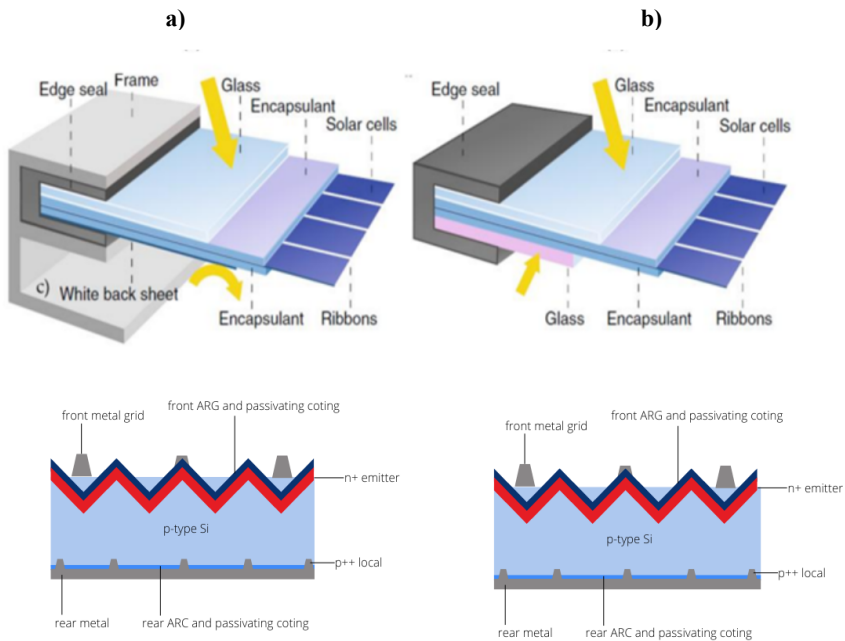


Figure 11.26. The difference of solar cells between a) single-sided module b) double-sided module and c) single-sided module (PERC) d) bifacial module (PERC). Source: own elaboration based on [301]

Simulation

Based on simulation results and theoretical questions, a comparative analysis of photovoltaic installations using single- and double-sided photovoltaic cells was carried out. The criteria taken into account were the angle of inclination in relation to the surface (in this case a flat roof) and the direction towards the Sun. The main objective of the project is to demonstrate the performance differences between single- and double-sided photovoltaic modules and to show that bifacial panels in photovoltaic installations increase their electricity generation efficiency.

The plants compared have the same inverters, the same number of modules and components, and are installed in the same building. The following variables were used in the simulation analysis: roof slope and orientation of the panels with respect to sunlight. The results of the annual reports have also been taken into account, focusing on the increased efficiency and energy production aspect of individual PV installations. In conclusion, the simulations aim to confirm the hypothesis and to present the conclusions drawn from the reports obtained.

The components used in the two installations studied are similar, resulting in a more detailed analysis and subsequent comparison of the designed PV installations between each other, taking into account not only the same shading at the location or weather conditions, but also other factors.

The photovoltaic system used for the comparison differed in the orientation of the photovoltaic modules arranged towards the southeast and southwest, as well as in the angle of arrangement in relation to the ground: 30°, 45°, 60° and 90°. According to the project, each installation has common parameters and elements:

- the location of the Faculty of Electrical Engineering and Computer Science building of Lublin University of Technology;
- LG photovoltaic panels used (single-sided LG Electronics Inc. LG335N1K-V5 335 W and bifacial - LG Electronics Inc. LG340N1T-V5 Bifacial 340);
- 30 modules (3 rows of 10 modules per row), generator output 10.05 kWp;
- inverter, model SUN2000-10KTL-M1 (380 Vac), Huawei Technologies.

Simulation results

Table 11.8 summarises the comparison of all different cases of simulations performed. The basic parameters on which the analysis was conducted, including not only the aforementioned tilt angle and the direction of the panels, but also the energy produced by the PV system, the coefficient of performance (PR), the share of solar energy in covering demand and reduction in efficiency due to shading. As the results show, both the tilt angle and the orientation of the modules contribute to the differences in system performance. The simulations clearly show how much the correct orientation of the modules with respect to the sun affects the performance of the PV system, especially for systems with double-sided modules, which are 12% more efficient than single-sided modules. Much better results are obtained for installations with panels facing southwest. For single-sided panels, the maximum efficiency was 76.5%, while the maximum efficiency of the system with double-sided panels was 81.8% (example 13, panel angle 30° to ground). Based on the results of the analysis presented in Table 11.8, it can be concluded that double-sided photovoltaic panels are distinguished by higher efficiency, performance, lower annual power losses and thermal efficiency compared to single-sided cells.

Another factor to be taken into account are the losses due to shading. Here again, the performance of bifacial panels is much better, with annual shading losses of only 9.0% in the best case and 32.8% in the worst case, compared to single-sided: 16.5% in the best and 48.1% in the worst cases.

Shading of PV systems not only leads to a significant reduction in their efficiency, but also to significant heating of the shaded parts. Figures 11.27 and 11.28 present visualisation of a PV installation with modules facing southwest on the roof of the Faculty of Electrical Engineering and Computer Science.

Table 11.8. Summary and comparison of all cases of simulations performed

Example	Inclination angle	Energy produced by the PV system (AC grid)	Performance Ratio (PR)	Reducing production by shading	Direction
	°	kWh/year	%	%/year	
SINGLE-SIDED MODULES					
generator output 10.2 kWp, area 51.4 m ² , number of modules 30, 1 inverter					
1	30°	9 733 kWh	76.5%	16.6%/ year	Southwest
2	45°	9 052 kWh	71.8%	21.8%/ year	
3	60°	7 724 kWh	64.8%	29.4%/ year	
4	90°	5 348 kWh	59.8%	35.0%/ year	
5	30°	7 992 kWh	75.3%	17.9%/ year	Southeast
6	45°	6 676 kWh	66.2%	27.8%/ year	
7	60°	5 585 kWh	59.8%	34.8%/ year	
8	90°	3 444 kWh	47.5%	48.1%/ year	
DOUBLE-SIDED MODULES					
generator output 10,2 kWp, area 51,4 m ² , number of modules 30, 1 inverter					
9	30°	11 243 kWh	81.8%	9.0%/year	Southwest
10	45°	10 419 kWh	74.6%	16.5%/year	
11	60°	9 304 kWh	68.6%	22.7%/year	
12	90°	7 500 kWh	58.4%	30.9%/year	
13	30°	8 638 kWh	74.2%	17.2%/year	Southeast
14	45°	7 476 kW	65.4%	26.4%/year	
15	60°	6 525 kWh	59.5%	32.5%/ year	
16	90°	7 719 kWh	53.1%	32.8%/year	



Figure 11.27. Visualisation of a PV installation with modules facing south-west on the roof of the Faculty of Electrical Engineering and Computer Science of LUT. Source: own elaboration

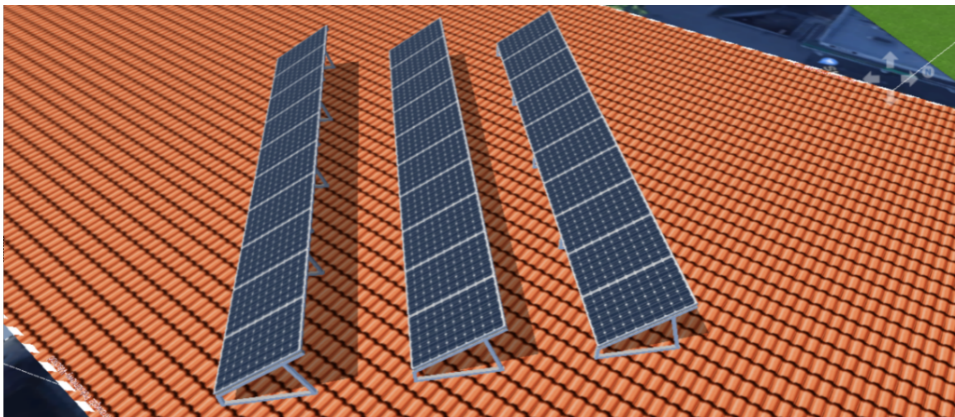


Figure 11.28. Visualisation of a PV installation with modules facing south-west on the roof of the Faculty of Electrical Engineering and Computer Science of Lublin University of Technology; close-up view on the installation. Source: own elaboration

In all simulations, the energy generated by the system exceeds the actual energy consumption, so that most of the energy can be fed back into the grid, thus generating a profit. Again, systems with PV modules installed on both sides lead the way. This is due to the high electricity consumption. Under the conditions prevailing in Poland, double-sided panels oriented at an angle of 30° to the ground and facing southwest are the most effective. This arrangement ensures that the installation will produce the greatest amount of electricity throughout the year. This is confirmed by individual data reports showing the amount of electricity produced per year.

Conclusion

Solar modules produce electricity and can be used both for personal use in private homes and in commercial buildings. To increase the efficiency of photovoltaic systems, the most important factors are the location, the angle of inclination to the Earth's surface and the orientation in relation to the Sun.

Photovoltaics are a rapidly developing technology with new components or changes every day. Solar panels, which are the most important part of a PV system, also need to be improved to work better and more efficiently and to overcome current limitations. New ways to increase the efficiency and effectiveness of the panels are constantly emerging. Bifacial solar panel technology is becoming increasingly important as they can generate energy from both sides. The biggest advantage of a bifacial photovoltaic module over a single-sided PV module is the higher total energy production.

Based on the designed installations, all cases have been analysed, simulating the annual electricity production and power growth depending on the position and angle of the panels. The performance of each installation is shown in a table comparing all calculated cases, taking into account the panel type. It shows that the most efficient photovoltaic in-plants are those with bifacial panels.

11.7. Executive elements and application of automation

Mentor: *Piotr Filipek*

Master's degree student: *Bartłomiej Stadnik*

Introduction

The word “automatics” covers both the mathematical theory of control and the more practical side of the word, i.e., the use of appropriate executive elements to control technological processes. Initially, automation developed with the aim of minimizing the chance of human error and shifting repetitive and monotonous activities onto machines. Gradually, the number of reasons for increasing the degree of automation of certain processes increased, e.g., much faster and more accurate performance of given activities than by a human, eliminating the risk of introducing contamination, the possibility of faster and more effective control and protection of production stages. To automate the technological process, engines, robots and sensors are used.

Executive elements of automation

Probably in nearly every production process there is a stage of transporting products by means of conveyor belts. Induction motors are most often used to drive them due to their low price, high reliability and simplicity of construction. In terms of energy savings, Europe's electricity consumption by conveyor systems is around 2% in the industrial sector and 11% in the tertiary sector [302]. The rotational speed of such motors can be controlled by scalar control method. In the case of using the conveyor belt drive motor, where the shaft load changes during operation and the it is important to hold a constant rotational speed, the control is vectorial. Vector control allows constant values of torque and speed to be maintained despite changes in the motor's load [303].

Table 11.9. Number of fractional power motors in EU for different industrial and tertiary sectors [302]

Nonmetallic mineral sector	313 650
Pulp paper and print	49 200
Food beverage and tobacco	2 851 100
Chemical	429 800
Machinery and metal	5 146 600
Iron and steel	388 700
Tertiary sector	15 791 600

Continuing with the conveyor belt example, we usually want to know, for example, how many products have been moved over time or where they are located. To obtain this knowledge, sensors are used that detect these products, depending on the electrical properties of the material from which the example product is made. A product made of a material which is a dielectric can be detected by capacitive sensors (Figure 11.29) which respond to a change in the electric field when the detected object is introduced in front of the sensor face. The electric field in such a sensor is created by two electrodes that are arranged concentrically.

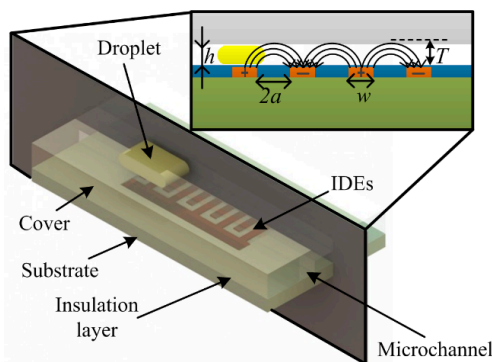


Figure 11.29. Structure of the sensing elements and cross-section of the capacitive sensor, showing how distinct materials cross the sensing area and the electrical field lines. Source: reprinted from [304], which is under Attribution 3.0 Unported (CC BY 3.0) license

In the event that the object we want to detect is made of metal, an inductive sensor can be used, which works in a similar way as a capacitive sensor, but the detecting field is a magnetic field. The coil of the inductive sensor generates a magnetic field of a specific energy; when the detected object is introduced into this field, i.e., in front of the sensor, the object will absorb some of the energy, which will be immediately detected by the sensor.

Reflective photoelectric sensors are also popular sensors [305]. Such sensors are often used e.g., in machine door security systems to monitor that they are closed. Such sensors consist of a transmitter and a receiver, housed in the same housing. For example, they can be mounted on the door frame, when the door is open, it will not impact the luminous flux emitted by the transmitter, when it is closed, the door will reflect the beam, the receiver will detect it and send an appropriate signal.

Signals from these sensors contribute to the control of individual stages of the technological process. The control is carried out by a programmed PLC (programmable logic controller), which is based on a microprocessor and allows you to perform functions such as logic, counting, counting time or data storage. The PLC controller is the brain of each automated process, collects signals from individual sensors, through the implemented program, at appropriate times through the controller outputs, it can turn on the operation of e.g., a belt-thrust engine, turn off the operation of the entire machine by detecting open doors, and provide the operator with parameters from read sensors. The program for the controller is most often created in the Ladder Diagram, Function Block Diagram or Instruction list language.

While discussing the PLC, it is also worth mentioning the topic of HMI panels. The HMI (Human-Machine Interface) panel is a touch panel with an interface for the machine operator. Such a panel makes it possible to preview the displayed data collected from the controller controlling a certain industrial process, to supervise the performance indicators, as well as the inputs and outputs of the controller [306, 307]. The typical PLC cycle is shown in Figure 11.30. Through the HMI communicating with the PLC, apart from monitoring information, it is also possible to perform more radical operations, such as complete shutdown of the machine, acceleration of production [306].

CPU Operating Cycle

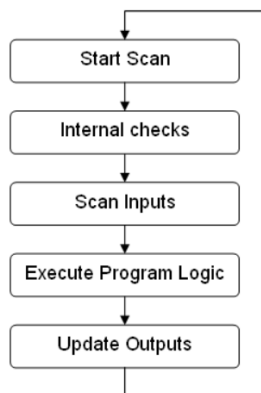


Figure 11.30. Typical PLC operating cycle. Source: own elaboration based on [307]

Robots have also become an inseparable element of production lines. Currently, robots are very accurate and fast, and due to the possibility of using various types of grippers, they can be used in many processes, e.g., transferring a large number of materials at once, welding car parts, welding or surfacing (Figure 11.31).



Figure 11.31. The scale of using robots in the automation of industrial processes. Source: reprinted from shutterstock.com after obtaining a standard license (for journalistic use only)

It is possible for a robot to cooperate with vision systems that allow tracking and capturing appropriate objects, e.g., on a conveyor belt. The robots are also characterised by hygienic working conditions, the ability to work in cold stores and resistance to water and cleaning agents when used in the food industry. The first robot installed in an automated production process was in Japan in 1996, the Motoman SV035 robot, which was to follow the production line [308].

Application of automatic control system for the production of plates

The sheet metal sector constitutes a significant part of the products of the steel industry and has a great influence on the national economy. With constantly changing product requirements and the complexity of the process, creating a control system for an automated panel production line is problematic.

In the past, only a few pioneering companies in the automation industry could afford it, but this changed after the standardisation of working elements and the continuous development of the field of automation. The paper [309] describes in detail a plate production line working process. The slabs formed by continuous casting are then sent for reheating in the furnace, after reheating, the slabs are descaled with limescale. In the next step, the plates are rolled by rolling mills

equipped with appropriate systems for controlling the thickness of the plates. The plates are cooled, then flattened again while hot, and transferred to the bed where they cool freely. After cooling, the boards are cut to appropriate measurements and sent to the warehouse.

Typically, the control system of such a production line is spread over several levels. The first level includes the basic automation system, includes control sequences and the control functions of a dedicated production unit. This ensures that the unit is working properly and coordinated. The second level is responsible for process automation and supervises the process in a dedicated unit, i.e., the area of the rolling mill. This level is to determine the appropriate settings for the control in the first level. The communication, tracking and information management functions are also performed at this level. The third level is the production execution system, which is where production control takes place. Figure 11.32 shows a practical control system for the panel production process. The third level consists of two PLCs: SIMATIC S7-400 is responsible for logical and sequential control of actuators, while SIMATIC TD PLC is used for technological control of the mill.

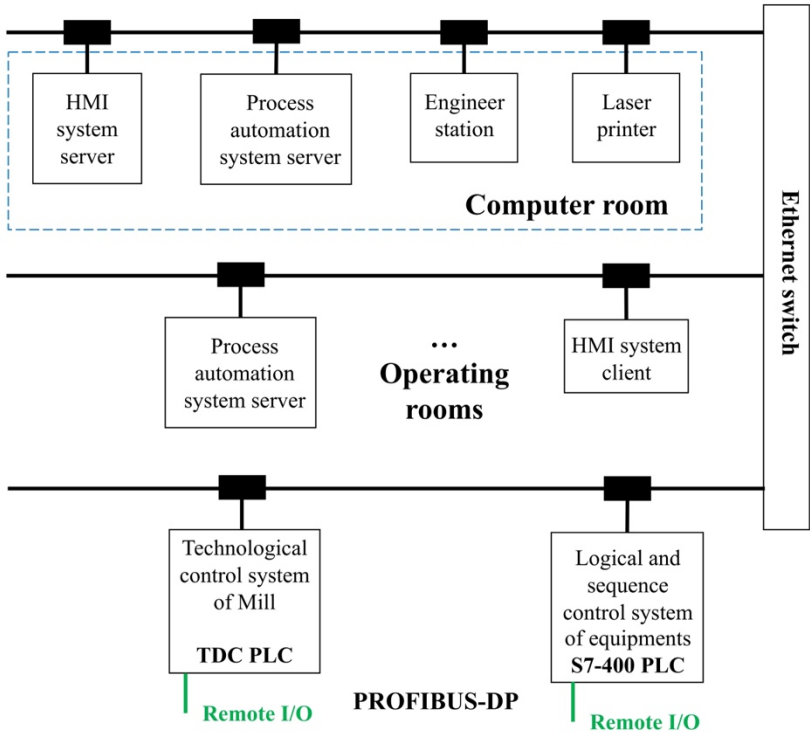


Figure 11.32. Individual levels of the automatic control system. Source: own elaboration based on [309]

The third level consists of two PLCs: SIMATIC S7-400 is responsible for logical and sequential control of actuators, while SIMATIC TD PLC is used for technological control of the mill. The controllers are connected to the actuators via PROFIBUS-DP. The individual levels of the control system communicate with each other via the Ethernet Switch. It can also be noticed that the second level, i.e., the HMI panels, are located in the operator's rooms so that the operators have access to them. The first level is where the servers, PC or printer are located in another room. In this production line, the rolling mill automation system controls the roller table, main control, roll change control, material tracking, real data handling, gap control, hydraulic control of the gap width and control of the mill stand [309].

The plate production line control system has been used in several factories in China. The system does not cause problems and the production efficiency is at a high level (Table 11.10). One mill with a diameter of 3500 mm produces over 100,000 tons of product per month. The quality of the product is determined on the basis of how accurately the thickness of the sheet was produced.

Table 11.10. Guaranteed value of the accuracy of the plate thickness of the described production line [309]

	Production target thickness range (mm)	Thickness tolerance (mm)
Thickness accuracy along one plate length	$6 \leq h \leq 10$	≤ 0.08
	$10 < h \leq 20$	≤ 0.10
	$20 < h \leq 30$	≤ 0.12
	$30 < h \leq 50$	≤ 0.16
	$50 < h$	≤ 0.24
Thickness accuracy for different plates	$6 \leq h \leq 10$	≤ 0.10
	$10 < h \leq 20$	≤ 0.12
	$20 < h \leq 30$	≤ 0.15
	$30 < h \leq 50$	≤ 0.20
	$50 < h$	≤ 0.30

Semi-autonomous robot for library management

One of the tasks of process automation is to dump repetitive, monotonous, and often time-consuming tasks onto machines. A robot has been developed that carries out the process of returning books to the appropriate shelves itself [310]. This robot will be able to retrieve the book, identify the shelf location by scanning the tag where that book should be put away, and then move to that shelf to put the book back in its place.

The chassis frame is made of steel profiles, it is required to stabilise the base and provide a rigid structure for the rest of the robot structure and components. The books are stacked in a special container, which is equipped with a rotating platform, which is driven by a stepper motor. This platform is used to properly position the book so that the gripper can pick up the book to put away. After retrieving the book from the container, the actuator pushes the remaining books to fill the space. The books are put down thanks to a crank-slide mechanism with a gripper that takes the book from the container. The gripper, by attaching it to the slider, can move linearly in 20 cm increments. The grapple is located on a platform that is raised by a scissor lift. The stepper motor is responsible for the operation of the lift.

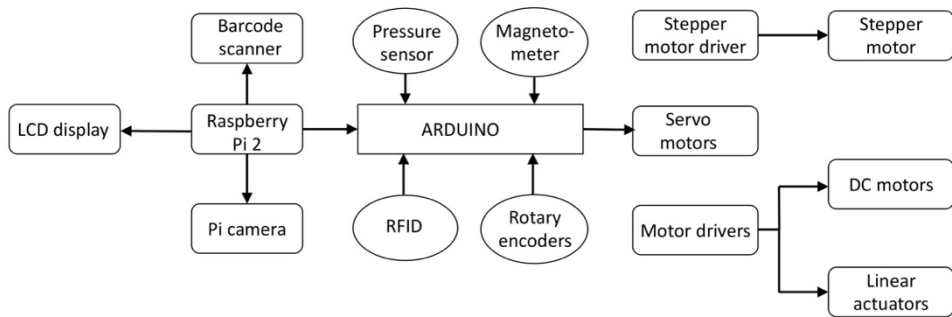


Figure 11.33. Embedded system architecture. Source: own elaboration based on [310]

To ensure good manoeuvrability and a zero turning radius, a skid steer drive was used. Each wheel has a radius of 5 cm, and the wheels are driven at different speeds in both directions, independently of each other. DC motors attached to the chassis were used to drive the wheels.

The Figure 11.33 shows the architecture of the system that powers peripherals and reads environmental variables. It operates on the basis of commands generated by the software. The drive motors and linear actuator are powered by a three-cell 11.1 V battery. The same battery also powers the sensors and motor controllers after the voltage is properly regulated by a DC-DC converter. To ensure high torque on the shaft of stepper motors, they are powered by a second battery, 6-cell with a voltage of 22.2 V. The model is equipped with a barcode scanner that reads the barcodes on each book to obtain information about its location. An RFID sensor has been attached to the chassis, which reads RFID tags placed at the junctions of the library. This is to create a mapping tree so that the robot can move along the shelves. A pressure sensor on the gripper was also used to make sure that the book is properly held. A Raspberry Pi camera has been installed at the front of the robot to catch lines on the floor along which the robot is to move.

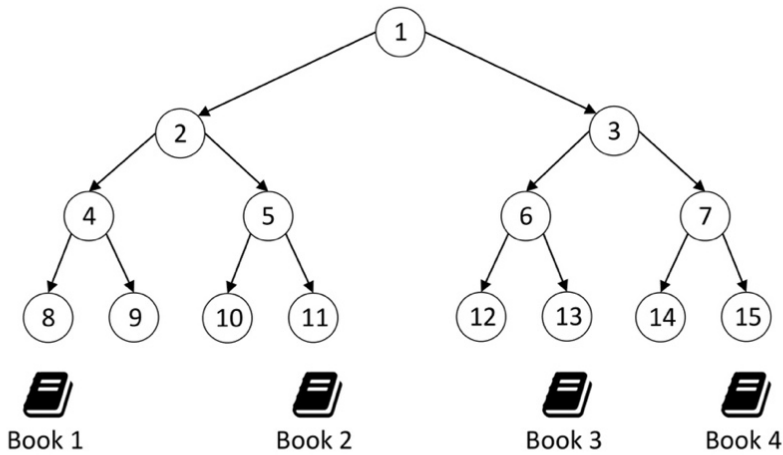


Figure 11.34. Example of pathing. Source: own elaboration based on [310]

At the beginning of each run, a one-dimensional table of sequential nodes is generated. The barcodes read from books provide information about the assigned shelf according to the mapping established during configuration. Then, the optimal path that the robot should travel to put away all the books is analysed.

Figure 11.34 shows a map of nodes, some of which are shelves – this information is obtained after scanning the code on a book – and some are junctions, which are identified by the RFID sensor detecting RFID tags on the floor. Book 4, the last in the robot’s container, will be the first to be put on the shelf. For example, the path to Book 4 would be 1-3-7-15, similarly for the rest of the books it would be 1-2-4-8, 1-2-5-11, and 1-3-6-13. After the robot returns to Book 4, the next book will be Book 3, and so on. Finally, the path will be 1-3-7-15-7-3-6-13-6-3-1-2-5-11-5-2-4-8-4-2-1.

Summary

Recently, the automation of industrial processes not only allows the human factor to be minimised, but also to completely eliminate it, and mainly allows multiple accelerations and improvements of production, standardisation of the product through repeatability and production in conditions unbearable for humans. Today, in addition to the automation of industrial processes, automated machines have started to replace people in quite trivial positions, such as e.g., a supermarket cashier or in library services, as in the case discussed.

12. Summary

The progressive increase in demand for electricity brings with it challenges for the power industry in order to develop technologies allowing efficient and environmentally compatible energy generation. Unfortunately, neither energy systems nor the environment are developing in a sustainable manner. Most energy systems are based on the production of energy from non-renewable sources. A significant part of the power contained in the fuel is irretrievably lost, the quality of the energy deteriorates, and the emission of fossil fuel combustion products into the atmosphere pollutes the natural environment.

Air pollution is the biggest environmental problem because combustion products in the form of volatile carbon compounds, sulphur and nitrogen are often transported by the wind to regions distant from the place where they are produced. There, reacting with the moisture in the atmosphere, they form acids and get into surface waters through rainfall, causing acidification of the environment, damaging vegetation and adversely affecting water resources and soil. We can observe many examples of the negative impact of technology and human activity on water quality, which covers large areas and huge amounts of water bodies. One of such phenomena is industrial and municipal waste, including toxic waste, the storage, neutralisation and utilisation of which causes air, surface and groundwater and soil pollution. Soil and land are also subject to adverse impacts related to agricultural activity and the use of artificial fertilisers, which significantly contribute to the deterioration of their biological and chemical quality.

Currently, the greatest potential of energy systems development lies in the use of renewable energy sources, in particular solar energy. Another is the improvement of the efficiency of conventional electricity generation systems through the use of heat and electricity cogeneration. Great hopes are placed on the use of fuel cells and superconducting electrical energy storage systems. In the case of environmental protection systems, technologies using low-temperature atmospheric pressure plasma demonstrate great potential to solve the problems of air, water, lands and soil pollution.

Thanks to the proper use of various electromagnetic technologies, including superconductivity, plasma, electromagnetic compatibility, electrostatics, electronic and nanomaterials, electromobility, photovoltaics, smart grids and electricity management, power losses related to the production, distribution and use of energy have been reduced, and the emission of harmful compounds has been partially inhibited as well. Many problems are still waiting to be solved and electromagnetic technologies can contribute to improving this situation.

This book presents selected advanced technologies to solve the energy and environmental problems that both Poland and Japan have in common and that require interdisciplinary and international cooperation.

The implementation of the *Pol-Jap Energo-Eco Studies and Expert Visits* project within the framework of NAWA program on Academic International Partnership provides an opportunity to overcome these problems and to train a new generation of engineers and scientists who understand the problems of sustainable energy and environmental development and are open to such cooperation.

References

1. Martenson, A., *Energy use-for what?*, [In:] Series of Booklets from The Baltic University Programme: Energy. From Fossil Fuels to Sustainable Energy Resources, ed. J. Salay, Lund University, Lund, Sweden, 1996.
2. Harrison, R. M. *Pollution-Causes, Effects and Control*, Cambridge, UK, The Royal Society of Chemistry, 1996.
3. Eren H., *Environmental Impacts of Technology*, ed. J. Webster, Hoboken NJ, USA, John Wiley & Sons, Inc., 2001.
4. Dudley, B. *BP Statistical Review of World Energy*; BP Statistical Review: London, UK, 2019.
5. *EU Focus on Clean Air*; Publication of European Commission; EU: Brussels, Belgium, 2006.
6. Halit E., *Environmental Impact of Technology*, [In:] Wiley Encyclopedia of Electrical and Electronic Engineering, ed. J. Wenster, Hoboken NJ, USA, John Wiley & Sons, Inc., 1999, p. 1–33. DOI: <https://doi.org/10.1002/047134608X.W7303>
7. Harrison R. M., *Pollution Causes, effects and control*, Cambridge, UK, The Royal Society of Chemistry, 1996.
8. Lieberman M. A., Lichtenberg A.J., *Principles of Plasma Discharges and Materials Processing*, Hoboken NJ, USA, John Wiley & Sons, Inc. 1994.
9. Kordus A., *Plasma. Properties and application in techniques*, Warsaw, WNT, 1985 (in Polish).
10. Low Temperature Plasmas. Fundamentals, Technologies and Techniques; volume 1 and 2, Second Revised and Enlarged Editions; Edited by Hipler R., Kersten H., Schmidt, M., Schoenbach K. H.; ISBN: 978-3-527-40673-9, March 2008, 945 pages.
11. Krall N. A., Trivelpiece A. W., *Principles of Plasma Physics*, San Francisco, USA, San Francisco Press Inc., 1986.
12. Jingru Y., Zilong Z., Yiyang Z., Junqin L., Xuemei Z., *Experimental study of single-electron detachment for Cu, Ag, Au, Co, and Ir in collisions with Kr and Xe*, “Atomic Data and Nuclear Data Tables”, 2014, vol. 100, no. 5, p. 1189–1196. DOI: <https://doi.org/10.1016/j.adt.2014.02.005>
13. Becker H., Kogelschatz U., Schoenbach K. H., *Non-equilibrium Air Plasmas at Atmospheric Pressure*, Boca Raton Florida USA, CRC Press, 2004.
14. Stryczewska H.D., Stepień M.A., Boiko O., *Plasma and Superconductivity for the Sustainable Development of Energy and the Environment*, “Energies” 2022, vol. 15, no. 11, art. no. 4092. DOI: <https://doi.org/10.3390/en15114092>
15. Stryczewska H. D., *Plasma Technologies in Energy and Environmental Engineering*, Lublin, Poland, Electrotechnical Committee of Polish Academy of Science PAN, 2009 (in Polish).
16. Penetrante, M.; Schultheis, S.E. (Eds.) *Non-Thermal Plasma Techniques for Pollution Control, Part. A: Overview, Fundamentals and Supporting Technologies*; NATO ASI Series G: Ecological Science; Springer: Berlin/Heidelberg, Germany, 1993; Volume 34.
17. Bogaerts A., Neyts E.C., *Plasma Technology: An Emerging Technology for Energy Storage*, “ACS Energy Letters”, 2018, vol. 3, p. 1013–1027. DOI: <https://doi.org/10.1021/acsenenergylett.8b00184>.
18. Gherardi N., Gouda G., Gat E., Ricard A., Massines A., *Transition from glow silent discharge to micro-discharges in nitrogen gas*, “Plasma Sources Science and Technology”, 2000, vol. 9, p. 340–346. DOI: <https://doi.org/10.1088/0963-0252/9/3/312>
19. Stryczewska H.D., Boiko O., *Applications of Plasma Produced with Electrical Discharges in Gases for Agriculture and Biomedicine*, “Applied Sciences”, 2022, vol. 12, no. 9, art. no. 4405. DOI: <https://doi.org/10.3390/app12094405>
20. Dors M., Kurzyńska D., *Tar Removal by Nanosecond Pulsed Dielectric Barrier Discharge*, “Applied Sciences”, 2020, vol. 10, art. no. 991. <https://doi.org/10.3390/app10030991>
21. Yasuoka K., Endo Y., Ishii S., *Experimental study on ozone generation using DC driven microplasma*, [In:] Proceedings of HAKONE 8: International Symposium on High Pressure, Low Temperature Plasma Chemistry, Puhajarve, Estonia, 21-25 July, 2002.

22. Mitsugi F., Furukawa J., Ohshima T., Kawasaki H., Kawasaki T., Aoqui S., Stryczewska H.D., *Observation of dynamic behavior of gliding arc discharge*, "The European Physical Journal - Applied Physics", 2013, vol. 61, no. 2, art. no. 24308.
DOI: <https://doi.org/10.1051/epjap/2012120408>
23. Matsuura T., Taniguchi K., Watanabe T., A New Type of Arc Plasma Reactor with Twelve-Phase Alternating Current Discharge for Synthesis of Carbon Nanotubes, Proceedings of 17th International Symposium on Plasma Chemistry, Toronto, Canada, August 7–12, 2005.
24. Czernichowski A., Gliding Discharge Reactor for H₂S Valorization or Destruction. In Non-Thermal Plasma Techniques for Pollution Control, Part. A: Overview, Fundamentals and Supporting Technologies, Proceedings of the NATO Advanced Research Work-shop on Non-Thermal Plasma Techniques for Pollution Control, held at Cambridge, UK, 21–25 September 1992; Penetrante, M., Schultheis, S.E., Eds.; NATO ASI Series G: Ecological Science; Springer: Berlin/Heidelberg, Germany, 1992; Volume 34, p. 393
25. Lesueur H., Czernichowski A., Chapelle J., *Apparatus for generation of low temperature plasmas by the formation of gliding arc discharges*, Patent Application, France, National registration No 8814932, 1990.
26. Stryczewska H. D., Janowski T. Komarzyniec G., *Gliding Arc Discharge in the Triple-Electrode System*, "Acta Agrophysica", 2002, vol. 80, p. 63–70.
27. Rutberg Ph. G., Safronov A. A., Popov S. D., Surov A. V., Nakonechny Gh. V., *Investigation of voltage and current variations in a multiphase AC electric arc system*, 12th International Congress on Plasma Physics, Nice, France 25–29 October 2004.
28. Stryczewska H. D., *Electromagnetic power supply system for plasma reactors with gliding arc discharge*, Lublin, Poland, Lublin University of Technology, 1998 - habilitation monograph (in Polish).
29. Boeck W., Pfeiffer W., *Conduction and Breakdown in Gases*, Hoboken NJ, USA, John Wiley & Sons Inc., 1999.
30. Komarzyniec G., *Analysis of the operation of a five-column transformer in the arc power supply system of a plasma reactor*, Lublin, Poland, Lublin University of Technology, 2008 – doctoral dissertation (in Polish).
31. Królikowski C., *Technique of connecting electric power circuits*, Warsaw, PWN, 1990 (in Polish).
32. Ciok Z., *Mathematical models of the switching arc*, Warsaw, PWN, 1987 (in Polish).
33. Stryczewska H.D., *Cold Plasma Technologies. Generation, Modeling and Applications*, "Prace Naukowe Politechniki Śląskiej. Elektryka", 2011, vol. 217, no. 1, p. 41–61 (in Polish).
34. Jaroszyński L., *Analysis of a plasma arc reactor using the nonlinearity of the magnetic core of power supply transformers*, Lublin, Poland, Lublin University of Technology, 2000 – doctoral dissertation (in Polish).
35. Sawicki A., *A Modified Mayr-Pentegov Model of the Electric Arc with Dynamically Variable Parameters*, "Acta Energetica", 2020, vol. 3, no. 44, p. 8–15.
36. Diatczyk J., *Study of the temperature field in the discharge chamber of a plasma reactor*, Lublin, Poland, Lublin University of Technology, 2007 – doctoral dissertation (in Polish).
37. Diatczyk J., Stryczewska H. D., Komarzyniec G., *Modeling of the temperature distribution in arc discharge plasma reactor*, "Journal of AOTs", 2006, vol. 9, no 2, p. 171–178.
38. Stryczewska H. D., *Supply Systems of Non-Thermal Plasma Reactors. Construction Review with Examples of Applications*, "Applied Sciences", 2020, vol. 10, no. 9, art. no. 3242.
DOI: <https://doi.org/10.3390/app10093242>
39. Stryczewska H. D., *Analysis of integrated electromagnetic power supplies for discharge devices*, Lublin, Poland, Lublin University of Technology, 1996, pp.132 (in Polish).
40. Stryczewska H. D., Jakubowski T., Kalisiak S., Gizewski T., Pawlat J., *Power systems of plasma reactors for non-thermal plasma generation*, "Journal of Advanced Oxidation Technologies", 2013, vol. 16, p. 52-62. DOI: <https://doi.org/10.1515/jaots-2013-0105>
41. Stryczewska H., *Power System of Low Temperature Plasma Reactor*, Urząd Patentowy Rzeczypospolitej Polskiej, patent PL180063, approved 29.12.2000 r.
42. Stryczewska H., Janowski T., *Plasma Reactor Power Supply*, Urząd Patentowy Rzeczypospolitej Polskiej, patent PL193498, approved 28.02.2007 r.

43. Krupski P., Stryczewska H., *Układ i sposób zasilania reaktora plazmowego ze ślizgającym się wyladowaniem*, Urząd Patentowy Rzeczypospolitej Polskiej, patent B1 233868, approved 31.12.2019 r.
44. Diatczyk J., *Modeling discharge length for GA plasma reactor*, "Przegląd Elektrotechniczny", 2012, vol. 88, no. 6, p. 89–91.
45. Baba T., Takeuchi Y., Stryczewska H.D., Aoqui S., *Study of 6 electrodes gliding arc discharge configuration*, "Przegląd Elektrotechniczny", 2012, vol. 88, p. 86–88.
46. Krupski P., *Analysis of cooperation of the converter supply system with the miniature non-thermal plasma generator*, Lublin, Poland, Lublin University of Technology, 2019 – doctoral dissertation (in Polish).
47. Stryczewska H. D., Sikorski A., Ruszczyk A., Komarzyniec G., *Gliding arc plasma reactor supplied from AC/DC/AC inverter*, [In:] 18th International Symposium on Plasma Chemistry, Kyoto, Japan, August 26 – 31, 2007.
48. Komarzyniec G., Aftyka M., *Operating Problems of Arc Plasma Reactors Powered by AC/DC/AC Converters*, "Applied Sciences", 2020, vol. 10, no. 9, art. no. 3295; DOI: <https://doi.org/10.3390/app10093295>
49. Zhang H., Ma D., Qiu R., Tang Y., Du C. *Non-thermal plasma technology for organic contaminated soil remediation: A review*, "Chemical Engineering Journal", 2017, vol. 313, p. 157–170. DOI: <https://doi.org/10.1016/J.CEJ.2016.12.067>
50. Mitsugi F., Nagatomo T., Takigawa K., Sakai T., Ikegami T., Nagahama K., Ebihara K., Sung T., Teii S., *Properties of soil treated with ozone generated by surface discharge*, "IEEE Transactions on Plasma Science", 2014, vol. 42, no. 12, p. 3706–3711. DOI: <https://doi.org/10.1109/TPS.2014.2350533>.
51. Mitsugi F., Ebihara K., Aoqui S., Stryczewska H. D., *Review of Developments in Application of Ozone in Agriculture*, [In:] 16th High Pressure Low Temperature Plasma Chemistry Symposium HAKONE XVI, Beijing, China, September 2–7, 2018.
52. Szymański Ł., Kolacinski Z., Raniszewski G., *Influence of Contaminants on Arc Properties during Treatment of Polluted Soils in Electric Arc Plasma*, "Journal of Advanced Oxidation Technologies", 2012, vol. 15, p. 34–40. DOI: <https://doi.org/10.1515/jaots-2012-0104>
53. Stryczewska H. D., Ebihara K., Muszański R., *Mobile installations of air, water and soil treatment with ozone*, [In:] 23rd International Conference on Advanced Oxidation Technologies for Treatment of Water, Air and Soil-(AOTs-23), Clearwater Beach, Florida, USA, 2017, pp. 43–44.
54. Yamashita Y., Yamashita T., Hashimoto Y., Ebihara K., Mitsugi F., Ikegami T., Stryczewska H. D., Pawłat J., Teil S., Sung T. L., *Backpack-type ozone-mist sterilization system developed for non-chemical agriculture processes*, [In:] 8th International Conference ELMECO-8 Electromagnetic Devices and Processes in Environment Protection, 28 September –1 October, Nałęczów, Poland, 2014.
55. Ebihara K.; Takayama M.; Stryczewska H. D.; Ikegami T.; Gyouotoku Y.; Tachibana M., *Wide range concentration control of dielectric barrier discharge generated ozone for soil sterilization*, "IEEJ Transactions on Fundamentals and Materials", 2006, vol. 126, p. 963-969. <https://doi.org/10.1541/-ieejfms.126.963>
56. Pawłat J.; Stryczewska H. D.; Ebihara K., *Sterilization Techniques for Soil Remediation and Agriculture Based on Ozone and AOP*, "Journal of Advanced Oxidation Technologies", 2010, vol. 13, p.138–145. DOI: <https://doi.org/10.1515/jaots-2010-0201>
57. Stryczewska H. D.; Pawłat J., Ebihara K., *Non-thermal plasma aided soil decontamination*, "Journal of Advanced Oxidation Technologies", 2013, vol. 16, p. 23–30. DOI: <https://doi.org/10.1515/jaots-2013-0103>
58. Pawłat J., Stryczewska H. D., Ebihara K., Mitsugi F., Sung T., *AOTs and solar energy for air, water and soil treatment*, "Transactions of the Materials Research Society of Japan", 2014, vol. 39, p. 117–120. DOI: <https://doi.org/10.14723/-tmrsj.39.117>

59. Plasma for Bio-Decontamination, Medicine and Food Security. Proceedings of the NATO Advanced Research Workshop on Plasma for Bio-Decontamination, Medicine and Food Security, Demänovská Dolina, Slovakia, 15–18 March 2011, eds: Machala, Z., Hensel K., Akishev Yu.; Springer: Dordrecht, The Netherlands, 2012. <https://doi.org/10.1007/978-94-007-2852-3>.
60. Domonkos M., Tichá P., Trejbal J., Demo P., *Applications of Cold Atmospheric Pressure Plasma Technology in Medicine, Agriculture and Food Industry*, “Applied Sciences”, 2021, vol. 11, art. no. 4809. DOI: <https://doi.org/10.3390/app11114809>.
61. Starek A., Pawlat J., Chudzik B., Kwiatkowski M., Terebun P., Sagan A., Andrejko D., *Evaluation of selected microbial and physicochemical parameters of fresh tomato juice after cold atmospheric pressure plasma treatment during refrigerated storage*, “Scientific Reports”, 2019, vol. 9, art. no. 8407. DOI: <https://doi.org/10.1038/s41598-019-44946-1>
62. Dasan B.G., Onal-Ulusoy B.A., Pawlat J., Diatczyk J., Sen Y.S., Mutlu M., *New and Simple Approach for Decontamination of Food Contact Surfaces with Gliding Arc Discharge Atmospheric Non-Thermal Plasma*, “Food and Bioprocess Technology”, 2017, vol. 10, p. 650–661. DOI: <https://doi.org/10.1007/s11947-016-1847-2>
63. Hati S., Patel M., Yadav D., *Food bioprocessing by non-thermal plasma technology*, “Current Opinion in Food Science”, 2018, vol. 19, p. 85–91. DOI: <https://doi.org/10.1016/j.cofs.2018.03.011>.
64. Yousefi M., Mohammadi M.A., Zabihzadeh Khajavi M., Ehsani A., Scholtz V., *Application of Novel Non-Thermal Physical Technologies to Degrade Mycotoxins*, “Journal of Fungi”, 2021, vol. 7, art. no. 395. DOI: <https://doi.org/10.3390/jof7050395>
65. Stryczewska H. D., *Application of non-thermal plasma in agriculture*, [In:] Workshop of Application of Advanced Plasma Technologies in CE Agriculture, Ljubljana, Slovenia, 17–21 April, 2016.
66. Fridman G., Ayan H., Fridman A., Gutsol A., Vasilets V., Friedman G. Shereshevsky A., Balasubramanian M., Peddinghaus M., Brooks A., *Sterilization of Living Human and Animal Tissue by Non-Thermal Atmospheric Pressure Dielectric Barrier Discharge Plasma*, Proceedings of IEEE 34th International Conference on Plasma Science (ICOPS), Albuquerque, USA, 17–22 June, 2007. DOI: <https://doi.org/10.1109/PPPS.2007.4345979>
67. Kuo S.P., *Air plasma for medical applications*, “Journal of Biomedical Science”, 2012, vol. 5, p. 481–495. DOI: <http://doi.org/10.4236/jbise.2012.59061>
68. Sakudo A., Yagyu Y., Onodera T., *Disinfection and Sterilization Using Plasma Technology: Fundamentals and Future Perspectives for Biological Applications*, “International Journal of Molecular Sciences”, 2019, vol. 20, art. no. 5216. DOI: <https://doi.org/10.3390/ijms20205216>
69. Keidar M., *Adaptive Plasmas for Plasma Medicine*, [In:] 74th Annual Gaseous Electronics Conference (online), College Park, USA, October 4–8, 2021.
70. Stoffels E., *Tissue Processing” with atmospheric plasmas*, “Contributions to Plasma Physics”, 2007, vol. 47, p. 40–48. DOI: <https://doi.org/10.1002/ctpp.200710007>
71. Lendeckel D., Eymann C., Emicke P., Daeschlein G., Darm K., O’Neil S., Beule A.G., von Woedtke T., Völker U., Weltmann K-D, Jünger M., Hosemann W., Scharf C., *Proteomic changes of tissue-tolerable plasma treated airway epithelial cells and their relation to wound healing. Proteomic changes of tissue-tolerable plasma treated airway epithelial cells and their relation to wound healing*, “BioMed Research International”, 2015, art. no. 506059. DOI: <https://doi.org/10.1155/2015/506059>
72. Hasse S., Hahn O., Kindler S., von Woedtke T., Metelmann H.R., Masur K., *Atmospheric pressure plasma jet application on human oral mucosa modulates tissue regeneration*, “Plasma Medicine”, 2014, vol. 4, p. 117–1129. DOI: <https://doi.org/10.1615/PLASMAMED.2014011978>
73. Plasmatis Initiative Group, *Declaration of the 1st International Workshop on Plasma Tissue Interactions*, [In:] ncbi.nlm.nih.gov [access: 19.06.2022]. <https://www.ncbi.nlm.nih.gov/pmc/articles/PMC2831525/>

74. Hammann A., Huebner N-O., Bender C., Ekkernkamp A., Hartmann B., Hinz P., Kindel E., Koban I., Koch S., Kohlmann T., Lademann J., Matthes R., Müller G., Titze R., Weltmann K-D., Kramer A., *Antiseptic efficacy and tolerance of tissue-tolerable plasma compared with two wound antiseptics on artificially bacterially contaminated eyes from commercially slaughtered pigs*, "Skin Pharmacology and Physiology", 2010, vol. 23, p. 328–32.
DOI: <https://doi.org/-10.1159/000314724>
75. Komarzyniec G., Stryczewska H.D., Muszański R., *Autonomous Water Treatment Installation Energized from PV Panels*, "Journal of Advanced Oxidation Technologies", 2010, vol. 13, p. 146–152. DOI: <https://doi.org/10.1515/jaots-2010-0202>
76. Stryczewska H. D., Komarzyniec G. K., *Properties of gliding arc (GA) reactors energized from AC/DC/AC power converters*, [In:] Proceedings of IEEE Region 8 International Conference on Computational Technologies in Electrical and Electronics Engineering SIBIRCON-2010, Irkutsk, Russia, 11–15 July, 2010.
DOI: <https://doi.org/10.1109/-SIBIRCON.2010.5555156>
77. Krupski P., Stryczewska H.D., *A Gliding Arc Microreactor Power Supply System Based on Push-Pull Converter Topology*, "Applied Sciences", 2020, vol. 10, p. 1–8.
DOI: <https://doi.org/10.3390/-app10113989>
78. Krupski P., Stryczewska H.D., *GLIDARC reactor power supply with ignition improvement*, "COMPEL - The International Journal for Computation and Mathematics in Electrical and Electronic Engineering", 2019, vol. 38, p. 1274–1284.
DOI: <https://doi.org/10.1108/COMPEL-12-2018-0540>
79. Komarzyniec G., Stryczewska H. D., Krupski P., *The Influence of the Architecture of the Power System on the Operational Parameters of the Glidarc Plasma Reactor*, in 2019 IEEE Pulsed Power & Plasma Science (PPPS), Orlando, FL, USA, 2019, p. 1–4.
DOI: <https://doi.org/10.1109/PPPS34859.2019.9009870>
80. Krupski P., Stryczewska H., *The Investigation of The Properties of High-voltage Transformer in Nonthermal Plasma Pulse Power Supply*, in 14th Selected Issues of Electrical Engineering and Electronics (WZEE), 2018, p. 1–4.
81. Krupski P., Stryczewska H. D., Komarzyniec G., *The Push-Pull Plasma Power Supply - A Combining Technique for Increased Stability*, in 2019 IEEE Pulsed Power & Plasma Science (PPPS), 2019, p. 1–4. DOI: <https://doi.org/10.1109/PPPS34859.2019.9009934>
82. Komarzyniec G., Stryczewska H. D., Aftyka M., *Reduction of the Conducted Disturbances Generated by the Ignition Systems of Glidarc Plasma Reactors*, 2019 IEEE Pulsed Power & Plasma Science (PPPS), 2019, p. 1–4.
DOI: <https://doi.org/10.1109/PPPS34859.2019.9009976>
83. Pawlat J., Diatczyk J., Komarzyniec G., Gizewski T., Stryczewska H. D., Mitsugi F., Ebihara K., Aouqi S., Nakamiya T., *Solar energy for soil conditioning*, in: EUROCON – International Conference on Computer as a Tool (EUROCON), 2011, 27–29 April 2011, Lisbon, Portugal, pp. 1–4.
84. Pawlat J., Stryczewska H., *Application of solar energy in the processes of gas, water and soil treatment: w Solar Power*, [In:] Solar Power, ed. Rugescu R. D., Croatia, 2012, p. 105–132.
DOI: <https://doi.org/10.5772/26629>
85. Stryczewska H. D., Pawlat J., *Technologies of air, water and soil treatment based on solar energy and advanced oxidation processes*, [In:] Modern Power Engineering 1, ed. W. Wójcik, Lublin, Poland, Lublin University of Technology, 2011, p. 176–197.
86. Stryczewska H.D., Ebihara K., Takayama M., Gyuotoku Y., Tachibana M., *Non-Thermal Plasma-Based Technology for Soil Treatment*, "Plasma Processes and Polymers", 2005, vol. 2, p. 238–245. DOI: <https://doi.org/10.1002/ppap.200400061>
87. Ebihara K., Mitsugi F., Ikegami T., Nakamura N., Hashimoto Y., Yamashita Y., Baba S., Stryczewska H.D., Pawlat J., Teii S., Sung T.L., *Ozone-mist spray sterilization for pest control in agricultural management*, "The European Physical Journal Applied Physics", 2013, vol. 61, art. no. 24318. DOI: <https://doi.org/10.1051/epjap/2012120420>
88. Bekeschus S., von Woedtke T., Emmert S., Schmidt A., *Medical gas plasma-stimulated wound healing: Evidence and mechanisms*, "Redox Biology", 2021, vol. 46, art. no. 102116.
DOI: <https://doi.org/10.1016/j.redox.2021.102116>

89. Moreau M., Orange N., Feuilloley M.G.J., *Non-thermal plasma technologies: new tools for bio-decontamination*, "Biotechnology Advances", 2008, vol. 26, p. 610–607.
DOI: <https://doi.org/10.1016/j.biotechadv.2008.08.001>
90. Haertel B., von Woedtke T., Weltmann K.D., Lindequist U., *Physical plasma—possible application in wound healing*, "Biomolecules & Therapeutics", 2014, vol. 22, p. 477–490.
DOI: <https://doi.org/10.4062/biomolther.2014.105>
91. Ebihara K., Sugimoto S., Ikegami T., Mitsugi F., Stryczewska H.D., *Application of Gaseous Ozone to Agricultural Soil Sterilization*, in 6th International Conference on Electromagnetic Devices and Processes in Environment Protection (ELMECO-6), Nałęczów, Poland, June 24–28, 2008, p. 11–12.
92. Ebihara K., Ikegami T., Mitsugi F., Ikegami T., Stryczewska H.D., Goutoku Y., Proceedings of the applications of plasma to bio-medical Engineering, December 15–17, Lunghwa University of Science and Technology, Taoyuan, Taiwan, 2008.
93. Ebihara K., Mitsugi F., Ikegami T., Ikegami T., Stryczewska H.D., in 6th Asia-Pacific International Symposium on Basic and Application of Plasma Technology, Dec.14–16, Hsinchu, Taiwan, X07, pp. 7, 2009.
94. Ebihara K., Mitsugi F., Ikegami T., Sakai T., Ikegami T., Stryczewska H.D., in The 16th International Conference on Advanced Oxidation Technologies for Treatment of Water, Air and Soil, San Diego, California, Nov.15–18, 2010, pp. 104–105.
95. Ebihara K., Stryczewska H.D., Ikegami T., Mitsugi F., Pawlat J., On-site ozone treatment for agricultural soil and related applications, "Przegląd Elektrotechniczny", 2011, NR7/2011, p. 148–152.
96. Ebihara K., Stryczewska H.D., Mitsugi F., Ikegami T., Sakai T., Pawlat J., Teii S., *Recent development of ozone treatment for agricultural soil sterilization and biomedical prevention*, "Przegląd Elektrotechniczny", 2012, NR6/2012, p. 92–94.
97. Ebihara K., Mitsugi F., Ikegami T., Nakamura N., Hashimoto Y., Yamashita Y., Baba S., Stryczewska H.D., Pawlat J., Teii S., Sung T.L., *Ozone-mist spray sterilization for pest control in agricultural management*, "The European Physical Journal Applied Physics", 2013, vol. 61, art. no. 24318, p. 1–5. DOI: <https://doi.org/10.1051/epjap/2012120420>
98. Ebihara K., Mitsugi F., Ikegami T., Yamashita Y., Hashimoto Y., Yamashita T., Kanazawa S., Stryczewska H.D., Pawlat J., Teii S., Sung T-L., *Sterilization Characteristics of Ozone-mist Spray for Chemical Free Agriculture*, "International Journal of Plasma Environmental Science and Technology", 2016, vol. 10, no.1, p. 11–15.
99. Ebihara K., Mitsugi F., Aouki S., Yamashita Y., Baba S., Stryczewska H.D., *Deep learning technology for remote identification of insect pest and plant growth in ozone-mist sterilization*, [In]: 10th International Conference on Electromagnetic Devices and Processes in Environment Protection (ELMECO-X), May 26–27, 2022, Lublin, Poland.
100. Richardson A. D., Jenkins J. P., Brawswell R.H., Hollinger D.Y., Smith M., *Use of digital webcam images to track spring green-up in a deciduous broadleaf forest*, "Oecologia", 2007, vol. 152, p. 323–334.
101. Boehm D., Canal C., *Application of Plasma Technology in Bioscience and Biomedicine*, "Applied Sciences", 2021, vol. 11, art. no. 7203. DOI: <https://doi.org/10.3390/app11167203>
102. Rezaei F., Vanraes P., Nikiforov A., Morent R., De Geyter N., *Applications of Plasma-Liquid Systems: A Review*, "Materials" 2019, vol. 12, art. no. 2751.
DOI: <https://doi.org/10.3390/ma12172751>
103. Kim J., Choi K.H., Kim Y., Park B.J., Cho G., *Wearable Plasma Pads for Biomedical Applications*, "Applied Sciences", 2021, vol. 17, art. no. 1308.
DOI: <https://doi.org/10.3390/app7121308>
104. Zhou R. W., Zhou R. S., Wang P. Y., Xian Y. B., Mai-Prochnow A., Lu X. P., Cullen P. J., Ostrikov K., Bazaka K., *Plasma-activated water: generation, origin of reactive species and biological applications*, "Journal of Physics D: Applied Physics", 2020, vol. 53, art. no. 303001. DOI: <https://doi.org/10.1088/1361-6463/ab81cf>
105. Laroussi M., *Sterilization of contaminated matter with an atmospheric pressure plasma*, "IEEE Transactions on Plasma Science", 1996, vol. 24, p. 1188–1191.
DOI: <https://doi.org/10.1109/27.533129>

106. Laroussi, M., *Sterilization of liquids using a plasma glow discharge*, United States Patent House, patent no. 5,876,663, approved 02.03.1999.
107. Laroussi M., *Cold Plasma in Medicine and Healthcare: The New Frontier in Low Temperature Plasma Applications*, "Frontiers in Physics", 2020, vol. 8, art. no. 74.
DOI: <https://doi.org/10.3389/fphy.2020.00074>
108. Boudam M.K, Moisan M., *Synergy effect of heat and UV photons on bacterial-spore inactivation in an N₂-O₂ plasma-afterglow sterilizer*, "Journal of Physics D: Applied Physics", 2010, vol. 43, art. no. 295202.
DOI: <https://doi.org/10.1088/0022-3727/43/29/295202>
109. Isbary G., Morfill G., Schmidt H. U., Georgi M., Ramrath K., Heinlin J., Karrer S., Landthaler M., Shimizu T., Steffes B., Bunk W., Monetti R., Zimmermann J. L., Pompl R., Stolz W., *A first prospective randomized controlled trial to decrease bacterial load using cold atmospheric argon plasma on chronic wounds in patients*, "British Journal of Dermatology", 2010, vol. 163, p. 78–82. DOI: <https://doi.org/10.1111/j.1365-2133.2010.09744.x>
110. Vandamme M., Robert E., Pesnel S., Barbosa E., Dozias S., Sobilo J., Lerondel S., Le Pape A., Pouvesle J. M., *Antitumor effect of plasma treatment on U87 glioma xenografts: preliminary results*, "Plasma Process and Polymers", 2010, vol. 7, p. 264–273.
DOI: <https://doi.org/10.1002/ppap.200900080>
111. Gałęzewski L. Wilgotność gleby. Metodyczny aspekt badań rolniczych. Bydgoszcz, Wydawnictwo Uczelniane Uniwersytetu Technologiczno-Przyrodniczego w Bydgoszczy, 2020.
112. Topp G. C., Davis J. L., Annan A. P., *Electromagnetic determination of soil water content: Measurements in coaxial transmission lines*, "Water Resources Research", 1980, vol. 16, p. 574–582. DOI: <https://doi.org/10.1029/wr016i003p00574>
113. Malicki M. A., Skierucha W., Elektryczny pomiar wilgotności gleby metodą TDR, "Acta Agrophysica", 2002, vol. 72, p. 89–98.
114. Majcher J., Kafarski M., Wilczek A., Woszczyk A., Szyplowska A., Lewandowski A., Szerement J., Skierucha W., *Application of a Monopole Antenna Probe with an Optimized Flange Diameter for TDR Soil Moisture Measurement*, "Sensors", 2020, vol. 20, no. 8, p. 1–13. DOI: <https://doi.org/10.3390/s20082374>
115. Majcher J., Kafarski M., Wilczek A., Szyplowska A., Lewandowski A., Woszczyk A., Skierucha W., *Application of a dagger probe for soil dielectric permittivity measurement by TDR*, "Measurement", 2021, vol. 178, p. 1–13. DOI: <https://doi.org/10.1016/j.measurement.2021.109368>
116. Kozak J., Majka M., Janowski T., Kozak S., Wojtasiewicz G., Kondratowicz-Kucewicz B., *Tests and Performance Analysis of Coreless Inductive HTS Fault Current Limiters*, "IEEE Transactions on Applied Superconductivity", 2011, vol. 21, no. 3, p. 1303–1306. DOI: <https://doi.org/10.1109/TASC.2010.2101033>
117. Majka M., Kozak J., Kozak S., Wojtasiewicz G., Janowski T., *Design and Numerical Analysis of the 15 kV Class Coreless Inductive Type SFCL*, "IEEE Transactions on Applied Superconductivity", 2015, vol. 25, no. 3, p. 1–5.
DOI: <https://doi.org/10.1109/TASC.2014.2375344>
118. Kozak J., Majka M., Blazejczyk T., Berowski P., *Tests of the 15-kV Class Coreless Superconducting Fault Current Limiter*, "IEEE Transactions on Applied Superconductivity", 2016, vol. 26, no. 3, p. 1–4. DOI: <https://doi.org/10.1109/TASC.2016.2524504>
119. Majka M., Kozak J., *Superconducting Fault Current Limiter for the Electric Power System*, "Acta Physica Polonica A", 2016, vol. 130, no. 2, p. 581–584.
DOI: <https://doi.org/10.12693/APhysPolA.130.581>
120. Majka M., Kozak S., *The Coreless Superconducting Fault Current Limiter 15 kV 140 A*, "Przegląd Elektrotechniczny", 2016, vol. 1, no. 7, p. 40–43.
DOI: <https://doi.org/10.15199/48.2016.07.06>
121. Kozak J., Majka M., Kozak S., *Experimental Results of a 15 kV, 140 A Superconducting Fault Current Limiter*, "IEEE Transactions on Applied Superconductivity", 2017, vol. 27, no. 4, p. 1–4. DOI: <https://doi.org/10.1109/TASC.2017.2651120>

122. Kozak J., Majka M., Janowski T., Kozak S., *Design and Development of the First Polish Superconducting Fault Current Limiter For MV Distribution Systems*, "Physics Procedia", 2012, vol. 36, p. 845–848. DOI: <https://doi.org/10.1016/j.phpro.2012.06.138>
123. Kozak J., Majka M., Janowski T., Kozak S., *Nadprzewodnikowy bezrdzeniowy indukcyjny ogranicznik prądu zwarciovego średniego napięcia*, „Przegląd Elektrotechniczny”, 2012, vol. 88, no. 9b/2012, p. 245–248.
124. Kozak J., Majka M., Kozak S., Janowski T., *Design and Tests of Coreless Inductive Superconducting Fault Current Limiter*, "IEEE Transactions on Applied Superconductivity", 2012, vol. 22, no. 3, p. 5601804–5601804. DOI: <https://doi.org/10.1109/TASC.2011.2178977>
125. Majka M., Kozak J., Janowski T., Kozak S., *Analiza skuteczności działania bezrdzeniowych indukcyjnych nadprzewodnikowych ograniczników prądu wykonanych z taśmy nadprzewodnikowej pierwszej i drugiej generacji*, „Przegląd Elektrotechniczny”, 2012, vol. 88, no. 8/2012, p. 32–35.
126. Kozak J., Majka M., Kozak S., Janowski T., *Comparison of Inductive and Resistive SFCL*, "IEEE Transactions on Applied Superconductivity", 2013, vol. 23, no. 3, p. 5600604–5600604. DOI: <https://doi.org/10.1109/TASC.2012.2231714>
127. Majka M., Kozak S., *Zastosowanie taśm I i II generacji do budowy nadprzewodnikowych ograniczników prądu*, „Przegląd Elektrotechniczny”, 2009, vol. 85, no. 5/2009, p. 183–185.
128. Janowski T., Wojtasiewicz G., Kondratowicz-Kucewicz B., Kozak S., Kozak J., Majka M., *Superconducting Winding for Inductive Type SFCL Made of HTS Tape with Increased Resistivity*, "IEEE Transactions on Applied Superconductivity", 2009, vol. 19, no. 3, p. 1884–1887.
129. Kozak S., Janowski T., Wojtasiewicz G., Kozak J., Kondratowicz-Kucewicz B., Majka M., *The 15 kV Class Inductive SFCL*, "IEEE Transactions on Applied Superconductivity", 2010, vol. 20, no. 3, p. 1203–1206. DOI: <https://doi.org/10.1109/TASC.2010.2042697>
130. Majka M., Kozak J., Kozak S., *HTS Tapes Selection for Superconducting Current Limiters*, "IEEE Transactions on Applied Superconductivity", 2017, vol. 27, no. 4, p. 1–5. DOI: <https://doi.org/10.1109/TASC.2017.2669191>
131. Czerwinski D., Jaroszynski L., Janowski T., Majka M., Kozak J., *Analysis of Alternating Overcurrent Response of 2G HTS Tape for SFCL*, "IEEE Transactions on Applied Superconductivity", 2014, vol. 24, no. 3, p. 1–4. DOI: <https://doi.org/10.1109/TASC.2013.2281494>
132. Czerwinski D., Jaroszynski L., Majka M., Kozak J., Charnas B., *Comparison of Overcurrent Responses of 2G HTS Tapes*, "IEEE Transactions on Applied Superconductivity", 2016, vol. 26, no. 3, p. 1–4. DOI: <https://doi.org/10.1109/TASC.2016.2520080>
133. Czerwinski D., Jaroszynski L., Kozak J., Majka M., *Equivalent electromagnetic model for current leads made of HTS tapes*, „Przegląd Elektrotechniczny”, 2012, vol. 88, no. 9b/2012, p. 230–233.
134. Kozak J., Majka M., A method of soldering copper tips to a superconducting tape, Urząd Patentowy Rzeczypospolitej Polskiej, patent PL 220314 B1, approved 03.03.2014 r.
135. Kozak J., Majka M., Kozak S., *Design Considerations on a Resistive Superconducting Fault Current Limiter*, "Acta Physica Polonica A", 2020, no. 5, vol. 138, p. 710–714. DOI: <https://doi.org/10.12693/APhysPolA.138.710>
136. Majka M., Surdacki P., *Magnetic Field Diffusion in the HTS Ring for the Fault Current Limiter Application*, „Przegląd Elektrotechniczny”, 2005, vol. 81, no. 12/2005, p. 118–120.
137. Stryczewska H. D., Janowski T., Wac-Włodarczyk A., *Technologie nadprzewodnikowe i plazmowe w energetyce*, Lublin, Lubelskie Towarzystwo Naukowe, 2009.
138. Szwed G., Majcher J., *Wykorzystanie pola elektrostatycznego w separacji rozdrobnionych materiałów roślinnych*, „Acta Agrophysica”, 2010, vol. 15, no. 2, p. 417–427.
139. Dłużewski M., Dłużewska A., *Technologia żywności, cz. 2*, Warsaw, WSiP S.A. 2001, p. 40–63.

140. Grochowicz J., *Maszyny do czyszczenia i sortowania nasion*. Lublin, Wydawnictwo AR, 1994.
141. Majcher J., *Przegląd metod segregacji nasion*, [In] Doktorant a innowacyjność podejmowanych tematów badań, ed. M. Kuczera, Kraków, Poland, CREATIVETIME, 2011, p. 66–70.
142. Majcher J., *Wykorzystanie uzwojenia bifilarnego w procesie elektroseparatoracji rozdrobnionych materiałów pochodzenia roślinnego*, „Prace Instytutu Elektrotechniki”, 2010, vol. 247, p. 117–126.
143. Wójcicki M., *Maszyny i narzędzia rolnicze*, Warsaw, National Agricultural and Forest Publishing House, 1958.
144. Osborne T.B., *Middlings purifier*, U.S. Patent Office Official Gazette, patent no. 224719, approved 17.02.1880.
145. Murata Y., *Electrostatic separation*, “Proceedings of the IEJ”, 1982, vol. 6, no. 3, p. 159–162.
146. Pietrzyk W., *Elektrofiltr bifilarny do usuwania pyłów pochodzenia roślinnego*, Lublin, Wydawnictwo Naukowe FRNA, 2008 (in Polish).
147. Rawa H., *Elektryczność i magnetyzm w technice*, Warsaw, Wydawnictwo Naukowe PWN, 1994 (in Polish).
148. Majcher J., Szwed G., *Segregacja szczególnie trudnych do rozdzielenia grup roślin przy pomocy pola elektrostatycznego*, „Prace Instytutu Elektrotechniki”, 2011, vol. 251, p. 21–29.
149. Scibisz M., *Komputerowa analiza rozkładu pola elektrycznego wokół uzwojenia odpylacza bifilarnego*, „Inżynieria Rolnicza”, 2005, vol. 8, no. 68, p. 377–383 (in Polish).
150. Majcher J., *The use of an electroseparator with bifilar winding for extracting germ from crushed rape seed*, “Przegląd Elektrotechniczny”, 2020, vol. 96, no. 9, p. 71–73.
DOI: <https://doi.org/10.15199/48.2020.09.15>
151. Clayton R. P., *Introduction to Electromagnetic Compatibility*, Hoboken NJ USA, Wiley, 2006.
152. Mazurek P., *Laboratorium podstaw kompatybilności elektromagnetycznej*, Lublin, Politechnika Lubelska, 2012 (in Polish).
153. Mazurek P., *Selected aspects of electrical equipment operation with respect to power quality and EMC*, “Przegląd Elektrotechniczny”, 2017, vol. 93, no. 1, p. 21–24.
154. Ott H.W., *Electromagnetic Compatibility Engineering*, Hoboken NJ USA, Wiley, 2009.
155. Weston D., *Electromagnetic Compatibility Principles and Applications, Second Edition, Revised and Expanded*, Boca Raton Florida USA, CRC Press, 2017.
156. Mazurek P., *Filtrowanie zaburzeń przewodzonych toru zapłonu reaktora plazmowego typu GlidArc*, „Przegląd Elektrotechniczny”, 2012, vol. 88, no. 2, p. 45–47 (in Polish).
157. Mazurek P., *Identyfikacja zaburzeń elektromagnetycznych w torze zasilania reaktora plazmowego przy różnych mieszaninach gazowych*, „Przegląd Elektrotechniczny”, 2014, vol. 90, no. 7, p. 203–206 (in Polish).
158. Mazurek P., Pawłat J., Kwiatkowski M., *Badanie zaburzeń przewodzących w torze zasilania reaktorów BDB i GlidArc*, „Przegląd Elektrotechniczny”, 2015, vol. 11, p. 50–53 (in Polish).
159. Mazurek P., *Wpływ przepływu gazu roboczego na zaburzenia przewodzone w torze zapłonu trójfazowego reaktora plazmowego typu GlidArc*, „Przegląd Elektrotechniczny”, 2019, vol. 95, no. 3, p. 37–40 (in Polish).
160. Mazurek P., *Analiza konfiguracji elektrod w odniesieniu do zaburzeń przewodzonych w reaktorze plazmowym*, „Przegląd Elektrotechniczny”, 2019, vol. 95, no. 12, p. 176–179 (in Polish).
161. Mazurek P., *Chosen Aspects of the Electromagnetic Compatibility of Plasma Reactors with Gliding Arc Discharges*, “Applied Sciences”, 2020, vol. 10, no. 11, art. no. 3789.
DOI: <https://doi.org/10.3390/app10113789>
162. Stryczewska H. D., *Technologie plazmowe w energetyce i inżynierii środowiska*, Lublin, Wydawnictwo Politechniki Lubelskiej, 2009 (in Polish).
163. Mitsugi F., Nakamiya T., Sonoda Y., Pawłat J., Aouqi S., Ikegami T., Kawasaki H., Stryczewska H. D., *Analysis of discharge dound and I-V characteristic on gliding arc discharge*, „Przegląd Elektrotechniczny”, 2016, vol. 92, no. 6, p. 119–122.

164. Mitsugi F., Ebihara K., Horibe N., Aouji S., Nagahama K., *Practical Soil Treatment in a Greenhouse Using Surface Barrier Discharge Ozone Generator*, “IEEE Transactions on Plasma Science”, 2017, vol. 45, p. 3082–3088.
DOI: <https://doi.org/10.1109/TPS.2017.2720423>
165. Pawłat J., Diatczyk J., Gunaydin-Dasan B., Onal-Ulusoy B., Mok Y. S., *Mini glide-arc plasma reactor for biological decontamination*, “European Journal of Medical Technologies”, 2017, vol. 14, no. 1, p. 29–32.
166. Stryczewska H. D., Jakubowski T., Kalisiak S., Gizewski T., Pawłat J., *Power systems of plasma reactors for non-thermal plasma generation*, “Journal of Advanced Oxidation Technologies”, 2013, vol. 16, no. 1, p. 52–62.
167. Mazurek P., *Wprowadzenie do badań zaburzeń przewodzonych w instalacji reaktora plazmowego*, „Elektro.info”, 2010, vol. 12, p. 32–34 (in Polish).
168. Mazurek P., *Zaburzenia promieniowane reaktora plazmowego typu GlidArc*, „Przegląd Elektrotechniczny”, 2011, vol. 87, no. 12b, p. 121–124 (in Polish).
169. Al-Saadi M., Patkowski B., Zaremba M., Karwat A., Pol M., Chelchowski Ł., Mierlo J. V., Berecibar M., *Slow and Fast Charging Solutions for Li-Ion Batteries of Electric Heavy-Duty Vehicles with Fleet Management Strategies*, “Sustainability”, 2021, vol. 13, no. 19, art. no. 10639. DOI: <https://doi.org/10.3390/su131910639>
170. Awadallah M. A., Singh B. N., Venkatesh B., *Impact of EV Charger Load on Distribution Network Capacity: A Case Study in Toronto*, “Canadian Journal of Electrical and Computer Engineering”, 2016, vol. 39, p. 268–273. DOI: <https://doi.org/10.1109/cjece.2016.2545925>
171. Christidis P., Focas C., *Factors Affecting the Uptake of Hybrid and Electric Vehicles in the European Union*, “Energies”, 2019, vol. 12, no. 18, art. no. 2414.
DOI: <https://doi.org/10.3390/en12183414>
172. Chudy A., Mazurek P., *Electromobility – the Importance of Power Quality and Environmental Sustainability*, “Journal of Ecological Engineering”, 2019, vol. 20, p. 15–23.
DOI: <https://doi.org/10.12911/22998993/112713>
173. Chudy A.; Stryczewska H.D., *Electromagnetic Compatibility Testing of Electric Vehicles and Their Chargers*, “Informatyka, Automatyka, Pomiary w Gospodarce i Ochronie Środowiska”, 2020, vol. 10, p. 70–73. DOI: <https://doi.org/10.35784/iapgos.1687>
174. International Electrotechnical Commission. IEC 61851-21-2 - Electric vehicle conductive charging system — Part 21-2: Electric vehicle requirements for conductive connection to an AC/DC supply — EMC requirements for off board electric vehicle charging systems. International Electrotechnical Commission: Geneva, Switzerland, 2018
175. Mazurek P., Chudy A., *Zagadnienia jakości energii stacji ładowania pojazdów elektrycznych*, „Przegląd Elektrotechniczny”, 2021, vol. 4, p. 103–108 (in Polish).
176. Mazurek P., *Wybrane zagadnienia prawne i techniczne w zakresie emc stacji ładowania pojazdów elektrycznych*, „Przegląd Elektrotechniczny”, 2021, vol. 97, no. 1, p. 156–161 (in Polish).
177. Mazurek P., Chudy A., *An Analysis of Electromagnetic Disturbances from an Electric Vehicle Charging Station*, “Energies”, 2022, vol. 15, no. 1, p. 1–16.
178. Wang L., Qin Z., Slangen T., Bauer P., van Wijk T., *Grid Impact of Electric Vehicle Fast Charging Stations: Trends, Standards, Issues and Mitigation Measures - An Overview*, “IEEE Open Journal of Power Electronics”, 2021, vol. 2, p. 56–74.
DOI: <https://doi.org/10.1109/ojpe.2021.3054601>
179. Zagrajek K., Paska J., Kłos M., Pawlak K., Marchel P., Bartecka M., Michalski Ł., Terlikowski P., *Impact of Electric Bus Charging on Distribution Substation and Local Grid in Warsaw*, “Energies”, 2020, vol. 13, no. 5, art. no. 1210.
DOI: <https://doi.org/10.3390/en13051210>
180. Zheng Y., Niu S., Shang Y., Shao Z., Jian L., *Integrating plug-in electric vehicles into power grids: A comprehensive review on power interaction mode, scheduling methodology and mathematical foundation*, “Renewable and Sustainable Energy Reviews”, 2019, vol. 112, p. 424–439. DOI: <https://doi.org/10.1016/j.rser.2019.05.059>

181. Lucas A., Bonavitacola F., Kotsakis E., Fulli G., *Grid harmonic impact of multiple electric vehicle fast charging*, "Electric Power Systems Research", 2015, vol. 127, p. 13–21.
DOI: <https://doi.org/10.1016/j.eprsr.2015.05.012>
182. Grill A., *Diamond-like Carbon: state of the art*, "Diamond and Related Materials", 1999, vol.8, p. 428–434.
183. Lin C.R., Wei D.H., Chang C.K., Liao W.H., *Optical Properties of Diamond-like Carbon Films for Antireflection Coating by RF Magnetron Sputtering Method*, "Physics Procedia", 2011, vol. 18, p. 46–50.
184. Fiaschi G., Rota A., Ballestrazzi A., Marchetto D., Vezzalini E., Valeri S., *A Chemical, Mechanical, and Tribological Analysis of DLC Coatings Deposited by Magnetron Sputtering*, "Lubricants", 2019, vol. 7, no. 4, pp. 1–18.
DOI: <https://doi.org/10.3390/lubricants7040038>
185. Gutensohn K., Beythien C., Bau J., Fenner T., Grewe P., Koester R., Padmanaban K., Kuehl P., *In Vitro Analyses of Diamond-like Carbon Coated Stents: Reduction of Metal Ion Release, Platelet Activation, and Thrombogenicity*, "Thrombosis Research", 2000, vol. 99, p. 577–585. DOI: [https://doi.org/10.1016/s0049-3848\(00\)00295-4](https://doi.org/10.1016/s0049-3848(00)00295-4)
186. Enomoto K., Hasebe T., Asakaw R., Kamijo A., Yoshimoto Y., Suzuki T., Takahashi K., Hotta A., *Controlling the drug release rate from biocompatible polymers with micro-patterned diamond-like carbon (DLC) coating*, "Diamond and Related Materials", 2010, vol. 19, p. 806–813. DOI: <https://doi.org/10.1016/j.diamond.2010.01.053>
187. Tsujioka M., *The Technological Trend and Application of Environment-friendly Hard Coating*, "Journal of the Surface Finishing Society of Japan", 2012, vol. 63, p.134–139.
DOI: <https://doi.org/10.4139/sfj.63.134>
188. Matsumoto R., Sadki El-H. S., Tanaka H., Yamamoto S., Adachi S., Younis A., Takeya H., Takano Y., *Concurrent synthesis and boron-doping of amorphous carbon films by focused ion beam-assisted chemical vapor deposition*, "Thin Solid Films", 2021, vol. 730, art. no. 138704.
DOI: <https://doi.org/10.1016/j.tsf.2021.138704>
189. Kuo M-T., May P. W., Gunn A., Ashfold M. N. R., Wild R. K., *Studies of phosphorus doped diamond-like carbon films*, "Diamond and Related Materials", 2000, vol. 9, p. 1222–1227.
DOI: [https://doi.org/10.1016/S0925-9635\(99\)00305-2](https://doi.org/10.1016/S0925-9635(99)00305-2)
190. Allon-Alaluf M., Croitoru N., *Electrical measurements of iodine doped amorphous diamond like films grown on silicon substrate*, "Applied Physics Letters", 1996, vol. 69, p. 2932–2934.
DOI: <https://doi.org/10.1063/1.117328>
191. Omer A. M. M., Adhikari S., Adhikary S., Rusop M., Uchida H., Umeno M., Soga T., *Iodine doping in amorphous carbon thin-films for optoelectronic devices*, "Physica B", 2006, vol. 376–377, p. 316–319. DOI: <https://doi.org/10.1016/j.physb.2005.12.081>
192. Yamazato M., Saida Y., Higa A., Toguchi M., *Dedoping phenomenon of iodine-doped a-C:H films*, "Diamond and Related Materials", 2008, vol. 17, p. 1652–1654.
DOI: <https://doi.org/10.1016/j.diamond.2008.02.029>
193. Dayana K., Fadzilah A. F., Ishak A., Rusop M., *Properties of Iodine Doped Amorphous Carbon Thin Films Grown by Thermal CVD*, "Solid State Science and Technology", 2017, vol. 25, p. 126–134. DOI: <https://doi.org/10.4028/www.scientific.net/AMR.667.294>
194. Park H., Lee S., Kim H. J., Woo D., Park S. J., Lee J. M., Yoon E., Lee G., *Effects of nitrogen doping in amorphous carbon layers on the diffusion of fluorine atoms: A first-principles study*, "Journal of Applied Physics", 2019, vol. 125, art. no. 155701.
DOI: <https://doi.org/10.1063/1.5064437>
195. Kudo S., Yamazato M., Higa A., *Electrical and structural changes of amorphous carbon thin films induced by exposure to iodine vapor*, "Proceedings of the International Workshop on Environmental Engineering", 2019, p.134–135.
196. Oshiro T., Begum F., Yamazato M., Higa A., Maehama T., Toguchi M., *The structures and properties of a-C:H films deposited at a wide range of relative hydrogen gas flow rate by RF sputtering*, "Thin Solid Films", 2006, vol. 506–507, p. 92–95.
DOI: <https://doi.org/10.1016/j.tsf.2005.08.096>

197. Oshiro T., Yamazato M., Higa A., Toguchi M., *Analysis of trans-Polyacetylene Chains in Hydrogenated Amorphous Carbon Films*, "Japanese Journal of Applied Physics", 2007, vol. 46, p. 756–760. DOI: <https://doi.org/10.1143/JJAP.46.756>
198. Yamazato M., Mizuma I., Higa A., *Structure and electrical properties of a-C:H thin films deposited by RF sputtering*, "Diamond and Related Materials", 2010, vol. 19, p. 695–698. DOI: <https://doi.org/10.1016/j.diamond.2010.01.035>
199. Fujimoto F., Ootuka A., Komaki K., Iwata Y., Yamane I., Yamashita H., Hashimoto Y., Tawada Y., Nishimura K., Okamoto H., Hamakawa Y., *Hydrogen Content in a-SiC:H Films Prepared by Plasma Decomposition of Silane and Methane or Ethylene*, "Japanese Journal of Applied Physics", 1984, vol. 23, p. 810-814. DOI: <https://doi.org/10.1143/JJAP.23.810>
200. Robertson J., *Diamond-like amorphous carbon*, "Materials Science and Engineering", 2002, vol. R37, p. 129–281, 2002.
201. Luo M., Zhou P. H., Liu Y. F., Wang X., Xie J. L., *Electric-Field-Induced Amplitude Tuning of Ferromagnetic Resonance Peak in Nano-granular Film FeCoB-SiO₂/PMN-PT Composites*, "Nanoscale Research Letters", 2016, vol. 11, art. no. 493. DOI: <https://doi.org/10.1186/s11671-016-1717-x>
202. Massango H., Tsutaoka T., Kasagi T., Yamamoto S., Hatakeyama K., *Complex permeability and permittivity spectra of percolated Fe₅₀Co₅₀/Cu granular composites*, "Journal of Magnetism and Magnetic Materials", 2017, vol. 442, p. 403–408. DOI: <https://doi.org/10.1016/j.jmmm.2017.07.018>
203. Wu H. P., Ma X. F., Zhang Z., Zhu J., Wang J., Chai G. Z., *Dielectric tunability of vertically aligned ferroelectric-metal oxide nanocomposite films controlled by out-of-plane misfit strain*, "Journal of Applied Physics", 2016, vol. 119, no. 15, art. no. 154102. DOI: <https://doi.org/10.1063/1.4947052>
204. Fedotova J. A., Koltunowicz T. N., Zukowski P., *Transport ładunków i właściwości strukturalne wybranych nanokompozytów metal-dielektryk*, Lublin, Poland, Wydawnictwo Politechniki Lubelskiej, 2012.
205. Svitlo I. A., Fedotov A. K., Saad A., Milosavljevic M., Fedotova J. A., Koltunowicz T. N., Zukowski P., *Low-Temperature DC Carrier Transport in (Fe_{0.45}Co_{0.45}Zr_{0.10})_x(Al₂O₃)_{1-x} Nanocomposites Manufactured by Sputtering in Pure Ar Gas Atmosphere*, "Advances in Condensed Matter Physics", 2015, vol. 2015, art. no. 320187.
206. Gholipur R., Khorshidi Z., Bahari A., *A Study on Double Negative Properties of Metal-Dielectric Nanocomposites*, "JOM", 2016, vol. 68, no. 6, p. 1577–1581. DOI: <https://doi.org/10.1007/s11837-016-1926-x>
207. Nadiv R., Shtein M., Shachar G., Varenik M., Regev O., *Optimal nanomaterial concentration: harnessing percolation theory to enhance polymer nanocomposite performance*, "Nanotechnology", 2017, vol. 28, no. 30, art. no. 305701. DOI: <https://doi.org/10.1088/1361-6528/aa793e>
208. Carriao M.S., Bakuzis A.F., *Mean-field and linear regime approach to magnetic hyperthermia of core-shell nanoparticles: can tiny nanostructures fight cancer?*, "Nanoscale", 2016, vol. 8, no. 15, p. 8363–8377. DOI: <https://doi.org/10.1039/C5NR09093H>
209. Chao H. K., Koski J., Riggleman R. A., *Solvent vapor annealing in block copolymer nanocomposite films: a dynamic mean field approach*, "Soft Matter", 2017, vol. 13, no. 1, p. 239–249. DOI: <https://doi.org/10.1039/C6SM00770H>
210. Tran A. K., Sapkota A., Wen J. M., Li J. P., Takei M., *Linear relationship between cytoplasm resistance and hemoglobin in red blood cell hemolysis by electrical impedance spectroscopy & eight-parameter equivalent circuit*, "Biosensors & Bioelectronics", 2018, vol. 119, p. 103–109. DOI: <https://doi.org/10.1016/j.bios.2018.08.012>
211. Munstedt H., Stary Z., *Is electrical percolation in carbon-filled polymers reflected by rheological properties?*, "Polymer", 2016, vol. 98, p. 51–60. DOI: <https://doi.org/10.1016/j.polymer.2016.05.042>

212. Larkin A. V., Fedotov A. K., Fedotova J. A., Koltunowicz T. N., Zukowski P., *Temperature and frequency dependences of real part of impedance in the FeCoZr-doped PZT nanogranular composites*, "Materials Science-Poland", 2012, vol. 30, no. 2, p. 75–81.
DOI: <https://doi.org/10.2478/s13536-012-0015-2>
213. Koltunowicz T. N., Zhukowski P., Fedotov A. K., Larkin A. V., Patryn A., Andryevskyy B., Saad A., Fedotova J. A., Fedotova V. V., *Influence of Matrix Type on Negative Capacitance Effect in Nanogranular Composite Films FeCoZr-Insulator*, "Elektronika ir Elektrotechnika", 2013, vol. 19, no. 4, p. 37–40.
DOI: <http://dx.doi.org/10.5755/j01.eee.19.4.1693>
214. Zukowski P., Koltunowicz T. N., Boiko O., Bondariev V., Czarnacka K., Fedotova J. A., Fedotov A. K., Svito I., *Impedance model of metal-dielectric nanocomposites produced by ion-beam sputtering in vacuum conditions and its experimental verification for thin films of $(\text{FeCoZr})_x(\text{PZT})_{(100-x)}$* , "Vacuum", 2015, vol. 120, p. 37–43.
DOI: <https://doi.org/10.1016/j.vacuum.2015.04.035>
215. Koltunowicz T. N., Zukowski P., Boiko O., Fedotova J. A., Method of manufacturing a capacitor for integrated circuits, patent no. B1 235371, approved 29.07.2019 (in Polish).
216. Koltunowicz T. N., Zukowski P., Bondariev V., Fedotov A. K., Fedotova J., Saad A., *Voltage and Current Resonance in Nanocomposite $(\text{FeCoZr})_x(\text{CaF}_2)_{100-x}$ Produced by Ion-Beam Sputtering in Pure Argon Atmosphere*, "Acta Physica Polonica A", 2015, vol. 128, no. 5, p. 897–900. DOI: <https://doi.org/10.12693/APhysPolA.128.897>
217. Hemprowicz P., *Elektrotechnika i elektronika dla nieelektryków*, Warsaw, WNT, 2013 (in Polish).
218. Koltunowicz T. N., Fedotova J. A., Zhukowski P., Saad A., Fedotov A., Kasiuk J. V., Larkin A. V., *Negative Capacitance in (FeCoZr) - (PZT) nanocomposite film*, "Journal of Physics D-Applied Physics", 2013, vol. 46, art. no. 125304.
DOI: <https://doi.org/10.1088/0022-3727/46/12/125304>
219. Koltunowicz T. N., Zukowski P., Boiko O., Saad A., Fedotova J. A., Fedotov A. K., Larkin A. V., Kasiuk J., *AC Hopping Conductance in Nanocomposite Films with Ferromagnetic Alloy Nanoparticles in a PbZrTiO_3 Matrix*, "Journal of Electronic Materials", 2015, vol. 44, no. 7, p. 2260–2268. DOI: <https://doi.org/10.1007/s11664-015-3685-9>
220. Boiko O., Koltunowicz T. N., Zukowski P., Fedotov A. K., Larkin A. V., *The effect of sputtering atmosphere parameters on dielectric properties of the ferromagnetic alloy – ferroelectric ceramics nanocomposite $(\text{FeCoZr})_x(\text{PbZrTiO}_3)_{100-x}$* , "Ceramics International", 2017, vol. 43, p. 2511–2516. DOI: <https://doi.org/10.1016/j.ceramint.2016.11.052>
221. Bolkowski S., *Elektrotechnika*, Warsaw, Poland, School and Pedagogical Publishing Houses WSiP, 2016 (in Polish).
222. Buczaj M., Michalak D., *Smart City. Elementy zarządzania środowiskiem i infrastrukturą inteligentnego miasta*, Warsaw, Poland, Texter, 2018 (in Polish).
223. PN–HD 60364. Instalacje elektryczne niskiego napięcia. PWN Publishing House, Warsaw – grupa arkuszy norm (in Polish).
224. Markiewicz H., *Instalacje elektryczne*, Warsaw, WNT, 2008 (in Polish).
225. Petykiewicz P., *Nowoczesna instalacja elektryczna w inteligentnym budynku*, Warsaw, COSiW SEP, 2001 (in Polish).
226. Buczaj M., *Integracja systemów sterowania i nadzoru w budynkach w aspekcie realizacji przez nie zadań systemów alarmowych*, „Logistyka”, vol. 6/2011, p. 335–342 (in Polish).
227. Buczaj M., *Systemy sterowania i nadzoru szyte na miarę*, „Zabezpieczenia”, vol. 6, no. 88/2012, p. 20–24 (in Polish).
228. Horyński M., *Efektywne wykorzystanie energii w domach z odnawialnymi źródłami energii*, „TTS Technika Transportu Szynowego”, 2013, vol. 10, p. 827–836 (in Polish).
229. Lewandowski W. M., *Proekologiczne odnawialne źródła energii*, Warsaw, Poland, WNT, 2010 (in Polish).
230. Malicki W., Miedziński B., Rutecki K., Habrych M., *Ogniwa fotowoltaiczne w elektrycznych instalacjach zasilających*, „Mechanizacja i Automatyzacja Górnictwa”, 2010, vol. 7, p. 121–125 (in Polish).
231. Tytko R., *Odnawialne źródła energii*, Warsaw, Poland, OWG, 2009 (in Polish).

232. Mikulik J., *Budynek Inteligentny. Tom II. Podstawowe systemy bezpieczeństwa w budynkach inteligentnych*, Gliwice, Poland, Wydawnictwo Politechniki Śląskiej, 2010 (in Polish).
233. Niezabitowska E., *Budynek inteligentny. Tom I. Potrzeby użytkownika a standard budynku inteligentnego*, Gliwice, Poland, Wydawnictwo Politechnik Śląskiej, 2005 (in Polish).
234. Sinopoli J., *Smart building system for architects, owners and builders*, New York, USA, Elsevier, 2010.
235. Pelech A., *Wentylacja i klimatyzacja. Podstawy*, Wrocław, Poland, Oficyna Wydawnicza Politechniki Wrocławskiej, 2008 (in Polish).
236. *Desigo system – build the future today*, [In:] new.siemens.com [access: 19.06.2022].
<https://new.siemens.com/global/en/products/buildings/automation/desigo.html>
237. *Meternet – liczniki zdalnego odczytu i rejestracji*, [In:] fif.com.pl [access: 19.06.2022].
www.fif.com.pl/pl/62-meternet-system-zdalnego-odczytu-i-rejestracji
238. *Poznaj nasz produkt Energia@4*, [In:] numeron.pl [access: 19.06.2022].
<https://www.numeron.pl/energia4>
239. Komarnicki P., Wenge C., Pietracho R., *Elektromobilność – integracja pojazdów elektrycznych z infrastrukturą sieci elektroenergetycznej*, „Przegląd Elektrotechniczny”, 2020, vol. 1, no. 5, p. 3-15.
240. Sharma H., Rylander M., Dorr D., *Grid Impacts Due to Increased Penetration of Newer Harmonic Sources*, “IEEE Transactions on Industry Applications”, 2016, vol. 52, no. 1, p. 99–104. DOI: <https://doi.org/10.1109/REPCon.2013.6681854>
241. Bollen M., Ronnberg S., Zavoda F., Langella R., Djokic S., Cui P., Meyer J., Cuk V., *Consequences of smart grids for power quality: Overview of the results from CIGRE joint working group C4.24/CIREC*, [In:] IEEE PES Innovative Smart Grid Technologies Conference Europe (ISGT-Europe), Torino, Italy, September 26-29, 2017.
242. Chudy A., Mazurek P., *Electromobility – the Importance of Power Quality and Environmental Sustainability*, “Journal of Ecological Engineering”, 2019, vol. 20, no. 10, p. 15–23.
DOI: <https://doi.org/10.12911/22998993/112713>
243. *Global EV Outlook 2021*, [In:] iea.org [access: 29.04.2022].
<https://www.iea.org/reports/global-ev-outlook-2021>
244. *Napędzamy elektromobilność!*, [In:] pspa.com.pl [access: 29.04.2022]. <https://pspa.com.pl/>
245. Firlt A., Hanzelka Z., Piątek K., Barcentewicz S., Chmielowiec K., Dutka M., *Monitorowanie jakości dostawy energii elektrycznej z uwzględnieniem supra-harmonicznych oraz synchronozatorów*, „Przegląd Elektrotechniczny”, 2020, vol. 1, no. 3, p. 61–64 (in Polish).
246. Nour M., Chaves-Ávila J. P., Magdy G., Sánchez-Miralles Á., *Review of Positive and Negative Impacts of Electric Vehicles Charging on Electric Power Systems*, “Energies”, 2020, vol. 13, no. 18, art. no. 4675. DOI: <https://doi.org/10.3390/en13184675>
247. Khalid M. R., Alam M. S., Sarwar A., Jamil Asghar M. S., *A Comprehensive review on electric vehicles charging infrastructures and their impacts on power-quality of the utility grid*, “eTransportation”, 2019, vol. 1, no. 3, art. no. 100006.
DOI: <https://doi.org/10.1016/j.etrans.2019.100006>
248. Kim K., Song C. S., Byeon G., Jung H., Kim H., Jang G., *Power demand and total harmonic distortion analysis for an EV charging station concept utilizing a battery energy storage system*, “Journal of Electrical Engineering & Technology”, 2013, vol. 8, p. 1234–1242.
DOI: <https://doi.org/10.5370/JEET.2013.8.5.1234>
249. Chudy A., Mazurek P., *Wprowadzenie do projektowania algorytmów zarządzających siecią dystrybucji energii z obciążeniami ładowania pojazdów*, „Przegląd Elektrotechniczny”, 2022, vol. 1, no. 1, p. 73–76 (in Polish).
250. Mazurek P., Chudy A., *An Analysis of Electromagnetic Disturbances from an Electric Vehicle Charging Station*, “Energies”, 2022, vol. 15, no. 1, art. no. 244.
DOI: <https://doi.org/10.3390/en15010244>
251. Mazurek P., Chudy A., *Zagadnienia jakości energii stacji ładowania pojazdów elektrycznych*, „Przegląd Elektrotechniczny”, 2021, vol. 1, no. 4, p. 105–110 (in Polish).

252. Ahmadi A., Tavakoli A., Jamborsalamati P., Rezaei N., Miveh M. R., Gandoman F. H., Heidari A., Nezhad A. E., *Power quality improvement in smart grids using electric vehicles: a review*, "IET Electrical Systems in Transportation", 2019, vol. 9, no. 2, p. 53–64.
DOI: <https://doi.org/10.1049/iet-est.2018.5023>
253. Regulation of the Minister of Economy dated May 4, 2007 on detailed conditions of functioning of the power system, Journal of Laws of 29 May 2007, item 623.
254. PN-EN 50160:2010, *Voltage characteristics of electricity supplied by public electricity networks* (in Polish).
255. Alam M. J. E., Muttaqi K. M., Sutanto D., *Effective Utilization of Available PEV Battery Capacity for Mitigation of Solar PV Impact and Grid Support with Integrated V2G Functionality*, "IEEE Transactions on Smart Grid", 2016, vol. 7, no. 3, p. 1562–1571.
DOI: <https://doi.org/10.1109/TSG.2015.2487514>
256. Marra F., Yang G. Y., Fawzy Y. T., Traeholt C., Larsen E., Garcia Valle R., Jensen M. M., *Improvement of Local Voltage in Feeders with Photovoltaic Using Electric Vehicles*, "IEEE Transactions on Power Systems", 2013, vol. 28, no. 3, p. 3515–3516.
DOI: <https://doi.org/10.1109/TPWRS.2013.2248959>
257. Bątkiewicz-Pantuła M., *The problem of determining the coefficient of flicker in accordance to normative regulations*, "Przegląd Elektrotechniczny", 2020, vol. 1, no. 1, p. 54–57.
258. Slade P. G., *The Vacuum Interrupter Theory, Design, and Application*, Boca Raton Florida USA, CRC Press, 2021.
259. Montreal Protocol on Substances that Deplete the Ozone Layer, Montreal, 1987.
260. Kyoto Protocol to the United Nations Framework Convention on Climate Change, Kyoto, 1997.
261. Regulation (EU) No 517/2014 of the European Parliament and of the Council on fluorinated greenhouse gases of 16 April 2014.
262. Power engineering, distribution and transmission, Polish Power Transmission and Distribution Association's Report, Poznań, 2021.
263. Lee W. Y., Jun J. U., Oh H. S., Park J. K., Oh Y. H., Song K. D., Jang H. J., *Comparison of the Interrupting Capability of Gas Circuit Breaker According to SF₆, g₃, and CO₂/O₂ Mixture*, "Energies", 2020, vol. 13, art. no. 6388. DOI: <https://doi.org/10.3390/en13236388>
264. Stoczko S., Szewczyk M., Pochanke Z., Chmielak W., *Experimental study on field emission current in vacuum interrupter at functional limit of vacuum pressure*, "Electric Power Systems Research", 2021, vol. 191, art. no. 106860.
DOI: <https://doi.org/10.1016/j.epsr.2020.106860>
265. Li S., Geng Y., Liu Z., Wang J., *"V" shape curves of physical parameters of field emitters versus applied voltage toward breakdown in vacuum*, "IEEE Transactions on Dielectrics and Electrical Insulation", 2008, vol. 25, p. 749–755.
DOI: <https://doi.org/10.1109/TDEI.2018.007038>
266. Gortschakow S., Franke S., Methling R., Gonzalez D., Lawall A., Taylor E. D., *Graskowski F., Properties of Vacuum Arcs Generated by Switching RMF Contacts at Different Ignition Positions*, "Energies", 2020, vol. 13, art. no. 5596. DOI: <https://doi.org/10.3390/en13215596>
267. Węgierek P., Lech M., Kozak C., Pastuszak J., *Methodology for testing the electric strength of vacuum chambers designed for modern medium voltage switchgear*, "Metrology and Measurement Systems", 2020, vol. 27, p. 687–700.
DOI: <https://doi.org/10.24425/mms.2020.134847>
268. Lech M., Węgierek P., *Breakdown Initiation and Electrical Strength of a Vacuum Insulating System in the Environment of Selected Noble Gases at AC Voltage*, "Energies", 2022, vol. 15, art. no. 1154. DOI: <https://doi.org/10.3390/en15031154>
269. Węgierek P., Lech M., *Test stand for testing and diagnostics of medium voltage vacuum interrupters*, "Przegląd Elektrotechniczny", 2021, vol. 97, no. 2, p. 176–179.
270. Węgierek P., Lech M., Kostyła D., Kozak C., *Study on the Effect of Helium on the Dielectric Strength of Medium-Voltage Vacuum Interrupters*, "Energies", 2021, vol. 14, art. no. 3742.
DOI: <https://doi.org/10.3390/en14133742>

271. Mohanty S. P., Choppali U., Koungianos E., *Everything you wanted to know about smart cities: the internet of things is the backbone*, "IEEE Consumer Electronics Magazine", 2016, vol. 5, p. 60–70. DOI: <https://doi.org/10.1109/MCE.2016.2556879>.
272. Nam T., Pardo T. A., *Smart city as urban innovation: Focusing on management, policy, and context*, [In:] Proceedings of the 5th international conference on theory and practice of electronic governance, Tallinn, Estonia, September 26–28, 2011, p. 185–94. DOI: <https://doi.org/10.1145/2072069.2072100>
273. Fang X., Misra S., Xue G., Yang D., *Smart grid—the new and improved power grid: A survey*, "IEEE Communications Surveys & Tutorials", 2012, vol. 14, p. 944–80. DOI: <https://doi.org/10.1109/SURV.2011.101911.00087>
274. *The History of Making the Grid Smart*, [In:] ethw.org [access: 26.05.2022]. https://ethw.org/The_History_of_Making_the_Grid_Smart
275. Yu Y., Luan W., *Smart grid and its implementations*, Proceedings of the CSEE, 2009, vol. 29, no. 34, pp. 1–8.
276. Greer C., Wollman D. A., Prochaska D. E., Boynton P. A., Mazer J. A., Nguyen C. T., *NIST framework and roadmap for smart grid interoperability standards, release 3.0*, 2014. DOI: <https://doi.org/10.6028/NIST.SP.1108r3>
277. *Kolekcja zdjęć; obrazy, grafiki, wektory i filmy bez tantiem | Adobe Stock*, [In:] stock.adobe.com [access: 01.06.2022]. <https://stock.adobe.com/pl/images/smart-grid-vector-diagram/109606618>
278. Gouveia C., Rua D., Soares F. J., Moreira C., Matos P., Lopes J. P., *Development and implementation of Portuguese smart distribution system*, "Electric Power Systems Research", 2015, vol. 120, p. 150–62. DOI: <https://doi.org/10.1016/j.epsr.2014.06.004>
279. Delfanti M., Fasciolo E., Olivieri V., Pozzi M., *A2A project: A practical implementation of smart grids in the urban area of Milan*, "Electric Power Systems Research", 2015, vol. 120, p. 2–19. DOI: <https://doi.org/10.1016/j.epsr.2014.11.019>
280. Delfanti M., Falabretti D., Fiori M., Merlo M., *Smart Grid on field application in the Italian framework: The AS SE. M. project*, "Electric Power Systems Research", 2015, vol. 120, p. 56–69. DOI: <https://doi.org/10.1016/j.epsr.2014.09.016>
281. Bracco S., Delfino F., Pampararo F., Robba M., Rossi M., *A mathematical model for the optimal operation of the University of Genoa Smart Polygeneration Microgrid: Evaluation of technical, economic and environmental performance indicators*, "Energy", 2014, vol. 64, p. 912–922. DOI: <https://doi.org/10.1016/j.energy.2013.10.039>
282. López G., Moreno J., Amaris H., Salazar F., *Paving the road toward smart grids through large-scale advanced metering infrastructures*, "Electric Power Systems Research", 2015, vol. 120, p. 194–205. DOI: <https://doi.org/10.1016/j.epsr.2014.05.006>
283. Adamec M., Pavlatka P., Stary O., *Costs and benefits of smart grids and accumulation in Czech distribution system*, "Energy Procedia", 2011, vol. 12, p. 67–75. DOI: <https://doi.org/10.1016/j.egypro.2011.10.011>
284. Węgierek P., Staszak S., Pastuszek., *EKTOS – innovative medium voltage outdoor vacuum disconnecter in a closed housing dedicated to the network Smart Grids*, "Wiadomości Elektrotechniczne", 2019, vol. R87, no. 11, p. 21–25.
285. Chmielak W., *Review of methods of diagnostics of the vacuum in vacuum circuit breakers*, "Przegląd Elektrotechniczny", 2014, vol. 90, no. 2, p. 213–216. DOI: <https://doi.org/10.12915/pe.2014.02.54>
286. Bang S., Lee H. W., Lee B. W., *Real-Time Monitoring of the Vacuum Degree Based on the Partial Discharge and an Insulation Supplement Design for a Distribution Class Vacuum Interrupter*, "Energies", 2021, vol. 14, art. no. 7891. DOI: <https://doi.org/10.3390/en14237891>
287. Damstra G. C., *Pressure Estimation in Vacuum Circuit Breakers*, "IEEE Transactions on Dielectrics and Electrical Insulation", 1995, vol. 2, no. 2., p. 198–201. DOI: <https://doi.org/10.1109/94.388240>

288. *Informacja statystyczna o energii elektrycznej*, [In:] are.waw.pl [access: 19.06.2022].
<https://www.are.waw.pl/component/phocadownload/category/32-informacja-statystyczna-o-energii-elektrycznej?download=153:informacja-statystyczna-o-energii-elektrycznej-nr-2-338-luty-2022>
289. *Jak działa fotowoltaika? Działanie instalacji fotowoltaicznej w pigułce*, [In:] eon.pl [access: 17.06.2022].
<https://www.rynekelektryczny.pl/produkcja-energii-z-malych-instalacji-oze/>
290. *Małe instalacje OZE – produkcja i moc zainstalowana*, [In:] rynekelektryczny.pl [access: 17.06.2022].
<https://eon.pl/dla-domu/portal-o-odnawialnych-zrodlach-energii/energia-ze-slonca/fotowoltaika-jak-dziala>, access of 17.06.2022
291. Jaskółowski W., *Instalacje fotowoltaiczne*, Warsaw, Zeszyty Naukowe SGSP, 2016 (in Polish).
292. Flizikowski J., Mroziński A., *Inżynieria instalacji fotowoltaicznych*, Bydgoszcz, Poland, Grafpol, 2016 (in Polish).
293. *Branża fotowoltaiczna to znacząca siła na polskim rynku*, [In:] ieo.pl [access: 19.06.2022].
<https://ieo.pl/pl/raport-pv-2021>
294. *Rynek Mikroinstalacji Fotowoltaicznych POLSKA '20 – nowy raport Stowarzyszenia Branży Fotowoltaicznej POLSKA PV*, [In:] polskapv.pl [access: 17.06.2022].
<https://polskapv.pl/rynek-mikroinstalacji-fotowoltaicznych-polska-20-nowy-raport-stowarzyszenia-branzy-fotowoltaicznej-polska-pv/>
295. *Budowa ogniwa fotowoltaicznego i zasady jego działania*, [In:] stiloenergy.pl [access: 17.06.2022].
<https://stiloenergy.pl/budowa-ogniwa-fotowoltaicznego-i-zasada-dzialania/>
296. Lewandowski W. M., *Proekologiczne Źródła energii*, Warsaw, WNT, 2006.
297. Stryczewska H. D., Nalewaj, K., Pawłat J., Ratajczak E., Goleman R., *Energie odnawialne Przegląd technologii i zastosowań*, Lublin, Poland, Wydawnictwo Politechniki Lubelskiej, 2012.
298. Olczak P., Olek M., Matuszewska D., Dyczko A., Mania T., *Monofacial and Bifacial Micro PV Installation as Element of Energy Transition—The Case of Poland*, “Energies”, 2021, vol. 14, art. no. 499. DOI: <https://doi.org/10.3390/en14020499>
299. *Advanced Module Technologies 2019 Report download*, [In:] taiyangnews.info [access: 17.06.2022].
<http://taiyangnews.info/reports/advanced-module-technologies-2019>
300. *Solar Photovoltaic System Design Basics*, [In:] www.energy.gov [access: 17.06.2022].
<https://www.energy.gov/eere/solar/solar-photovoltaic-system-design-basics>
301. Kopecek R., Libal J., *Towards large-scale deployment of bifacial photovoltaics*, “Nature Energy”, 2018, vol. 3, p. 443–446.
302. Boglietti A., Cavagnino A., Jennings S., Popescu M., Staton D. A., *Assessment of fractional and small power three phase induction motors for conveyor applications*, [In:] The XIX International Conference on Electrical Machines - ICEM 2010, Rome, Italy, 6-8 September, 2010, p. 1–6. DOI: <https://doi.org/10.1109/ICELMACH.2010.5607722>
303. *Zasada działania falownika – sterowanie wektorowe lub skalarne*, [In:] fif.com.pl [access: 19.06.2022].
https://www.fif.com.pl/pl/aktualnosci/50_zasada-dzialania-falownika-sterowanie-wektoro.html
304. Dong T., Barbosa C., *Capacitance Variation Induced by Microfluidic Two-Phase Flow across Insulated Interdigital Electrodes in Lab-On-Chip Devices*, “Sensors”, 2015, 15(2), p. 2694-2708. DOI: <https://doi.org/10.3390/s150202694>
305. *What is a photoelectric sensor?*, [In:] keyence.eu [access: 19.06.2022].
<https://www.keyence.eu/ss/products/sensor/sensorbasics/photoelectric/info/>
306. *What is HMI?*, [In:] inductiveautomation.com [access: 19.06.2022].
<https://www.inductiveautomation.com/resources/article/what-is-hmi>
307. *Is a PLC fast enough to meet my application's requirements?*, [In:] motioncontroltips.com [access: 19.06.2022].
<https://www.motioncontroltips.com/faq-plc-fast-enough-meet-applications-requirements/>

308. *Robotyzacja w przemyśle spożywczym*, [In:] par.pl [access: 19.06.2022].
https://par.pl/2007/files/01-07_artykul2p.pdf
309. Zhi-jie J., Chun-yu H., Jun W., Zhong Z., *Development and application of automation control system to plate production line*, [In:] 11th International Conference on Control Automation Robotics & Vision, Singapore, 7–10 December, 2010, p. 678–681.
DOI: <https://doi.org/10.1109/ICARCV.2010.5707251>
310. Krishnan S. V., Singh V., Shah P., Yadav A., Panampilly G., Saha S., Shukla H. D., *Development of an RFID-Based Semi-autonomous Robotic Library Management System*, [In:] 4th International Conference on Automation, Control and Robots (ICACR), Rome, Italy, 11–13 October, 2020, p. 26–31, DOI: <https://doi.org/10.1109/ICACR51161.2020.9265493>



POLITECHNIKA LUBELSKA



HENRYKA D. STRYCZEWSKA PhD DSc Eng. is a full professor at the Lublin University of Technology, Department of Electrical Engineering and Electrotechnologies, a senior member of the IEEE, and a member of the Presidium of the Electrotechnical Committee of the Polish Academy of Science (KE PAN). She is the coordinator and manager of international scientific programs: the 5th EU FP (contract No. ENK6-CT-2002-80668: European Center of Excellence on the Application of Superconductivity and Plasma Technologies in Power Engineering ASPPECT [2002–2006], the 7th FP of EU – Maria Curie Reintegration grant “Plasma Sterilization” [2010–2014], the 7th FP of EU – KORANET

Project, Environmental and Biomedical Applications of Gliding Arc Discharge Plasma [ENV-BIO-GA; 2012–2014]). Her major research area includes supply systems for ozone generators and non-thermal plasma reactors, in particular with gliding arc discharge, electromagnetic processes, and devices used in environmental protection technologies.



KENJI EBIHARA received the DEng in Electrical Engineering, Kyushu University in 1979. From 1984 to 2007, he was Professor of Kumamoto University and is Professor Emeritus of same University. He has been Director of Environment and Energy Laboratory established in 2009. He was awarded the order of the Sacred Treasure, Gold Rays with Neck Ribbon in November 2021. He is the author of five books, more than 100 journal papers, 120 conference papers, 40 seminar and invited lectures and seven patents. His research interests include ozone sterilization for agriculture and plant growth as well as bio-medical treatment. He was awarded the order of the Sacred Treasure in 2021.

ISBN 978-83-7947-556-8



9 788379 475568

